Many-body theory of electron-phonon coupling in polar semiconductors and superconductors



Nikolaus Kandolf

Corpus Christi College

University of Oxford

A thesis submitted for the degree of

Doctor of Philosophy

Trinity 2022

Acknowledgements

I want to thank Feliciano Giustino both for giving me the chance to work with him, and for inviting me to America. I also want to thank my coworkers in Austin, Annecy Liddell, Hyungjun Lee, Chao Lian, Viet-Anh Ha, Joshua Leveillee, Jon Lafuente Bartolomé, Sabyasachi Tiwari, and Weng Hong Sio, as well as my collaborators Carla Verdi and Roxana Margine for being extremely helpful and supportive during this time.

I wish to thank my parents, Christine and Helmut, for encouraging me to take risks and try things out, and my brothers, Leonhard and Christian, for being extremely delightful individuals to spend time with.

Next, I want to thank the many great friends I made in Oxford who made my time at Corpus the happiest time in my life so far: Martin Abel, Faseeha Ayaz, Serte Donderwinkel, Kate Farrow, Maria del Rocío Gómez-Ruiz, Llewelyn Hopwood, Robert Laurella, Tara Lee, Walker Mimms, Aleksander Ulatowski, Anna Verde, Andrea Vitangeli, Philip Wilson, Karl-Michael Ziems, among others.

I also wish to thank my former teachers for giving me chances to grow and giving access to tremendous opportunity: Georg Kresse, Menno Bokdam, Claudia Draxl, Caterina Cocchi, Martin Fally, Jürgen Klepp, Herwig Burian, Gerhild Graf, Beate Kröpfl, Daniela Glantschnig.

Abstract

In polar semiconductors and insulators, thermal vibrations of the ionic lattice give rise to long-ranged electric fields that can scatter electrons and holes very efficiently. This interaction is known as Fröhlich coupling, and it is the source for a range of intriguing many-body effects in these materials.

We consider two scenarios: Firstly, the normal state, in which Fröhlich coupling can give rise to a coupled electron-phonon state, or "polaron", which causes a strong renormalisation of the electronic energy with major implications for excitation energies and charge-carrier mobilities in a material. A characteristic feature of polaron spectra, e.g. as observed in photoemission experiments, are low-energy sidebands near the main photoemission peak whose energetics are of the order of the most strongly coupled phonon modes. These sidebands are often referred to as "polaron satellites".

Secondly, the superconducting state, in which Fröhlich coupling provides the attractive pairing potential required for the formation of Cooper pairs. A paradigmatic example for the large class of polar semiconductors is $SrTiO_3$, which hosts a strongly renormalised polaronic state in the conduction band, and whose phase diagram features a superconducting dome as a function of electron doping.

In this thesis, we employ an analytical model of Fröhlich-type coupling between a parabolic electron band with finite electron occupation and a dispersionless LO phonon to study the coupled electron-phonon state in doped $SrTiO_3$. Our analytical approach allows us to model all the relevant interactions with arbitrary resolution and provides insights into the intriguing many-body effects in Fröhlich-type semiconductors.

In the normal state, we calculate the interacting electron spectral function from a Green's function theory of electron phonon coupling for a range of doping levels and coupling strengths. Electron-phonon coupling is taken into account at the level of the Fan-Migdal self-energy. We compare the spectral functions obtained from two approximations to the interacting Green's function for a wide range of Fermi energies and coupling strengths, derive analytical expressions for the quasiparticle renormalisation as a function of electron doping, and discuss limiting cases of the second-order self-energy approximation.

In the superconducting state, we employ Migdal-Eliashberg theory to calculate the critical temperature T_C of doped $SrTiO_3$ as a function of doping level. In particular, our analytical approach allows us to explicitly model the attractive Fröhlich interaction and repulsive Coulomb interaction at generalised frequencies and momenta. Very good

qualitative agreement of our results with experimental data is obtained. We emphasise the major contribution of free-carrier screening to the effective pairing potential, and we investigate promising avenues for improving the predictive power of *ab initio* calculations of the superconducting T_{C}.

Contents

1 Introduction **1**

1.1 Fröhlich quasiparticle spectra in the normal state 6

1.2 Fröhlich superconductivity in doped $SrTiO_3$ 9

1.3 Outline of the thesis 12

2 Electron-phonon interactions from first principles **15**

2.1 Normal state 16

2.1.1 Electron-phonon Hamiltonian 17

2.1.2 Electron Green's function 19

2.1.3 Electron self-energy 21

2.1.4 Screened Coulomb interaction 25

2.1.5 Dyson quasiparticle spectrum 27

2.1.6 Cumulant expansion quasiparticle spectrum 30

2.2 Superconducting state 36

2.2.1 Migdal-Eliashberg theory 37

2.2.2 Linearised Migdal-Eliashberg equations 44

2.2.3 Morel-Anderson Coulomb potential 45

2.2.4 Fermi-surface restricted equations 47

2.2.5 McMillan equation 48

3 Fröhlich coupling in doped $SrTiO_3$ **50**

3.1 STO electronic structure from first-principles 51

3.1.1 Cubic phase 52

3.1.2 Tetragonal phase 55

3.2 The doped Fröhlich model 57

3.3 Free-carrier screening 60

3.3.1 Free-carrier screening of the Fröhlich interaction 62

3.3.2 Free-carrier screening of the Coulomb interaction 64

4 Polaron spectra in doped semiconductors 66
4.1 Single electron in the conduction band . . . 68
4.1.1 Quasiparticle properties . . . 71
4.1.2 Satellite properties . . . 73
4.2 Finite Fermi level in the conduction band . . . 73
4.2.1 Quasiparticle properties . . . 76
4.2.2 Satellite properties . . . 80
4.3 Finite Fermi level including free-carrier screening . . . 81
4.3.1 Quasiparticle properties . . . 82
4.3.2 Satellite properties . . . 84
4.4 Experimental quasiparticle weight . . . 85

5 Phonon-mediated superconductivity in doped oxides 88
5.1 McMillan equation . . . 89
5.2 Fermi-surface restricted Migdal-Eliashberg . . . 91
5.3 Linearised Migdal-Eliashberg . . . 93
5.3.1 The role of electron-electron interactions in real systems . . . 95

6 Computational setup 97
6.1 Implementation . . . 97
6.1.1 Initialisation . . . 98
6.1.2 Calculation of the renormalisation functions . . . 100
6.1.3 Diagonalisation of the kernel matrix . . . 101
6.2 Convergence of computational parameters for T_C calculation . . . 102
6.3 Test case: Non-polar hole-doped diamond . . . 103

7 Superconducting dome in doped $SrTiO_3$ 107
7.1 Bare kernel . . . 108
7.2 Mass renormalisation function . . . 109
7.3 Energy shift . . . 111
7.4 Chemical potential . . . 111
7.5 Superconducting dome in doped $SrTiO_3$ . . . 113
7.6 Electronic screening . . . 115

8 Conclusions 118

Appendix

Appendix A Born-von Kármán boundary conditions 123

Appendix B Debye-Waller self-energy 125

Appendix C Phonon-plasmon polaritons **127**

Appendix D Derivation of the Fan-Migdal self-energy **129**
D.1 Single electron in the conduction band 129
D.2 Finite Fermi level in the conduction band 130
D.3 Finite Fermi level including free-carrier screening 131

Appendix E Effective mass of the retarded cumulant **133**

Appendix F Quasiparticle energy and effective mass at finite Fermi energy **134**

Appendix G Quasiparticle energy and effective mass at finite Fermi energy including free-carrier screening **137**

Appendix H Anisotropic linearised Migdal-Eliashberg equations for the doped Fröhlich solid **140**

References **142**

1 Introduction

In this thesis, we consider interactions between electrons and phonons in ionic crystals. If the atomic bonds in a crystal have a strong ionic character, as is the case for instance in many oxide materials, vibrations of the crystal lattice can generate long-ranged electric fields.[1] This polarisation field can then scatter free charge carriers and thereby strongly affect the dynamics of electrons and holes in the crystal.

It is possible to observe the effect of this interaction on electronic states using, for example, angle-resolved photoemission spectroscopy (ARPES).[2–9] In such an experiment, electrons are extracted from a sample via laser or synchrotron light. The energy and momentum of the electron prior to exiting the sample is then reconstructed by an analyser. This setup provides a direct image of the momentum-resolved electron spectral function, that is, the band structure of the interacting electron. In Figs. 1.1 and 1.2, we show two examples of experimental ARPES measurements of the doped conduction band of polar $SrTiO_3$ [reprinted from Refs. [6] and [7]]. Note that similar spectra have been reported for, among others, TiO_2,[4] EuO,[9] $CaMnO_3$,[10] and ZnO.[11]

In a simple physical picture, we can describe the many-body renormalisation effects as follows: One assumes that a negatively charged electron passing through the crystal causes a small deformation of the lattice by attracting the positively charged cations and repelling the negatively charged anions. This causes a local polarisation in the crystal which moves along with the electron (one speaks of the "dressing" of the electron by

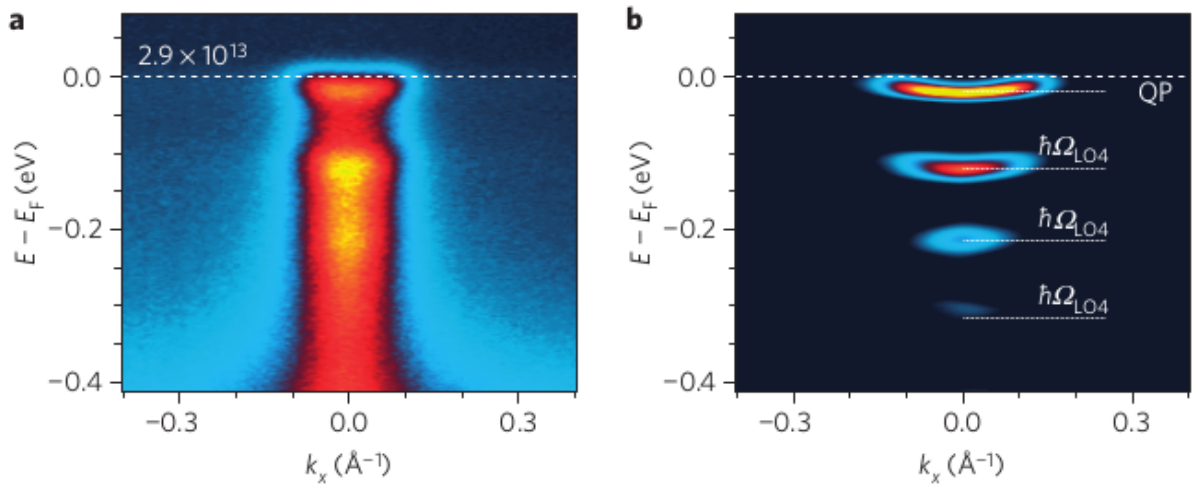


Figure 1.1: Experimental photoemission spectrum of the conduction band of doped $SrTiO_3$, at a charge-carrier concentration of $n_0 = 2.9 \times 10^{13}$ cm^{-3}. reprinted from Ref. [6]. (a) Intensity map of the raw experimental data as a function of energy relative to the Fermi level (dashed white line) and momentum relative to the zone centre. (b) Curvature plot of the raw data (second derivative with respect to the frequency) highlighting the characteristic satellite structure. The energy of the highest LO phonon mode is equal to $\hbar\Omega_{\mathrm{LO4}} \approx$100 meV.

a polarisation cloud).[12–15] The coupled electron-phonon state is referred to as electron "quasiparticle" (QP), or "polaron".[16]

In the analysis of experimental spectra such as the one shown in Figs 1.1 (b) and 1.2 (b)-(d) and (f), it is customary to distinguish between the main quasiparticle, meaning the peak with the highest intensity close to the Fermi energy, and the satellites. In this thesis, we follow this nomenclature as we aim to connect our results to experimental observation. However, from a theoretical point of view, there is no *a priori* reason to introduce such a distinction as the quasiparticle is simply defined as all the poles of the interacting Green's function, including both the "main" peak and all additional sidebands.

The broadening of the QP peak is proportional to the reciprocal of the scattering rate, or, equivalently, to the finite lifetime of the coupled state. The energy and effective mass of the quasiparticle peak are renormalised with respect to the non-interacting system: in general, one observes that electron-phonon interactions increase the mass of the conduction electrons.

The formation of satellite states in photoemission spectra is not unique to polarons: coupled electron-plasmon or electron-magnon states, among others, have been shown to

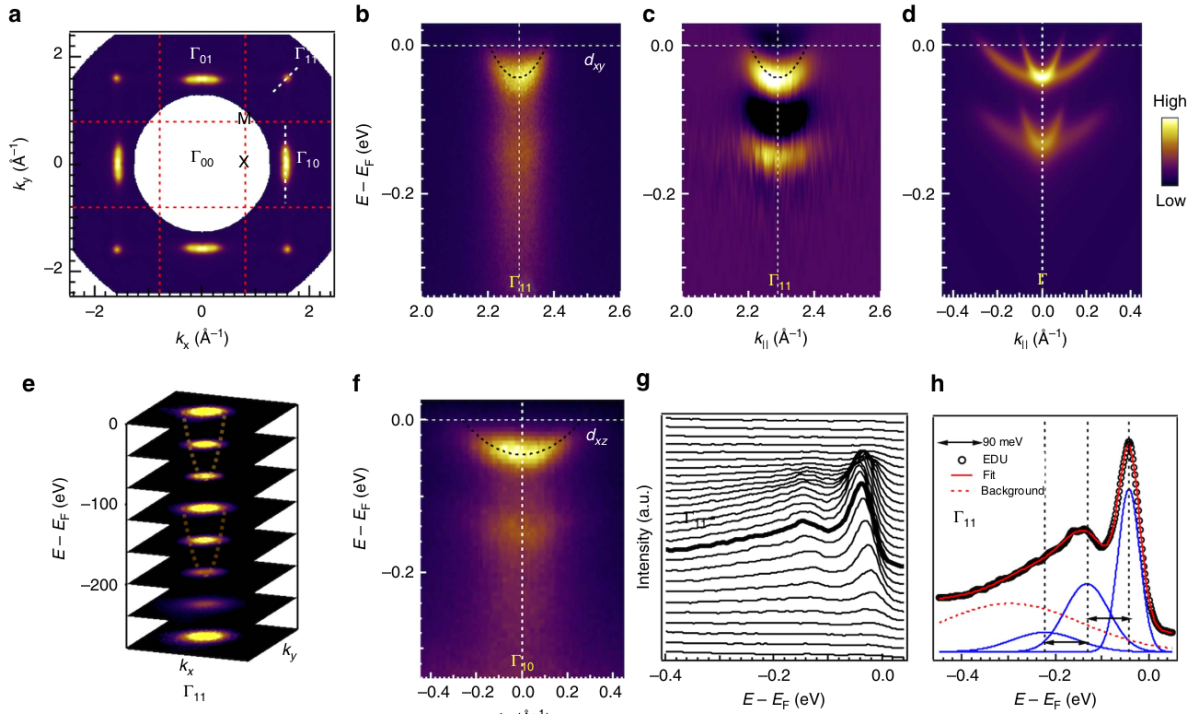


Figure 1.2: Fröhlich polaron spectrum in doped $SrTiO_3$ obtained from ARPES, reprinted from Ref. [7]. (a) Fermi surface in $k_x - k_y$ space indicating the Γ_{10} and Γ_{11} high-symmetry points in the Brillouin zone. (b) Dispersion from Γ_{11} along [11] direction, the orbital character of the conduction band is d_{xy}. (c) Curvature plot of *b*. (d) Simulated polaron dispersion with d_{xy}/d_{yz} and d_{xz} orbital characters. (e) Constant-energy contour of the electron pocket. (f) Dispersion from Γ_{10} along [10] direction, the orbital character of the conduction band is d_{xz} (g) Energy distribution curves of the spectrum in *b* (h) Franck-Condon line shape fitting.

give rise to kinks and satellites.[17,18] In the case of doped $SrTiO_3$, however, the satellites are offset by integer multiples of the highest LO phonon energy, and their position remains constant when the doping level is varied.[2,6,7] Taken together, these facts are a strong indication of electron-phonon coupling, and to confirm this hypothesis, one would like to rely on theoretical spectra calculated from first principles.

For metallic systems, many-body spectra have been investigated theoretically since the 1960s,[19] and first experimental reports became available at the turn of the century.[20] As long as the Fermi energy (measured from the bottom of the conduction band) is much larger than the energy of the relevant phonon modes, the so-called Migdal theorem ensures that many-body effects are well captured in a lowest-order perturbation expansion of the interaction.[21] The situation is different in doped polar semiconductors. Here, the electronic and phonon energy ranges are inverted, and the Migdal approximation is not valid. The

investigation into useful techniques to model electronic spectra in these systems accurately and from first principles is ongoing. We present several contributions to this discussion in Chapter 4 below.

On a macroscopic scale, electron-phonon interactions connect electrical and finite-temperature effects, e.g. causing the electrical resistivity and charge-carrier mobility of a solid to become dependent on temperature. Moreover, they give rise to perhaps the most fascinating property of the electrical conductivity in metals and doped semiconductors: the emergence of a superconducting state below some critical temperature T_C.

In Fig. 1.3, we show the measured superconducting critical temperature of doped $SrTiO_3$ as a function of charge-carrier concentration, as reported by Refs. [22] and [23]. Note the interesting dome shape of T_C in this plot, which we will discuss in detail below.

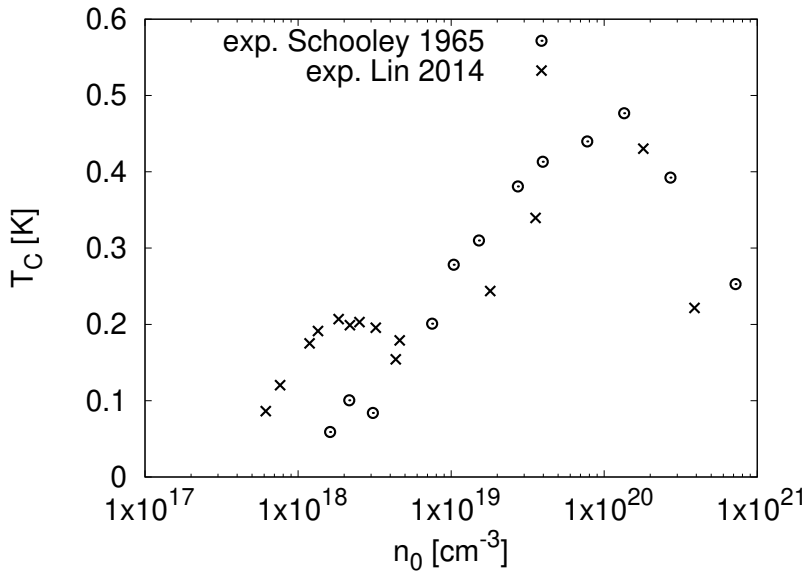


Figure 1.3: Experimental superconducting T_C as reported by Schooley et al. (1965), Ref. [22], shown as black circles, and Lin et al. (2014), Ref. [23], indicated by black crosses.

The fundamental process underpinning the emergence of a superconducting state is the pairing of electrons in a Fermi sea. As first demonstrated by Cooper,[24] even a small net attractive force can lead to the formation of bound electron states, known as Cooper pairs. The number of electrons in the Fermi sea that enter such a bound state depends on the temperature in the systems, as finite-temperature excitations counteract the attractive force on the electrons; the critical temperature T_C marks the onset of pair formation in the system.

As the temperature in the system is reduced below T_C, and more and more electrons form bound states, one observes the opening of an energy gap in the electronic spectrum: Cooper pairs are composite bosons and therefore conform to Bose-Einstein rather than Fermi-Dirac statistics. This allows the coupled states to occupy the same energy eigenstate, which lowers the total energy in the system. Moreover, formerly occupied electronic states near the Fermi surface become vacant, causing the opening of an energy gap.[25]

This energy gap is one of the hallmarks of a superconductor, and it can be measured e.g. via electron tunnelling,[26] or photoemission spectroscopy.[5] As certain states in the continuous electron spectrum are now forbidden, an excitation of one of the remaining electrons must possess an energy that is larger than the gap energy. This effectively suppresses electronic scattering, and the metal becomes a perfect conductor.

Following the discovery of the isotope effect,[27] Fröhlich was the first to explore lattice vibrations as the source for the attractive potential needed for Cooper pair formation.[28] In keeping with our simple physical picture, one notes that the characteristic frequency related to the motion of an electron in a metal is much larger than typical phonon frequencies, $E_F/\hbar \gg \omega_{ph}$. Therefore, one assumes that the time it takes for the ionic lattice to build up a polarisation in response to a passing electron is so long, that the electron causing this deformation has moved on before the response of the lattice is complete. As a result, the local deformation in the ionic lattice causes a net attractive potential that can then interact with another passing electron. This process is referred to as the "exchange of a virtual phonon".[29]

The first theories of superconductivity were most successful in the description of nonpolar metallic systems.[25,30] However, in the meantime, superconducting states have been observed in a wide range of materials, including doped polar semiconductors.[31–35] Recent years have seen great interest in understanding the pairing mechanism in ionic crystals, not least because a superconducting state with a critical temperature of $T_C \approx 100$ K has been observed at the interface of FeSe and $SrTiO_3$.[5,36–43] There exist now rigorous theoretical methods that allow predictive calculations of the superconducting gap and critical temperature from first principles.[44–46] However, the long-range electron-phonon interaction in ionic crystals poses a particular challenge to numerical calculations.

To address this challenge, we present a theoretically rigorous approach to overcome these limitations in Chapter 7.

1.1 Fröhlich quasiparticle spectra in the normal state

The most important contribution to the total electron-phonon coupling in a polar semiconductor is described by the Fröhlich interaction potential. It describes the coupling of electrons to the long-ranged electric fields caused by lattice vibrations in an ionic crystal lattice. These electric fields can scatter electrons and holes very effectively.[47–50]

In a crystal with volume Ω, the Fröhlich coupling matrix element describing the scattering of an electron in state $\mathbf{k}$ into another state $\mathbf{k}' = \mathbf{k} + \mathbf{q}$ is given as:[47]

$$g(\mathbf{q}) = g(|\mathbf{q}|) = \frac{i}{|\mathbf{q}|}\left[\frac{4\pi\,\alpha\,\hbar(\hbar\omega_{\mathrm{ph}})^{3/2}}{\Omega\sqrt{2m_0}}\right]^{1/2}, \tag{1.1}$$

where $\hbar\omega_{\mathrm{ph}}$ is the energy of the phonon mediating the interaction, and m_0 is the band mass of the electron. The strength of the interaction is quantified by the dimensionless Fröhlich coupling constant:

$$\alpha = \frac{e^2}{4\pi\epsilon_0\,\hbar}\sqrt{\frac{m_0}{2\hbar\omega_{\mathrm{ph}}}}\left(\frac{1}{\varepsilon_\infty} - \frac{1}{\varepsilon_0}\right), \tag{1.2}$$

where e is the unit charge of an electron ϵ_0 is the vacuum dielectric constant, and ε_∞ and ε_0 are the dielectric constants of the solid in the optical and static limits, respectively.

We wish to reproduce experimental polaron spectra for systems with Fröhlich-type electron phonon coupling, such as those shown in Figs. 1.1 and 1.2 of doped $SrTiO_3$. Within the framework of a many-body quantum field theory, this is done by constructing the interacting electron Green's function G of the system, and then evaluating its spectrum, that is, its imaginary part. To obtain the function G, one starts from a description of the electronic structure in the ground state, as obtained e.g. from density-functional theory. All energy contributions arising from many-body interactions are captured by a nonlocal quantity known as the electron self-energy Σ, which itself is also evaluated from ground-state properties. A detailed derivation for many-body electron spectra is presented in Chapter 2.

During the past few years, the modelling of Fröhlich couplings has received considerable attention. This process was fuelled in particular by the development of efficient *ab initio*

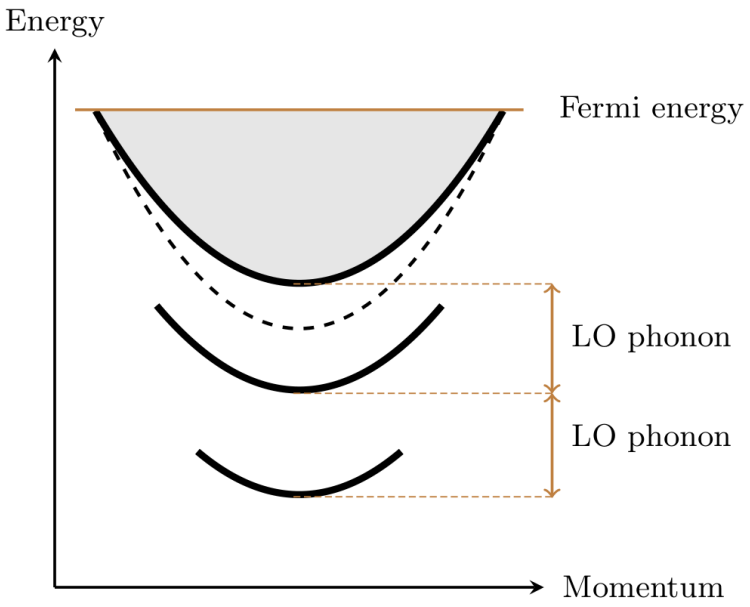


Figure 1.4: Illustration of the many-body renormalisation of the conduction band bottom of a polar semiconductor by the Fröhlich interaction. A parabolic conduction band minimum is doped with electrons up to E_F. The dashed line indicates the non-interacting band structure, solid lines show the renormalised band minimum and phonon sidebands. The energy separation between the QP band and the sidebands is an integer multiple of the LO phonon energy.

techniques to describe long-range electron phonon interactions.[51–54] Moreover, at least in the case of standard metals, where the Fermi energy E_F is much larger than the characteristic phonon energy $\hbar\omega_\mathrm{ph}$, $\hbar\omega_\mathrm{ph}/E_\mathrm{F} \ll 1$, Migdal's theorem guarantees that the interaction is well described by non-crossing electron-phonon self-energy diagrams.[21,29,50]

However, if one attempts to model ARPES spectra of semiconductors, one finds oneself in a theoretically challenging doping regime: Since only occupied electronic states can be probed by ARPES, it is necessary to dope electrons into the sample in order to image the band edges. A schematic illustration of this setup is shown in Fig. 1.4. The distance between the Fermi surface and the bottom of the conduction band in these systems is hence comparable to the characteristic phonon energy, or even smaller. This scenario falls outside of the validity limit of the Migdal approximation. As a result, calculations on these systems based on the Migdal approximation suffer from well-documented shortcomings, for example incorrect energetics of the satellite structures shown in Fig. 1.4.[55–59]

One promising strategy to overcome this limitation is provided by the cumulant expansion method.[60–62] In its original formulation, this approach was introduced to study the coupling of core holes to plasma excitations in metals.[60] The generalisation of this approach to valence electrons[61] enabled the first *ab initio* calculations of plasmon satellites in elemental metals.[62] More recently, the cumulant approach has been employed to improve

the description of spectral satellites arising from electron-plasmon interactions in GW calculations.[17,63–70] In the context of electron-phonon physics, the cumulant expansion has successfully been employed to calculate phonon sidebands in systems exhibiting Fröhlich coupling.[9,55–59,71–73]

Despite these advances on the front of *ab initio* calculations, a major limitation that one encounters is the often prohibitive computational expense involved: To model low-energy spectra accurately, first-principles calculations of Fröhlich couplings require extremely dense Brillouin zone and energy grids. As a result, it is difficult to systematically explore the parameter space and extract general trends.

An alternative route to investigating Fröhlich coupling in solids involves an analytical description of the long-range electron-phonon interaction in doped semiconductors, following the seminal work by Fröhlich.[1] In what is now known as the Fröhlich model, one considers an electron in a parabolic band coupled to a dispersionless LO phonon.[1,15,74–77] A number of important contributions on electron-phonon interactions and polarons have taken the Fröhlich model as a starting point,[29,48,49] and it is routinely used for testing advanced many-body techniques such as the diagrammatic Monte Carlo method.[78,79]

In Chapter 4, we generalise the Fröhlich model to the case of doped semiconductors. In particular, we take into account effects of band filling [cf. Fig. 1.4] and free-carrier screening due to the dopant electrons. Within our analytical approach, we calculate theoretical polaron spectra and obtain general expressions for the energy and effective mass of the QP as a function of electron doping. Moreover, we explore the evolution of the quasiparticle properties as a function of the electron-phonon coupling strength, and determine limiting cases for the applicability of our second-order expansion of the electron self-energy.

We find that without including free carriers, the Fröhlich model cannot reproduce the correct energetic ordering of bands and satellites as observed in experiment [cf. Figs. 1.1 and 1.2]. Also, without taking into account free-carrier screening effects, we find that our model overestimates the effective electron-phonon coupling strength at high doping. In line with previous literature, we confirm that the cumulant expansion provides a more accurate description of the polaron satellites than the Dyson's equation approach.

1.2 Fröhlich superconductivity in doped $SrTiO_3$

The superconducting state in doped STO has been the object of renewed interest in recent years. Most notably, the experimental observation of a critical temperature of 80 or even 100 K in STO interfaced with a single layer of FeSe has been received with great excitement.[5,36–43] In the superconducting phases in both the bulk and the FeSe/STO interface systems, polaron satellites have been observed in photoemission spectroscopy. This is seen as a strong indication that coupling of conduction electrons to the highest LO phonon mode is at the origin of Cooper pairing in this system.[5,39,80]

Also interfaces of STO with $LaAlO_3$[81,82] and $LaTiO_3$[83,84] have been shown to be superconducting [albeit only at temperatures of the order of a few hundred meV].

From a theoretical vantage point, superconductivity in STO stands out as being the first confirmed superconducting semiconductor,[85] after the existence of such a system had been conjectured e.g. by Cohen, among others.[31–33] This finding has been vital to our understanding of superconductivity, and it has since been confirmed that most semiconductors become superconducting at very low temperatures.[34,35]

Moreover, STO is the first superconductor with a perovskite structure, preceding the discovery of high-T_C cuprates,[86,87] and one of the first superconductors exhibiting a superconducting dome.

Only a year after the experimental confirmation of a finite T_C in STO due to Schooley and Hosler,[85] the same authors uncovered that the critical temperature was in fact strongly dependent on the charge-carrier concentration in the system.[22] This has been confirmed more recently by Lin and coworkers:[23] In Fig. 1.3, we reprint experimental data of the superconducting T_C of bulk STO as a function of charge-carrier density n_0 as presented in Refs. [22] and [23].

We wish to highlight the fact that STO becomes superconducting at extremely low doping levels, with the lowest non-zero T_C reported by Ref. [88] at $n_0 = 6.5 \times 10^{17}\text{cm}^{-3}$. If one assumes an average band mass of $m_0 \approx 1.3 m_e$ [see Sec. 3.1], this doping concentration corresponds to a Fermi energy of less than 1 meV. This is remarkable as many semiconductors are not even conducting at such low charge-carrier concentrations: Bulk

silicon for example only displays finite zero-temperature conductivity at charge-carrier concentrations above $3.5 \times 10^{18}\text{cm}^{-3}$.[89,90]

To understand this phenomenon, consider the empirical Mott criterion for degenerate semiconductors: one finds that a critical charge-carrier density n_c is required to give rise to the insulator-metal transition in these systems. For a large class of materials, this charge-carrier density is given by the relation $n_c^{1/3}\, a_0 \approx 0.26$,[89,90] where

$$a_0^* = \frac{\varepsilon_0/\epsilon_0}{m_0/m_e}\, a_0. \tag{1.3}$$

The quantity a_0^* is called the *effective* Bohr radius in the material, which characterises the dielectric environment experienced by the free carriers. Here, ε_0/ϵ_0 is the static dielectric constant in units of the vacuum permittivity ϵ_0, m_0/m_e is the bare mass of the conduction band in units of the electron rest mass m_e, and a_0 is the Bohr radius in vacuum.

At low temperatures, quantum zero-point fluctuations prevent the manifestation of a long-range ferroelectric order in STO. Instead, the system remains paraelectric in the ground state and exhibits a very large static dielectric constant.[91,92] As a consequence, the effective Bohr radius in STO is much larger than in most semiconductors, and the metal-insulator transition can occur at charge-carrier densities as low as $n_0 = 8 \times 10^{15}\text{cm}^{-3}$.[93]

It follows that the superconducting dome in STO may be special because it appears in a doping range in which most other semiconductors do not yet exhibit a sharp Fermi surface. Some contributions in the literature even suggest that the appearance of the superconducting dome may be directly linked to the proximity of the ferroelectric phase via the softening of a TO phonon mode involved in the transition.[94–96] However, one finds that electron-phonon coupling to LO phonon modes is orders of magnitude stronger compared to TO modes.

More generally, an intense debate about the origin of superconductivity in STO persists in the literature, despite the fact it was first observed almost six decades ago.[97] A number of model theories have been put forward, ranging from attractive coupling due to intervalley scattering,[31,98] to long-range coupling to optical phonons[33,99–101] and plasmons.[102,103]

In the scope of this thesis, we investigate the superconducting state using one of the most mature *ab initio* many-body theories for modelling phonon-mediated superconductivity,

namely Migdal-Eliashberg (ME) theory.[21,104] ME theory is a generalisation of a one-electron Green's function theory to describe pairs of electrons at finite temperature. A generalised self-energy is derived containing both attractive electron-phonon coupling and repulsive electron-electron interactions. This approach correctly returns the many-body renormalisation of the electron quasiparticles at the level of the Fan-Migdal approximation. Moreover, for temperatures $T < T_\mathrm{C}$ it gives access to the full momentum- and frequency-resolved superconducting gap function Δ.[44,105–107]

Given its complexity, various approximations to the full system of ME equations have been derived in order to make *ab initio* calculations tractable. For nonpolar materials, it is a good approximation to assume that the main contribution to Cooper pair formation arises from electronic states at the Fermi edge.[106,108] This assumption allows one to reduce the computational demand by restricting the momentum integration to the Fermi surface, and it has been employed successfully in numerical calculations.[44,109,110] An equivalent description of superconducting properties can also be obtained from superconducting density-functional theory (SCDFT).[45,46]

For isotropic metals, one can achieve an even more drastic reduction of the computational cost by employing the semiempirical McMillan equation.[30] In this approach, electron-phonon interactions are represented by a single scalar parameter, which is obtained from a Fermi-surface average of all interactions.[111,112]

In this thesis, we show that superconducting pairing interactions in doped polar semiconductors cannot be described on the Fermi surface alone, but rather need to be calculated for a finite momentum grid in the Brillouin zone. Most common implementations of ME theory can therefore not be employed to model the superconducting transition in these systems. Rather, in Chapter 5, we derive an alternative approach based on the linearised gap equation near $T \approx T_\mathrm{C}$.

We implement an isotropic version of the linearised ME equations for the doped Fröhlich model. As before, the use of an analytical model reduces the computational complexity of the task to a tractable level. Our results are benchmarked against experimental measurements of the superconducting T_C of STO, see Chapter 7. We achieve remarkable

qualitative agreement of our calculation results with experimental data, and discuss promising avenues for further improvements of the predictive power of our approximation.

1.3 Outline of the thesis

In Chapter 2, we introduce the theoretical concepts for a many-body theory of electron-phonon interactions. Section 2.1 reviews the normal-state equations for the interacting electron Green's function, starting from the most general nonrelativistic Hamiltonian for a coupled electron-phonon system. We introduce the concepts of the electron Green's function, electron self-energy and screened Coulomb interaction. Eventually, we give the definition for the electron spectral function, and discuss the Dyson's equation and cumulant expansion approaches for practical calculations.

The ME equations for the superconducting state are derived in Sec 2.2. We introduce both the most general formulation of ME theory, and the linearised equations for temperatures $T \approx T_{\mathrm{C}}$. Then, we introduce further approximations to the full system of equations, namely the Morel-Anderson pseudopotential, the Fermi-surface restricted equations, and the McMillan equation.

Next, in Chapter 3, we introduce the doped Fröhlich model, which we use to model electron-phonon interactions in doped STO. In Sec. 3.1, we present a first-principles study of the ground state of STO in both the cubic and tetragonal phases. From this study, we extract the parameters for our model system, which we formally introduce in Sec. 3.2. Lastly, we observe that free-carrier screening effects have a major effect on many-body interactions in the system, which is why we dedicate Sec. 3.3 to the dielectric function of a free electron gas.

In Chapter 4, we present our results for the electron quasi-particle in the normal state. In particular, we review the cases of a single electron in the conduction band [Sec. 4.1], a finite Fermi sea without free-carrier screening [Sec. 4.2], and the fully interacting system including electronic screening by free charge carriers [Sec. 4.3]. We conclude this chapter with an analysis of the spectral weight of the quasiparticle and a comparison against experiment [Sec. 4.4].

Chapter 5 discusses problems with conventional approximations to ME theory when applied to polar semiconductors: In particular, we consider the McMillan equation in Sec. 5.1, and the Fermi-surface restricted equations in Sec. 5.2. Ultimately, we develop an alternative approach to modelling the pairing potential in ionic crystals starting from the linearised ME equations in Sec. 5.3. This is the approach we employ in the remaining chapters to model the superconducting state in doped STO.

The details of our numerical implementation are presented in Chapter 6. Section 6.1 relates all equations as they are implemented in our code. Convergence tests with respect to the main convergence parameters are presented in Sec. 6.2, and in Sec. 6.3, we use the test case of non-polar holed-doped diamond to confirm the validity of our approach.

In Chapter 7, we present the results of our calculation for the superconducting T_C of doped STO. The superconducting dome is calculated for four different approximation levels of the full theory. In Sec. 7.1, we neglect all renormalisation effects of the quasiparticle. Then, in Secs. 7.2 and 7.3, we take into account the renormalisation of the QP state in our calculation of the superconducting state, however without explicitly enforcing the particle number conservation condition. In Sec. 7.4, we complete the full ME equations by also taking into account particle number conservation. Our results are discussed and compared to experimental data in Sec. 7.5. While we find very good qualitative agreement with experiment, our predicted T_C overestimates experimental data by a factor of 100. Eventually, in Sec. 7.6, we explore future opportunities to improve the accuracy in our calculations via an improved description of free-carrier screening. Finally, we summarise all results from the main text Sec. 8.

In the appendices, we provide further details for some of the introduced concepts. Appendix A discusses the concept of the Born-von Kármán boundary conditions which are used in most implementations of electronic structure codes. In App. B, we show that the Debye-Waller self-energy introduced in Sec. 2.1.3 vanishes for a parabolic electron band. In App. C, we present a simple model for phonon-plasmon coupling, or the formation of a phonon-plasmon polariton. In App. D we detail steps of the derivation of the Fan-Migdal self-energy for the Fröhlich model. Appendix E shows that the doping-dependent effective mass in the retarded cumulant behaves as in the lesser cumulant for vanishing Fermi

energy. In App. F, we present the full analytical expressions for the renormalised QP energy and effective mass of the Fröhlich model at finite Fermi energy, followed by the same equations for the screened system in App. G. Finally, we give further details about the anisotropic linearised Migdal-Eliashberg equations in Appendix H.

2

Electron-phonon interactions from first principles

In this chapter, we present a many-body Green's function formalism for modelling electron-phonon interactions in the normal and superconducting states. In both states, the central quantities of the formalism are the electron Green's function G, which describes the electron dynamics, and the electron self-energy Σ, which accounts for changes in the electronic energy due to its interaction with other particles.

We start from the most general assumptions about a coupled system of electrons and lattice ions, and derive the self-consistently defined equations for the electron Green's function, self-energy and vertex function. Then, we show how one can simplify these equations to obtain useful quantities that enable calculations for real systems.

In Sec. 2.1, we construct the interacting Green's function in the normal state to study the spectral properties of the coupled electron-phonon system. To do this we introduce the electron spectral function A, which allows us to relate our results to electronic spectra obtained in photoemission experiments. In particular, we study the renormalisation of the quasiparticle and the appearance of satellite sidebands, cf. Figs. 1.1 and 1.2.

In Sec. 2.2, we employ a generalised Green's function which allows us to model electron pair formation within the very elegant Migdal-Eliashberg theory in the superconducting state. Below the superconducting transition temperature T_{C}, many-body interactions

between electrons and phonons give rise to a net attractive potential, which causes the formation of Cooper pairs. Moreover, one observes a non-vanishing energy gap in the electronic spectrum. The Migdal-Eliashberg equations allow us to evaluate this superconducting gap as a function of temperature, from which we can then make predictive estimates for the T_C in the system.

2.1 Normal state

We begin this section by writing down the most general nonrelativistic Hamiltonian for a coupled system of electrons and nuclei [Sec. 2.1.1]. Then, in Sec. 2.1.2, we introduce the Green's function of the electron, and derive its equation of motion in the context of the electron-phonon Hamiltonian. To solve this equation of motion, we introduce the notion of an electron self-energy, and show how to obtain it from a self-consistent formulation of a nonlinear system of equations [Sec. 2.1.3]. We then move on to review the most common approximations employed in electronic structure theory that allow practical calculations. The resulting expressions for the electron self-energy are known as the Fan-Migdal and Debye-Waller self-energies.

In Sec. 2.1.4, we briefly review the screened Coulomb interaction in a polar crystal, and connect our results to the *GW* approximation for electron-electron interactions in semiconductors. We also introduce the random-phase approximation for practical calculations of the screened Coulomb interaction.

Ultimately, we arrive at the simplified expressions for the electron self-energy and interacting Green's function that enable numerical calculations. In this work, we will study the spectral properties of the interacting electron-phonon system with the aim of reproducing experimental spectra, such as the one shown in Figs. 1.1 and 1.2. There is a great deal of interest in such calculations of many-body spectra, as the comparison to experiment not only allows one to benchmark existing theories, it also inspires further investigations into the many-body effects at play.

We give formal definitions for the energy, spectral weight and effective mass of the main QP peak, by which we mean the one dispersive peak that carries the most spectral weight. In addition, we show how the formation of polaron satellites is built into our

many-body formalism. It is expected that a good framework for calculating spectral functions gives an accurate description of these satellites: In experiment, the appearance of equally spaced sidebands near a QP peak is often the strongest indicator for the presence of electron-boson coupling in a system.

To contribute to the discussion around the correct approach to modelling the polaron quasiparticle and satellites in doped semiconductors, we compare two widely used approaches to constructing the interacting electron Green's function: In Secs. 2.1.5 and 2.1.6, we introduce the Dyson's equation approach and cumulant expansion formalism. Afterwards, in Chapter 4 we will employ both approaches and compare the results for the polaron spectrum in doped semiconductors.

2.1.1 Electron-phonon Hamiltonian

The standard reference for a modern formulation of the many-body theory of electron-phonon interactions is the review by Giustino,[50] whose derivations we follow closely throughout this section. Originally, first contributions to a field theory of electron-phonon coupling in a homogeneous electron gas are due to, among others, Hedin,[113] Migdal,[21] and Engelsberg and Schrieffer.[19] The most general formulation of the problem is presented in the seminal works by Baym,[114] and Hedin and Lundqvist.[115]

The Hamiltonian for a coupled system of electrons and nuclei can be written as:[50]

$$\hat{H} = \hat{T}_\mathrm{e} + \hat{T}_\mathrm{n} + \hat{U}_\mathrm{ee} + \hat{U}_\mathrm{nn} + \hat{U}_\mathrm{en}, \tag{2.1}$$

where $\hat{T}_\mathrm{e}$ and $\hat{T}_\mathrm{n}$ are the electronic and nuclear kinetic energies, and $\hat{U}_\mathrm{ee}$, $\hat{U}_\mathrm{nn}$, and $\hat{U}_\mathrm{en}$ are the interactions between electrons and electrons, nuclei and nuclei, and electrons and nuclei. We now introduce each of its contributions:

The first term in Eq. (2.1) is the electron kinetic energy:[50]

$$\hat{T}_\mathrm{e} = -\frac{\hbar^2}{2m_e}\int d\mathbf{x}\, \hat{c}^\dagger(\mathbf{x})\nabla^2\hat{c}(\mathbf{x}), \tag{2.2}$$

where m_e is the mass of an electron in vacuum. The variable $\mathbf{x}$ indicates both the position $\mathbf{r}$ and spin σ. The integral over $\mathbf{x}$ is assumed to extend over the entire crystal, i.e. over supercell of infinite size. This assumption helps simplify our formalism in two ways: In

real space, we do not have to explicitly sum over lattice vectors $\mathbf{R}_p$ of the supercell. In reciprocal space, all summations over scattering wave vectors $\mathbf{q}$ can be replaced by an integral over the first Brillouin zone of volume Ω_{BZ}. Details of the so-called Born-von Kármán boundary conditions are discussed in Appendix A.

The operators in Eq. (2.2), $\hat{c}^\dagger(\mathbf{x})$ and $\hat{c}(\mathbf{x})$, are the electronic field creation and annihilation operators. They obey the anti-commutation relations for fermions:

$$\left\{\hat{c}(\mathbf{x}), \hat{c}(\mathbf{x}')\right\} = \left\{\hat{c}^\dagger(\mathbf{x}), \hat{c}^\dagger(\mathbf{x}')\right\} = 0 \qquad \text{and} \qquad \left\{\hat{c}(\mathbf{x})^\dagger, \hat{c}(\mathbf{x}')\right\} = \delta(\mathbf{x} - \mathbf{x}'), \tag{2.3}$$

where $\left\{\hat{a}, \hat{b}\right\} = \hat{a}\hat{b} + \hat{b}\hat{a}$.

The second term in Eq. (2.1) is the nuclear kinetic energy:[50]

$$\hat{T}_{\mathrm{n}} = -\sum_{\kappa\alpha p} \frac{\hbar^2}{2M_\kappa} \frac{\partial^2}{\partial \tau_{\kappa\alpha p}^2}, \tag{2.4}$$

where M_κ is the mass of nucleus κ, and $\tau_{\kappa\alpha p}$ is the position coordinate of nucleus κ in unit cell p along the Cartesian direction α. The latter is often written as $\boldsymbol{\tau}_{\kappa p} = \boldsymbol{\tau}^0_{\kappa p} + \Delta\boldsymbol{\tau}_{\kappa p}$, where $\boldsymbol{\tau}^0_{\kappa p}$ is the equilibrium position of nucleus κ in unit cell p, and $\Delta\boldsymbol{\tau}_{\kappa p}$ is its displacement away from the equilibrium position.

The third term in Eq. (2.1) is the electron-electron interaction:[50]

$$\hat{U}_{\mathrm{ee}} = \frac{1}{2} \int d\mathbf{r} \int d\mathbf{r}' \, \hat{n}_{\mathrm{e}}(\mathbf{r}) \left[\hat{n}_{\mathrm{e}}(\mathbf{r}') - \delta(\mathbf{r} - \mathbf{r}')\right] \, v(\mathbf{r}, \mathbf{r}'), \tag{2.5}$$

where the $\hat{n}_{\mathrm{e}}(\mathbf{r})$ is the electron particle density operator, and $v(\mathbf{r}, \mathbf{r}')$ is the Coulomb interaction between two particles with charge e. They are defined as:

$$\hat{n}_{\mathrm{e}}(\mathbf{r}) = \sum_\sigma \hat{c}^\dagger(\mathbf{x})\hat{c}(\mathbf{x}) \qquad \text{and} \qquad v(\mathbf{r}, \mathbf{r}') = \frac{e^2}{4\pi\,\epsilon_0\,|\mathbf{r} - \mathbf{r}'|}, \tag{2.6}$$

respectively.

The fourth term in Eq. (2.1) is the nucleus-nucleus interaction:[50]

$$\hat{U}_{\mathrm{nn}} = \frac{1}{2} \sum_{\kappa' p' \neq \kappa p} Z_\kappa Z_{\kappa'} \, v(\boldsymbol{\tau}^0_{\kappa p} + \Delta\hat{\boldsymbol{\tau}}_{\kappa p}, \boldsymbol{\tau}^0_{\kappa' p'} + \Delta\hat{\boldsymbol{\tau}}_{\kappa' p'}), \tag{2.7}$$

where Z_κ is the atomic number of nucleus κ, and $\Delta\hat{\boldsymbol{\tau}}_{\kappa p}$ is the displacement *operator* of nucleus κ in unit cell p away from equilibrium $\boldsymbol{\tau}^0_{\kappa p}$.

Eventually, the fifth term in Eq. (2.1) is the electron-nucleus interaction:[50]

$$\hat{U}_{\mathrm{en}} = \int d\mathbf{r} \int d\mathbf{r}' \, \hat{n}_{\mathrm{e}}(\mathbf{r}) \hat{n}_{\mathrm{n}}(\mathbf{r}') \, v(\mathbf{r}, \mathbf{r}'), \tag{2.8}$$

where the nuclear charge density operator is given by

$$\hat{n}_{\mathrm{n}}(\mathbf{r}) = -\sum_{\kappa p} Z_{\kappa} \, \delta \left(\mathbf{r} - \boldsymbol{\tau}^{0}_{\kappa p} - \Delta \hat{\boldsymbol{\tau}}_{\kappa p} \right). \tag{2.9}$$

Note that electrons and nuclei are treated differently within these definitions for Eq. (2.1): The electron-electron interaction in Eq. (2.5) describes a continuous charge distribution arising from indistinguishable particles. To avoid a self-interaction contribution to U_{ee} one includes the Dirac delta in its definition. The nucleus-nucleus interaction in Eq. (2.7), on the other hand, treats nuclei as distinguishable particles, and their total interaction is therefore written as the summation over all pairwise contributions.

Lastly, note that we can define a total particle density,

$$\hat{n} = \hat{n}_{\mathrm{e}} + \hat{n}_{\mathrm{n}}, \tag{2.10}$$

where the associated charge densities are given in units of the electron charge e.

2.1.2 Electron Green's function

In this subsection, we show how to derive a Green's function for the motion of an electron from the full Hamiltonian of the coupled electron-ion system given in Eq. (2.1). The solution of its equation of motion involves contributions from a nonlocal, time-dependent interaction known as the electron self-energy, which we will also introduce.

Using the definitions made in Eqs. (2.2)-(2.9), we write:[50]

$$\begin{aligned} \hat{H} &= \hat{T}_{\mathrm{n}} + \hat{U}_{\mathrm{nn}} + \int d\mathbf{x} \, \hat{c}^{\dagger}(\mathbf{x}) \left[-\frac{\hbar^2}{2m_e} \nabla^2 + \hat{V}_{\mathrm{n}}(\mathbf{r}) \right] \hat{c}(\mathbf{x}) \\ &+ \frac{1}{2} \int d\mathbf{x} d\mathbf{x}' \, v(\mathbf{r}, \mathbf{r}') \, \hat{c}^{\dagger}(\mathbf{x}) \hat{c}^{\dagger}(\mathbf{x}') \hat{c}(\mathbf{x}') \hat{c}(\mathbf{x}), \end{aligned} \tag{2.11}$$

where one defines the nuclear potential

$$\hat{V}_{\mathrm{n}}(\mathbf{r}) = \int d\mathbf{r}' \, v(\mathbf{r}, \mathbf{r}') \, \hat{n}_{\mathrm{n}}(\mathbf{r}'). \tag{2.12}$$

Next, we introduce the time-ordered one-electron Green's function at zero temperature:[29,116,117]

$$G(\mathbf{x},\mathbf{x}',t-t') = -\frac{i}{\hbar}\langle 0|\hat{T}\,\hat{c}(\mathbf{x},t)\,\hat{c}^\dagger(\mathbf{x}',t')|0\rangle, \tag{2.13}$$

where $|0\rangle$ is the ground state of the system, and $\hat{T}$ is the time-ordering operator for fermions, defined as:

$$\hat{T}\,\hat{c}(\mathbf{x},t)\,\hat{c}^\dagger(\mathbf{x}',t') = \Theta(t-t')\,\hat{c}(\mathbf{x},t)\,\hat{c}^\dagger(\mathbf{x}',t') - \Theta(t'-t)\,\hat{c}^\dagger(\mathbf{x}',t')\,\hat{c}(\mathbf{x},t), \tag{2.14}$$

with the Heaviside function $\Theta(t)$.

For $t > t'$, the Green's function describes a scalar product between the initial state $\hat{c}^\dagger(\mathbf{x}',t')|0\rangle$ and the final state $\hat{c}^\dagger(\mathbf{x},t)|0\rangle$. Assume an electron is created with a combined position and spin variable $\mathbf{x}'$ at time t'. The Green's function then yields the probability amplitude of detecting an electron at $\mathbf{x}$ at a later time $t > t'$. If $t < t'$, the Green's function describes the same process but for holes rather than electrons.[29]

In Eq. (2.13), the electron field operators are written in the Heisenberg picture, which gives them an explicit time dependence:

$$\hat{c}(\mathbf{x},t) = e^{i\hat{H}\,t/\hbar}\,\hat{c}(\mathbf{x})\,e^{-i\hat{H}\,t/\hbar} \tag{2.15}$$

Inserting our Hamiltonian from Eq. (2.11) into the corresponding Heisenberg equation of motion,

$$i\hbar\,\frac{\partial}{\partial t}\,\hat{c}(\mathbf{x},t) = \left[\hat{c}(\mathbf{x},t),\hat{H}\right], \tag{2.16}$$

we find

$$i\hbar\frac{\partial}{\partial t}\,\hat{c}(\mathbf{x},t) = \left[-\frac{\hbar^2}{2m_e}\nabla^2 + \int d\mathbf{r}'\,v(\mathbf{r},\mathbf{r}')\,\hat{n}(\mathbf{r}',t)\right]\,\hat{c}(\mathbf{x},t), \tag{2.17}$$

where $\hat{n}(\mathbf{r}',t)$ is the particle density operator in the Heisenberg representation, cf. Eq. (2.15).

At this point, we modify our Hamiltonian by adding a small time-dependent electric potential $\varphi(\mathbf{r},t)$. This perturbation will be set to zero at the end of our derivation. Formally, this is done to be able to employ Schwinger's functional derivative technique further below. Physically, one thinks of this electric potential as causing a forced oscillation in the system, which can be tuned to detect eigenmodes of the fully interacting system.[116] We have:

$$\hat{H} \to \hat{H} + \hat{H}_1 \qquad \text{where} \qquad \hat{H}_1(t) = \int d\mathbf{r}\,\hat{n}(\mathbf{r},t)\,\varphi(\mathbf{r},t). \tag{2.18}$$

In analogy to Eq. (2.17), we write down the Heisenberg equation for the electron Green's function. In doing so, we observe the anti-commutation relations [Eq. (2.3)], and note that the derivative of a Heaviside function is a Dirac delta. We find:[115]

$$\left[i\hbar\frac{\partial}{\partial t}+\frac{\hbar^2}{2m_e}\nabla^2-\varphi(\mathbf{r},t)\right]G(\mathbf{x},\mathbf{x}',t-t') \tag{2.19}$$
$$+\quad\frac{i}{\hbar}\int d\mathbf{r}''dt''\,v(\mathbf{r},\mathbf{r}'',t-t'')\langle 0|\hat{T}\,\hat{n}(\mathbf{r}'',t'')\,\hat{c}(\mathbf{x},t)\,\hat{c}^\dagger(\mathbf{x}',t')|0\rangle=\delta(\mathbf{x}-\mathbf{x}')\delta(t-t')$$

The time-dependent Coulomb potential is simply given as $v(\mathbf{r},\mathbf{r}'',t-t'')=v(\mathbf{r},\mathbf{r}'')\delta(t-t'')$. Note that the first line in Eq. (2.19) describes single-particle properties, whereas the second line describes the interaction of this particle with the rest of the system. In particular, note that the term $\langle 0|\hat{T}\,\hat{n}(\mathbf{r}'',t'')\,\hat{c}(\mathbf{x},t)\,\hat{c}^\dagger(\mathbf{x}',t')|0\rangle$ contains four field operators $\hat{c}$ and describes two-particle correlations.

The interaction between the single particle and the full system is in general non-local and dependent on time. To account for this interaction, one defines the self-energy operator Σ via:[115]

$$\left[i\hbar\frac{\partial}{\partial t}+\frac{\hbar^2}{2m_e}\nabla^2-V_{\text{tot}}(\mathbf{r},t)\right]G(\mathbf{x},\mathbf{x}',t-t') \tag{2.20}$$
$$-\quad\int d\mathbf{x}''dt''\,\Sigma(\mathbf{x},\mathbf{x}'',t-t'')\,G(\mathbf{x}'',\mathbf{x}',t''-t')=\delta(\mathbf{x}-\mathbf{x}')\delta(t-t'),$$

where we have separated out the total electrostatic potential acting on the electronic and nuclear charges, averaged over the many-body ground state:[50]

$$V_{\text{tot}}(\mathbf{r},t)=\int d\mathbf{r}'\,v(\mathbf{r},\mathbf{r}')\,\langle\hat{n}(\mathbf{r}',t)\rangle+\varphi(\mathbf{r},t). \tag{2.21}$$

2.1.3 Electron self-energy

In Eq. (2.20), we introduced the concept of the electron self-energy, however we still need an explicit definition of Σ. This is done here by evaluating the functional derivative of Eq. (2.20) with respect to the perturbation potential φ.

At this point, it is customary to lighten the notation by defining

$$(\mathbf{x},t)\,\text{or}\,(\mathbf{r},t)\;\to 1\qquad(\mathbf{x}',t')\,\text{or}\,(\mathbf{r}',t')\;\to 2\qquad(\mathbf{r},t+\eta)\;\to 1^+\qquad\text{and so on.} \tag{2.22}$$

We will also use $\langle\cdot\rangle$ to indicates the average over the ground state $|0\rangle$.

We continue from Eq. (2.19):

$$\left[i\hbar\frac{\partial}{\partial t}+\frac{\hbar^2}{2m_e}\nabla^2-\varphi(1)\right]G(1,2)+\frac{i}{\hbar}\int d(3)\,v(1,3)\langle\hat{T}\,\hat{n}(3)\,\hat{c}(1)\,\hat{c}^\dagger(2)|0\rangle=\delta(1,2). \quad (2.23)$$

Using the identity:[50]

$$\frac{\delta\,G(1,2)}{\delta\,\varphi(3)}=-\frac{i}{\hbar}\langle\hat{T}\;[\hat{n}(3)-\langle\hat{n}(3)\rangle]\;\hat{c}(1)\hat{c}^\dagger(2)\rangle, \quad (2.24)$$

and the definition of the total average potential:

$$V_{\rm tot}(1)=\int d(2)\,v(1,2)\,\langle\hat{n}(2)\rangle+\varphi(1). \quad (2.25)$$

we reach:[50]

$$\left[i\hbar\frac{\partial}{\partial t_1}+\frac{\hbar^2}{2m_e}\nabla^2(1)-V_{\rm tot}(1)-i\hbar\int d(3)\,v(1^+,3)\frac{1}{\delta\,\varphi(3)}\right]G(1,2)=\delta(1,2). \quad (2.26)$$

Here, $(1^+)=(\mathbf{r},t+\eta)$ indicates a positive infinitesimal along the time axis that ensures the correct time ordering.

Next, we note that the response of the total average potential $V_{\rm tot}$ to a small variation in the external potential, $\delta\varphi$, defines the electronic screening function of the system:[115]

$$\varepsilon^{-1}(1,2)=\frac{\delta\,V_{\rm tot}(1)}{\delta\,\varphi(2)}=\delta(1,2)+\int d(3)\,v(1,3)\frac{\delta\,\langle\hat{n}(3)\rangle}{\delta\,\varphi(2)} \quad (2.27)$$

The screened Coulomb interaction is then given by:

$$W(1,2)=\int d(3)\,\varepsilon^{-1}(1,3)\,v(3,2)=\int d(3)v(1,3)\,\varepsilon^{-1}(2,3). \quad (2.28)$$

To get access to the self-energy, we have to multiply G^{-1} onto Eq. (2.23) from the right. We use the relationship:[50]

$$\frac{\delta\,G(1,2)}{\delta\,\varphi(3)}=-\int d(4,5)\,G(1,4)\frac{\delta\,G^{-1}(4,5)}{\delta\,\varphi(3)}G(5,2), \quad (2.29)$$

which we then expand using the chain rule:

$$\frac{\delta\,G^{-1}(4,5)}{\delta\,\varphi(3)}=\int d(6)\,\frac{\delta\,G^{-1}(4,5)}{\delta\,V_{\rm tot}(6)}\frac{\delta V_{\rm tot}(6)}{\delta\,\varphi(3)}. \quad (2.30)$$

The three-point function in Eq. (2.30) is called the "vertex":

$$\Gamma(1,2,3)=-\frac{\delta\,G^{-1}(1,2)}{\delta\,V_{\rm tot}(3)}. \quad (2.31)$$

Eventually, our field theoretic description of the coupled electron-phonon system can be written in terms of a system of three coupled nonlinear equations. First, the electron self-energy [compare Eqs. (2.26)-(2.31)]:[50]

$$\Sigma(1,2) = i\hbar \int d(3,4)\, G(1,3)\, \Gamma(324)\, W(4,1^+). \tag{2.32}$$

Second, the vertex [invert Eq. (2.20)]:[50]

$$\Gamma(1,2,3) = \delta(1,2)\,\delta(1,3) + \int d(4,5,6,7)\, \frac{\delta\,\Sigma(1,2)}{\delta\, G(4,5)}\, G(4,6)\, G(7,5)\, \Gamma(673). \tag{2.33}$$

Third, the electron Green's function:[50]

$$\left[i\hbar \frac{\partial}{\partial t_1} + \frac{\hbar^2}{2m_e}\nabla^2(1) - V_{\mathrm{tot}}(1) \right] G(1,2) - \int d(3)\, \Sigma(1,3)\, G(3,2) = \delta(1,2). \tag{2.34}$$

Fan-Migdal and Debye-Waller electron self-energies

The full self-energy in Eq. (2.32) is not useful for practical calculations. One therefore introduces a series of approximations to obtain an expression for Σ that can be employed in *ab initio* calculations.

The approach most common to electronic structure calculations is the treatment of the nuclei as classical particles clamped to their equilibrium positions. For such a system, one can define the electron Green's function and self-energy *at clamped nuclei*:[50]

$$\left[i\hbar \frac{\partial}{\partial t} + \frac{\hbar^2}{2m_e}\nabla^2 - V^{\mathrm{cn}}_{\mathrm{tot}}(1) \right] G^{\mathrm{cn}}(1,2) - \int d(3)\, \Sigma^{\mathrm{cn}}(1,3)\, G^{\mathrm{cn}}(3,2) = \delta(1,2),$$

Within this approximation, the total average potential at clamped nuclei, $V^{\mathrm{cn}}_{\mathrm{tot}}$ is calculated from the total density of electrons and nuclei at clamped ions, $\langle \hat{n}^{\mathrm{cn}} \rangle = \langle \hat{n}_e + \hat{n}_n \rangle$.

We discuss two contributions to the electron self-energy in this approximation. The first is a dynamical correction to the electronic energies known as the the Fan-Migdal self-energy:[21,50,118]

$$\Sigma^{\mathrm{FM}}(1,2) = i\hbar \int d(3,4)\, G(1,3)\, \Gamma(3,2,4)\, W_{\mathrm{ph}}(4,1^+), \tag{2.35}$$

where W_{ph} is the nuclear contribution to the screened Coulomb interaction, which we will discuss in Sec. 2.1.4. The Fan-Migdal self-energy is equivalent to the GW self-energy at clamped nuclei, which we discuss in Sec. 2.1.4.

The second contribution accounts for the missing term in $V_{\mathrm{tot}}^{\mathrm{cn}}$ due to the clamped-ion approximation. This term is known as the Debye-Waller self-energy:[50,119,120]

$$\Sigma^{\mathrm{DW}}(1,2) = \int d(3)\, v(1,3)\, [\langle \hat{n}(3) \rangle - \langle \hat{n}^{\mathrm{cn}} \rangle]\, \delta(1,2). \tag{2.36}$$

Typically, the Debye-Waller term is only weakly dispersive and its main contribution to electronic spectra is a constant energy shift. While this is important for calculations of the phonon-induced band gap renormalisation in semiconductors and insulators,[121–123] it has little effect on the dispersion of the quasiparticle. Moreover, we find that within our model system, the Debye-Waller self-energy contribution vanishes altogether, as we show in Appendix B. We hence focus the remainder of our discussion on the Fan-Migdal self-energy.

To be able to perform calculations with Σ^{FM}, the following further approximations are usually employed:[50] *(1)* The vertex is set to $\Gamma(1,2,3) = \delta(1,3)\delta(2,3)$. This approximation is well justified in metals with high Fermi energies: Migdal has shown that in these systems, higher-order corrections to this vertex are of the order of $\sqrt{m_e/M_\kappa}$, and can therefore be neglected.[21] *(2)* The fully interacting Green's function G is replaced by an independent-particle Green's function evaluated at clamped nuclei. *(3)* The phonon contribution to W_{ph} is evaluated for a noninteracting phonon spectrum. *(4)* Electronic screening in W_{ph} is taken into account at the level of the random-phase approximation plus exchange-correlation effects. *(5)* The frequency dependence of the electron-phonon coupling is neglected.

After performing a Fourier transformation to momentum and frequency space, we can write down the ground state electron-phonon self-energy in the basis of independent electron states with band index n and crystal momentum $\mathbf{k}$:

$$\begin{aligned} \Sigma_{n\mathbf{k}}(\omega) &= \frac{1}{\hbar} \sum_{m\nu} \int \frac{d\mathbf{q}}{\Omega_{\mathrm{BZ}}} |g_{mn\nu}(\mathbf{k},\mathbf{q})|^2 \\ &\times \left[\frac{1 - f_{m\mathbf{k}+\mathbf{q}}}{\omega - \epsilon_{m\mathbf{k}+\mathbf{q}}/\hbar - \omega_{\mathbf{q}\nu} + i\eta} + \frac{f_{m\mathbf{k}+\mathbf{q}}}{\omega - \epsilon_{m\mathbf{k}+\mathbf{q}}/\hbar + \omega_{\mathbf{q}\nu} + i\eta} \right]. \end{aligned} \tag{2.37}$$

Note that we used the retarded formulation here, in which the infinitesimal η has a positive sign everywhere. The time-ordered expression can be obtained by changing the sign of η in the second term in brackets, which inverts the sign of the imaginary part of Σ for states $k > k_{\mathrm{F}}$. Both formulations ultimately give rise to the same electronic spectra.[29]

In Eq. (2.37), $|g_{mn\nu}(\mathbf{k},\mathbf{q})|^2$ is the electron-phonon matrix element describing scattering of an electron from a state $(n,\mathbf{k})$ with energy $\epsilon_{n\mathbf{k}}$ into a state $(m,\mathbf{k}+\mathbf{q})$ with state $\epsilon_{m\mathbf{k}+\mathbf{q}}$ via a phonon with scattering wavevector $\mathbf{q}$ in branch ν and energy $\omega_{\mathbf{q}\nu}$. The occupation factors at T=0 are equal to $f_{m\mathbf{k}+\mathbf{q}} = 1$ for occupied states and $f_{m\mathbf{k}+\mathbf{q}} = 0$ for unoccupied states, and $\eta > 0$ is again a positive infinitesimal.

2.1.4 Screened Coulomb interaction

We can express the screened Coulomb interaction in terms of the response in the electronic and nuclear particle density $\hat{n}$ resulting from a change of the total average potential V_{tot}. This leads to the definition of a polarisation propagator P.

First, combine the following equations from Sec. 2.1.3:

$$V_{\text{tot}}(1) = \int d(2)\, v(1,2)\, \langle \hat{n}(2) \rangle + \varphi(1), \tag{2.25}$$

$$\varepsilon^{-1}(1,2) = \frac{\delta\, V_{\text{tot}}(1)}{\delta\, \varphi(2)} = \delta(1,2) + \int d(3)\, v(1,3) \frac{\delta\, \langle \hat{n}(3) \rangle}{\delta\, \varphi(2)} \tag{2.27}$$

$$W(1,2) = \int d(3)\, \varepsilon^{-1}(1,3)\, v(3,2) = \int d(3) v(1,3)\, \varepsilon^{-1}(2,3), \tag{2.28}$$

to obtain:[50]

$$W(1,2) = v(1,2) + \int d(3,4)\, v(1,3)\, \frac{\delta \langle \hat{n}(3) \rangle}{\delta\, V_{\text{tot}}(4)} W(4,2). \tag{2.38}$$

The polarisation propagator is then defined as:[50]

$$P(1,2) = \frac{\delta \langle \hat{n}(1) \rangle}{\delta\, V_{\text{tot}}(2)}. \tag{2.39}$$

We can express the dielectric function ε and the screened Coulomb interaction W in terms of this polarisation operator:

$$\varepsilon(1,2) = \delta(1,2) - \int d(3)\, v(1,3)\, P(3,2), \tag{2.40}$$

and

$$W(1,2) = v(1,2) + \int d(3,4)\, v(1,3)\, P(3,4)\, W(4,2) = \int d(3)\, \varepsilon_{\text{e}}^{-1}(1,3) v(3,2). \tag{2.41}$$

Using again the approximation of clamped nuclei, we can define a polarisation propagator P_e related to the electronic response alone:[50]

$$P_{\mathrm{e}}(1,2) = \frac{\delta \langle \hat{n}_{\mathrm{e}}(1) \rangle}{\delta V_{\mathrm{tot}}(2)} = -i\hbar \sum_{\sigma} \int d(3,4) G(1,3) G(4,1^{+}) \Gamma(3,4,2). \tag{2.42}$$

The second equality can be obtained from combining Eqs. (2.29) and (2.31), and by realising that the electron density can be related to the electron Green's function via:[50]

$$\langle \hat{n}_{\mathrm{e}}(1) \rangle = -i\hbar \sum_{\sigma} G(1,1^{+}). \tag{2.43}$$

The corresponding dielectric function and screened Coulomb interaction are simply given by the expressions:[50]

$$\varepsilon_{\mathrm{e}}(1,2) = \delta(1,2) - \int d(3)\, v(1,3)\, P_{\mathrm{e}}(3,2), \tag{2.44}$$

and

$$W_{\mathrm{e}}(1,2) = v(1,2) + \int d(3,4)\, v(1,3)\, P_{\mathrm{e}}(3,4)\, W_{\mathrm{e}}(4,2) = \int d(3)\, \varepsilon_{\mathrm{e}}^{-1}(1,3) v(3,2). \tag{2.45}$$

One can show that the difference between the total screened Coulomb interaction W and the electronic contribution W_{e} is exactly the nuclear contribution W_{ph} we encountered in the definition of the Fan-Migdal self-energy in Eq. (2.35):[50]

$$W_{\mathrm{ph}}(1,2) = W(1,2) - W_{\mathrm{e}}(1,2). \tag{2.46}$$

Electron self-energy in the random-phase approximation

Still within the approximation of clamped nuclei, it is possible to derive a simple expression for the electronic dielectric function ε_{e} and the corresponding screened Coulomb interaction W_{e}.

Bohm and Pines were the first to introduce the random-phase approximation to the calculation of electron-electron interactions,[124–126] and Hedin later applied the RPA in the context of Green's functions.[113] As in the Migdal approximation for the electron-phonon self-energy, it involves setting the vertex equal to:[127]

$$\Gamma(1,2,3) = \delta(1,2)\delta(1,3). \tag{2.47}$$

This leads to a simple expression for the polarisation propagator in Eq. (2.39):[127]

$$P(1,2) = -iG(1,2^+)G(2,1). \tag{2.48}$$

The corresponding electron self-energy due to electron-electron interactions is then given as [cf. Eqs. (2.45) and (2.32)]:[127]

$$\Sigma(1,2) = i\hbar\, G(1,2)\, W(1^+,2). \tag{2.49}$$

This is the GW approximation for electron correlations. Its equivalent for electron-phonon interactions is the Fan-Migdal self-energy discussed in Sec. 2.1.3.

Expanding the polarisation propagator in a basis of plane waves and frequencies, we obtain:[29]

$$P(\mathbf{q},\omega) = \sum_m \int \frac{d\mathbf{k}}{\Omega_{\mathrm{BZ}}} \frac{f_{n\mathbf{k}} - f_{m\mathbf{k}+\mathbf{q}}}{\epsilon_{n\mathbf{k}} - \epsilon_{m\mathbf{k}+\mathbf{q}} + \hbar\omega + i\eta}. \tag{2.50}$$

The corresponding dielectric function is given as:

$$\varepsilon^{\mathrm{RPA}}(\mathbf{q},\omega) = 1 - v(\mathbf{q})\, P(\mathbf{q},\omega), \tag{2.51}$$

where $v(\mathbf{q})$ is the Coulomb potential from Eq. (2.6)in reciprocal space.

2.1.5 Dyson quasiparticle spectrum

Building on our results from the previous sections, we now want to move towards practical calculations of the interacting electron-phonon state in doped semiconductors. Here, we will employ Dyson's equation to construct the interacting electron Green's function from the Fan-Migdal self-energy given in Eq. (2.37). The imaginary part of G can then be related to the photoemission spectra measured in experiment through the so-called "electron spectral function".

The Dyson equation for the interacting Green's function in the clamped-ion approximation is given by:[50]

$$G(1,2) = G^{\mathrm{cn}}(1,2) + \int d(3,4)\, G^{\mathrm{cn}}(1,3)\Sigma(3,4)G(4,2). \tag{2.52}$$

In practical calculations, one usually terminates the series after the first term:

$$\begin{aligned} G(\mathbf{x},\mathbf{x}',t-t') &= G^0(\mathbf{x},\mathbf{x}',t-t') \\ &+ \int d\mathbf{x}_1\, d\mathbf{x}_2\, dt_1\, dt_2\, G^0(\mathbf{x},\mathbf{x}_1,t-t_1)\, \Sigma(\mathbf{x}_1,\mathbf{x}_2,t_1-t_2)\, G^0(\mathbf{x}_2,x',t_2-t') \end{aligned} \tag{2.53}$$

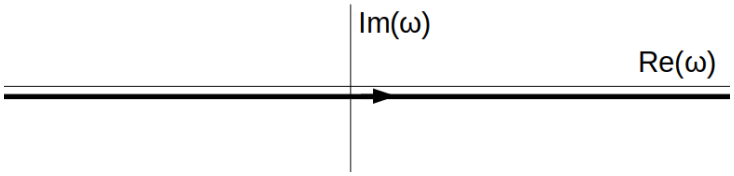


Figure 2.1: Contour C for the spectral representation of the retarded Green's function

The integrals in Eq. (2.53) define a convolution of the Green's function with the self-energy in position $\mathbf{x}$ and time t. After projecting the Green's function onto a basis of Bloch functions, and considering only diagonal terms of the Green's function, one recovers the simple expression:

$$G_{n\mathbf{k}}(\omega) = \frac{1}{\hbar\omega - \epsilon_{n\mathbf{k}} - \Sigma_{n\mathbf{k}}(\omega)}, \tag{2.54}$$

where we have used the noninteracting Green's function:[29]

$$G^0_{n\mathbf{k}}(\omega) = \frac{1}{\hbar\omega - \epsilon_k + i\eta}. \tag{2.55}$$

A time-dependent Green's function can be thought of as a time- and position-correlation function of the motion of the interacting electron. The frequency-dependent expression in Eq. (2.54), on the other hand, gives us access to its spectral properties. In particular, it allows us to study the density of states of the interacting electron-phonon system as a function of frequency (energy) and momentum. To this end, define the electron spectral function:[19]

$$A_{\mathbf{k}}(\omega) = \frac{1}{\pi}\sum_n \left|\mathrm{Im}\, G_{n\mathbf{k}}(\omega)\right|. \tag{2.56}$$

This function represents the $\mathbf{k}$-dependent density of states that is probed in ARPES experiments.[128,129]

One can also invert the relation and express the Green's function in its spectral representation:[115]

$$G_{n\mathbf{k}}(\omega) = \int_C d\omega' \frac{A_{n\mathbf{k}}(\omega')}{\omega - \omega'}. \tag{2.57}$$

The contour for the retarded Green's function is shown in Fig. 2.1

In the Dyson equation approach introduced above, we can combine Eqs. (2.56) and (2.54) to express the spectral function directly in terms of the self-energy:

$$A_{\mathbf{k}}(\omega) = \frac{1}{\pi}\sum_n \frac{\mathrm{Im}\,\Sigma_{n\mathbf{k}}(\omega)}{\left[\hbar\omega - \epsilon_{n\mathbf{k}} - \mathrm{Re}\,\Sigma_{n\mathbf{k}}(\omega)\right]^2 + \left[\mathrm{Im}\,\Sigma_{n\mathbf{k}}(\omega)\right]^2}. \tag{2.58}$$

This spectral function will exhibit peaks near the poles of the interacting Green's function. The poles are in general complex quantities defined as:[19,130]

$$E_{n\mathbf{k}} = \epsilon_{n\mathbf{k}} + \Sigma_{n\mathbf{k}}(E_{n\mathbf{k}}/\hbar), \tag{2.59}$$

where (using the shorthands $E^{\mathrm{R}}_{n\mathbf{k}} = \mathrm{Re}E_{n\mathbf{k}}$ and $E^{I}_{n\mathbf{k}} = \mathrm{Im}E_{n\mathbf{k}}$):

$$E^{\mathrm{R}}_{n\mathbf{k}} = \epsilon_{n\mathbf{k}} + \mathrm{Re}\Sigma_{n\mathbf{k}}(E^{\mathrm{R}}_{n\mathbf{k}}/\hbar + E^{\mathrm{I}}_{n\mathbf{k}}/\hbar) \tag{2.60}$$

represents the renormalised energy, and

$$E^{\mathrm{I}}_{n\mathbf{k}} = \mathrm{Im}\Sigma_{n\mathbf{k}}(E^{\mathrm{R}}_{n\mathbf{k}}/\hbar + E^{\mathrm{I}}_{n\mathbf{k}}/\hbar) = \hbar/\tau_{n\mathbf{k}} \tag{2.61}$$

corresponds to the finite lifetime of the coupled state. As the self-energy is a non-linear function of the energy, it is possible to find more than one pole at a given $\mathbf{k}$ vector in the spectrum, giving rise to the satellite structure. The residue of the pole is given as:

$$Z_{n\mathbf{k}} = \left[1 - \frac{1}{\hbar}\frac{\partial\,\Sigma_{n\mathbf{k}}(\omega)}{\partial\omega}\right]^{-1}_{\omega=E_{n\mathbf{k}}/\hbar}. \tag{2.62}$$

This quantity is also known as the quasiparticle renormalisation factor, and it describes the spectral weight of the quasiparticle at $E_{n\mathbf{k}}$.

To discuss the energy renormalisation in experiment, one usually prefers a real quasiparticle energy $E_{n\mathbf{k}}$. As we will see in Ch. 4, the imaginary part of the electron self-energy is negligibly small in the vicinity of the Fermi surface and if $T = 0$. This justifies the definition of a purely real quasiparticle energy:

$$E_{n\mathbf{k}} = \epsilon_{n\mathbf{k}} + \mathrm{Re}\,\Sigma_{n\mathbf{k}}(E_{n\mathbf{k}}/\hbar), \tag{2.63}$$

or, linearised around $\epsilon_{n\mathbf{k}}$:

$$E_{n\mathbf{k}} = \epsilon_{n\mathbf{k}} + Z_{n\mathbf{k}}\,\mathrm{Re}\,\Sigma_{n\mathbf{k}}(\epsilon_{n\mathbf{k}}/\hbar), \tag{2.64}$$

with the real renormalisation factor:

$$Z_{n\mathbf{k}} = \left[1 - \frac{1}{\hbar}\frac{\partial\,\mathrm{Re}\,\Sigma_{n\mathbf{k}}(\omega)}{\partial\omega}\right]^{-1}_{\omega=E_{n\mathbf{k}}/\hbar}. \tag{2.65}$$

Note that the definition of the quasiparticle energy given in Eq. (2.63) corresponds to the QP peak in Brillouin-Wigner perturbation theory.[29]

For the real quasi-particle energy defined in (2.63), we can also give a straightforward definition of the renormalised quasiparticle mass m^* near the bottom of the band, assuming the non-interacting electron band has a bare mass of $m_{0,n}$:

$$\frac{1}{m_n^*} = \frac{1}{\hbar^2}\frac{\partial^2 E_{nk}}{\partial k^2}\bigg|_{k=0} = \frac{1}{m_{0,n}} + \frac{1}{\hbar^2}\frac{\partial^2 \mathrm{Re}\Sigma_{nk}}{\partial k^2}\bigg|_{k=0}, \tag{2.66}$$

where $k = |\mathbf{k}|$.

To evaluate the second derivative of the self-energy in k, one can use the chain rule to write

$$\frac{\partial^2 E_{nk}}{\partial k^2}\bigg|_{k=0} = \frac{\partial E_{nk}}{\partial \epsilon_{nk}}\frac{d^2\epsilon_{nk}}{dk^2} = \frac{\partial E_{nk}}{\partial \epsilon_{nk}}\frac{1}{m_0}. \tag{2.67}$$

Ultimately, one finds:[131]

$$\frac{m_n^*}{m_{0,n}} = \frac{1 - \frac{1}{\hbar}\partial \mathrm{Re}\Sigma(\epsilon_{nk}/\hbar, E_{nk}/\hbar)/\partial E_{nk}}{1 + \frac{1}{\hbar}\partial \mathrm{Re}\Sigma(\epsilon_{nk}/\hbar, E_{nk}/\hbar)/\partial \epsilon_{nk}}\bigg|_{k=0}. \tag{2.68}$$

2.1.6 Cumulant expansion quasiparticle spectrum

In metals with high Fermi energies, $E_\mathrm{F} \gg \hbar\omega_\mathrm{ph}$, Migdal's theorem ensures that the vertex Γ [cf. Eq. (2.33)] can be neglected.[21]

In doped semiconductors, however, the adiabaticity criterion $E_\mathrm{F} \gg \hbar\omega_\mathrm{ph}$ is often not fulfilled. As a result, the approximations made in Sec. 2.1.5 do not capture the spectral properties of a doped semiconductor very well. In particular, the characteristic satellite structure of the polaron [cf. Figs. 1.1 and 1.2] is not correctly reproduced in Dyson's equation [see our discussion in Chapter 4].

A promising strategy to improve the predictive power of the electron spectral function in the anti-adiabatic limit $E_\mathrm{F} \ll \hbar\omega_\mathrm{ph}$ involves the inclusion of higher-order electron-phonon diagrams beyond the Fan-Migdal self-energy. While such an approach is potentially very costly, there exists a simple approach in which the resummation over certain types of Feynman diagrams is implicit in the formalism. This approach is known as the cumulant expansion formalism.[9,17,55–73]

Motivation for the functional form of cumulant expansion

In the cumulant expansion approximation, the electron Green's function is expanded in terms of an exponential function:[68]

$$G_{n\mathbf{k}}(t-t') = G^0_{n\mathbf{k}}(t-t')\, e^{C_{n\mathbf{k}}(t-t')}, \tag{2.69}$$

where $G^0_{n\mathbf{k}}(t-t')$ is the noninteracting electron Green's function, and $C_{n\mathbf{k}}(t-t')$ is the (electron) cumulant function. A motivation for this choice of expansion is given in Ref. [68]: Start from the coupled electron-boson Hamiltonian:

$$\begin{aligned} \hat{H} &= \sum_{n\mathbf{k}} \epsilon_{n\mathbf{k}} \hat{c}^\dagger_{n\mathbf{k}} \hat{c}_{n\mathbf{k}} + \sum_{\mathbf{q}\nu} \hbar\omega_{\mathbf{q}\nu} \left(\hat{a}^\dagger_{\mathbf{q}\nu} \hat{a} + 1/2 \right) \\ &+ g \sum_{\substack{\mathbf{kq} \\ nm\nu}} V_{mn\nu}(\mathbf{k},\mathbf{q})\, \hat{c}^\dagger_{m\mathbf{k}+\mathbf{q}} \hat{c}_{n\mathbf{k}} \left(\hat{a}_{\mathbf{q}\nu} + \hat{a}^\dagger_{-\mathbf{q}\nu} \right), \end{aligned} \tag{2.70}$$

where g is the coupling constant of the perturbation, and $V_{mn\nu}(\mathbf{k},\mathbf{q})$ is the electron-boson coupling matrix element. The electron and boson contributions on the first line constitute the unperturbed Hamiltonian $\hat{H}^0$ whose eigenstates are assumed to be known. The electron-boson coupling on the second line describes a perturbation $g\hat{V}$. Note that an alternative derivation of the Fan-Migdal electron self-energy [Eq. (2.37)] starts from a coupled electron-phonon Hamiltonian such as the one in Eq. (2.70); see Ref. [50].

The evolution of the electron creation (annihilation) operators is given by the usual expression:

$$\hat{c}^\dagger_{n\mathbf{k}}(t) = e^{i\hat{H}t/\hbar}\, \hat{c}^\dagger_{n\mathbf{k}}\, e^{-i\hat{H}t/\hbar}, \tag{2.71}$$

and the time-evolution operator is written as:

$$e^{-i\hat{H}t/\hbar} = e^{-i\left(\hat{H}^0 + g\hat{V}\right)t/\hbar} = e^{-i\hat{H}^0 t/\hbar} U_{\mathrm{I}}(t), \tag{2.72}$$

where $U_{\mathrm{I}}(t) = e^{i\hat{H}^0 t/\hbar} e^{-i\hat{H}t/\hbar}$ is the operator describing the time evolution that is due to the perturbation $g\hat{V}$, i.e. the time-evolution operator in the interaction picture.

In the time domain, the non-interacting Green's function of an electron is defined as:

$$G_{n\mathbf{k}}(t-t') = -\frac{i}{\hbar}\theta(t-t') e^{-\frac{i}{\hbar}(\epsilon_{n\mathbf{k}} - i\eta)(t-t')}. \tag{2.73}$$

Using $U_{\mathrm{I}}(t)$, we can then express the fully interacting electron Green's function as [cf. Eq. (2.13)]:

$$G_{n\mathbf{k}}(t-t') = G^0_{n\mathbf{k}}(t-t') \langle n\mathbf{k}| U_{\mathrm{I}}(t-t') |n\mathbf{k}\rangle, \tag{2.74}$$

where $|n\mathbf{k}\rangle = \hat{c}^\dagger_{n\mathbf{k}}|0\rangle$. It is always possible to express the time evolution operator $U_{\mathrm{I}}(t)$ in exponential form,[132] and averages of such generalised exponential operators can be conveniently calculated using a cumulant expansion in powers of the coupling constant g.[133,134] Therefore, we write:

$$\langle n\mathbf{k}| U_{\mathrm{I}}(t-t') |n\mathbf{k}\rangle = e^{C_{n\mathbf{k}}(t-t')}, \tag{2.75}$$

where the cumulant function

$$C_{n\mathbf{k}}(t-t') = \sum_{l=2}^{\infty} C^{(l)}_{n\mathbf{k}}(t-t') \tag{2.76}$$

is an infinite ascending series of cumulants in even powers of g, i.e. $C^{(l)}_{n\mathbf{k}} \propto g^l$. In applications of the cumulant to electron-phonon spectra, substantial improvements of the satellite structure are already achieved with only the lowest (i.e. second in g) order of the cumulant expansion. This is also the approximation used in this thesis.

Derivation of the hole cumulant

Before we continue, we need to highlight the fact that the cumulant expansion can only be rigorously defined for the propagation of a particle in one time direction, i.e. it can only describe hole states below the Fermi surface or electron states above the Fermi surface. The reason for this will become clear during the derivation. Within Green's function theory, these states are described by the lesser or greater Green's functions $G^{\gtrless}_{n\mathbf{k}}$ and self-energies $\Sigma^{\gtrless}_{n\mathbf{k}}$.

As we are interested in modelling many-body states below the Fermi surface, we present here the derivation of the hole cumulant presented in Ref. [135]. The derivation of the electron cumulant follows the same steps, and all results will be presented below.

To obtain the functional form of the cumulant function, we compare the expansions in the coupling strength g of the exponential in Eq. (2.69) to the expansion of the Dyson equation in Eq. (2.54):

$$G^{<}_{n\mathbf{k}}(t'-t) = G^{<,0}_{n\mathbf{k}}(t'-t)\,\left[1 + C^{<}_{n\mathbf{k}}(t'-t) + \frac{1}{2}\left(C^{<}_{n\mathbf{k}}(t'-t)\right)^2 + ...\right] \tag{2.77}$$

and

$$G^{<}_{n\mathbf{k}}(t'-t) = G^{<,0}_{n\mathbf{k}}(t'-t) + \frac{1}{2\pi}\int_{-\infty}^{\infty} d\omega\, G^{<,0}_{n\mathbf{k}}(\omega)\,\Sigma^{<}_{n\mathbf{k}}(\omega)\,G^{<,0}_{n\mathbf{k}}\,e^{-i\omega t} + ..., \tag{2.78}$$

where

$$\Sigma^{<}_{n\mathbf{k}}(\omega) = \frac{1}{\hbar}\sum_{m\nu}\int \frac{d\mathbf{q}}{\Omega_{\mathrm{BZ}}}|g_{mn\nu}(\mathbf{k},\mathbf{q})|^2 + \frac{f_{m\mathbf{k}+\mathbf{q}}}{\omega - \epsilon_{m\mathbf{k}+\mathbf{q}}/\hbar + \omega_{\mathbf{q}\nu} - i\eta} \tag{2.79}$$

is the lesser Fan-Migdal self-energy. The greater self-energy is given by:

$$\Sigma^{>}_{n\mathbf{k}}(\omega) = \frac{1}{\hbar}\sum_{m\nu}\int \frac{d\mathbf{q}}{\Omega_{\mathrm{BZ}}}|g_{mn\nu}(\mathbf{k},\mathbf{q})|^2\frac{1 - f_{m\mathbf{k}+\mathbf{q}}}{\omega - \epsilon_{m\mathbf{k}+\mathbf{q}}/\hbar - \omega_{\mathbf{q}\nu} + i\eta}, \tag{2.80}$$

and their relation to the retarded self-energy in Eq. (2.37) is given by $\Sigma^{\mathrm{R}} = \Sigma^{<} + (\Sigma^{>})^*$.[59]

Define the second-order variation in the Green's function as:

$$\begin{aligned}\Delta G^{<}_{n\mathbf{k}}(t'-t) &= G^{<,0}_{n\mathbf{k}}(t'-t)\,C^{<}_{n\mathbf{k}}(t'-t) \\ &= \frac{1}{2\pi}\int_{t'}^{t} dt_1 \int_{t'}^{t} dt_2\, G^{<,0}_{n\mathbf{k}}(t'-t_1)\,\Sigma^{<}_{n\mathbf{k}}(t_1-t_2)\,G^{<,0}_{n\mathbf{k}}(t_2-t).\end{aligned} \tag{2.81}$$

Using the definition of the lesser (hole) Green's function,

$$G^{<,0}_{n\mathbf{k}}(t'-t) = \frac{i}{\hbar}\theta\left(t'-t\right)\,e^{\frac{i}{\hbar}(\epsilon_{n\mathbf{k}}+i\eta)(t-t')}, \tag{2.82}$$

we can simplify Eq. (2.81) as:

$$\Delta G^{<}_{n\mathbf{k}}(t) = \frac{i}{\hbar}\theta(-t)\,e^{-\frac{i}{\hbar}(\epsilon_{n\mathbf{k}}+i\eta)t}\frac{i}{2\pi\,\hbar}\int_{t}^{\infty} dt_1 \int_{t_1}^{\infty} d\tau\, e^{\frac{i}{\hbar}(\epsilon_{n\mathbf{k}}+i\eta)\,\tau}\Sigma^{<}_{n\mathbf{k}}(\tau), \tag{2.83}$$

where we set $t' = 0$ and $\tau = t_1 - t_2$. By comparison with Eq. (2.81), we can now write down the explicit form of the second-order cumulant:

$$C^{<}_{n\mathbf{k}}(t) = \frac{i}{2\pi\,\hbar}\int_{t}^{\infty} dt_1 \int_{t_1}^{\infty} d\tau\, e^{\frac{i}{\hbar}(\epsilon_{n\mathbf{k}}+i\eta)\,\tau}\Sigma^{<}_{n\mathbf{k}}(\tau), \tag{2.84}$$

Next, one makes use of the spectral representation of the self-energy:

$$\Sigma_{n\mathbf{k}}(\omega) = \underbrace{\int_{0}^{E_{\mathrm{F}}/\hbar} d\omega' \frac{\Gamma_{n\mathbf{k}}(\omega')}{\omega - \omega' - i\eta}}_{=\Sigma^{<}_{n\mathbf{k}}(\omega)} + \underbrace{\int_{E_{\mathrm{F}}/\hbar}^{\infty} d\omega' \frac{\Gamma_{n\mathbf{k}}(\omega')}{\omega - \omega' + i\eta}}_{=\Sigma^{>}_{n\mathbf{k}}(\omega)}, \tag{2.85}$$

where

$$\Gamma_{n\mathbf{k}}(\omega) = -\frac{1}{\pi}\mathrm{Im}\Sigma_{n\mathbf{k}}(\omega)\,\mathrm{sgn}(\hbar\omega - E_\mathrm{F}), \tag{2.86}$$

is the corresponding spectral function. After some manipulation, one arrives at:[135]

$$\begin{aligned} C^<_{n\mathbf{k}}(t) &= \frac{-1}{\hbar}\int_{-\infty}^{E_\mathrm{F}/\hbar} d\omega\,\Gamma_{n\mathbf{k}}(\omega)\frac{1+i(\epsilon_{n\mathbf{k}}/\hbar-\omega-i\eta)\,t - e^{i(\epsilon_{n\mathbf{k}}/\hbar-\omega-i\eta)t}}{(\epsilon_{n\mathbf{k}}/\hbar-\omega-i\eta)^2} \\ &= -\frac{it}{\hbar}\Sigma_{n\mathbf{k}}(\epsilon_k) + \frac{1}{\hbar}\frac{\partial\,\Sigma^<_{n\mathbf{k}}}{\partial\omega}\bigg|_{\hbar\omega=\epsilon_{n\mathbf{k}}} + \frac{1}{\hbar}\int_{-\infty}^{E_\mathrm{F}/\hbar} d\omega\frac{e^{i(\epsilon_{n\mathbf{k}}-\omega-i\eta)t}}{(\epsilon_{n\mathbf{k}}-\omega-i\eta)^2}\Gamma_{n\mathbf{k}}(\omega). \end{aligned} \tag{2.87}$$

In the second step, we used again the spectral representation from Eq. (2.85) and the fact that

$$\begin{aligned} \frac{-1}{\hbar}\int_{-\infty}^{E_\mathrm{F}/\hbar} d\omega'\frac{\Gamma_{n\mathbf{k}}(\omega')}{(\epsilon_{n\mathbf{k}}-\omega'-i\eta)^2} &= \frac{1}{\hbar}\frac{\partial}{\partial\omega}\int_{-\infty}^{E_\mathrm{F}/\hbar} d\omega'\frac{\Gamma_{n\mathbf{k}}(\omega')}{\epsilon_{n\mathbf{k}}-\omega'-i\eta}\bigg|_{\hbar\omega=\epsilon_{n\mathbf{k}}} \\ &= \frac{1}{\hbar}\frac{\partial\Sigma^<_{n\mathbf{k}}(\omega)}{\partial\omega}\bigg|_{\hbar\omega=\epsilon_{n\mathbf{k}}}. \end{aligned} \tag{2.88}$$

Equation (2.87) allows us to divide the spectrum into a quasiparticle part and a satellite part:

$$C^{<,\mathrm{QP}}_{n\mathbf{k}}(t) = -\frac{it}{\hbar}\Sigma_{n\mathbf{k}}(\epsilon_k) + \frac{1}{\hbar}\frac{\partial\,\Sigma^<_{n\mathbf{k}}}{\partial\omega}\bigg|_{\hbar\omega=\epsilon_{n\mathbf{k}}} \tag{2.89}$$

$$C^{<,\mathrm{S}}_{n\mathbf{k}}(t) = \frac{1}{\hbar}\int_{-\infty}^{E_\mathrm{F}/\hbar} d\omega\frac{e^{i(\epsilon_{n\mathbf{k}}-\omega-i\eta)t}}{(\epsilon_{n\mathbf{k}}-\omega-i\eta)^2}\Gamma_{n\mathbf{k}}(\omega). \tag{2.90}$$

Definitions (2.89) and (2.90) allow us to isolate the quasiparticle part of the Green's function:

$$G^{<,\mathrm{QP}}_{n\mathbf{k}}(t) = \frac{i}{\hbar}\theta(-t)\,e^{\frac{-i}{\hbar}(\epsilon_{n\mathbf{k}}+\Sigma_{n\mathbf{k}}(\epsilon_k))t + \partial\,\Sigma^<_{n\mathbf{k}}/\hbar\partial\omega|_{\hbar\omega=\epsilon_{n\mathbf{k}}}} \tag{2.91}$$

Taking a closer look at Eq. (2.91), we find that the noninteracting electron energy $\epsilon_{n\mathbf{k}}$ is again renormalised by the real part of Σ, while the imaginary part contributes to finite lifetime broadening. The role of the self-energy derivative becomes clearer when considering the corresponding quasiparticle spectral function:

$$A^{<,\mathrm{QP}}_{n\mathbf{k}}(\omega) = \frac{Z^<_{n\mathbf{k}}\,(1-f_{n\mathbf{k}})}{\pi}\frac{\mathrm{Im}\,\Sigma^<_{n\mathbf{k}}(\epsilon_{n\mathbf{k}})\cos\alpha^<_{n\mathbf{k}} - [\hbar\omega-\epsilon_{n\mathbf{k}}-\mathrm{Re}\,\Sigma^<_{n\mathbf{k}}(\epsilon_{n\mathbf{k}})]\sin\alpha^<_{n\mathbf{k}}}{[\hbar\omega-\epsilon_{n\mathbf{k}}-\mathrm{Re}\,\Sigma^<_{n\mathbf{k}}(\epsilon_{n\mathbf{k}})]^2 + [\mathrm{Im}\,\Sigma^<_{n\mathbf{k}}(\epsilon_{n\mathbf{k}})]^2},$$

where we write:

$$\alpha^<_{n\mathbf{k}} = \left|\frac{\partial\,\mathrm{Im}\,\Sigma^<_{n\mathbf{k}}(\omega)}{\partial\omega}\right|_{\omega=\epsilon_{n\mathbf{k}}/\hbar} \qquad \text{and} \qquad Z^<_{n\mathbf{k}} = \exp\left(\frac{\partial\,\mathrm{Re}\,\Sigma^<_{n\mathbf{k}}(\omega)}{\partial\omega}\right)_{\omega=\epsilon_{n\mathbf{k}}/\hbar}. \tag{2.92}$$

For $\alpha^{<}_{n\mathbf{k}} = 0$, the main quasiparticle peak has a Lorentzian lineshape, as is expected for an ideal quasiparticle state.[130] In general, however, the shape of the main quasiparticle is asymmetric about its peak and resembles a Fano lineshape. This difference is due to the nonzero imaginary part of the self-energy derivative. Note that a similarly asymmetric lineshape can be obtained in the Dyson equation approach if the quasiparticle energy is treated as a complex quantity [cf. Eq. (2.59)].[130]

The total spectrum can be written as the sum of $A^{<,\mathrm{QP}}_{n\mathbf{k}}$ and a convolution between the quasiparticle and the satellite part:

$$\begin{aligned} A^{<}_{n\mathbf{k}}(\omega) &= A^{<,\mathrm{QP}}_{n\mathbf{k}}(\omega) + \frac{1}{2\pi}\int_{-\infty}^{\infty} dt e^{i\omega t}\, e^{\frac{-i}{\hbar}\epsilon_{n\mathbf{k}} + C^{<,\mathrm{QP}}_{n\mathbf{k}}(t)} \left[e^{C^{<,\mathrm{S}}_{n\mathbf{k}}(t)} - 1\right] \\ &= A^{<,\mathrm{QP}}_{n\mathbf{k}}(\omega) + A^{<,\mathrm{QP}}_{n\mathbf{k}}(\omega) * A^{<,\mathrm{S}}_{n\mathbf{k}}, \end{aligned} \tag{2.93}$$

where

$$\begin{aligned} A^{<,\mathrm{S}}_{n\mathbf{k}}(\omega) &= \frac{1}{2\pi}\int_{-\infty}^{\infty} e^{i\omega t}\left[e^{C^{<,\mathrm{S}}_{n\mathbf{k}}(t)} - 1\right] \\ &= \frac{1}{2\pi}\int_{-\infty}^{\infty} e^{i\omega t}\left[C^{<,\mathrm{S}}_{n\mathbf{k}}(t) + \frac{1}{2!}\left(C^{<,\mathrm{S}}_{n\mathbf{k}}(t)\right)^2 + ...\right] \\ &= \frac{\mathrm{Im}\,\Sigma^{<}_{n\mathbf{k}}(\epsilon_{n\mathbf{k}}/\hbar + \omega) - [\mathrm{Im}\,\Sigma^{<}_{n\mathbf{k}}(\epsilon_{n\mathbf{k}}/\hbar) + \hbar\omega\,\alpha^{<}_{n\mathbf{k}}]}{\pi\,\hbar^2\omega^2}, \end{aligned} \tag{2.94}$$

and the last equality is obtained after Fourier transforming $C^{<,\mathrm{S}}_{n\mathbf{k}}(t)$ to frequency space [cf. Ref. [135]].

The derivation for the greater (electron) cumulant follows essentially the same steps, and it is described in Refs. [59, 68]. For completeness, we summarise the final results for both hole and electron cumulants:

$$\begin{aligned} A^{\gtrless}_{n\mathbf{k}}(\omega) &= A^{\gtrless,\mathrm{QP}}_{n\mathbf{k}}(\omega) + A^{\gtrless,\mathrm{QP}}_{n\mathbf{k}}(\omega) * A^{\gtrless\mathrm{S}}_{n\mathbf{k}}(\omega) \\ &+ \frac{1}{2}A^{\gtrless,\mathrm{QP}}_{n\mathbf{k}}(\omega) * A^{\gtrless,\mathrm{S}}_{n\mathbf{k}}(\omega) * A^{\gtrless,\mathrm{S}}_{n\mathbf{k}}(\omega) + \cdots, \end{aligned} \tag{2.95}$$

$$\begin{aligned} A^{\gtrless,\mathrm{QP}}_{n\mathbf{k}}(\omega) &= \frac{Z^{\gtrless}_{n\mathbf{k}}}{\pi}\begin{pmatrix} 1 - f_{n\mathbf{k}} \\ f_{n\mathbf{k}} \end{pmatrix} \\ &\times \frac{\mathrm{Im}\,\Sigma^{\gtrless}_{n\mathbf{k}}(\epsilon_{n\mathbf{k}})\cos\alpha^{\gtrless}_{n\mathbf{k}} - \left[\hbar\omega - \epsilon_{n\mathbf{k}} - \mathrm{Re}\,\Sigma^{\gtrless}_{n\mathbf{k}}(\epsilon_{n\mathbf{k}})\right]\sin\alpha^{\gtrless}_{n\mathbf{k}}}{\left[\hbar\omega - \epsilon_{n\mathbf{k}} - \mathrm{Re}\,\Sigma^{\gtrless}_{n\mathbf{k}}(\epsilon_{n\mathbf{k}})\right]^2 + \left[\mathrm{Im}\,\Sigma^{\gtrless}_{n\mathbf{k}}(\epsilon_{n\mathbf{k}})\right]^2}, \end{aligned} \tag{2.96}$$

$$A^{\gtrless\mathrm{S}}_{n\mathbf{k}}(\omega) = \frac{\mp\mathrm{Im}\,\Sigma^{\gtrless}_{n\mathbf{k}}(\epsilon_{n\mathbf{k}}/\hbar + \omega) - \left(\mp\mathrm{Im}\,\Sigma^{\gtrless}_{n\mathbf{k}}(\epsilon_{n\mathbf{k}}/\hbar) \mp \hbar\omega\,\alpha^{\gtrless}_{n\mathbf{k}}\right)}{\pi\,\hbar^2\omega^2}, \tag{2.97}$$

and

$$\alpha^{\gtrless}_{n\mathbf{k}} = \left| \frac{\partial \operatorname{Im} \Sigma^{\gtrless}_{n\mathbf{k}}(\omega)}{\partial \omega} \right|_{\omega=\epsilon_{n\mathbf{k}}/\hbar}, \qquad Z^{\gtrless}_{n\mathbf{k}} = \exp\left(\frac{\partial \operatorname{Re} \Sigma^{\gtrless}_{n\mathbf{k}}(\omega)}{\partial \omega} \right)_{\omega=\epsilon_{n\mathbf{k}}/\hbar}. \tag{2.98}$$

The peak energy is given by:

$$E^{\gtrless}_{n\mathbf{k}} = \epsilon_{n\mathbf{k}} + \operatorname{Re} \Sigma^{\gtrless}_{n\mathbf{k}}(\epsilon_{n\mathbf{k}}). \tag{2.99}$$

At the bottom of a parabolic band, the effective mass along $\mathbf{k}$ away from Γ is equal to

$$\frac{m^{\gtrless,*}_{n}}{m_{0,n}} = \left[1 + \frac{1}{\hbar} \frac{\partial \operatorname{Re} \Sigma^{\gtrless}_{nk}(\omega)}{\partial \omega} + \frac{\partial \operatorname{Re} \Sigma^{\gtrless}_{nk}(\omega)}{\partial \epsilon_{nk}} \right]^{-1}_{\epsilon_{nk}=0,\omega=0}. \tag{2.100}$$

Successive terms of the series expansion in Eq. (2.95) represent a sequence of satellites, one per convolution. As we will show in Chapter 4, higher-order convolutions correspond to weaker satellites located further away from the QP peak. In practice, the first two to three satellites carry the majority of the spectral weight of the incoherent part and are the features usually resolved in experiments.

2.2 Superconducting state

We now turn to the superconducting state in doped semiconductors. The field theory developed in Sec. 2.1 can be very elegantly generalised to the treatment of coupled electron pairs at finite temperatures. This generalisation is known as Migdal-Eliashberg theory, and we introduce it Sec. 2.2.1.

Within ME theory, one constructs a generalised self-energy comprising both attractive electron-phonon and repulsive electron-electron interactions. From this total effective self-energy, one then derives a system of four coupled nonlinear equations. The solutions to these equations can be related to the spectral properties of the interacting system.

In particular, one of the four equations describes the superconducting gap Δ. This gap can be resolved in experiment, and it is one of the hallmarks of superconductivity in system. Within ME theory, the gap function Δ is only different from zero in the superconducting state. We can therefore determine the critical temperature T_{C} by calculating the superconducting gap for a range of temperatures. The highest temperature for which there exists a nontrivial solution for Δ is defined as the critical temperature.

Until recently, a direct numerical solution of the full set of ME equations from first principles would have exceeded available computational resources. Even today, a naive implementation of ME theory would require immense computing power, as this system of four coupled nonlinear equations must be solved on an extremely dense mesh of momentum and frequency grid points. As a result, all hitherto available implementations of ME theory make use of one or several approximations to the full theory.

We dedicate the remainder of this section to the discussion of some of the most important approximations to ME theory. In particular, we are interested in the question which of these approximations are valid for the treatment of polar semiconductors. We first present the approximations here, before we then move on to test them on a model of a polar semiconductor in Chapter 5 below.

Firstly, we discuss the linearised ME equations in Sec. 2.2.2, in which one uses the fact that the superconducting gap Δ is small at temperatures $T \approx T_\mathrm{C}$. Next, in Sec. 2.2.3, we present a very common approximation that allows one to condense the total repulsive Coulomb interaction in the system into one simple empirical parameter. This so-called "Morel-Anderson pseudopotential" is widely used in *ab initio* calculations of superconductors. Then, in Sec. 2.2.4, we further simplify our equations by only considering electron pairing across the Fermi surface, i.e. between states $(n, \mathbf{k})$ with $\epsilon_{n\mathbf{k}} = E_\mathrm{F}$. This is a good approximation especially for nonpolar metallic systems. The last approximation that we discuss here is the McMillan equation, which is a semi-empirical equation for the superconducting T_C of simple superconductors such as elemental metals.

2.2.1 Migdal-Eliashberg theory

Migdal-Eliashberg theory[21,104] formulates the groundbreaking theory of superconductivity by Bardeen, Cooper and Schrieffer (BCS)[25] as a many-body Green's function problem, and generalises its applicability to the case of strong electron-phonon coupling.

A convenient framework to express the ME equations is provided by the Nambu-Gor'kov formalism:[136,137] In this approach, the electron Green's function, and self-energy are expressed in terms of 2×2 matrices, which allows to treat correlations between pairs of electrons in a unified formalism. As we will see below, in the normal state, the

Green's function matrix $\hat{G}$ is diagonal, where the component $\left[\hat{G}\right]_{11}$ describes an electron in a Bloch state $(n\mathbf{k}\uparrow)$, and the component $\left[\hat{G}\right]_{22}$ describes the state $(n-\mathbf{k}\downarrow)$. The off-diagonal elements of $\hat{G}$ are related to the superconducting order parameter, and only become non-zero below the critical temperature. In the superconducting state, their magnitude increases with the attractive pair potential.

Classic references for the following derivation are Refs.[105, 106]. A more modern formulation of the equations is found e.g. in Refs.[44, 107], which we follow closely.

One starts from a two-component field operator

$$\Psi_{n\mathbf{k}} = \begin{pmatrix} \hat{c}_{n\mathbf{k}\uparrow} \\ \hat{c}^{\dagger}_{n-\mathbf{k}\downarrow} \end{pmatrix}, \tag{2.101}$$

and the corresponding time-ordered Green's function:

$$\hat{G}_{n\mathbf{k}}(\tau) = -\langle \hat{T}_{\tau} \Psi_{n\mathbf{k}}(\tau) \Psi^{\dagger}_{n\mathbf{k}}(0) \rangle. \tag{2.102}$$

Here, $\hat{T}_{\tau}$ the time-ordering operator for the imaginary time τ and $\Psi_{n\mathbf{k}}(\tau)$ is the two-component field operator in the Heisenberg picture. The brackets $\langle\cdot\rangle$ indicate a grand-canonical thermodynamic average. Broken down into components, $\hat{G}$ consists of

$$\hat{G}_{n\mathbf{k}}(\tau) = -\begin{pmatrix} \langle \hat{T}_{\tau}\, \hat{c}_{n\mathbf{k}\uparrow}(\tau)\, \hat{c}^{\dagger}_{n\mathbf{k}\uparrow}(0) \rangle & \langle \hat{T}_{\tau}\, \hat{c}_{n\mathbf{k}\uparrow}(\tau)\, \hat{c}_{n-\mathbf{k}\downarrow}(0) \rangle \\ \langle \hat{T}_{\tau}\, \hat{c}^{\dagger}_{n-\mathbf{k}\downarrow}(\tau)\, \hat{c}^{\dagger}_{n\mathbf{k}\uparrow}(0) \rangle & \langle \hat{T}_{\tau}\, \hat{c}^{\dagger}_{n-\mathbf{k}\downarrow}(\tau)\, \hat{c}_{n-\mathbf{k}\downarrow}(0) \rangle \end{pmatrix} \tag{2.103}$$

In this matrix, the diagonal elements correspond to the standard quasiparticle Green's functions for the states $(n\mathbf{k},\uparrow)$ and $(n-\mathbf{k},\downarrow)$, respectively. The off-diagonal elements represent Gor'kov's anomalous Green's functions $F_{n\mathbf{k}}(\tau)$ and $F^{*}_{n\mathbf{k}}(\tau)$ which describe the Cooper pairs. These functions are only non-zero if pair formation is energetically favoured, i.e. below the critical temperature T_{C}.

Next, we express the frequency-dependent Green's function in terms of a sum over imaginary Matsubara frequencies. This leads to two formal simplifications: Firstly, it allows one to avoid numerical complications from the poles of the Green's function near the real axis, and secondly, the definition of the Matsubara frequencies provides an organic framework to incorporate temperature directly into the formalism:

$$\hbar\omega_j = (2j+1)\pi k_{\mathrm{B}} T \quad \text{with} \quad j \in \mathbb{Z}, \tag{2.104}$$

where T is the absolute temperature, and k_B is the Boltzmann constant. The Green's function is Fourier transformed according to

$$\hat{G}_{n\mathbf{k}}(\tau) = k_\mathrm{B}T \sum_{i\omega_j} e^{-i\omega_j\tau} \hat{G}_{n\mathbf{k}}(i\omega_j). \tag{2.105}$$

In Matsubara frequency space, the number of particles in the unit cell is obtained from the relation

$$N_e = 2k_\mathrm{B}T \sum_{n'\mathbf{k}'\omega'_j} G_{n'\mathbf{k}'}(i\omega'_j)\, e^{i\omega'_j\, 0^+}. \tag{2.106}$$

After Fourier transformation, the matrix elements of $\hat{G}$ look like

$$\hat{G}_{n\mathbf{k}}(i\omega_j) = \begin{pmatrix} G_{n\mathbf{k}}(i\omega_j) & F_{n\mathbf{k}}(i\omega_j) \\ F^*_{n\mathbf{k}}(i\omega_j) & -G_{n-\mathbf{k}}(-i\omega_j) \end{pmatrix} \tag{2.107}$$

Now we can write down the Dyson equation for the interacting system in matrix form [cf. Eq. (2.54)]:

$$\hat{G}^{-1}_{n\mathbf{k}}(i\omega_j) = \left[\hat{G}^0_{n\mathbf{k}}(i\omega_j)\right]^{-1} - \hat{\Sigma}_{n\mathbf{k}}(i\omega_j) \tag{2.108}$$

We expand the 2×2 matrices in (2.108) in terms of the Pauli matrices

$$\hat{\tau}_0 = \begin{pmatrix} 1 & 0 \\ 0 & 1 \end{pmatrix} \qquad \hat{\tau}_1 = \begin{pmatrix} 0 & 1 \\ 1 & 0 \end{pmatrix} \qquad \hat{\tau}_2 = \begin{pmatrix} 0 & -i \\ i & 0 \end{pmatrix} \qquad \hat{\tau}_3 = \begin{pmatrix} 1 & 0 \\ 0 & -1 \end{pmatrix}. \tag{2.109}$$

First, the non-interacting Green's function $\left[\hat{G}^0_{n\mathbf{k}}\right]^{-1}$ has to have the form

$$\begin{aligned} \left[\hat{G}^0_{n\mathbf{k}}(i\omega_j)\right]^{-1} &= i\hbar\omega_j\hat{\tau}_0 - (\epsilon_{n\mathbf{k}} - \mu_\mathrm{C})\hat{\tau}_3 \\ &= \begin{pmatrix} i\hbar\omega_j - (\epsilon_{n\mathbf{k}} - \mu_\mathrm{C}) & 0 \\ 0 & i\hbar\omega_j + (\epsilon_{n\mathbf{k}} - \mu_\mathrm{C}) \end{pmatrix} \end{aligned} \tag{2.110}$$

with the chemical potential μ_C. From here, we recover the known expressions for the non-interacting electron Green's function expanded in Matsubara frequencies,

$$G^0_{n\mathbf{k}}(i\omega_j) = \frac{1}{i\hbar\omega_j - (\epsilon_{n\mathbf{k}} - \mu_\mathrm{C})} \quad \text{and} \quad G^0_{n-\mathbf{k}}(-i\omega_j) = \frac{-1}{i\hbar\omega_j + (\epsilon_{n-\mathbf{k}} - \mu_\mathrm{C})}. \tag{2.111}$$

The Pauli matrices form a basis for the vector space of 2×2 Hermitian matrices. Therefore, we can expand:

$$\begin{aligned} \hat{\Sigma}_{n\mathbf{k}}(i\omega_j) &= i\hbar\omega_j \left(1 - Z_{n\mathbf{k}}(i\omega_j)\right) \hat{\tau}_0 + \chi_{n\mathbf{k}}(i\omega_j)\hat{\tau}_3 \\ &+ \phi_{n\mathbf{k}}(i\omega_j)\hat{\tau}_1 + \bar{\phi}_{n\mathbf{k}}(i\omega_j)\hat{\tau}_2, \end{aligned} \tag{2.112}$$

where we introduce the scalar functions $Z_{n\mathbf{k}}(i\omega_j)$, $\chi_{n\mathbf{k}}(i\omega_j)$, $\phi_{n\mathbf{k}}(i\omega_j)$, and $\bar{\phi}_{n\mathbf{k}}(i\omega_j)$. With this, we can return to Eq. (2.108) [see Sec. 7 in Ref.[106]]:

$$\begin{aligned}\hat{G}^{-1}_{n\mathbf{k}}(i\omega_j) &= i\hbar\omega_j Z_{n\mathbf{k}}(i\omega_j)\hat{\tau}_0 - \left(\epsilon_k + \chi_{n\mathbf{k}}(i\omega_j) - \mu_{\mathrm{C}}\right)\hat{\tau}_3 \\ &- \phi_{n\mathbf{k}}(i\omega_j)\hat{\tau}_1 - \bar{\phi}_{n\mathbf{k}}(i\omega_j)\hat{\tau}_2 \end{aligned} \tag{2.113}$$

Lastly, inverting the expression for the Green's function, we obtain:

$$\begin{aligned}\hat{G}_{n\mathbf{k}}(i\omega_j) &= \Big[i\hbar\omega_j\, Z_{n\mathbf{k}}(i\omega_j)\hat{\tau}_0 + \left[\epsilon_{n\mathbf{k}} - \mu_{\mathrm{C}} + \chi_{n\mathbf{k}}(i\omega_j)\right]\hat{\tau}_3 \\ &+ \phi_{n\mathbf{k}}(i\omega_j)\hat{\tau}_1 + \bar{\phi}_{n\mathbf{k}}(i\omega_j)\hat{\tau}_2\Big] / \det\left(\hat{G}^{-1}_{n\mathbf{k}}\right), \end{aligned} \tag{2.114}$$

where

$$\begin{aligned}\det\left(\hat{G}^{-1}_{n\mathbf{k}}\right) &= \left[i\hbar\omega_j\, Z_{n\mathbf{k}}(i\omega_j)\right]^2 - \left[\epsilon_{n\mathbf{k}} - \mu_{\mathrm{C}} + \chi_{n\mathbf{k}}(i\omega_j)\right]^2 \\ &- \phi^2_{n\mathbf{k}}(i\omega_j) - \bar{\phi}^2_{n\mathbf{k}}(i\omega_j) \end{aligned} \tag{2.115}$$

Above the critical temperature, $\phi_{n\mathbf{k}}$ and $\bar{\phi}_{n\mathbf{k}}$ must vanish as the Green's function is diagonal in this case. Then, $Z_{n\mathbf{k}}$ and $\chi_{n\mathbf{k}}$ can be related back to the normal-state Fan-Migdal self-energy from Eq. (2.37):

$$i\hbar\omega_j\left[1 - Z_{n\mathbf{k}}(i\omega_j)\right] = \frac{1}{2}\left[\Sigma_{n\mathbf{k}}(i\omega_j) - \Sigma_{n\mathbf{k}}(-i\omega_j)\right] \tag{2.116}$$

$$\chi_{n\mathbf{k}}(i\omega_j) = \frac{1}{2}\left[\Sigma_{n\mathbf{k}}(i\omega_j) + \Sigma_{n\mathbf{k}}(-i\omega_j)\right] \tag{2.117}$$

Next, we turn to the definition of the electron self-energy. We know that the pairing interaction is the combined action of attractive electron-phonon and repulsive electron-electron interactions:

$$\hat{\Sigma}_{n\mathbf{k}}(i\omega_j) = \hat{\Sigma}^{\mathrm{ep}}_{n\mathbf{k}}(i\omega_j) + \hat{\Sigma}^{\mathrm{c}}_{n\mathbf{k}}(i\omega_j). \tag{2.118}$$

We review both contributions here:

Electron-phonon self-energy

As before, the electron-phonon self-energy at the state $\mathbf{k}$ within the first Brillouin zone is given by [see appendix of Ref. [138]]:

$$\hat{\Sigma}^{\mathrm{ep}}_{n\mathbf{k}}(i\omega_j) = -k_{\mathrm{B}}T \sum_{\substack{n'\,\mathbf{k}' \\ \nu\,\omega'_j}} |g_{nn'\nu}(\mathbf{k},\mathbf{k}')|^2\, \hat{\tau}_3\, \hat{G}_{n'\mathbf{k}'}(i\omega'_j)\, \hat{\tau}_3\, D_{\mathbf{k}-\mathbf{k}'\nu}(i\omega_j - i\omega'_j), \tag{2.119}$$

where $g_{nn'\nu}(\mathbf{k},\mathbf{k}')$ is the fully screened electron-phonon matrix element, and $D_{\mathbf{k}-\mathbf{k}'\nu}(i\omega_j)$ is the interacting phonon propagator.

As with the electron Green's function, we can re-write the interacting phonon propagator in terms of its spectral representation [cf. Eq. 2.57]:

$$D_{\mathbf{k}-\mathbf{k}'\nu}(i\omega_j) = -\int_0^\infty d\omega\, B_{\mathbf{k}-\mathbf{k}'\nu}(\omega) \frac{2\omega}{\omega_j^2 + \omega^2}, \tag{2.120}$$

where $B_{\mathbf{k}-\mathbf{k}'\nu}$ is the phonon spectral function

$$B_{\mathbf{k}-\mathbf{k}'\nu}(\omega) = -\frac{1}{\pi}\mathrm{Im}\left[D_{\mathbf{k}-\mathbf{k}'\nu}(\omega + i\eta)\right]. \tag{2.121}$$

Phonon energies calculated from first principles are typically very accurate. For the full phonon spectrum, we would also need information about the phonon linewidth, which is not accessible in density-functional perturbation theory (DFPT). However, as the phonons are integrated over in ME theory, deviations from the average phonon energy cancel out, and we can make the approximation:

$$B^0_{\mathbf{k}-\mathbf{k}'\nu}(\omega) = \frac{\delta(\omega - \omega_{\mathbf{k}-\mathbf{k}'\nu})}{\hbar}. \tag{2.122}$$

The non-interacting phonon propagator then becomes

$$D^0_{\mathbf{k}-\mathbf{k}'\nu}(i\omega_j) = -\frac{2}{\hbar}\int_0^\infty d\omega\, \delta(\omega - \omega_{\mathbf{k}-\mathbf{k}'\nu})\, \frac{\omega}{\omega_j^2 - \omega^2} = -\frac{2}{\hbar}\frac{\omega_{\mathbf{k}-\mathbf{k}'\nu}}{\omega_j^2 + \omega^2_{\mathbf{k}-\mathbf{k}'\nu}} \tag{2.123}$$

This allows us to define the electron-phonon function

$$\lambda_{nn'\mathbf{k}\mathbf{k}'}(i\omega_j - i\omega'_j) := \frac{2N_{\mathrm{F}}}{\hbar}\sum_\nu |g_{nn'\nu}(\mathbf{k},\mathbf{k}')|^2 \frac{\omega_{\mathbf{k}-\mathbf{k}'\nu}}{(\omega_j - \omega'_j)^2 + \omega^2_{\mathbf{k}-\mathbf{k}'\nu}}, \tag{2.124}$$

where N_F is the density of electronic states at the Fermi level. Now we can write the electron-phonon self-energy as:

$$\hat{\Sigma}^{\mathrm{ep}}_{n\mathbf{k}}(i\omega_j) = \frac{k_\mathrm{B}T}{N_\mathrm{F}} \sum_{n\mathbf{k}'\omega'_j} \hat{\tau}_3 \, \hat{G}_{n\mathbf{k}'}(\mathbf{k}', i\omega'_j) \, \hat{\tau}_3 \, \lambda_{nn'\mathbf{k}\mathbf{k}'}(i\omega_j - i\omega'_j). \tag{2.125}$$

Note that the factor N_F in the definition of λ is in principle redundant, but it ensures that the electron-phonon coupling function is a dimensionless quantity.

Electron-electron self-energy

This contribution to the electron self-energy arises from the Coulomb repulsion between the two electrons after a Cooper pair has been formed. Starting from the electron-electron self-energy in the GW approximation given in Eq. (2.49), one finds:

$$\hat{\Sigma}^{\mathrm{c}}_{n\mathbf{k}}(i\omega_j) = -k_\mathrm{B}T \sum_{n'\mathbf{k}'\omega'_j} \hat{\tau}_3 \, \hat{G}_{n\mathbf{k}}(i\omega'_j) \, \hat{\tau}_3 \, W_{nn'\mathbf{k}\mathbf{k}'}(i\omega_j - i\omega'_j). \tag{2.126}$$

Here, $W_{nn'\mathbf{k}\mathbf{k}'}(i\omega_j - i\omega'_j)$ is the Coulomb matrix element for scattering a Cooper pair from a state $|n\mathbf{k}\uparrow, n-\mathbf{k}\downarrow\rangle = |n\mathbf{k}\uparrow\rangle \otimes |n-\mathbf{k}\downarrow\rangle$ to a state $|n'\mathbf{k}'\uparrow, n'-\mathbf{k}'\downarrow\rangle = |n'\mathbf{k}'\uparrow\rangle \otimes |n'-\mathbf{k}'\downarrow\rangle$, where $\otimes$ indicates a tensor product:[139]

$$W_{nn'\mathbf{k}\mathbf{k}'}(i\omega_j - i\omega'_j) = \langle n'\mathbf{k}'\uparrow, n'-\mathbf{k}'\downarrow | W(\mathbf{r}, \mathbf{r}', i\omega_j - i\omega'_j) | n\mathbf{k}\uparrow, n-\mathbf{k}\downarrow\rangle \tag{2.127}$$

This matrix element accounts for the Coulomb interaction between the two electrons of the Cooper pair, which is an additional two-electron interaction that is not present in the normal state. It is assumed that all normal-state electron correlations are already accounted for in the non-interacting electron energy $\epsilon_{n\mathbf{k}}$.

Full pairing self-energy

The full self-energy is given as:

$$\hat{\Sigma}_{n\mathbf{k}}(i\omega_j) = \frac{k_\mathrm{B}T}{N_\mathrm{F}} \sum_{n'\mathbf{k}'\omega'_j} \hat{\tau}_3 \, \hat{G}_{n'\mathbf{k}'}(i\omega'_j) \, \hat{\tau}_3 \, \left[\lambda_{nn'\mathbf{k}\mathbf{k}'}(i\omega_j - i\omega'_j) - N_\mathrm{F} W_{nn'\mathbf{k}\mathbf{k}'}(i\omega_j - i\omega'_j)\right], \tag{2.128}$$

where $\hat{G}_{n\mathbf{k}}$ is given by Eq. (2.114). Observing multiplication rules of the Pauli matrices, we can separate the diagonal and off-diagonal contributions to the Green's function as:[106]

$$\begin{aligned}
&\hat{\Sigma}_{n\mathbf{k}}(i\omega_j) \qquad (2.129)\\
&= k_\mathrm{B}T \sum_{n'\mathbf{k}'\omega'_j} \frac{\lambda_{nn'\mathbf{k}\mathbf{k}'}(i\omega_j - i\omega'_j)}{N_\mathrm{F}} \frac{i\hbar\omega'_j\, Z_{n'\mathbf{k}'}(i\omega'_j)\,\hat{\tau}_0 + \left[\epsilon_{n\mathbf{k}'} - \mu_\mathrm{C} + \chi_{n'\mathbf{k}'}(i\omega'_j)\right]\,\hat{\tau}_3}{\mathrm{det}\hat{G}^{-1}_{n\mathbf{k}'}(i\omega'_j)}\\
&-k_\mathrm{B}T \sum_{n'\mathbf{k}'\omega'_j} \left[\frac{\lambda_{nn'\mathbf{k}\mathbf{k}'}(i\omega_j - i\omega'_j)}{N_\mathrm{F}} - W_{nn'\mathbf{k}\mathbf{k}'}(i\omega_j - i\omega'_j)\right] \frac{\phi_{n'\mathbf{k}'}(i\omega'_j)\,\hat{\tau}_1 + \bar{\phi}_{n\mathbf{k}'}(i\omega'_j)\hat{\tau}_2}{\det\left(\hat{G}^{-1}_{n\mathbf{k}'}(i\omega'_j)\right)}.
\end{aligned}$$

The Coulomb contribution is only non-zero once Cooper pairs start forming, and hence is only added to the off-diagonal element of the self-energy. All electron correlations affecting the diagonal elements are assumed to be accounted for.

Taking a closer look at the off-diagonal element in Eqs. (2.114) and (2.129), we notice that $\phi_{n\mathbf{k}}$ and $\bar{\phi}_{n\mathbf{k}}$ fulfil the same equations and hence will be proportional:

$$\left(\phi, \bar{\phi}\right) = (\phi_0 \cos\alpha, \phi_0 \sin\alpha) \qquad (2.130)$$

Without loss of generality, one can then chose the gauge $\alpha = 0$, which yields $\bar{\phi} = 0$.[140]

In the last step, we compare coefficients of the Pauli matrices between Eqs. (2.129) and (2.112), to find a system of three coupled nonlinear equations:

$$\begin{aligned}
Z_{n\mathbf{k}}(i\omega_j) &= 1 + \frac{k_\mathrm{B}T}{\hbar\omega_j\, N_\mathrm{F}} \qquad (2.131)\\
&\times \sum_{n'\mathbf{k}'\omega'_j} \frac{\lambda_{nn'\mathbf{k}\mathbf{k}'}(i\omega_j - i\omega'_j)\,\hbar\omega'_j\, Z_{n'\mathbf{k}'}(i\omega'_j)}{\left[\hbar\omega'_j\, Z_{n'\mathbf{k}'}(i\omega'_j)\right]^2 + \left[\epsilon_{n'\mathbf{k}'} - \mu_\mathrm{C} + \chi_{n'\mathbf{k}'}(i\omega'_j)\right]^2 + \phi^2_{n'\mathbf{k}'}(i\omega'_j)}\\
\chi_{n\mathbf{k}}(i\omega_j) &= -\frac{k_\mathrm{B}T}{N_\mathrm{F}} \qquad (2.132)\\
&\times \sum_{n'\mathbf{k}'\omega'_j} \frac{\lambda_{nn'\mathbf{k}\mathbf{k}'}(i\omega_j - i\omega'_j)\,\left[\epsilon_{n'\mathbf{k}'} - \mu_\mathrm{C} + \chi_{n'\mathbf{k}'}(i\omega'_j)\right]}{\left[\hbar\omega'_j\, Z_{n'\mathbf{k}'}(i\omega'_j)\right]^2 + \left[\epsilon_{n'\mathbf{k}'} - \mu_\mathrm{C} + \chi_{n'\mathbf{k}'}(i\omega'_j)\right]^2 + \phi^2_{n'\mathbf{k}'}(i\omega'_j)}\\
\phi_{n\mathbf{k}}(i\omega_j) &= \frac{k_\mathrm{B}T}{N_\mathrm{F}} \qquad (2.133)\\
&\times \sum_{n'\mathbf{k}'\omega'_j} \frac{\left[\lambda_{nn'\mathbf{k}\mathbf{k}'}(i\omega_j - i\omega'_j) - N_\mathrm{F}\, W_{nn'\mathbf{k}\mathbf{k}'}(i\omega_j - i\omega'_j)\right]\,\phi_{n'\mathbf{k}'}(i\omega'_j)}{\left[\hbar\omega'_j\, Z_{n'\mathbf{k}'}(i\omega'_j)\right]^2 + \left[\epsilon_{n'\mathbf{k}'} - \mu_\mathrm{C} + \chi_{n'\mathbf{k}'}(i\omega'_j)\right]^2 + \phi^2_{n'\mathbf{k}'}(i\omega'_j)}
\end{aligned}$$

To determine the chemical potential explicitly, the ordinary Green's functions $\left[\hat{G}_{n\mathbf{k}}(i\omega_j)\right]_{11} = G_{n\mathbf{k}}(i\omega_j)$ must fulfil the particle number conservation condition given

in Eq. (2.134) [see e.g. Ref. [107]]:

$$\begin{aligned} N_e &= 1 - 2k_{\mathrm{B}}T \\ &\times \sum_{n'\mathbf{k}'\omega'_j} \frac{\epsilon_{n'\mathbf{k}'} - \mu_{\mathrm{C}} + \chi_{n'\mathbf{k}'}(i\omega'_j)}{\left[\hbar\omega'_j\, Z_{n'\mathbf{k}'}(i\omega'_j)\right]^2 + \left[\epsilon_{n'\mathbf{k}'} - \mu_{\mathrm{C}} + \chi_{n'\mathbf{k}'}(i\omega'_j)\right]^2 + \phi^2_{n'\mathbf{k}'}(i\omega'_j)}. \end{aligned} \tag{2.134}$$

Note that N_e in Eq. (2.134) is the number of particles in the Born-von Kármán supercell.

After solving this set of equations along the imaginary frequency axis, one can employ methods like the Padé approximation,[141–143] or an iterative analytic continuation,[144] to obtain the diagonal component of the single-particle Green's function:[44]

$$\left[\hat{G}_{n\mathbf{k}}(\omega)\right]_{11} = \frac{\hbar\omega Z_{n\mathbf{k}}(\omega) + \epsilon_{n\mathbf{k}} - \mu_{\mathrm{C}} + \chi_{n\mathbf{k}}(\omega)}{\left[\hbar\omega Z_{n\mathbf{k}}(\omega)\right]^2 - \left[\epsilon_k - \mu_{\mathrm{C}} + \chi_{n\mathbf{k}}\right]^2 - \left[Z_{n\mathbf{k}}(\omega)\,\Delta_{n\mathbf{k}}(\omega)\right]^2}, \tag{2.135}$$

where we defined the gap function $\Delta_{n\mathbf{k}}$ via:

$$\Delta_{n\mathbf{k}}(\omega) = \frac{\phi_{n\mathbf{k}}(\omega)}{Z_{n\mathbf{k}}(\omega)}. \tag{2.136}$$

The pole of Eq. (2.135) defines the QP energy:

$$E^2_{n\mathbf{k}} = \left[\frac{\epsilon_{n\mathbf{k}} - \mu_{\mathrm{C}} + \chi_{n\mathbf{k}}(\omega)}{Z_{n\mathbf{k}}(E_{n\mathbf{k}}/\hbar)}\right]^2 + \Delta^2_{n\mathbf{k}}(E_{n\mathbf{k}}/\hbar) \tag{2.137}$$

This expression allows us to discuss the physical meaning of the scalar functions introduced above Eq. (2.113). Firstly, $Z_{n\mathbf{k}}$ appears to renormalise the effective mass of the paired electrons. It is hence often referred to as mass renormalisation function. The electron energy is also directly moved away from its noninteracting energy via the function $\chi_{n\mathbf{k}}$. Lastly, $\Delta_{n\mathbf{k}}$ describes the opening of an energy gap in the QP dispersion of Eq. (2.137), and is therefore called the gap function. This energy gap in the electronic dispersion is the hallmark of a superconductor.

2.2.2 Linearised Migdal-Eliashberg equations

The self-consistent solution of the full set of Migdal-Eliashberg equations is not very easy to achieve. A common approximation is then to linearise Eqs. (2.131)-(2.134) near the critical temperature. We know that the gap equation $\Delta_{n\mathbf{k}}(i\omega_j)$ and hence the order

parameter $\phi_{n\mathbf{k}}(i\omega_j)$ vanish as $T \to T_{\rm C}$. Assuming that we are solving the equations at a temperature $T \approx T_{\rm C}$, we can neglect terms of ϕ to order higher than linear, and obtain:

$$\begin{aligned} Z_{n\mathbf{k}}(i\omega_j) &= 1 + \frac{k_{\rm B}T}{\hbar\omega_j\, N_{\rm F}} && (2.138)\\ &\times \sum_{n'\mathbf{k}'\omega'_j} \frac{\lambda_{nn'\mathbf{k}\mathbf{k}'}(i\omega_j - i\omega'_j)\,\hbar\omega'_j\, Z_{n'\mathbf{k}'}(i\omega'_j)}{\left[\hbar\omega'_j\, Z_{n'\mathbf{k}'}(i\omega'_j)\right]^2 + \left[\epsilon_{n'\mathbf{k}'} - \mu_{\rm C} + \chi_{n'\mathbf{k}'}(i\omega'_j)\right]^2} \\ \chi_{n\mathbf{k}}(i\omega_j) &= -\frac{k_{\rm B}T}{N_{\rm F}} && (2.139)\\ &\times \sum_{n'\mathbf{k}'\omega'_j} \frac{\lambda_{nn'\mathbf{k}\mathbf{k}'}(i\omega_j - i\omega'_j)\,\left[\epsilon_{n'\mathbf{k}'} - \mu_{\rm C} + \chi_{n'\mathbf{k}'}(i\omega'_j)\right]}{\left[\hbar\omega'_j\, Z_{n'\mathbf{k}'}(i\omega'_j)\right]^2 + \left[\epsilon_{n'\mathbf{k}'} - \mu_{\rm C} + \chi_{n'\mathbf{k}'}(i\omega'_j)\right]^2} \\ N_e &= 1 - 2k_{\rm B}T && (2.140)\\ &\times \sum_{n'\mathbf{k}'\omega'_j} \frac{\epsilon_{n'\mathbf{k}'} - \mu_{\rm C} + \chi_{n'\mathbf{k}'}(i\omega'_j)}{\left[\hbar\omega'_j\, Z_{n'\mathbf{k}'}(i\omega'_j)\right]^2 + \left[\epsilon_{n'\mathbf{k}'} - \mu_{\rm C} + \chi_{n'\mathbf{k}'}(i\omega'_j)\right]^2} \\ \phi_{n\mathbf{k}}(i\omega_j) &= \frac{k_{\rm B}T}{N_{\rm F}} && (2.141)\\ &\times \sum_{n'\mathbf{k}'\omega'_j} \frac{\left[\lambda_{nn'\mathbf{k}\mathbf{k}'}(i\omega_j - i\omega'_j) - N_{\rm F}\, W_{nn'\mathbf{k}\mathbf{k}'}(i\omega_j - i\omega'_j)\right]\,\phi_{n'\mathbf{k}'}(i\omega'_j)}{\left[\hbar\omega'_j\, Z_{n'\mathbf{k}'}(i\omega'_j)\right]^2 + \left[\epsilon_{n'\mathbf{k}'} - \mu_{\rm C} + \chi_{n'\mathbf{k}'}(i\omega'_j)\right]^2}. \end{aligned}$$

Note the simplification we have achieved here: Equations (2.138)-(2.140) are still self-consistent, but do not depend on the order parameter anymore. Instead, they become parameters for an eigenvalue equation:

$$\phi_{n\mathbf{k}}(i\omega_j) = \sum_{n'\mathbf{k}'\omega'_j} K_{nn'\mathbf{k}\mathbf{k}'}(i\omega_j - i\omega'_j)\,\phi_{n'\mathbf{k}'}(i\omega'_j), \qquad (2.142)$$

where we define the kernel matrix:

$$K_{nn'\mathbf{k}\mathbf{k}'}(i\omega_j - i\omega'_j; T) = \frac{k_{\rm B}T}{N_{\rm F}} \frac{\lambda_{nn'\mathbf{k}\mathbf{k}'}(i\omega_j - i\omega'_j) - N_{\rm F}\, W_{nn'\mathbf{k}\mathbf{k}'}(i\omega_j - i\omega'_j)}{\left[\hbar\omega'_j\, Z_{n'\mathbf{k}'}(i\omega'_j)\right]^2 + \left[\epsilon_{n'\mathbf{k}'} - \mu_{\rm C} + \chi_{n'\mathbf{k}'}(i\omega'_j)\right]^2}. \qquad (2.143)$$

If the eigenvalue of $K_{nn'\mathbf{k}\mathbf{k}'}(i\omega_j - i\omega'_j; T)$ equals unity, Eq. (2.142) is fulfilled and $T = T_{\rm C}$ [cf. section 16 in Ref. [106]]

2.2.3 Morel-Anderson Coulomb potential

In most metallic systems, one is more interested in an accurate description of the electron-phonon interaction, as the Coulomb repulsion across the Fermi surface typically varies more slowly. Therefore it is very common in *ab initio* calculations to replaces the full

Coulomb potential $V_{nn'\mathbf{kk}'}$ in Eqs. (2.133) by a constant parameter. This is achieved by the following procedure that is due to Morel and Anderson:[145]

One considers electron-electron interactions in a free electron gas with Fermi momentum $k_{\rm F}$ in a Brillouin zone with radius $2k_{\rm F}$. In the low-frequency limit, the dynamical screening of the Coulomb potential between two electrons can be approximated by the Thomas-Fermi dielectric function [Note that we will discuss electronic screening in more detail in Sec. 3.3]:

$$V(q) = \frac{4\pi\, e^2}{q^2\, \varepsilon^{\rm TF}(q)}, \qquad \text{where} \qquad \varepsilon^{\rm TF}(q) = 1 + \frac{q_{\rm TF}^2}{q^2}. \tag{2.144}$$

Here, n_0 is the charge-carrier density, and $\varepsilon^{\rm TF}(q)$ is the Thomas-Fermi (TF) dielectric function with the TF screening wavevector $q_{\rm TF}$ evaluated for the free electron gas:

$$q_{\rm TF}^2 = \frac{e^2}{\varepsilon_0}\frac{\partial n_0}{\partial E_{\rm F}} \tag{2.145}$$

One can calculate an average potential for scattering processes across the Brillouin zone via:

$$\begin{aligned} \mu &= \frac{N_{\rm F}}{4\pi}\int_0^{2k_{\rm F}} dq\, q\, V(q) = \frac{1}{4\pi^2\, v_{\rm F}}\int_0^{2k_{\rm F}} q\, dq\, \frac{4\pi\, e^2}{q_{\rm TF}^2 + q^2} \\ &= \frac{q_{\rm TF}^2}{8k_{\rm F}^2}\log\frac{q_{\rm TF}^2 + 4k_{\rm F}^2}{q_{\rm TF}^2} \leq \frac{1}{2}. \end{aligned} \tag{2.146}$$

Morel and Anderson have shown that on the level of BCS theory, the Coulomb average of Eq. (2.146) enters the gap equation via

$$\log\frac{2\hbar\omega_{\rm ph}}{\Delta} = \left[\lambda - \frac{\mu}{1 + \mu\log\left(E_{\rm F}/\hbar\omega_{\rm ph}\right)}\right]^{-1}, \tag{2.147}$$

i.e. the parameter μ is further reduced to

$$\mu^* = \frac{\mu}{1 + \mu\,\log\left(E_{\rm F}/\hbar\omega_{\rm ph}\right)}. \tag{2.148}$$

Gor'kov[99] argues that this reduction accounts for the energy difference between phonons and electrons in the adiabatic limit: The distance an electron travels during a phonon oscillation is approximately equal to

$$d \approx \frac{v_{\rm F}}{\omega_{\rm ph}} = \frac{\hbar k_{\rm F}}{m_0\omega_{\rm ph}} = \frac{2}{k_{\rm F}}\frac{E_{\rm F}}{\hbar\omega_{\rm ph}}. \tag{2.149}$$

In the adiabatic limit $\hbar\omega_{\rm ph} \ll E_{\rm F}$, and $2/k_{\rm F}$ is of the order of the inter atomic distance. It follows that the two electrons forming a Cooper pair will be more than one unit cell apart,

which in turn means that their mutual Coulomb repulsion is further reduced by dielectric screening on the atomic level. Most calculations use values of $\mu^* \approx 0.1 - 0.2$.[44,145]

Therefore, Eq. (2.148) is not valid in the anti-adiabatic limit $\hbar\omega_{\rm ph} \ll E_{\rm F}$, where the paired electrons are closer together, and inter-atomic screening is not effective.

2.2.4 Fermi-surface restricted equations

If the electron band is occupied up to a high energy $E_{\rm F} \ll \hbar\omega_{\rm ph}$, it is to good approximation antisymmetric in $\mathbf{k}$ about the chemical potential $\mu_{\rm C}$. In this case, we can neglect the function $\chi_{n\mathbf{k}}$, which is symmetric in $\mathbf{k}$ [cf. Eq. 2.132]. It follows that we are left with the two equations:

$$Z_{n\mathbf{k}}(i\omega_j) = 1 + \frac{k_{\rm B}T}{\hbar\omega_j\, N_{\rm F}} \sum_{n'\mathbf{k}'\omega'_j} \frac{\lambda_{nn'\mathbf{k}\mathbf{k}'}(i\omega_j - i\omega'_j)\, \hbar\omega'_j\, Z_{n'\mathbf{k}'}(i\omega'_j)}{\left[\hbar\omega'_j\, Z_{n'\mathbf{k}'}(i\omega'_j)\right]^2 + \left[\epsilon_{n'\mathbf{k}'} - E_{\rm F}\right]^2} \tag{2.150}$$

$$\begin{aligned}\phi_{n\mathbf{k}}(i\omega_j) &= \frac{k_{\rm B}T}{N_{\rm F}} \sum_{n'\mathbf{k}'\omega'_j} \\ &\times \frac{\left[\lambda_{nn'\mathbf{k}\mathbf{k}'}(i\omega_j - i\omega'_j) - N_{\rm F}\, W_{nn'\mathbf{k}\mathbf{k}'}(i\omega_j - i\omega'_j)\right]\, \phi_{n'\mathbf{k}'}(i\omega'_j)}{\left[\hbar\omega'_j\, Z_{n'\mathbf{k}'}(i\omega'_j)\right]^2 + \left[\epsilon_{n'\mathbf{k}'} - E_{\rm F}\right]^2}.\end{aligned} \tag{2.151}$$

Next, we re-write them as:

$$\begin{aligned}Z_{n\mathbf{k}}(i\omega_j) &= 1 + \frac{k_{\rm B}T}{\hbar\omega_j\, N_{\rm F}} \sum_{n'\mathbf{k}'\omega'_j} \lambda_{nn'\mathbf{k}\mathbf{k}'}(i\omega_j - i\omega'_j) \\ &\times \frac{\hbar\omega'_j}{|\hbar\omega'_j|} \frac{|\hbar\omega'_j\, Z_{n'\mathbf{k}'}(i\omega'_j)|}{|\hbar\omega'_j\, Z_{n'\mathbf{k}'}(i\omega'_j)|^2 + \left[\epsilon_{n'\mathbf{k}'} - E_{\rm F}\right]^2}\end{aligned} \tag{2.152}$$

$$\begin{aligned}Z_{n\mathbf{k}}(i\omega_j)\Delta_{n\mathbf{k}}(i\omega_j) &= \frac{k_{\rm B}T}{N_{\rm F}} \sum_{n'\mathbf{k}'\omega'_j} \frac{\lambda_{nn'\mathbf{k}\mathbf{k}'}(i\omega_j - i\omega'_j) - N_{\rm F}\, W_{nn'\mathbf{k}\mathbf{k}'}(i\omega_j - i\omega'_j)}{|\hbar\omega'_j|} \\ &\times \frac{|\hbar\omega'_j\, Z_{n'\mathbf{k}'}(i\omega'_j)|}{|\hbar\omega'_j\, Z_{n'\mathbf{k}'}(i\omega'_j)|^2 + \left[\epsilon_{n'\mathbf{k}'} - E_{\rm F}\right]^2} \Delta_{n'\mathbf{k}'}(i\omega'_j)\end{aligned} \tag{2.153}$$

where we have used the definition of the gap function, and the fact that $Z_{n\mathbf{k}}(i\omega_j) \geq 0$.

In Eqs, (2.152) and (2.153), we can identify the Lorentzian

$$L\left(\epsilon_{n\mathbf{k}} - E_{\rm F}, \sigma = \hbar\omega_j\, Z_{n\mathbf{k}}(i\omega_j)\right) = \frac{|\hbar\omega'_j\, Z_{n'\mathbf{k}'}(i\omega'_j)|}{|\hbar\omega'_j\, Z_{n'\mathbf{k}'}(i\omega'_j)|^2 + \left[\epsilon_{n'\mathbf{k}'} - E_{\rm F}\right]^2} \tag{2.154}$$

centred around $\epsilon_{n\mathbf{k}'} = E_\mathrm{F}$ with a broadening of $|\hbar\omega_j\, Z_{n\mathbf{k}}(i\omega_j)|$. The mass renormalisation function typically decays within a phononic energy range, which in a typical metallic system is much smaller than average electron energies. Therefore, in the limit

$$\lim_{\sigma\to 0} L\left(\epsilon_{n\mathbf{k}} - E_\mathrm{F}, \sigma\right) = \pi\, \delta\left(\epsilon_{n\mathbf{k}} - E_\mathrm{F}\right), \tag{2.155}$$

we reach:[44]

$$Z_{n\mathbf{k}}(i\omega_j) = 1 + \frac{\pi\, k_\mathrm{B}T}{\hbar\omega_j\, N_\mathrm{F}} \sum_{n'\mathbf{k}'\omega'_j} \delta\left(\epsilon_{n'\mathbf{k}'} - E_\mathrm{F}\right) \frac{\hbar\omega'_j\, \lambda_{nn'\mathbf{k}\mathbf{k}'}(i\omega_j - i\omega'_j)}{\sqrt{\hbar^2\omega_j'^2 + \Delta^2_{n'\mathbf{k}'}(i\omega'_j)}} \tag{2.156}$$

$$Z_{n\mathbf{k}}(i\omega_j)\Delta_{n\mathbf{k}}(i\omega_j) = \frac{\pi\, k_\mathrm{B}T}{N_\mathrm{F}} \sum_{n'\mathbf{k}'\omega'_j} \delta\left(\epsilon_{n'\mathbf{k}'} - E_\mathrm{F}\right) \frac{\left[\lambda_{nn'\mathbf{k}\mathbf{k}'}(i\omega_j - i\omega'_j) - \mu^*\right] \Delta_{n'\mathbf{k}'}(i\omega'_j)}{\sqrt{\hbar^2\omega_j'^2 + \Delta^2_{n'\mathbf{k}'}(i\omega'_j)}}, \tag{2.157}$$

Where in the last step we have replaced the full screened Coulomb interaction with the Morel-Anderson pseudopotential.

It is commonly assumed in the literature that the main contribution to Cooper pair formation stems from states very close to the Fermi surface.[106,146,147] From our derivation, it is clear that this is indeed true for metallic systems with high Fermi energies, as long as $\chi_{n\mathbf{k}} \approx 0$.

Due to their relative simplicity compared to the full set of ME equations, Eqs. (2.156) and (2.157) are widely used in *ab initio* calculations of the superconducting gap.[44,109,110]

2.2.5 McMillan equation

It was in bulk metals such as elemental Al where the earliest theories of superconductivity were most successful.[148] The Fermi surface in these systems is only weakly anisotropic, and therefore more simplified formulations of Eliashberg theory can be applied.

By averaging the momentum in Eqs. (2.156) and (2.157) over the Fermi surface, we obtain the isotropic equations:[44]

$$Z(i\omega_j) = 1 + \frac{\pi\, k_\mathrm{B}T}{\hbar\omega_j} \sum_{\omega'_j} \frac{\hbar\omega'_j}{\sqrt{R(i\omega'_j)}}\, \lambda(i\omega_j - i\omega'_j) \tag{2.158}$$

$$Z(i\omega_j)\Delta(i\omega_j) = \pi k_\mathrm{B}T \sum_{\omega'_j} \frac{\Delta(i\omega'_j)}{\sqrt{R(i\omega'_j)}} \left[\lambda(i\omega_j - i\omega'_j) - \mu^*\right]. \tag{2.159}$$

Here, $R(i\omega_j) = \hbar\omega_j^2 + \Delta^2(i\omega_j)$ and

$$\lambda(i\omega_j - i\omega_j') = \sum_{nn'\mathbf{k}\mathbf{k}'} \frac{\delta(\epsilon_{n\mathbf{k}} - E_\mathrm{F})}{N_\mathrm{F}} \frac{\delta(\epsilon_{n'\mathbf{k}'} - E_\mathrm{F})}{N_\mathrm{F}} \lambda_{nn'\mathbf{k}\mathbf{k}'}(i\omega_j - i\omega_j') \tag{2.160}$$

is the electron-phonon coupling function averaged over the Fermi surface.

Next, one assumes that the electron-phonon coupling function λ is simply a constant up to some cutoff ω_cut:

$$\lambda(\omega) = \begin{cases} \lambda & \omega < \omega_\mathrm{cut} \\ 0 & \omega > \omega_\mathrm{cut} \end{cases} . \tag{2.161}$$

After inserting Eq. (2.158) into (2.159) and summing over all frequencies, one reaches:[30]

$$\Delta_0 = \frac{\Delta_0 \left[\lambda - \mu^* - \mu^* \lambda \left(\langle\omega\rangle/\omega_\mathrm{cut}\right)\right] \log\left(\omega_\mathrm{cut}/T_\mathrm{C}\right)}{1+\lambda}, \tag{2.162}$$

where we define the average phonon frequency:[30]

$$\langle\omega\rangle = \frac{2}{\lambda}\int_0^\infty d\omega \, \frac{\alpha^2 F(\omega)}{\omega} \tag{2.163}$$

Ultimately, one solves for T_C in Eq. (2.162), and finds:

$$k_\mathrm{B} T_\mathrm{C} = \frac{\hbar\omega_\mathrm{log}}{1.2} \exp\left(-\frac{1.04\ (1+\lambda)}{\lambda - \mu^*\ (1+0.62\lambda)}\right). \tag{2.164}$$

with the constant:

$$\omega_\mathrm{log} = \exp\left(\frac{2}{\lambda}\int_0^\infty d\omega \, \frac{\alpha^2 F(\omega)}{\omega} \log\omega\right). \tag{2.165}$$

Equation (2.164) has been dubbed the "most popular T_C equation".[106] The empirical parameters have been optimised for elemental metals.

3

Fröhlich coupling in doped $SrTiO_3$

We now move towards the application of the theory introduced in Chapter 2 to doped polar semiconductors. A paradigmatic example of this class of materials is $SrTiO_3$: A strongly polar material with parabolic electron bands near the zone centre coupled to the LO Einstein phonon via long-range Fröhlich electron-phonon coupling.

In STO, one observes all the physical phenomena that we wish to investigate: Not only does its experimental photoemission spectrum exhibit a renormalised quasiparticle band with clearly resolved sidebands, as shown in Figs. 1.1, 1.2. Bulk STO also becomes superconducting below a critical temperature $T_C \lesssim 0.5$ K, as can be seen from the experimental data presented in Fig. 1.3.

The aim of this thesis is to elucidate the role that Fröhlich coupling plays in the emergence of these phenomena, and we do this by developing an analytical model. This approach has two advantages: The first advantage is that it allows us to make general statements that can also be applied to the case of other doped polar semiconductors. The second reason is a more practical one: The relevant interactions take place on extremely small energy and momentum scales, which makes numerical calculations from first principles prohibitively expensive. By employing an analytical model, such practical limitations can be avoided.

Nevertheless, our results still rest on a foundation of a predictive *first-principles* model of the STO ground state: We employ density-functional theory and density-functional

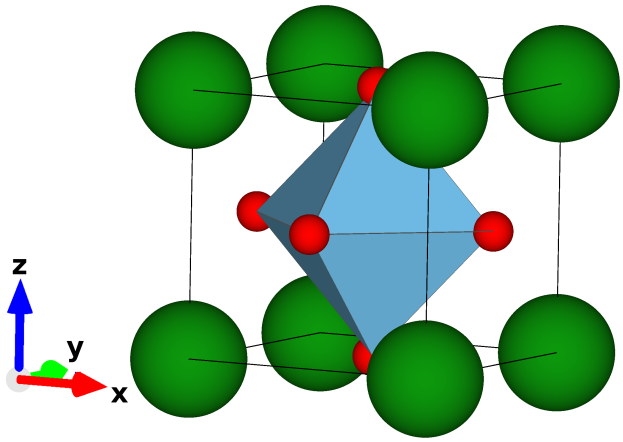


Figure 3.1: Cubic phase of $SrTiO_3$ (space group $Pm\bar{3}m$) at temperatures above 105 K with a lattice parameter of $a = 3.981$Å. Sr is shown in green, Ti in gray, and O in red.

perturbation theory to evaluate the bandstructures of the noninteracting electrons and phonons, and extract the electron-phonon coupling matrix element; see Sec. 3.1.

We then develop our model starting from the using the extracted *ab initio* parameters, the details of which are conveyed in Sec. 3.2. We discuss the analytical form of the long-range Fröhlich and Coulomb interactions in detail. Moreover, we find that a particularly important aspect of our model is how we treat electronic screening of the many-body interactions due to dopant charge carriers. Sec. 3.3 is dedicated to this question.

3.1 STO electronic structure from first-principles

Above a temperature of 105 K the crystal structure of $SrTiO_3$ is cubic (space group $Pm\bar{3}m$) with 5 atoms in its unit cell [see Fig. 3.1]. The band gap is indirect $R-\Gamma$ and has been measured at 3.25 eV.[149] The bottom of the conduction band at the zone centre is threefold degenerate, which is related to the full crystal symmetry of the cell. Spin-orbit coupling leads to a small off-splitting of one of the bands.

The phase transition to the low-temperature tetragonal phase involves an increase of the c/a ratio and a rotation of the central Ti-O_6 octahedra around the c axis. These rotations occur in opposite directions in neighbouring unit cells.[150]

Given the perovskite structure of STO, one could also expect to see soft phonon modes at the Γ point connected to a ferroelectric (FE) distortion in the unit cell.[151] Such a distortion would correspond to a displacement of the central Ti atom away from the centre of the oxygen octahedron, creating long-range ferroelectric ordering in the system. However,

in experiment, no ferroelectric phase is observed: it has been found that it is suppressed by quantum zero-point fluctuations.[92] Instead, the static dielectric constant ε_0 saturates at the extremely high value of $\varepsilon_0 = 2.4 \times 10^4 \epsilon_0$ as the temperature approaches zero.[91] STO has therefore been called an incipient ferroelectric.[152] Nevertheless, it is still possible to induce a ferroelectric phase transition, e.g. by the application of uniaxial stress.[153]

3.1.1 Cubic phase

This structure is most relevant for our investigation of normal-state properties.

We study the electronic structure of cubic STO using fully relativistic norm-conserving Perdew-Zunger LDA pseudopotentials including Ti $3s$ and $3p$ semi-core states.[154] The ground-state charge density is converged on an $8 \times 8 \times 8$ **k**-point grid up to a kinetic energy cutoff of 100 Ry. After structural relaxation, the LDA optimised lattice parameter is $a = 3.981\,\text{Å}$, which is in good agreement with the experimental lattice parameter of $a = 3.900\,\text{Å}$.[155] The volume of the unit cell is $\Omega_{\text{UC}} = 58.909\,\text{Å}^3$.

We find that the band edge is made up of oxygen p (valence) and titanium d orbitals (conduction). The bottom of the conduction band consists of three Ti t_{2g} orbitals (d_{xy},d_{xz},d_{yz}) and features two light and one heavy electron bands. Spin-orbit coupling causes a small energy splitting of $\Delta E_{1,2\to3} = 28$ meV between one of the light electron bands and the other two bands, cf. Figs. 3.2 and 3.3.

From our analysis of the effective mass tensor, we find that all three conduction bands are almost perfectly parabolic, with effective masses of $m_1 = 1.917\,m_e$ for the heavy electron band, and $m_2 = 0.718\,m_e$ and $m_3 = 1.036\,m_e$ for the light electron bands.

In Fig. 3.4 we show the phonon dispersion of the cubic phase calculated within density-functional perturbation theory (DFPT).[156,157] We employ a $4 \times 4 \times 4$ **q**-point mesh. With 5 atoms in the unit cell, the cubic structure has 3 acoustic and 12 optical phonon modes. At the zone centre, the energy of the highest LO phonon mode is given as $\hbar\omega_{\text{LO3}} = 106.3$ meV, in very good agreement with experiment.[158] The dielectric tensor in the cubic phase is isotropic, and we obtain ε_∞=6.23, in good agreement with the experimental value of $\varepsilon_\infty = 5.20$.[159]

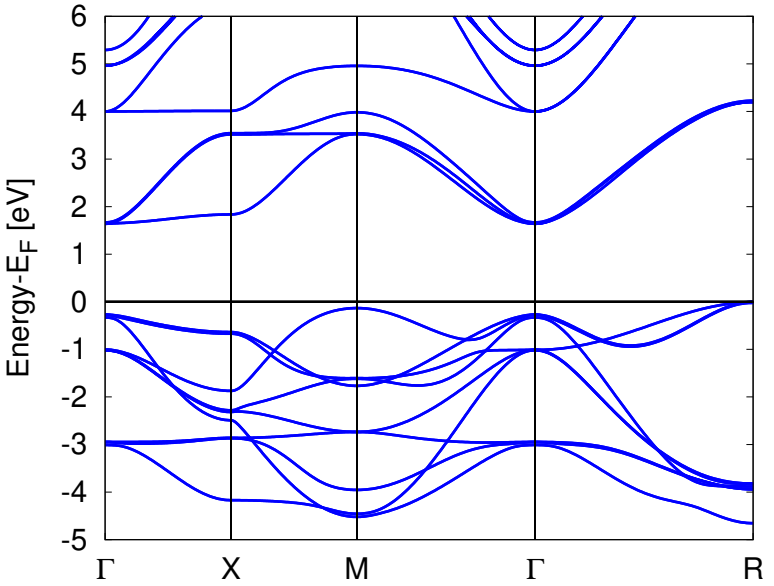


Figure 3.2: LDA electronic bandstructure along the high-symmetry path of the cubic phase of STO calculated on $8 \times 8 \times 8$ **k**-points.

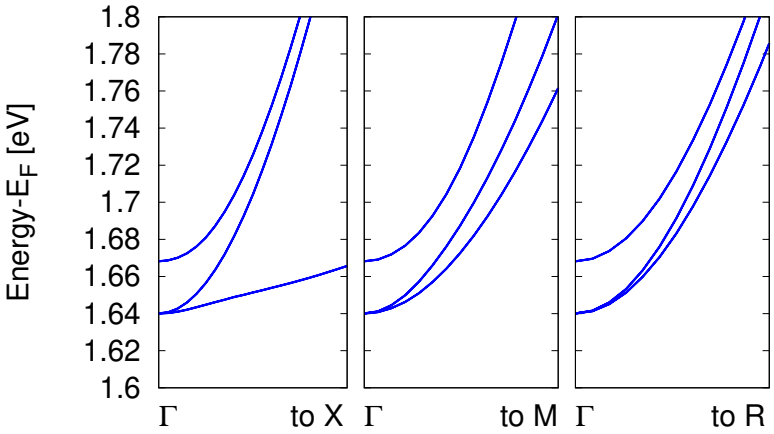


Figure 3.3: Detail of the LDA electronic bandstructure of cubic STO near the Γ point.

The appearance of soft phonon modes in the phonon dispersion in Fig. 3.4 indicates the structural instability of the cubic phase at low temperature. This is not surprising as we know that the real ground state of the system is tetragonal. The soft phonon mode at R point has been associated with the octahedral rotation in the phase transition at $T = 105$ K.[150,152] The soft M-point phonon is also associated with a similar octahedral rotation.[160] Moreover, some electronic-structure calculations have reported soft modes at Γ; however, it has been found that the softness or hardness of these modes is can be tuned via the lattice parameter employed in the calculation.[152]

The *ab initio* electron-phonon matrix element quantifying the interaction between electronic states $\epsilon_{n\mathbf{k}}$ and $\epsilon_{m\mathbf{k+q}}$ mediated by a phonon $\hbar\omega_{\mathbf{q}\nu}$ is defined as:[50]

$$g_{mn\nu}(\mathbf{k},\mathbf{q}) = \langle u_{m\mathbf{k+q}} | \Delta_{\mathbf{q}\nu} v^{\mathrm{KS}} | u_{n\mathbf{k}} \rangle_{\mathrm{uc}}. \tag{3.1}$$

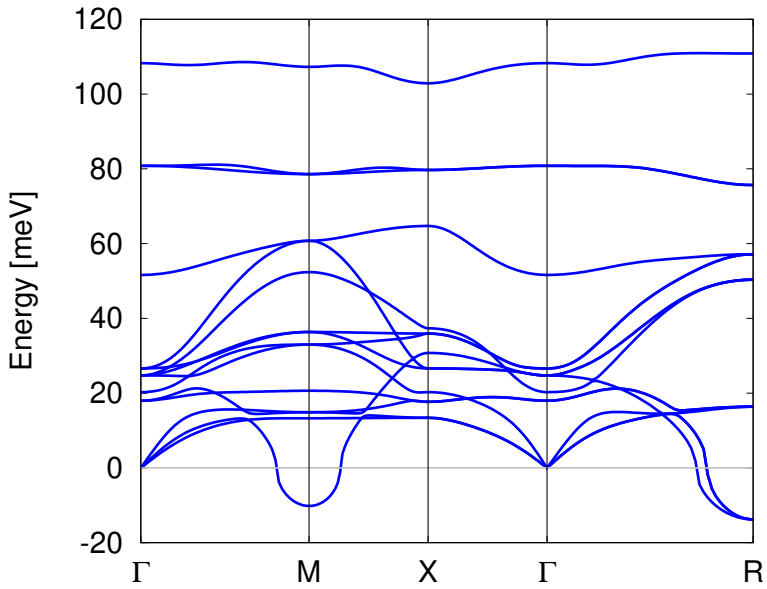


Figure 3.4: LDA phonon dispersion in the harmonic approximation along the high-symmetry path of the cubic phase of STO calculated on $8 \times 8 \times 8$ **k**- and $4 \times 4 \times 4$ **q**-points.

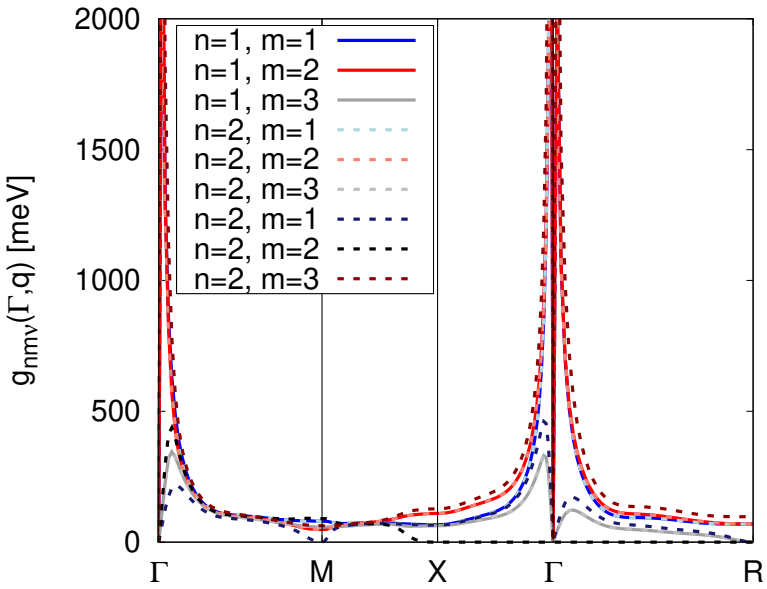


Figure 3.5: *Ab initio* electron-phonon coupling matrix element $g_{nm\nu}(\mathbf{k} = \Gamma, \mathbf{q})$ calculated for the cubic phase of STO. The matrix element is shown for coupling between the Γ point and states **q** along the high-symmetry path within the three lowest conduction bands $n, m = 1, 2, 3$ mediated by the highest LO phonon mode, $\nu =$ LO3.

As we are within DFPT, $u_{n\mathbf{k}}$ and $u_{m\mathbf{k+q}}$ are the Bloch-periodic components of the Kohn-Sham electron wave functions, and the term $\Delta_{\mathbf{q}\nu} v^{\mathrm{KS}}$ is related to the phonon-induced variation of the Kohn-Sham potential experienced by the electrons. The subscript *uc* indicates that the integration is performed over one unit cell of the crystal.

To arrive at Eq. (3.1), one starts from the first-order variation of the Kohn-Sham potential in the ionic displacements:[50]

$$V^{\mathrm{KS}}(\{\boldsymbol{\tau}_{\kappa p}\}) = V^{\mathrm{KS}}(\{\boldsymbol{\tau}^0_{\kappa p}\}) + \sum_{\kappa\alpha p} \frac{\partial V^{\mathrm{KS}}}{\partial \tau_{\kappa\alpha p}} \Delta\tau_{\kappa\alpha p}, \tag{3.2}$$

To express this variation in terms of normal-mode coordinates, one makes the definition:[50]

$$\partial_{\kappa\alpha,\mathbf{q}} v^{\mathrm{KS}} = \sum_p e^{-i\mathbf{q}\cdot(\mathbf{r}-\mathbf{R}_p)} \frac{\partial V^{\mathrm{KS}}}{\partial \tau_{\kappa\alpha}}\bigg|_{\mathbf{r}-\mathbf{R}_p}, \tag{3.3}$$

where the sum runs over all unit cells p in the Born-von Kármán supercell, and $\mathbf{R}_p$ is the lattice vector belonging to unit cell $\mathbf{R}_p$. The derivative appearing in Eq. (3.1) is then written as:[50]

$$\Delta_{\mathbf{q}\nu} v^{\mathrm{KS}} = \sum_{\kappa\alpha} \sqrt{\frac{\hbar}{2M_\kappa\,\omega_{\mathbf{q}\nu}}}\, e_{\kappa\alpha\nu}(\mathbf{q}) \partial_{\kappa\alpha,\mathbf{q}} v^{\mathrm{KS}}, \tag{3.4}$$

where $e_{\kappa\alpha,\nu}(\mathbf{q})$ is the eigenvector of the dynamical matrix of the crystal, and M_κ is the mass of ion κ. For a rigorous derivation, see Ref. [50].

In our model system, we only consider long-range electron-phonon coupling within the lowest three conduction bands mediated by the highest LO phonon mode. This coupling channel represents most of the electron-phonon interaction in doped STO and other polar oxides. In Fig. 3.5, we show the coupling matrix element [Eq. (3.1)] of cubic STO for m, n equal to the three lowest conduction bands and ν=15, the highest LO phonon mode. We plot the matrix element for $\mathbf{q}$ along the high-symmetry path in the cubic cell and $\mathbf{k} = \Gamma$.

The divergence of g at the zone centre indicates a strong contribution to long-range Fröhlich coupling characteristic of polar semiconductors. Moreover, we find strong intra-band coupling in all three bands, as well as strong inter-band coupling between the lowest two conduction bands, $n = 1, 2$. Coupling between the lower two conduction band and $n = 3$ is negligible in comparison. This behaviour is related to the twofold degeneracy of the conduction band at the Gamma point [cf. Fig. 3.3].

3.1.2 Tetragonal phase

We construct the tetragonal ground-state structure of $SrTiO_3$ by exploring the potential energy surface along the normal coordinate of the soft mode at the R point:[109] First, we expand the crystal cell to a $2 \times 2 \times 2$ supercell. Doing this folds the R point back into the Γ point in the supercell. Then we extract the eigenvector corresponding to the negative eigenmode of the dynamical matrix. We displace the atoms in the cell continuously along this eigenmode, monitoring the total energy of the system.

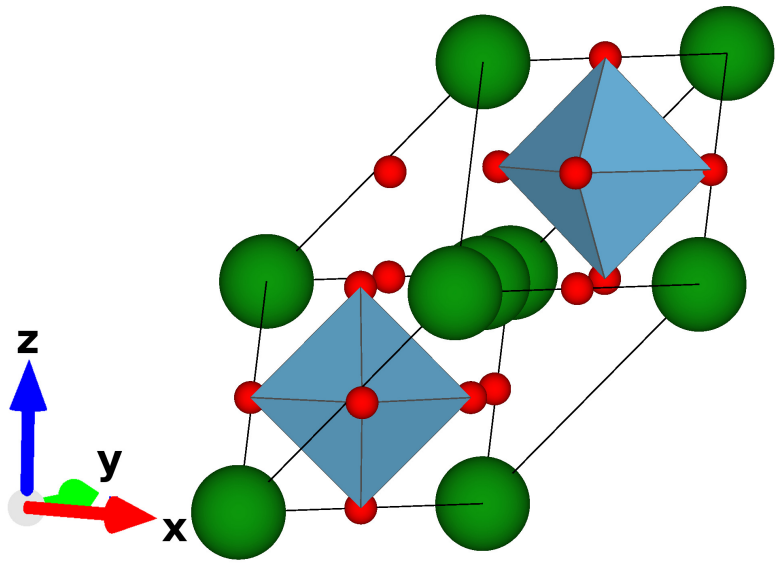


Figure 3.6: Distorted tetragonal cell obtained after full relaxation of the $2 \times 2 \times 2$ supercell obtained with the special displacement method. The oxygen octahedra are rotated by 8° in alternating directions around the axis of the tetragonal distortion. The lattice constant is $a = 3.995\,\text{Å}$ and the c/a ratio is 1.4%.

As the original structure exhibited negative phonon modes, we find that the total energy of the system decreases along the normal coordinate of the soft mode. After structural relaxation starting from the lowest energy configuration, we recover a new unit cell with tetragonal symmetry containing 10 atoms, shown in Fig. 3.6.

The new structure has a lattice parameter of $a = 5.595\,\text{Å}$ and a ratio $c/a = 1.007$. The volume of the unit cell is $\Omega_{\text{UC}} = 125.372\,\text{Å}^3$.

Note that the breaking of the cubic symmetry has fully lifted the degeneracy of the conduction band at Γ, cf. Figs. 3.7 and 3.8. The size of the band splitting at the zone centre is equal to $\Delta E_{1\to2} = 14\text{meV}$ between the first and second bands, and $\Delta E_{2\to3} = 38\text{meV}$ between the second and third bands. The tetragonal symmetry of the crystal is also visible in the effective masses. After diagonalisation of the effective mass tensor, we find that the effective masses along two normal coordinates agree, see Table 3.1.

The phonon dispersion of the tetragonal phase is given in Fig. 3.9. We find that

	n=1	n=2	n=3
m_1	0.905	1.022	4.902
m_2	1.645	1.443	0.840
m_3	1.645	1.443	0.840

Table 3.1: Eigenvalues of the effective mass tensor for the conduction bands of tetragonal $SrTiO_3$.

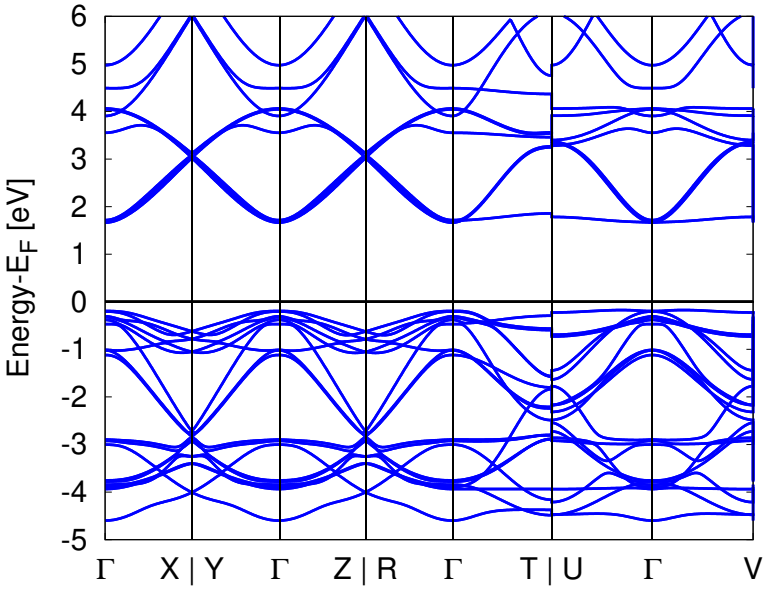


Figure 3.7: Electronic bandstructure of the distorted tetragonal cell of STO calculated on $6 \times 6 \times 6$ **k**points.

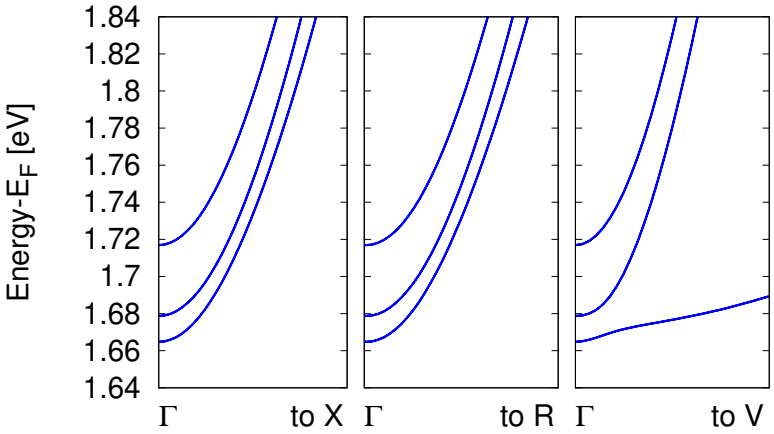


Figure 3.8: Detail of the electronic bandstructure near the Γ point.

the soft phonons have hardened, indicating no further structural instability. The energy of the highest LO phonon at Γ is equal to $\hbar\omega_{\mathrm{LO}} = 102.9$ meV. The eigenvalues of the dielectric tensor are given as $\varepsilon_{\infty,1,2} = 6.25$ and $\varepsilon_{\infty,3} = 6.27$.

3.2 The doped Fröhlich model

Using the parameters extracted in the previous section, we now construct our analytical model.

In good agreement with the bandstructures shown in Figs. 3.2 and 3.7 we assume that the conduction band in the zone centre of STO is a parabolic band with a given

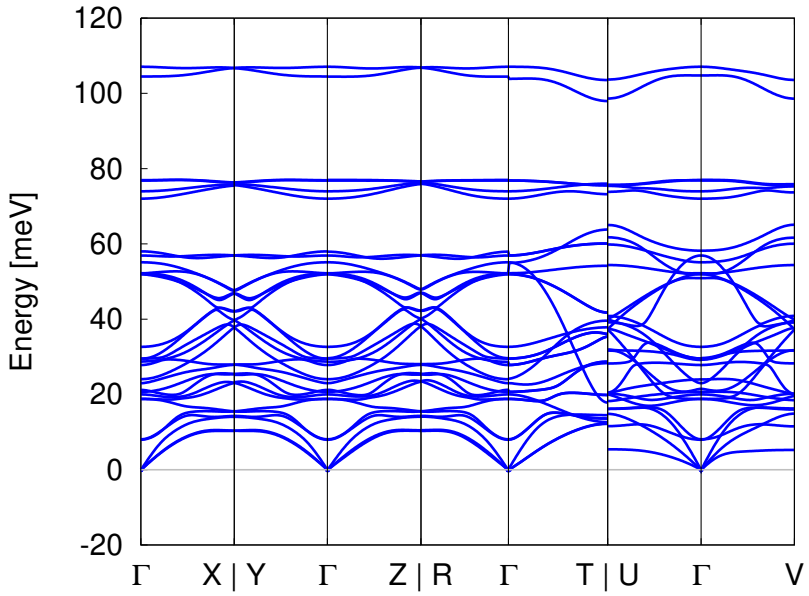


Figure 3.9: Phonon dispersion for the fully relaxed distorted tetragonal cell calculated on a $3 \times 3 \times 3$ **q**-point grid.

bare band mass m_0:

$$\epsilon_k = \frac{\hbar^2 k^2}{2m_0}. \tag{3.5}$$

Using the isotropic average of the lowest band in the tetragonal phase given in Table 3.1, we find $m_0 = 1.3\, m_e$.

In Chapters 4-7, finite occupation of the parabolic electron band plays a decisive role. To keep our formalism simple, we assume that so that the electron occupations are always well described by their value at the ground state:

$$f_{\mathbf{k}} = \theta(k_{\mathrm{F}} - |\mathbf{k}|) \qquad \text{where} \qquad k_{\mathrm{F}} \text{ is the Fermi wavevector.} \tag{3.6}$$

The main contribution to electron-phonon coupling stems from the LO3 mode. Given its flat dispersion shown in Figs. 3.4 and 3.9, we approximate it as an Einstein phonon:

$$\hbar\omega_q = \hbar\omega_0. \tag{3.7}$$

Using the average over the highest LO phonon modes in the tetragonal phase, we assume $\hbar\omega_0$ =102.9 meV.

In polar semiconductors, the main contribution to the total electron-phonon coupling is due to the long-range Fröhlich interaction, cf. Fig. 3.5. The characteristic singularity at $|\mathbf{q}| = 0$ corresponds to the onset of a macroscopic polarisation in the crystal, accompanied

by a uniform electric field. In Eqs. (1.1) and (1.2), we gave the analytical definitions of the Fröhlich coupling matrix element and the dimensionless coupling strength α. Note that in the polaron literature it is common to distinguish weak-coupling, intermediate coupling, and strong coupling depending on the value of α.[49] Although this separation is somewhat arbitrary, the onset of strong coupling is usually placed at $\alpha = 6$ for reasons that will become clear in Sec. 4.1.

To extract an effective α for our model from the *ab initio* electron-phonon coupling shown in Fig. 3.5, we first average over the total scattering from a state $(\mathbf{k} = \Gamma, n)$ to all other conduction states:

$$|g_n^{\mathrm{tot}}(q)|^2 = \sum_{m=1}^{3} |g(\Gamma, q)|^2. \tag{3.8}$$

Then, we calculate the spherical average of this total coupling matrix element,

$$|g_n^{\mathrm{tot}}|^2 = 4\pi \int_{\mathrm{BZ}} dq\, q^2\, |g_n^{\mathrm{tot}}(q)|^2. \tag{3.9}$$

From this quantity, we can extract our effective Fröhlich coupling strength via:

$$\alpha = |g_n^{\mathrm{tot}}|^2 \frac{\sqrt{2m_0}\Omega_{\mathrm{UC}}}{16\pi^2\, \hbar(\hbar\omega_0)^{3/2}}. \tag{3.10}$$

Using the values $m_0 = 1.3\, m_e$, $\hbar\omega_0$ =102.9 meV, and $\Omega_{\mathrm{UC}} = 125.372\,\text{Å}$, we reach $\alpha = 1.44$. This value is in good agreement with previous estimates.[161]

An important contribution to the pairing potential in the superconducting state is the repulsive Coulomb interaction between the two constituent electrons of a Cooper pair. The matrix element of this pairwise Coulomb interaction was given in Eq. (2.127). In the case of the Fröhlich model, it simplifies to:

$$V(\mathbf{k}, \mathbf{k}') = \frac{e^2}{\epsilon_0\, \Omega_{\mathrm{BZ}}} \frac{1}{|\mathbf{k} - \mathbf{k}'|^2}. \tag{3.11}$$

Note that Eq. (3.11) is expressed in terms of the bare Coulomb potential. In our calculations, however screening effects both due to the bound electrons in the crystal and due to the free dopant charge carriers lead to a strong reduction in the effective Coulomb interaction in our system. This is discussed in detail in the following section.

Lastly, note that our model parameters are summarised in Table 3.2 below.

α	$\hbar\omega_0$ [meV]	m_0 [m_e]	ε_∞
1.4	102.9	1.3	6.25

Table 3.2: Parametrisation of the doped Fröhlich solid based on first-principles calculations of $SrTiO_3$.

3.3 Free-carrier screening

In an undoped semiconductor, electronic screening due to valence-conduction transitions of bound electrons is taken into account via the bare band mass m_0 and the dielectric constant ε_∞. Adding dopant electrons creates a free electron cloud whose ability to shield electric fields in the solid increases with the doping level.

As we will show in Chapters 4 and 7, this additional screening channel must be accounted for to obtain reliable calculation results. Here, we first introduce an analytical expression for the dielectric function in the doped Fröhlich model. Then, we show how this screening function affects the long-range electron-phonon and electron-electron interactions.

We return to the polarisation propagator in the random-phase approximation, introduced in Sec.2.1.4:

$$P(\mathbf{q},\omega) = \sum_m \int \frac{d\mathbf{k}}{\Omega_{\mathrm{BZ}}} \frac{f_{n\mathbf{k}} - f_{m\mathbf{k}+\mathbf{q}}}{\epsilon_{n\mathbf{k}} - \epsilon_{m\mathbf{k}+\mathbf{q}} + \hbar\omega + i\eta}. \tag{2.50}$$

Together with the bare Coulomb potential $v(\mathbf{q})$, the dielectric function is then given as:

$$\varepsilon^{\mathrm{RPA}}(\mathbf{q},\omega) = 1 - v(\mathbf{q})\, P(\mathbf{q},\omega). \tag{2.51}$$

The momentum integral in $\varepsilon^{\mathrm{RPA}}$ can be performed analytically if one assumes parabolic electron bands. This is the case in our Fröhlich model. Eventually, one reaches:[115,162]

$$\begin{aligned} \varepsilon^{\mathrm{RPA}}(q,\omega) &= 1 + \left(\frac{4}{9\pi}\right)^{1/3} \frac{r_{\mathrm{S}}}{\pi} \frac{k_{\mathrm{F}}^3}{q^3} \\ &\times \left[\frac{2q}{k_{\mathrm{F}}} + f\left(\frac{q}{k_{\mathrm{F}}} + \frac{\hbar\omega/E_{\mathrm{F}}}{q/k_{\mathrm{F}}}\right) + f\left(\frac{q}{k_{\mathrm{F}}} - \frac{\hbar\omega/E_{\mathrm{F}}}{q/k_{\mathrm{F}}}\right)\right], \end{aligned} \tag{3.12}$$

where $f(z)$ is given by:

$$f(z) = \left(1 - \frac{z^2}{4}\right) \log \frac{z+2}{z-2}. \tag{3.13}$$

Note that in our system, the Fermi energy E_{F} is measured from the band bottom.

Eq. (3.12) is known as the Lindhard dielectric function. It is the dielectric function of a free electron gas in the random-phase approximation.

The quantity r_S in Eq. (3.12) is the Wigner-Seitz radius of the electron gas, i.e. the radius of a sphere that contains one electron on average. In the dielectric environment of the crystal, it is equal to:[29]

$$r_\mathrm{S} = \frac{m_0/m_e}{a_0\,\varepsilon_\infty}\left(\frac{3}{4\pi\,n_0}\right)^{1/3}, \tag{3.14}$$

where m_e is the mass of an electron in vacuum, and a_0 the Bohr radius.

The long-wavelength limit of the Lindhard function can be expressed as:[163]

$$\varepsilon^\mathrm{RPA}(q \ll k_\mathrm{F}, \omega) = 1 - \frac{\omega_\mathrm{pl}^2}{\omega^2} - \frac{3}{5}\frac{\omega_\mathrm{pl}^2}{\omega^4}\,(v_\mathrm{F}\,q)^2 + \mathcal{O}(q^4), \tag{3.15}$$

where

$$\hbar\omega_\mathrm{pl} = \frac{4\pi\,n_0\,e^2}{\varepsilon_\infty\,m_0} = \left(\frac{4}{9\pi}\right)\frac{16\,r_\mathrm{S}\,E_\mathrm{F}^2}{3\pi} \tag{3.16}$$

is the plasma frequency of the electron gas, i.e. the resonance frequency for collective excitations of the electrons in the Fermi sea.

The static limit of Eq. (3.12), on the other hand, can be written as:[163]

$$\varepsilon^\mathrm{RPA}(q, \omega = 0) = 1 + \frac{q_\mathrm{TF}^2}{q^2}\,F\left(q/2k_\mathrm{F}\right), \tag{3.17}$$

where

$$F(x) = \frac{1}{2} + \frac{1-x^2}{4x}\log\left|\frac{1+x}{1-x}\right|, \tag{3.18}$$

and q_TF is the Thomas-Fermi screening wavevector introduced in Eq. (2.145). In the case of a parabolic electron band with bare mass m_0, it can be expressed as:

$$q_\mathrm{TF}^2 = \frac{4k_\mathrm{F}}{\pi}\frac{e^2\,m_0}{\hbar^2\,\varepsilon_\infty}. \tag{3.19}$$

Note that $\lim_{x\to 0} F(x) = 1$ and that Eq. (3.17) reduces to the Thomas-Fermi dielectric function $\varepsilon^\mathrm{TF}(q) = 1 + q_\mathrm{TF}^2/q^2$ in the small-q limit [cf. Sec. 2.2.3].

3.3.1 Free-carrier screening of the Fröhlich interaction

The Fröhlich coupling matrix element defined in Eqs. (1.1) and (1.2) was derived to describe a single conduction electron in an insulator. The definition of the coupling strength α already contains the dielectric properties of the undoped crystal. In particular, it contains the static and optical dielectric constants of the undoped solid. To incorporate additional screening due to the free carriers, we modify the matrix element according to:[29,56]

$$g(\mathbf{k},\mathbf{k}') \to g^{\mathrm{scr}}(\mathbf{k},\mathbf{k}';\omega) = \frac{g(|\mathbf{k}-\mathbf{k}'|)}{\varepsilon^{\mathrm{RPA}}(|\mathbf{k}-\mathbf{k}'|,\omega)}, \tag{3.20}$$

where $\varepsilon^{\mathrm{RPA}}$ is the dielectric function of the free carriers in the random-phase approximation. Maintaining the dependence of g^{scr} on ω would further increase the complexity of our problem and introduce the need for a full frequency integration of all equations. To avoid this, we would like to approximate $\varepsilon^{\mathrm{RPA}}(\omega)$ by its value at some characteristic frequency.

The presence of the dielectric function has two effects: Firstly, it describes the ability of the electron cloud to screen the long-range Fröhlich interaction, which leads to a reduction of the effective coupling strength g in the system. The relevant frequency for the Fröhlich interaction is exactly the frequency of the LO phonon, ω_0.

Secondly, the screening function exhibits a pole at the plasma frequency of the dopant electron gas. When in resonance, the phonon and plasmon can hybridise and form a coupled boson, known as phonon-plasmon polariton.[164,165] We discuss this hybrid quasiparticle in some detail in Appendix C. Most importantly, coupling to plasma oscillations introduces a dependence of the boson energy on the doping level. However, no experimental report of polaron satellites in STO has found evidence for a doping dependence of the boson energy.[2,6,7] On the contrary, the spacing of the satellites in ARPES remains constant over several orders of magnitude.

We conclude that the renormalisation of the phonon energy due to coupling to a plasmon is negligible. A likely explanation for this is the relatively short lifetime of the polaron state. The reciprocal of the decay rate is given by the imaginary part of the Fan-Migdal self-energy, and a good estimate for this value in STO is $\hbar/\tau \approx 100$ meV. As shown in Fig. 3.10, the finite imaginary lifetime leads to a substantial broadening of the plasmon peak. In turn, this weakens the renormalisation of the phonon energy. In our

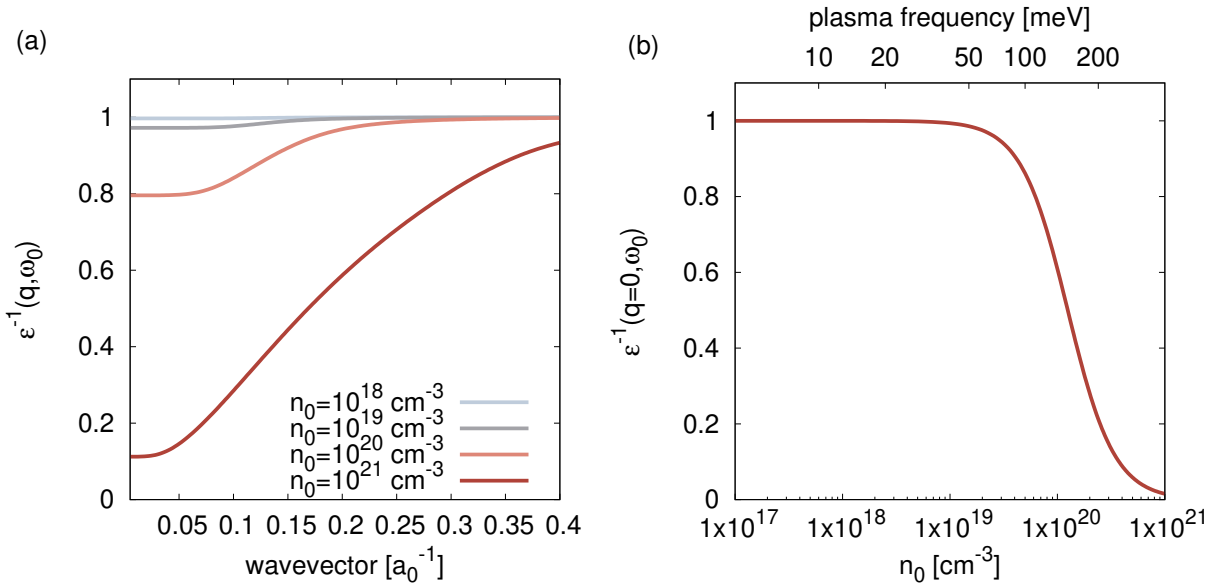


Figure 3.10: (a) Screening function for the electron-phonon interaction as a function of the scattering wavevector q for a range of doping levels. (b) Screening function at $q = 0$ across the doping range.

numerical calculations, we find that the polaron spectral function is not very sensitive to the exact value of $\hbar/\tau$ used, which is in agreement with previous reports.[56]

We therefore introduce the following approximation to Eq. (3.20): We evaluate the dielectric function of the free carriers at $\omega = \omega_0 + i/\tau$, where ω_0 is the frequency of the LO phonon in STO, and τ is the finite lifetime of the polaron state:

$$g(\mathbf{k},\mathbf{k}') \to g^{\mathrm{scr}}(\mathbf{k},\mathbf{k}') = \frac{g(|\mathbf{k}-\mathbf{k}'|)}{\varepsilon^{\mathrm{RPA}}(|\mathbf{k}-\mathbf{k}'|,\omega_0+i/\tau)} \tag{3.21}$$

Figure 3.10 shows the screening function $\varepsilon^{\mathrm{RPA}}(|\mathbf{k}-\mathbf{k}'|,\omega_0+i/\tau)$ for a range of doping levels using the bare electron mass and dielectric constant given in Table 3.2. In Fig. 3.10(a), we see that electron-phonon interactions are most strongly screened at small wavevector, while the screening declines in the short-range limit. In line with expectation, we find that screening effects are enhanced at higher doping levels. This enhancement is not linear, as can be seen in Fig. 3.10. Rather, the effect remains small until the plasma frequency ω_{pl} associated with the doping concentration reaches the level of the phonon frequency, which in this case is close to $\hbar\omega_0 \approx 100$ meV. Beyond this threshold, the Fröhlich interaction is screened very effectively.

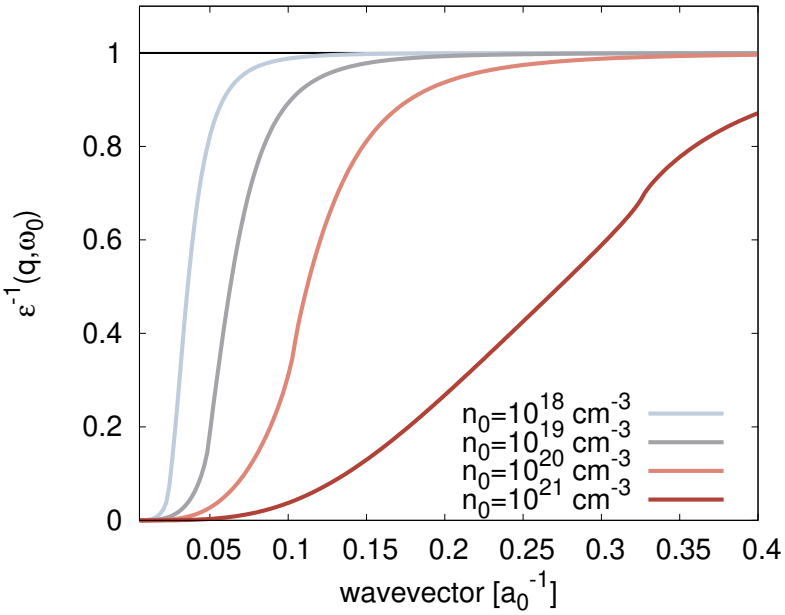


Figure 3.11: Screening function for the electron-electron interaction evaluated at $\omega = 0$ for the same range of doping levels as shown in Fig. 3.10. The screening effect is strongest up to a wavevector of $q = 2k_{\mathrm{F}}$.

3.3.2 Free-carrier screening of the Coulomb interaction

The screened Coulomb interaction was already introduced in Eq. (2.28),

$$W(\mathbf{r}, \mathbf{r}', \omega) = \int d\mathbf{r}'' \varepsilon^{-1}(\mathbf{r}, \mathbf{r}'', \omega)\, v(\mathbf{r}'', \mathbf{r}'), \tag{3.22}$$

where

$$v(\mathbf{r}, \mathbf{r}') = \frac{e^2}{4\pi\,\epsilon_0} \frac{1}{|\mathbf{r} - \mathbf{r}'|} \tag{3.23}$$

is the bare Coulomb interaction, and ε^{-1} contains all electronic screening effects. Static screening in the bulk crystal due to valence-to-conduction transitions is captured in the dielectric constant ε_∞. For our model system, the value of ε_∞ is given in Table 3.2. Further electronic screening arises from the free carriers in the conduction band, as described by Eq. (3.12). Combining both sources of screening, we can write the dynamically screened Coulomb interaction in the Fröhlich model as:

$$V_{\mathbf{k}\mathbf{k}'} \to W_{\mathbf{k}\mathbf{k}'}(\omega) = \frac{V_{\mathbf{k},\mathbf{k}'}}{\varepsilon_\infty\, \varepsilon^{\mathrm{RPA}}(|\mathbf{k} - \mathbf{k}'|, \omega)}. \tag{3.24}$$

Figure 3.11 illustrates the Lindhard screening function evaluated in the static limit $\left[\varepsilon^{\mathrm{RPA}}(q, \omega = 0)\right]^{-1}$. At zero frequency, the effect of screening is strongest.

Free-carrier screening of the Coulomb interaction is different from the screened Fröhlich interaction because electron-electron interactions at small q are effectively screened at all

doping levels. The Fröhlich interaction, on the other hand, only experiences substantial screening once the plasma oscillations reach a frequency that is comparable to that of the relevant phonon, $\omega_{\mathrm{pl}} \approx \omega_{\mathrm{ph}}$. Crucially, this means that there exists a doping range in which repulsive electron-electron interactions are suppressed by free carriers while attractive electron-phonon interactions remain unaffected. It is within this energy window that electron-phonon interactions in doped polar oxides dominate the physical picture and lead to the formation of polaron satellites and a superconducting phase transition.

4

Polaron spectra in doped semiconductors

In this chapter, we present our results for the QP spectra in the normal state as a function of electron doping. All results presented in this chapter are also discussed in Ref. [59].

This motivation for this investigation is fuelled by the emergence of extremely detailed experimental spectra of the polaron in STO [Figs. 1.1, 1.2]. In particular, the resolution of the QP satellites is remarkable. While there exist some *first-principles* studies of the electron spectral function of (doped) STO,[58,72,166] several important questions remain.

Figure 4.1 (a)-(c) shows the electron spectral function of doped STO presented in Ref. [166] using the Dyson's approach, the lesser (or time-ordered) cumulant expansion and the retarded cumulant expansion, respectively. In the Migdal approximation, the separation between the quasiparticle (near $E = 0$ eV) and the satellite (near $E = -0.1$ eV) is clearest. However, unlike in the experimental spectra, only one satellite is observed. The spectrum calculated with the lesser cumulant expansion in Fig. 4.1 (b) shows a single broad QP peak at the bottom of the conduction band with finite electron occupation. While no clear satellite structure is visible, nonzero spectral weight extends well below the band edge into the band gap. Broad vertical features appear on the left and right of the QP peak and extend to the lower end of the depicted energy range. Similar vertical features are also seen in the retarded cumulant in Fig. 4.1 (c).

Our analytical approach allows us to gain a better understanding of these calculated spectra. For instance, we will show below that the vertical streaks seen at the Fermi

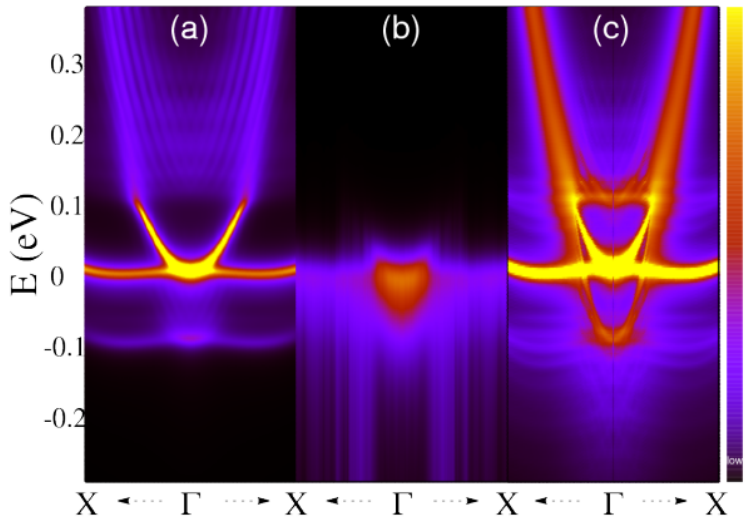


Figure 4.1: Electron spectral function of doped STO at 300 K centred around the Fermi energy, reprinted from Ref. [166]. (a) Spectral function obtained from the Dyson's equation approach. (b) Lesser cumulant expansion spectral function. (c) Retarded cumulant expansion spectral function

momentum in the cumulant spectra are intrinsic to the definition of the cumulant spectrum, and not mere numerical artefacts that could be removed by increasing numerical convergence parameters. Moreover, we find limiting cases for the applicability of both approaches as a function of the electron-phonon coupling strength α and the Fermi energy E_{F}. Lastly, we investigate the impact of free-carrier screening on the polaron spectra.

We discuss the electron spectral function across three scenarios: Firstly, section 4.1 reviews the effects of Fröhlich coupling between a single electron in the conduction band and the LO phonon. From here, we connect our results to the well-known Fröhlich polaron problem.

Then, in Sec. 4.2, we show the dramatic change in the electron spectral function if the conduction band is filled up to a finite Fermi momentum. Without explicitly accounting for the finite Fermi level, we find that ARPES spectra cannot be accurately modelled; however, we find that this level of theory tends to overestimate band renormalisation effects and can produce unphysical results.

In Sec. 4.3, we therefore further improve our description by explicitly taking into account free-carrier screening from the extra electrons. Modelling the delicate interplay between electron-phonon and electron-electron interactions poses a formidable challenge. The resulting spectra however are robust over a wide range of coupling strengths and Fermi energies.

For each approach, we analyse the QP band structure, the phonon satellites, and the mass enhancement, and we identify advantages and shortcomings. In particular, we show that both approaches yield anomalous electron mass enhancements at finite Fermi levels. This enhancement is so strong that the band curvature is inverted in a large region of the phase diagram, leading to a breakdown of the QP picture. This failure is more pronounced in the cumulant approach.

We conclude the chapter with Sec. 4.4, in which we discuss the spectral weight of the QP predicted in both the Dyson and cumulant approaches, and also relate it to experiment.

4.1 Single electron in the conduction band

The greater self-energy for the Fröhlich model, assuming $f_{\mathbf{k}} \equiv 0$ throughout the Brillouin zone, is given as [cf. Eq. (2.80)]:

$$\Sigma_k^>(\omega) = \frac{N_p}{\hbar} \int_{\mathrm{BZ}} \frac{d\mathbf{q}}{\Omega_{\mathrm{BZ}}} \frac{|g(q)|^2}{\omega - \epsilon_{\mathbf{k}+\mathbf{q}}/\hbar - \omega_0 + i\eta}. \tag{4.1}$$

As the occupation numbers are zero everywhere, the corresponding retarded self-energy is simply given via complex conjugation, $\Sigma_k^{\mathrm{R}} = (\Sigma_k^>)^*$.

After transforming Eq. (4.1) to spherical coordinates, we can integrate the self-energy analytically [see also Appendix D]:

$$\Sigma_k^>(\omega) = -i \frac{\alpha\,(\hbar\omega_0)^{3/2}}{2\pi\,\sqrt{\epsilon_k}} \log \frac{\sqrt{\hbar\omega - \Omega_0} + \sqrt{\epsilon_k}}{\sqrt{\hbar\omega - \Omega_0} - \sqrt{\epsilon_k}}, \tag{4.2}$$

where defined the shorthand $\Omega_0 = \hbar(\omega_0 - i\eta)$. This is the same result as reported in Refs. [29, 131], among others.

We plot the real and imaginary parts of the self-energy in Figs. 4.2 (a) and (b), respectively. The real part of Σ is negative everywhere, which indicates that electron-phonon interaction reduces the total energy of the system, and that a polaron is formed.[167]

The imaginary part of the self-energy is zero for frequencies ω below the threshold $\epsilon_k + \hbar\omega_0$ [see Fig. 4.2(b)]. The physical interpretation is the following: As long as the energy of the electron is lower than $\hbar\omega_0$, it does not have enough energy to excite a phonon and therefore therefore its lifetime is infinite.

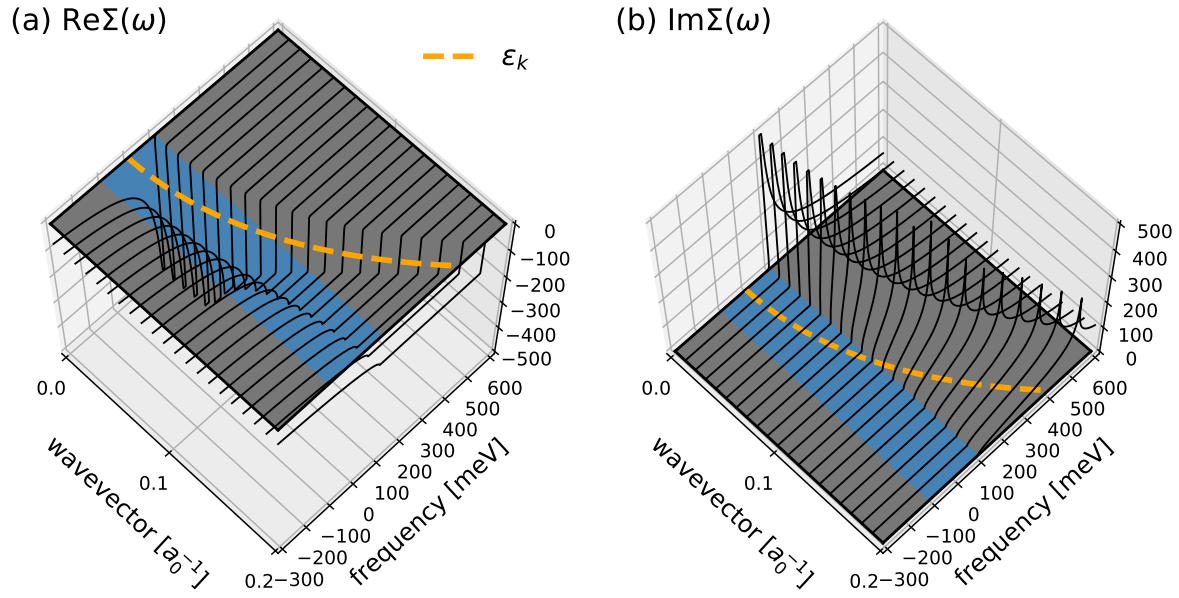


Figure 4.2: Self-energy for the undoped, empty-band Fröhlich model using the parameters provided in Table 3.2. (a) Real part of the greater self-energy (black lines) relative to the dispersion of the non-interacting electron in units of the phonon energy $\hbar\omega_0$ (dashed orange line). The blue area indicates the energy range $[\epsilon_0 - \hbar\omega_0, \epsilon_0 + \hbar\omega_0]$. (b) Imaginary part of the greater self-energy.

We find remarkable differences between the predicted QP energies and effective masses in the Dyson and cumulant approaches, even though they have been computed from the same self-energy. In the Dyson approach, the QP energy is obtained from:

$$E_k = \epsilon_k - i\frac{\alpha\,(\hbar\omega_0)^{3/2}}{2\pi\sqrt{\epsilon_k}}\log\frac{\sqrt{E_k-\Omega_0^*}+\sqrt{\epsilon_k}}{\sqrt{E_k-\Omega_0^*}-\sqrt{\epsilon_k}}. \tag{4.3}$$

At the band bottom, the QP energy and mass can be simplified to:[29]

$$\frac{E_0}{\hbar\omega_0} = -\frac{\alpha}{\sqrt{1-E_0/\hbar\omega_0}}, \tag{4.4}$$

$$\frac{m^*}{m_0} = \frac{1+\alpha/2}{1+\alpha/3}. \tag{4.5}$$

Equation Eq. (4.4) has two solutions, which correspond to the poles of the Green's function at $k = 0$ in the complex plane. One of the two solutions is purely real with $E_0^{\mathrm{R}} < \hbar\omega_0$, and one is complex with $E_0^{\mathrm{R}} > \hbar\omega_0$ and $E_0^{\mathrm{I}} < 0$. If the Green's function exhibits a pole on the real axis, the corresponding spectral function features a Dirac delta at this energy [cf. Fig. 4.3; note that the spectrum is calculated with a finite electron broadening $i\eta$]. The second peak appears more broadened as the position of the corresponding pole in

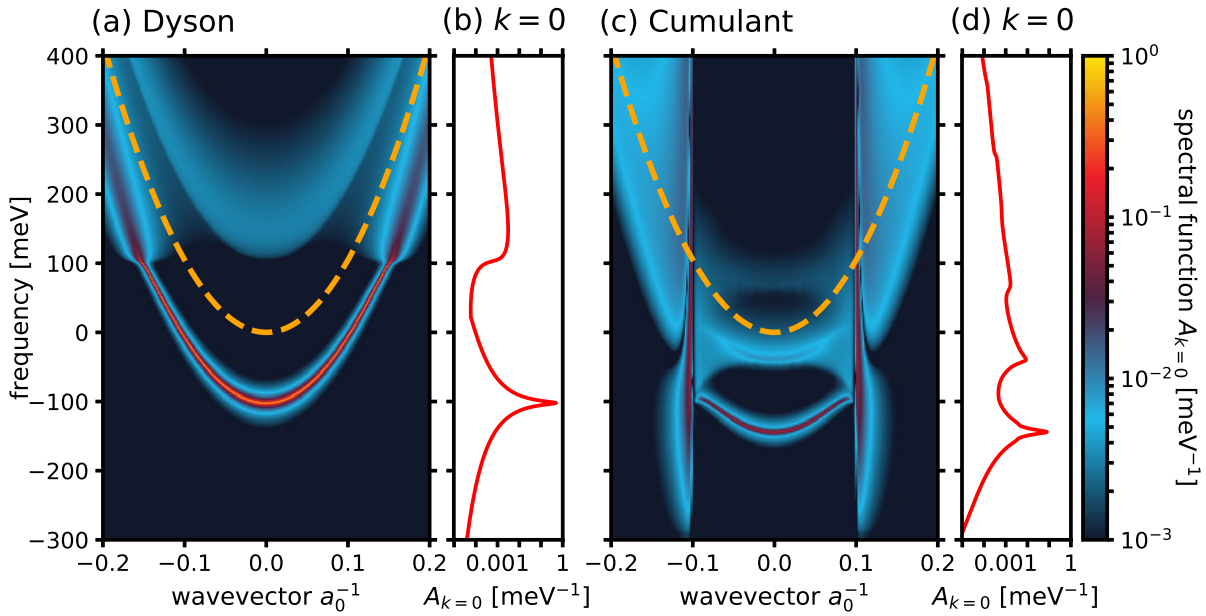


Figure 4.3: Spectral function for the undoped, empty-band Fröhlich model using the parameters provided in Table 3.2. (a) Colour plot of the Dyson spectral function of the undoped system. The dashed orange line indicates the dispersion of the non-interacting electron in units of the phonon energy $\hbar\omega_0$. (b) Logarithmic line plot of the Dyson spectral function at the Γ point. (c) Colour plot of the second-order cumulant spectral function. (d) Logarithmic line plot of the cumulant spectral function at the Γ point.

G is away from the real axis. Below we will refer to the first peak as the quasiparticle peak and to the second peak as the satellite.

Note that this distinction between quasiparticle and satellite is not as straightforward in the general case. It is a peculiarity of the Fröhlich model that the zero-temperature Fan-Migdal self-energy near the band bottom is purely real. It follows that we can treat the quasiparticle energy E_0 and the effective mass m^* at $k = 0$ as real quantities. For electronic states $\epsilon_{n\mathbf{k}} > \hbar\omega_0$, the imaginary self-energy is no longer zero, and the peak structure of the self-energy becomes more complicated. Most importantly, the QP energy must be evaluated using complex numbers [cf. Eq. (2.59) and Ref. [130]].

At weak coupling ($\alpha \ll 1$), we can expand Eqs. (4.4) and (4.5) as:

$$\frac{E_0}{\hbar\omega_0} = -\alpha + \frac{\alpha^2}{2} - \frac{5}{8}\alpha^3 + \mathcal{O}(\alpha^4), \quad (4.6) \qquad \frac{m^*}{m_0} = 1 + \frac{\alpha}{6} - \frac{\alpha^2}{18} + \mathcal{O}(\alpha^3). \quad (4.7)$$

Next, we turn to the cumulant expansion. The dispersion of the quasiparticle is described

by:

$$E_k^{>} = \epsilon_k + \frac{\alpha\,(\hbar\omega_0)^{3/2}}{2\pi\,\sqrt{\epsilon_k}} \arg \frac{\sqrt{\epsilon_k - \Omega_0} + \sqrt{\epsilon_k}}{\sqrt{\epsilon_k - \Omega_0} - \sqrt{\epsilon_k}}. \tag{4.8}$$

At the band bottom the cumulant QP energy and effective mass evaluate to:

$$\frac{E_0^{>}}{\hbar\omega_0} = -\alpha, \tag{4.9}$$

$$\frac{m^{*,>}}{m_0} = \frac{1}{1-\alpha/6}. \tag{4.10}$$

We see that also the cumulant QP energy is purely real, as both the imaginary self-energy and its derivative vanish at $\epsilon_{k=0}$. The low-coupling limit of the effective mass is given as:

$$\frac{m^{*,>}}{m_0} = 1 + \frac{\alpha}{6} + \frac{\alpha^2}{36} + \mathcal{O}(\alpha^3). \tag{4.11}$$

Note that Eq. (4.10) motivates the definition of the boundary between "weak" and "strong" coupling at $\alpha = 6$.

At this point it is interesting to address the question whether the Dyson equation or the cumulant approximation give the better description of the Fröhlich polaron. To answer this question, we consider the quasiparticle and the satellites separately.

4.1.1 Quasiparticle properties

For the undoped system, there exists a rigorous solution due to Feynman, which employs a path integral method.[15] Its results agree closely with advanced diagrammatic Monte Carlo calculations.[79] In the weak-coupling limit, Feynman's solutions are:

$$\frac{E_0}{\hbar\omega_0} = -\alpha - \frac{1}{81}\alpha^2 + \mathcal{O}(\alpha^3). \tag{4.12}$$

$$\frac{m^*}{m_0} = 1 + \frac{\alpha}{6} + 0.025\alpha^2 + \mathcal{O}(\alpha^3). \tag{4.13}$$

In Fig. 4.4 we compare Feynman's solution to the Dyson and cumulant quasiparticle properties.

Comparing the curves in Fig. 4.4 and analysing the expansion coefficients in the expressions for the effective mass, one can argue that the cumulant expansion yields the more accurate quasiparticle properties as it agrees more closely with Feynman's results. This view has been expressed in the literature.[57,58]

While this is true for low coupling strengths α, it is important to qualify this statement further. Most notably, the cumulant approach yields an unphysical divergence of the

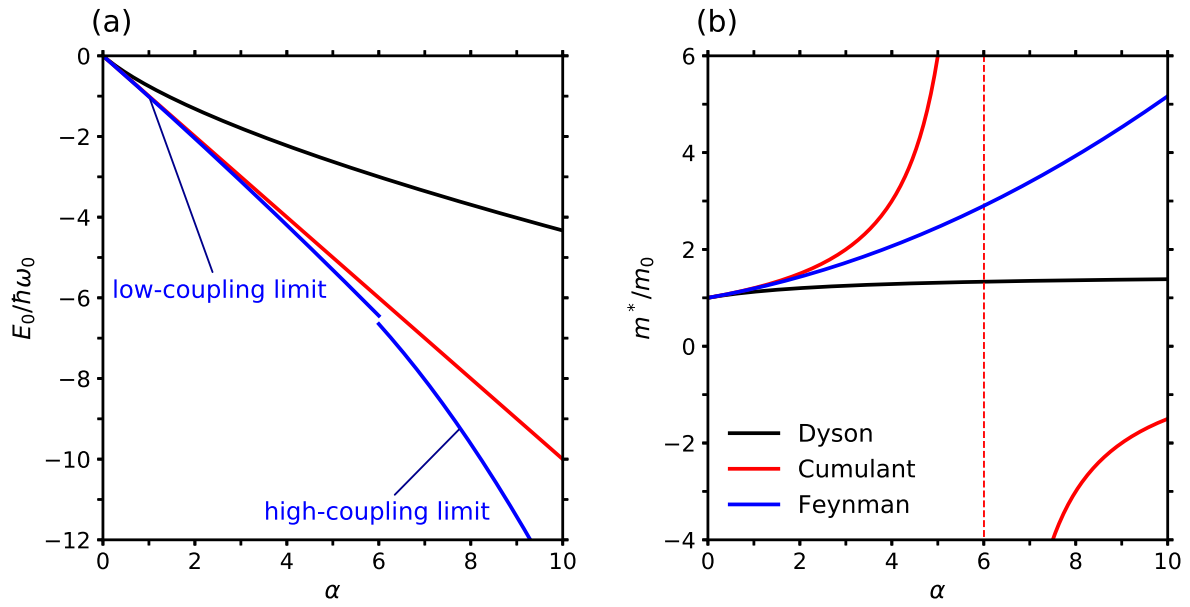


Figure 4.4: (a) Electron energy renormalisation in the undoped Fröhlich model as a function of the coupling strength α. Shown in blue are the weak- and strong-coupling limits of the Feynman model. The Dyson solution is shown in black, the cumulant solution is shown in red. (b) Electron mass renormalisation in the undoped Fröhlich model as a function of the coupling strength α.

effective mass at intermediate coupling with a singularity at $\alpha = 6$. The mass in the Dyson's approach may be less accurate, but it is robust across all considered coupling strengths.

In this context, we want to point out another important drawback of the cumulant spectral function: One obtains the cumulant QP energy from evaluating the electron self-energy in Eq. (4.2) at $\hbar\omega = \epsilon_k$. The resulting expression for E_k then contains a logarithmic singularity at $\epsilon_k = \hbar\omega_0$. In the spectral function in Fig. 4.3 (b), this singularity causes the appearance of unphysical vertical streaks at $k = \sqrt{2m_0\,\omega_0/\hbar^2}$.

We have encountered these artefacts in first-principles calculations of the cumulant spectral function. From our analytical derivation, we can confirm that their appearance is inherent to the definition of the cumulant spectral function, and cannot be avoided. Moreover, if interactions with several phonons are relevant to the polaron state, the corresponding spectrum features several logarithmic singularities. This represents an important weakness in the cumulant expansion and may limit its applicability to modelling polaron spectra of doped semiconductors.

4.1.2 Satellite properties

Comparing our calculated spectral functions in Figs 4.3 (a)-(d) to experiment, e.g. Fig. 1.1 and Fig. 1.2, we make two observations:

Firstly, as already discussed in numerous reports,[17,55–58,62–65,67–70,72,73,168–173] Dyson's approach yields only one satellite, to leading order located at a binding energy of $(1+\alpha)\hbar\omega_0$ from the QP peak [Fig. 4.3 (a)]. The cumulant method, on the other hand, yields multiple satellites which are separated from the QP peak by integer multiples of the boson energy $\hbar\omega_0$ [Fig. 4.3 (c)]. The cumulant spectrum is therefore in better agreement with experimental spectra [see also Refs. [2, 7]].

Secondly, in our empty-band model, both the Dyson's equation and the cumulant approach yield satellites located at energies *higher* than the QP band in our empty-band model. Experimental reality disagrees with this fact, as the satellites in Fig. 1.1 and Fig. 1.2 appear *below* the QP band. This discrepancy is related to the fact that ARPES probes *occupied* electronic states, while the empty-band Fröhlich model describes *unoccupied* states. A correct model of ARPES spectra therefore must contain a finite electron occupation numbers. We explore this scenario in the following section.

4.2 Finite Fermi level in the conduction band

After raising the Fermi level in the system, $E_{\mathrm{F}} > 0$, the lesser and greater self-energies are given by:

$$\Sigma_k^{<}(\omega) = \frac{N_p}{\hbar}\int_{\mathrm{BZ}} \frac{d\mathbf{q}}{\Omega_{\mathrm{BZ}}} \frac{|g(q)|^2\, f_{\mathbf{k}+\mathbf{q}}}{\omega - \epsilon_{\mathbf{k}+\mathbf{q}}/\hbar + \omega_0 - i\eta}, \tag{4.14}$$

$$\Sigma_k^{>}(\omega) = \frac{N_p}{\hbar}\int_{\mathrm{BZ}} \frac{d\mathbf{q}}{\Omega_{\mathrm{BZ}}} \frac{|g(q)|^2\, (1 - f_{\mathbf{k}+\mathbf{q}})}{\omega - \epsilon_{\mathbf{k}+\mathbf{q}}/\hbar - \omega_0 + i\eta}. \tag{4.15}$$

The lesser self-energy $\Sigma^{<}$ describes electron removal processes, while $\Sigma^{>}$ describes electron addition processes. To recover the retarded self-energy used in the Dyson equation, we use the relation $\Sigma^{\mathrm{R}} = \Sigma^{<} + (\Sigma^{>})^*$. Moreover, for simplicity, we assume $f_{\mathbf{k}} = \theta(k_{\mathrm{F}} - k)$ for the electron occupation numbers.

In this section, we ignore free-carrier screening, which will be included in Sec. 4.3. The results presented here are valid in the low-screening region where $\left(\varepsilon^{\mathrm{RPA}}(q,\omega_0+i/\tau\right)^{-1}$ is close to unity, cf. Fig. 3.10.

After carrying out the integrals in Eqs. (4.14) and (4.15) explicitly, we obtain the following self-energies [key steps of the derivation are provided in Appendix D]:

$$\begin{aligned}\Sigma_k^<(\omega) &= -\frac{\alpha\,(\hbar\omega_0)^{3/2}}{2\pi\sqrt{\epsilon_k}}\left[L\left(\sqrt{E_\mathrm{F}/\epsilon_k},\sqrt{(\hbar\omega+\Omega_0)/\epsilon_k}\right)\right.\\ &+ \left.\log\frac{\hbar\omega+\Omega_0-E_\mathrm{F}}{\hbar\omega+\Omega_0-\epsilon_k}\log\left|\frac{\sqrt{E_\mathrm{F}}+\sqrt{\epsilon_k}}{\sqrt{E_\mathrm{F}}-\sqrt{\epsilon_k}}\right|\right]-\mathrm{Re}\,\Sigma_{k_\mathrm{F}}^<(E_\mathrm{F}),\end{aligned} \tag{4.16}$$

with

$$\Sigma_{k_\mathrm{F}}^<(E_\mathrm{F}) = -\frac{\alpha\,(\hbar\omega_0)^{3/2}}{2\pi\sqrt{E_\mathrm{F}}}\left[\mathrm{Li}_2\frac{2\sqrt{E_\mathrm{F}}}{\sqrt{E_\mathrm{F}}+\sqrt{E_\mathrm{F}+\Omega_0}}+\mathrm{Li}_2\frac{2\sqrt{E_\mathrm{F}}}{\sqrt{E_\mathrm{F}}-\sqrt{E_\mathrm{F}+\Omega_0}}\right]. \tag{4.17}$$

and

$$\begin{aligned}\Sigma_k^>(\omega) &= \frac{\alpha\,(\hbar\omega_0)^{3/2}}{2\pi\sqrt{\epsilon_k}}\left[\log\frac{\hbar\omega-\Omega_0-E_\mathrm{F}}{\hbar\omega-\Omega_0+\epsilon_k}\log\left|\frac{\sqrt{E_\mathrm{F}}+\sqrt{\epsilon_k}}{\sqrt{E_\mathrm{F}}-\sqrt{\epsilon_k}}\right|\right.\\ &+ \left.L\left(\sqrt{E_\mathrm{F}/\epsilon_k},\sqrt{(\hbar\omega-\Omega_0)/\epsilon_k}\right)-i\pi\log\frac{\sqrt{\hbar\omega-\Omega_0}+\sqrt{\epsilon_k}}{\sqrt{\hbar\omega-\Omega_0}-\sqrt{\epsilon_k}}\right]-\mathrm{Re}\,\Sigma_{k_\mathrm{F}}^>(E_\mathrm{F}),\end{aligned} \tag{4.18}$$

with

$$\begin{aligned}\Sigma_{k_\mathrm{F}}^>(E_\mathrm{F}) &= -\frac{\alpha\,(\hbar\omega_0)^{3/2}}{2\pi\sqrt{E_\mathrm{F}}}\left[i\pi\,\log\frac{\sqrt{E_\mathrm{F}-\Omega_0}+\sqrt{E_\mathrm{F}}}{\sqrt{E_\mathrm{F}-\Omega_0}-\sqrt{E_\mathrm{F}}}\right.\\ &- \left.\mathrm{Li}_2\frac{2\sqrt{E_\mathrm{F}}}{\sqrt{E_\mathrm{F}}+\sqrt{E_\mathrm{F}-\Omega_0}}-\mathrm{Li}_2\frac{2\sqrt{E_\mathrm{F}}}{\sqrt{E_\mathrm{F}}-\sqrt{E_\mathrm{F}-\Omega_0}}\right].\end{aligned} \tag{4.19}$$

Define the auxiliary function L as:

$$L(z_1,z_2)=\mathrm{Li}_2\frac{1+z_1}{1+z_2}+\mathrm{Li}_2\frac{1-z_1}{1+z_2}-\mathrm{Li}_2\frac{1+z_1}{1-z_2}-\mathrm{Li}_2\frac{1-z_1}{1-z_2}, \tag{4.20}$$

where Li_2 denotes the dilogarithm function, and z_1, z_2 are complex-valued parameters.

Note that Eq. (4.18) correctly returns the corresponding equation for the undoped model, Eq. (4.2), upon taking the limit $E_\mathrm{F}\to 0$.

In metallic systems, the volume of the Fermi surface remains constant when many-body interactions are turned on adiabatically. This fact is known as Luttinger's theorem.[174] The

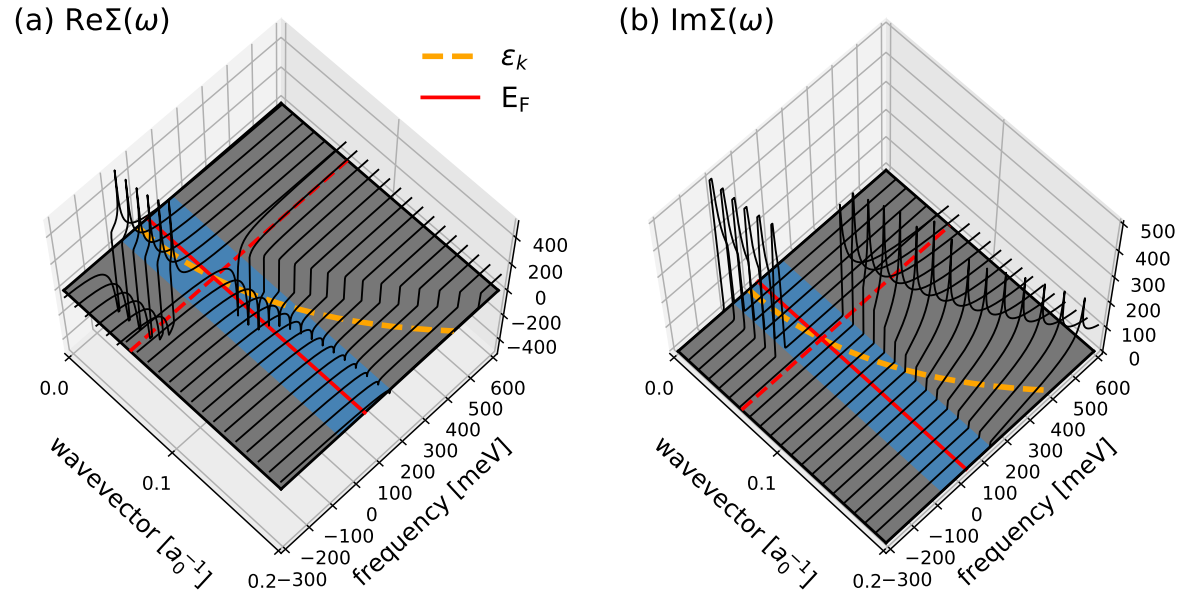


Figure 4.5: Self-energy for the Fröhlich model using the parameters provided in Table 3.2 at a Fermi energy of $E_F = 40$ meV. Free-carrier screening is not included. (a) Real part of the lesser and greater self-energies in the low-screening limit (black lines) relative to the dispersion of the non-interacting particle (dashed orange line). The solid and dashed red lines indicate the Fermi energy and Fermi momentum, respectively; the blue area indicates the energy range $[E_F - \hbar\omega_0, E_F + \hbar\omega_0]$. (b) Imaginary part of the self-energy.

charge-carrier concentration in the system is directly related to the Fermi wavevector k_F. Therefore, k_F and E_F must be the same for the independent particle and the interacting quasiparticle. To *enforce* this, we subtract the constant $\Sigma_{k_F}(E_F/\hbar)$ from our self-energy expression, cf. Eqs. (4.17) and (4.19), ensuring that $\mathrm{Re}\,\Sigma_{k_F}(E_F/\hbar) = 0$.

We show the real and imaginary parts of the doped self-energy for the model parameters given in Table 3.2 in Figs. 4.5 (a) and (b). Real Σ is now positive across the range of occupied states, passes through zero at $(k = k_F, \hbar\omega = E_F)$, and becomes negative for unoccupied states. The effective mass of the QP shown in Figs. 4.6 (a) and (c) is therefore higher than the bare electron mass. Moreover, mass renormalisation increases with the charge-carrier concentration.

Unlike for unoccupied states, the main peak structure in the imaginary self-energy at occupied states $k < k_F$ is now shifted to a lower energy, see Fig. 4.5 (b). As the satellite function is intimately linked to $\mathrm{Im}\Sigma_k^<$, cf. Eq. (2.97), we find that the polaron sidebands in Figs. 4.6 (a)-(d) now appear below the quasiparticle peak. For empty states, the situation remains unchanged.

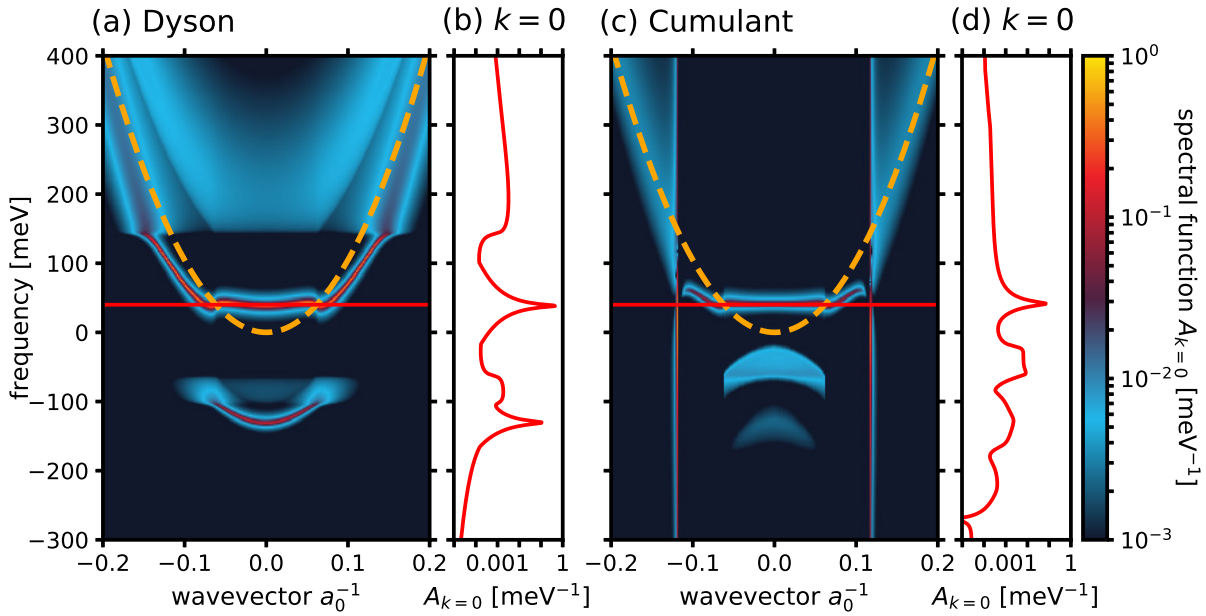


Figure 4.6: Spectral function for the Fröhlich model using the parameters provided in Table 3.2 at a Fermi energy of $E_F = 40$ meV. Free-carrier screening is not included. (a) Colour plot of the Dyson spectral function in the extreme anti-adiabatic limit relative to the non-interacting electron energy (dashed orange line) and the Fermi energy (red line). (b) Logarithmic line plot of the Dyson spectral function at the Γ point. (c) Colour plot of the second-order cumulant spectral function. (d) Logarithmic line plot of the cumulant spectrum at $k = 0$.

4.2.1 Quasiparticle properties

We have derived full analytical expressions for the energy and effective mass of quasiparticle in the Dyson and cumulant approaches. As in Sec. 4.1, the vanishing imaginary part of the zero-temperature electron self-energy in the energy window $[E_F - \hbar\omega_0; E_F + \hbar\omega_0]$ allows us to treat the quasiparticle energy and effective mass as real quantities. However, we find that their analytical form is cumbersome and not very instructive. They are therefore presented in Appendix F.

To still be able to discuss the renormalisation of the quasiparticle at finite Fermi energy, we have evaluated E_0 and m^* in both the Dyson equation approach and the cumulant expansion over a wide range of coupling constants α and Fermi energies E_F. Figure 4.7 shows the results for the renormalised QP energy at $k = 0$.

A darker shade of green in Figs. 4.7 (a) and (b) indicates that the QP energy lies lower below the Fermi level. This situation corresponds to a stable dressed electron, precisely as in the case of the undoped Fröhlich model. However, in our setup we also

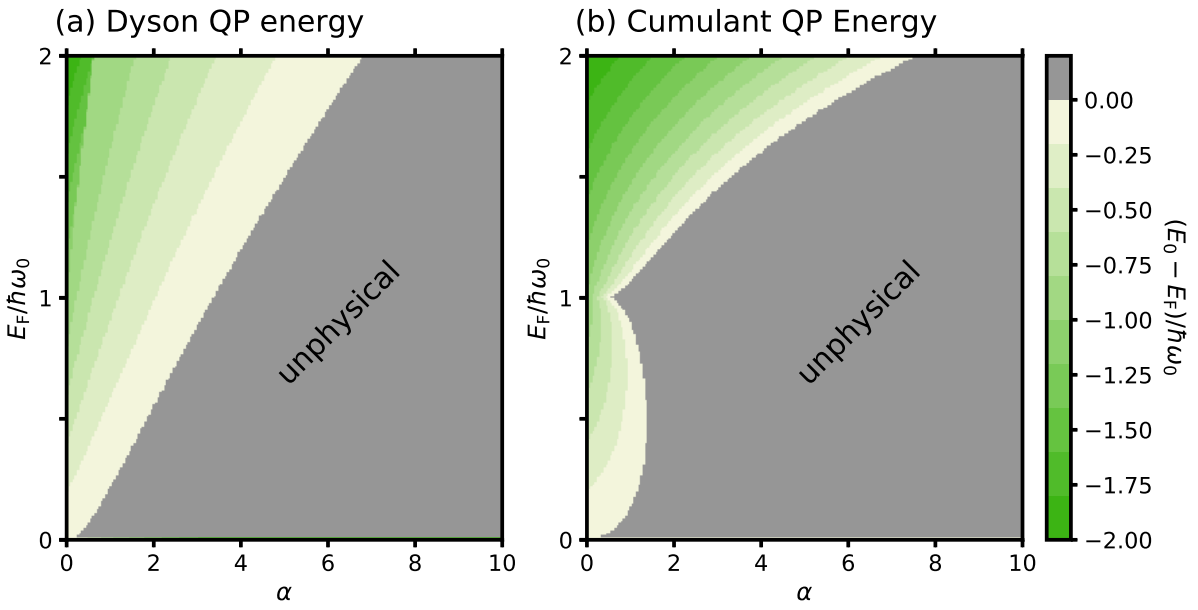


Figure 4.7: (a) Renormalised Dyson QP energy $E_0/\hbar\omega_0$ relative to the Fermi level. Negative QP energies E_0 (shown in green) indicate a higher binding energy of the interacting system; positive energies (shown in gray) imply that the renormalised QP energy lies above the Fermi level, and indicate a breakdown of the Fermi surface. (b) Renormalised second-order cumulant QP energy $E_0/\hbar\omega_0$ relative to the Fermi level.

find unphysical values for the quasiparticle renormalisation. More precisely, we find a situation where the QP peak is moved to such high energies that it would lie *above* E_F. this would mean a breakdown of the Fermi surface, and is an unphysical scenario. We explain this behaviour by reminding ourselves that the Fan-Migdal self-energy itself is only a second-order approximation to the full electron-phonon self-energy.

We also plot the renormalisation of the electron mass across the same range of coupling strengths and Fermi energies, see Figs. 4.8 (a) and (b). Concomitant with the breakdown of the Fermi surface observed in Fig. 4.7 we find areas in the phase space where overshooting mass renormalisation leads to an inversion of the curvature in the QP spectrum. This appearance of a negative effective mass is shown in gray, and is again an unphysical artefact resulting from the truncated self-energy expression.

We reiterate that the data presented in Figs. 4.7 and 4.8 do not account for free-carrier screening of the electron-phonon matrix elements. Including the free-carrier screening reduces the effective coupling strength at finite doping, which in turn helps extend the range of validity of the Dyson and cumulant approaches. Nevertheless, unphysical

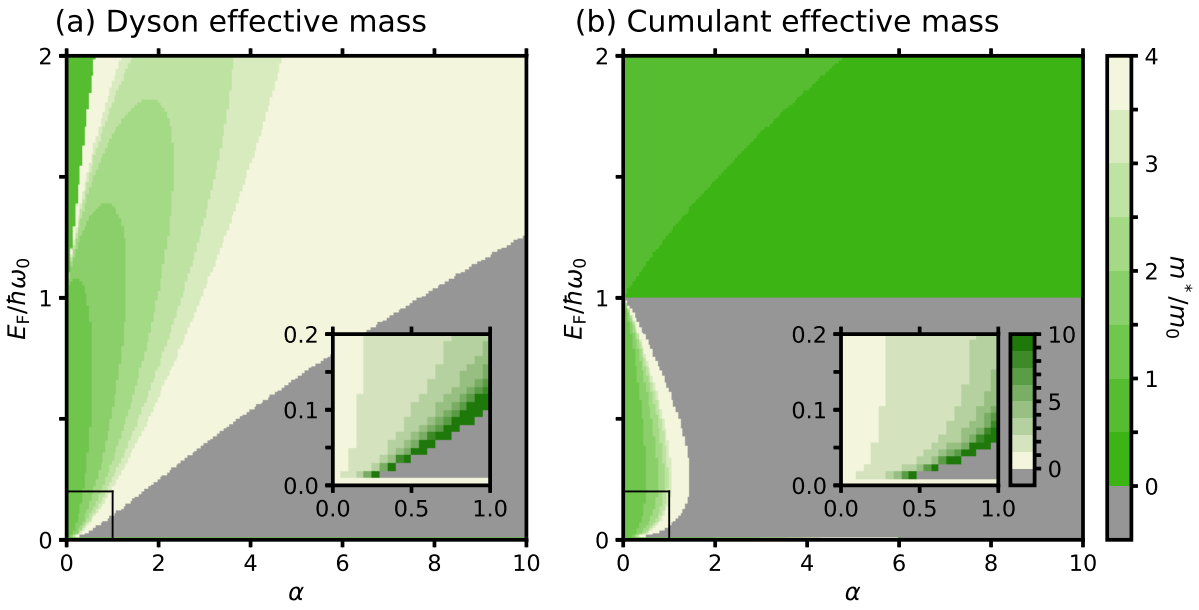


Figure 4.8: (a) Renormalised Dyson effective mass at the Γ point. Positive values of m^* (shown in green) indicate the renormalisation of the QP mass; negative values of m^* (shown in gray) indicate that the curvature of the QP spectrum at $k = 0$ has become negative, and signal a breakdown of the second-order expansion of the self-energy. The inset shows an enlarged view for $\alpha < 1$ and $E_F < 0.2\hbar\omega_0$; note that the colour scale in the inset has been extended to $m^*/m_0 = 10$. (d) Renormalised second-order cumulant effective mass.

solutions still exist, see Figs. 4.12 and 4.13.

An interesting observation related to the breakdown of the quasiparticle is its similarity to spectra obtained in Fröhlich's theory of superconductivity.[28] This precursor to BCS theory incorrectly predicts an inversion of the band curvature at strong coupling,[175] an artefact that was later resolved by Bardeen, Cooper and Schrieffer.

Besides this area of negative effective mass, there is a second region in the phase diagram in Fig 4.8 that predicts an unusual behaviour for the effective mass of the quasiparticle: Consider the insets in Figs. 4.8, which give an enlarged view of the low-doping limit for small α. We find that the effective mass in this region is renormalised to values of $m^* \gtrsim 10$.

At weak coupling, we take the limit $E_F \to 0$ in our analytical expressions for $E_0(E_F)$ and $m^*(E_F)$ [see Eqs. (F.3)-(F.7)]. For the Dyson approach, we find:

$$\frac{E_0}{\hbar\omega_0} = \frac{2\alpha}{\pi}\sqrt{\frac{E_F}{\hbar\omega_0}} + \frac{\alpha}{6}\frac{E_F}{\hbar\omega_0} + \mathcal{O}(E_F/\hbar\omega_0)^{3/2}, \tag{4.21}$$

$$\frac{m^*}{m_0} = -\frac{4\alpha}{3\pi}\sqrt{\frac{\hbar\omega_0}{E_F}} + \left(1 + \frac{5\alpha}{6}\right) - \frac{8\alpha}{3\pi}\sqrt{\frac{E_F}{\hbar\omega_0}} + \mathcal{O}(E_F/\hbar\omega_0)^{3/2} \tag{4.22}$$

and for the cumulant:

$$\frac{E_0^<}{\hbar\omega_0} = \frac{\alpha}{\pi}\sqrt{\frac{E_\mathrm{F}}{\hbar\omega_0}} + \mathcal{O}(E_\mathrm{F}/\hbar\omega_0)^{3/2}, \tag{4.23}$$

$$\frac{m^*}{m_0} = \frac{2\alpha}{3\pi}\sqrt{\frac{\hbar\omega_0}{E_\mathrm{F}}} + 1 + \frac{4\alpha}{3\pi}\sqrt{\frac{E_\mathrm{F}}{\hbar\omega_0}} + \mathcal{O}(E_\mathrm{F}/\hbar\omega_0)^{3/2}. \tag{4.24}$$

Note that this behaviour is independent of the specific implementation of the cumulant method: In appendix E, we show that the small-E_F behaviour of the retarded cumulant is very similar.[64]

To lowest order in E_F, the QP energy is linear in α and proportional to the density of states via $\propto \sqrt{E_\mathrm{F}}$. This result illustrates that the total electron-phonon interaction in a doped system is substantially enhanced by the presence of doping.

Moreover, we find that the effective mass in both the Dyson and cumulant approximations behave as $E_\mathrm{F}^{-1/2}$ in the extreme anti-adiabatic limit. This is a new result and may be an alternative explanation for the extremely high effective mass renormalisation observed in very low-doped STO.[176]

More generally, this result is significant for the interpretation of experimental data. Commonly, the curvature of the QP band obtained from ARPES is used to determine the dressed mass and hence the coupling strength α. Often, the coupling strength is determined by using the formula for the undoped Fröhlich model, Eqs. (4.5) or (4.10). However, as we have seen, the finite electron occupation that enables ARPES studies of the conduction band [cf. Figs. 1.1 and 1.2], can interfere strongly with the quasiparticle renormalisation. The physics of such a system are likely better captured by Eqs. (4.21)-(4.24).

In the comparison of Dyson and the cumulant, we are limited to the observation that the former provides stable solutions over a wider area of the phase space. As there exists no solution equivalent to Feynman's Fröhlich polaron treatment for the doped system, it is difficult to compare the calculated spectra.

In either case, intermediate-to-high coupling strengths and low doping levels quickly become problematic, while high doping levels and low coupling strengths lead to meaningful results. Probably, this was to be expected, since the Migdal theorem (which underpins the Fan-Migdal self-energy) is only valid within the adiabatic approximation, $\hbar\omega_0 \ll E_\mathrm{F}$.[21]

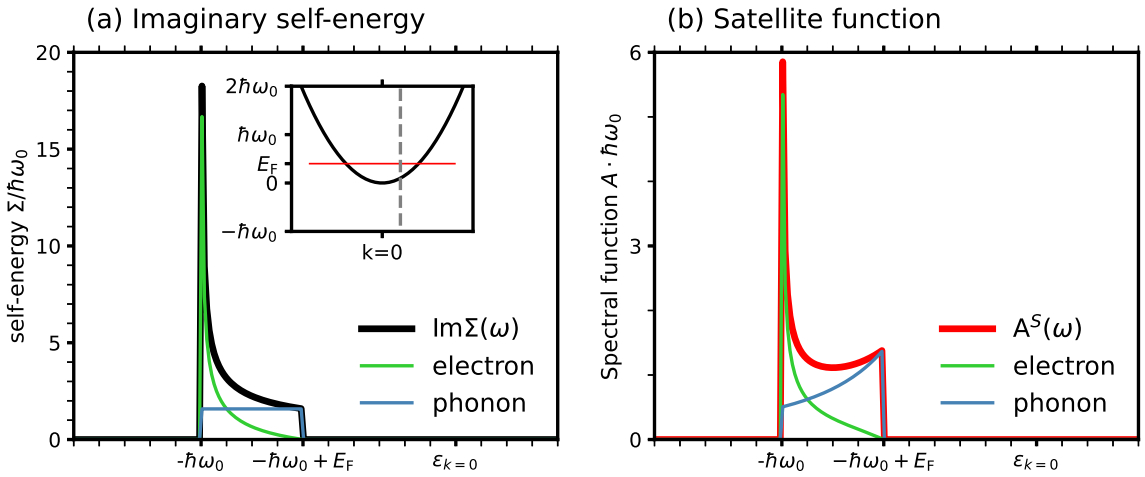


Figure 4.9: (a) Imaginary lesser self-energy at $\epsilon_k = 10$ meV at a Fermi energy of $E_\mathrm{F} = 40$ meV and using the parameters given in Table 3.2 (black line). Contributions to Eq. (4.16) arising from the singularity in the non-interacting *electron* Green's function are shown in green, those due to *phonon* emission and absorption processes across the entire Fermi sea appear in blue. (b) Corresponding satellite function $A^\mathrm{S}(\omega)$ (before convolution with the QP function, shown in red). Contributions to the satellite function due to the electron Green's function and phonon emission and absorption processes are shown in green and blue, respectively.

4.2.2 Satellite properties

Comparing again our calculated spectra in Figs. 4.6 (a) and (b) to experiment, Figs. 1.1 and 1.2, we firstly note that due to our explicit treatment of the finite Fermi energy, the satellites now appear below the QP peak.

As before, we confirm that the cumulant captures the satellite states better than the Dyson approach. The distance between the single satellite obtained from the Dyson equation is much larger than the phonon energy. Moreover, along the momentum axis, it extends extends beyond the Fermi momentum k_F, suggesting that unoccupied electronic states could also emit a phonon upon excitation. This does not conform to experiment, and can be traced back to the use of the retarded self-energy in A_k.

Our analytical approach allows us to go beyond the broad features of the spectral function. In particular, we find that the cumulant satellites consist of doublets [cf. 4.6 (d)]. To unravel its origin, we juxtapose the imaginary self-energy with the corresponding satellite function [cf. Eq. (2.97)]: Fig. 4.9 shows both quantities at $\epsilon_k = 10$ meV.

At finite doping, phonon emission and absorption processes can occur at all energies between $\epsilon_{k=0}$ and E_F. The imaginary self-energy is therefore different from zero in the

energy range $[-\hbar\omega_0, -\hbar\omega_0 + E_\mathrm{F}]$, [blue line in Fig. 4.9]. The energy of the lower edge of the satellite, $\hbar\omega = \epsilon_k - \hbar\omega_0$, is determined by the pole of the non-interacting electron Green's function, shifted by one phonon energy [green line in Fig. 4.9]. It follows that the two resulting peaks are separated exactly by the Fermi energy E_F.

In the intensity map of the spectrum, Fig. 4.6(c), the satellites do not simply follow the dispersion of the quasiparticle, as was suspected in earlier works on the cumulant.[71] Rather, they appear as near-elliptical shapes, adding spectral weight between the satellite peaks. This detail may provide an explanation for some of the broadening of spectral features seen e.g. in Fig. 1.1 (a) and Fig. 1.2, but not yet reproduced in previous *ab initio* calculations.

4.3 Finite Fermi level including free-carrier screening

In this last section we consider the most complex scenario: a Fröhlich model with doping as well as screening of the electron-phonon interaction by free carriers. This means that we modify the electron-phonon matrix element according to Eq. (3.21), see also Fig. 3.10. Due to the complicated dependence of the screened matrix element on the wave vector q, we express the screened self-energy in terms of one-dimensional integrals in q.

First, the screened lesser self-energy:

$$\begin{aligned}\Sigma_k^<(\omega) &= -\frac{\alpha\,(\hbar\omega_0)^{3/2}}{2\pi\,\sqrt{\epsilon_k}}\left[\int_0^{k_\mathrm{F}-k}\frac{dq}{|\varepsilon^\mathrm{RPA}(q)|^2\,q}\log\frac{\hbar\omega-\frac{\hbar^2(k+q)^2}{2m_0}+\Omega_0}{\hbar\omega-\frac{\hbar^2(k-q)^2}{2m_0}+\Omega_0}\right.\\ &+ \left.\int_{k_\mathrm{F}-k}^{k_\mathrm{F}+k}\frac{dq}{|\varepsilon^\mathrm{RPA}(q)|^2\,q}\log\frac{\hbar\omega-E_\mathrm{F}+\Omega_0}{\hbar\omega-\frac{\hbar^2(k-q)^2}{2m_0}+\Omega_0}\right]-\mathrm{Re}\Sigma^<_{k_\mathrm{F}}(E_\mathrm{F}),\end{aligned}\tag{4.25}$$

with

$$\Sigma^<_{k_\mathrm{F}}(E_\mathrm{F}) = \frac{\alpha\,\hbar\omega_0}{2\pi}\sqrt{\frac{\hbar\omega_0}{E_\mathrm{F}}}\int_0^{2k_\mathrm{F}}\frac{dq}{|\varepsilon^\mathrm{RPA}(q)|^2\,q}\log\left(1-\frac{\hbar^2(q^2-2k_\mathrm{F}q)}{2m_0\,\Omega_0}\right).\tag{4.26}$$

Next, the screened greater self-energy:

$$\begin{aligned}\Sigma_k^>(\omega) &= -\frac{\alpha\,(\hbar\omega_0)^{3/2}}{2\pi\,\sqrt{\epsilon_k}}\left[\int_{k_\mathrm{F}-k}^{k_\mathrm{F}+k}\frac{dq}{|\varepsilon^\mathrm{RPA}(q)|^2\,q}\log\frac{\hbar\omega-\frac{\hbar^2(k+q)^2}{2m_0}-\Omega_0}{\hbar\omega-E_\mathrm{F}-\Omega_0}\right.\\ &+ \left.\int_{k_\mathrm{F}+k}^{\infty}\frac{dq}{|\varepsilon^\mathrm{RPA}(q)|^2\,q}\log\frac{\hbar\omega-\frac{\hbar^2(k+q)^2}{2m_0}-\Omega_0}{\hbar\omega-\frac{\hbar^2(k-q)^2}{2m_0}-\Omega_0}\right]-\mathrm{Re}\Sigma^>_{k_\mathrm{F}}(E_\mathrm{F}),\end{aligned}\tag{4.27}$$

with

$$\Sigma^{>}_{k_\mathrm{F}}(E_\mathrm{F}) = -\frac{\alpha\,\hbar\omega_0}{2\pi}\sqrt{\frac{\hbar\omega_0}{E_\mathrm{F}}}\left[\int_0^{2k_\mathrm{F}}\frac{dq}{|\varepsilon^{\mathrm{RPA}}(q)|^2\,q}\log\left(1+\frac{\hbar^2(q^2-2k_\mathrm{F}q)}{2m_0\,\Omega_0}\right)\right.$$
$$\left. + \int_{2k_\mathrm{F}}^{\infty}\frac{dq}{|\varepsilon^{\mathrm{RPA}}(q)|^2\,q}\log\frac{1+\frac{\hbar^2(q^2+2k_\mathrm{F}q)}{2m_0\,\Omega_0}}{1+\frac{\hbar^2(q^2-2k_\mathrm{F}q)}{2m_0+\Omega_0}}\right]. \tag{4.28}$$

Figure 4.10 illustrates the effect of free-carrier screening on the real and imaginary parts of the self-energy of our model system at $E_\mathrm{F} = 80$ meV. In our model, this corresponds to a charge-carrier concentration of $n_0 = 4 \times 10^{19}$ cm^{-3}. At this doping level, we find for the screening function at the zone centre: $\left[\varepsilon^{\mathrm{RPA}}(q=0,\omega_0+i/\tau)\right] = 0.81$. As can also be seen in Fig. 4.10, the screening does vary across the Brillouin zone.

The corresponding Dyson spectral functions are shown in Figs. 4.11 (a)-(d), while the second-order cumulant spectral functions are shown in Figs. 4.11 (e)-(h). Firstly, observe the difference in effective mass between the screened and unscreened Dyson spectra, Figs. 4.11 (a) and (c). In fact, we find that at even higher screening $m^* \approx m_0$.

Secondly, note that the Fermi surface in the unscreened second-order cumulant spectrum in Fig. 4.11 (e) is breaking down due to (unphysically) strong renormalisation effects at the given α and E_F; cf. also the value of E_0 in Fig. 4.7(b) at $\alpha = 1.3$ and $E_\mathrm{F}/\hbar\omega_0 = 0.8$. As free-carrier screening at this doping level is already important, the situation in a real system should hence be better described by the spectrum in Fig. 4.11 (g).

4.3.1 Quasiparticle properties

For the closed-form expression for the screened quasiparticle energy and effective mass we refer to Appendix G. We evaluated these integrals over the same range of α and E_F as in Figs. 4.7 and 4.8, and present them in Figs. 4.12 and 4.13.

Most importantly, we find that the regions showing unphysical values for E_0 and m^* are reduced. The renormalisation is generally weaker, and, most importantly, for $E_\mathrm{F}/\hbar\omega_0 > 1.5$, the renormalised quantities return to values close to the non-interacting system. This suggests that first-principles polaron calculations with the cumulant expansion may indeed be possible for many weakly-coupled semiconductors, provided electronic screening effects are taken into account.

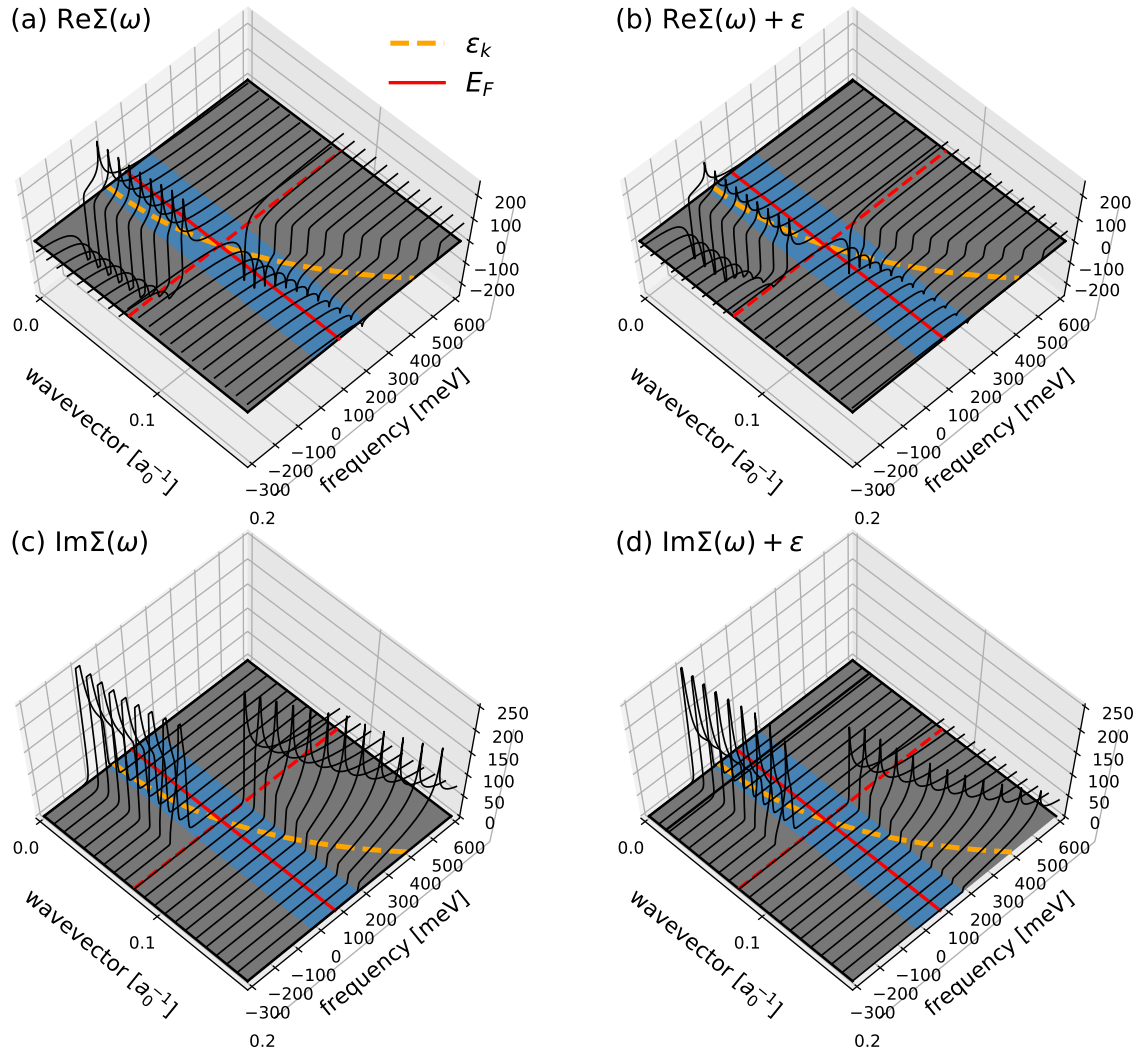


Figure 4.10: Self-energy for the Fröhlich model using the parameters provided in Table 3.2 at a Fermi energy of E_F=80 meV without free-carrier screening [$\Sigma(\omega)$] and with free carrier screening effects [$\Sigma(\omega) + \varepsilon$], respectively. (a) Real part of the lesser and greater self-energies without free-carrier screening (black lines) relative to the dispersion of the non-interacting particle (dashed orange line). The solid red line indicates the Fermi energy. The blue area indicates the energy range $[E_\mathrm{F} - \hbar\omega_0, E_\mathrm{F} + \hbar\omega_0]$. (b) Real part of the lesser and greater self-energies including free-carrier screening. (c) Imaginary part of the self-energy without free-carrier screening. (d) Imaginary part of the self-energy including free-carrier screening

Nonetheless, there remain large parts of the phase space in Figs 4.12 and 4.13 for which our current methods fail to produce physically accurate results. We argue therefore that more sophisticated many-body methods must be developed.

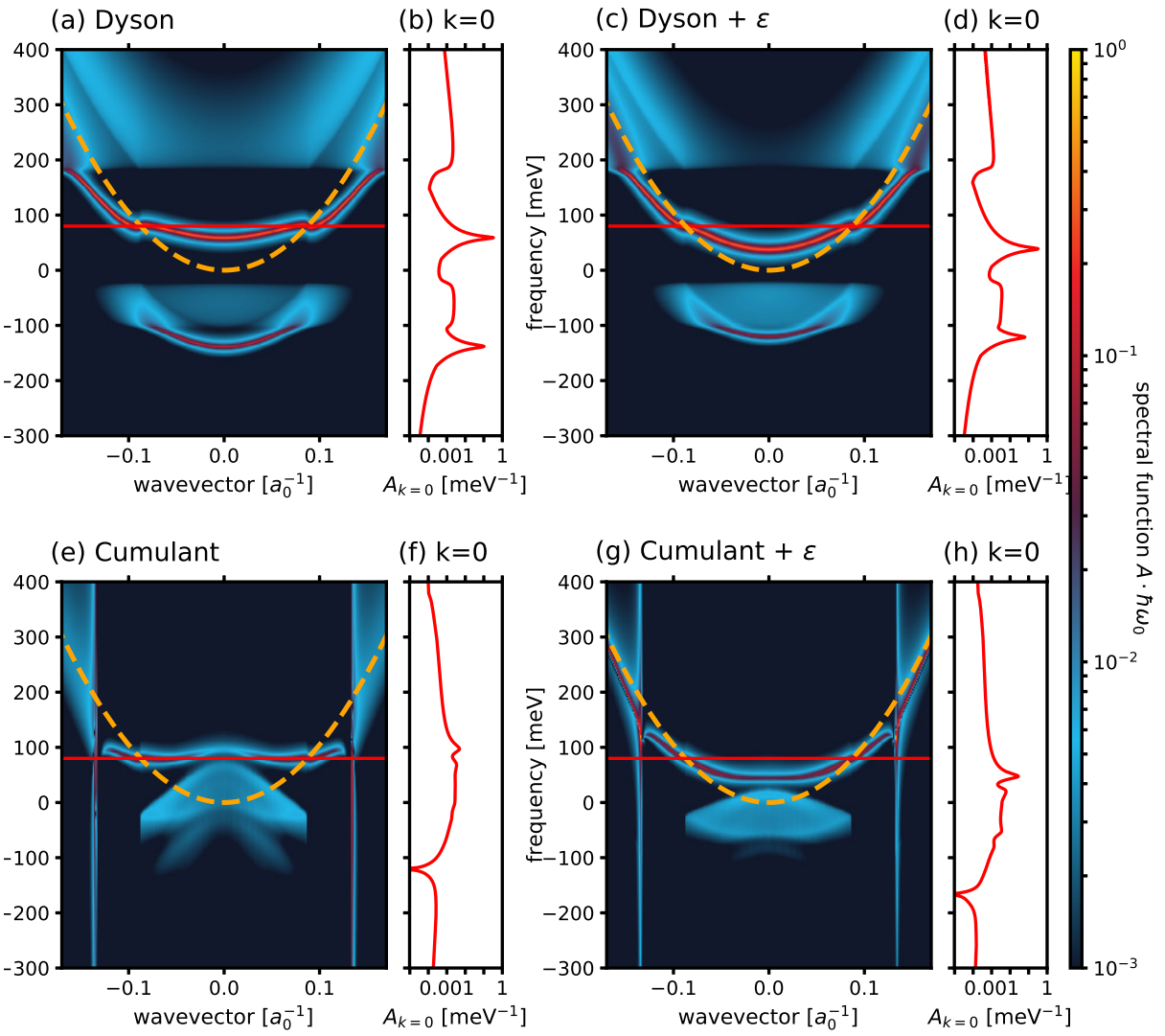


Figure 4.11: (a) Unscreened Dyson spectral function for the Fröhlich model using the parameters in Table 3.2 at a Fermi energy of E_F 80 meV. The non-interacting electron energy is indicated by the dashed gray line, the Fermi level by the solid red line. (b) Unscreened Dyson spectral function. (c) Logarithmic line plot of the Dyson spectral weight function at $k = 0$. (d) Logarithmic line plot of the Dyson spectral function at $k = 0$. (e) Screened cumulant spectral function. (f) Screened cumulant spectral function. (g) Logarithmic line plot of the screened cumulant spectral function (h) Logarithmic line plot of the screened cumulant spectral function.

4.3.2 Satellite properties

Turning to the satellites in Figs. 4.11 (a) and (c), we observe that the energy difference between QP and satellite in the screened system is reduced by approximately 50%. This result uncovers a pathological dependence of the satellite energy on the coupling strength in Dyson's approach: Unless the formation of a phonon-plasmon polariton is

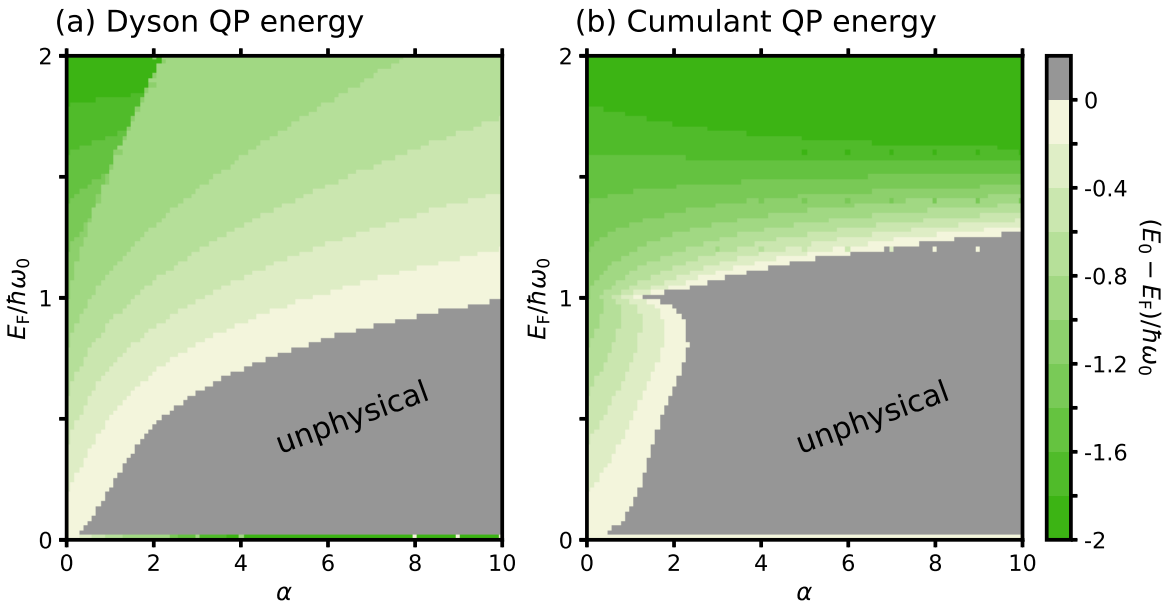


Figure 4.12: (a) Renormalised Dyson quasi-particle energy $E_0/\hbar\omega_0$ relative to the Fermi level, including screening by free carriers. Negative QP energies (shown in green) indicate a higher binding energy of the interacting system, whereas positive energies (in red) imply that the renormalised QP energy lies above the Fermi level, and indicate a breakdown of the Fermi surface. (b) Renormalised second-order cumulant quasi-particle energy relative to the Fermi surface.

involved [cf. Ref. [9] and Appendix C], the energy of the phonon should remain the same with or without screening. By contrast, the energy difference between the quasiparticle peak and the lower edge of the first satellites in the cumulant spectrum is the same in Figs. 4.11 (e) and (g), and it is equal to ω_0.

At this rather high Fermi energy, $E_F = 80$ meV, we find substantial spectral weight extending from the quasiparticle to lower energies. In fact, this situation agrees well with raw ARPES data reported at higher doping levels in Ref. [6].

4.4 Experimental quasiparticle weight

Returning once more to the experimental ARPES data in Figs. 1.1, we now take a look at Z_k, the measured quasiparticle weight. The lowest doping level considered in Ref. [6], $n_{2D} = 2.9 \times 10^{13}\text{cm}^{-2}$, corresponds to a Fermi wavevector of k_F=$0.041a_0^{-1}$, and using again our model band mass of m_0=1.3, a Fermi energy of $E_F = 23$meV. The phonon energy is given as $\hbar\omega_0$ =100 meV, and they estimate the Fröhlich coupling strength to be approximately $\alpha \approx 2 - 3$. Applying a Franck-Condon model to their energy-momentum

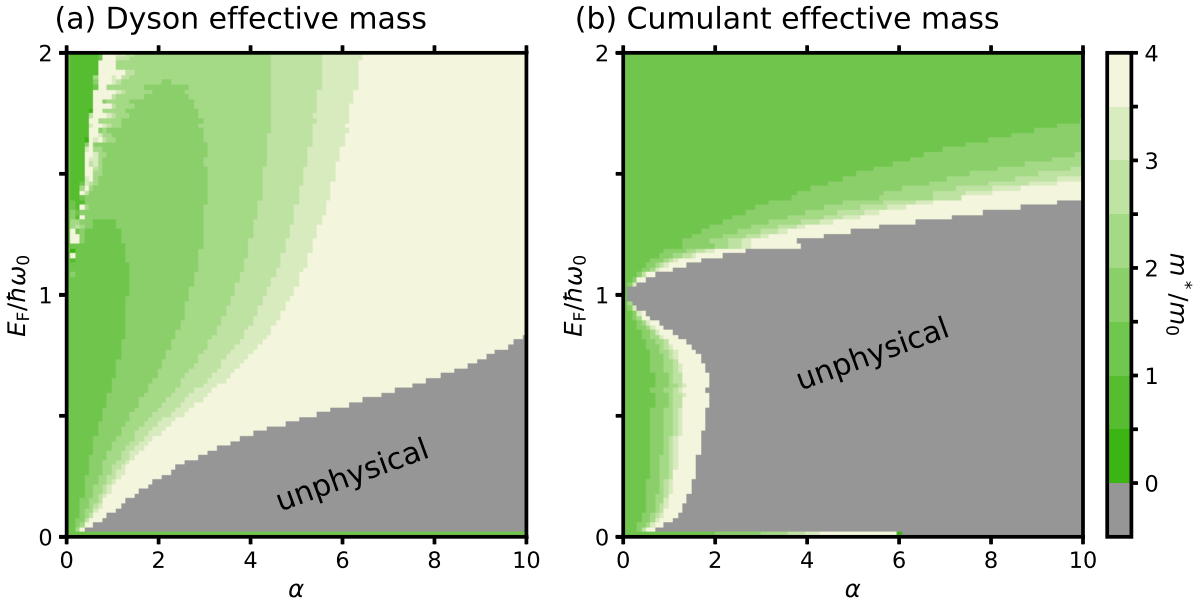


Figure 4.13: (c) Renormalised Dyson effective mass at the Γ point. Positive values of m^* (shown in green) indicates the renormalisation of the QP mass; negative values of m^* (shown in gray) indicate that the curvature of the QP spectrum at $k = 0$ has become negative, and signal a breakdown of the second-order expansion of the self-energy. (d) Renormalised second-order cumulant effective mass.

intensity map, they extract the value $Z \approx 0.2$ for the quasiparticle weight.

Equations (2.65) and (2.98) give the expressions for the Dyson and cumulant quasiparticle weights, respectively. To be able to evaluate them analytically, we have derived expressions for the frequency derivative of the self-energy for finite Fermi energy. For the Dyson equation approach, we need the derivative of the full retarded self-energy:[59]

$$\begin{aligned}\frac{1}{\hbar}\frac{\partial\Sigma_{k=0}(\omega)}{\partial\omega} &= -\frac{\alpha\,(\hbar\omega_0)^{3/2}}{2\pi\,(\hbar\omega+\Omega_0^*)^{3/2}}\left(\log\frac{\sqrt{\hbar\omega+\Omega_0^*}+\sqrt{E_\mathrm{F}}}{\sqrt{\hbar\omega+\Omega_0^*}-\sqrt{E_\mathrm{F}}}+\frac{2\sqrt{E_\mathrm{F}\,(\hbar\omega+\Omega_0^*)}}{\hbar\omega+\Omega_0-E_\mathrm{F}}\right)\\ &+ \frac{\alpha\,(\hbar\omega_0)^{3/2}}{2\pi\,(\hbar\omega-\Omega_0)^{3/2}}\left(\log\frac{\sqrt{\hbar\omega-\Omega_0}+\sqrt{E_\mathrm{F}}}{\sqrt{\hbar\omega-\Omega_0}-\sqrt{E_\mathrm{F}}}+\frac{2\sqrt{E_\mathrm{F}\,(\hbar\omega-\Omega_0)}}{\hbar\omega-\Omega_0-E_\mathrm{F}}+i\pi\right).\end{aligned}$$

We evaluate Eq. (4.29) at $k = 0$ and $E_{k=0} = \epsilon_{k=0} + Z_{k=0}\mathrm{Re}\Sigma_{k=0}(\epsilon_{k=0})$ [cf. Eq. (2.64)].

Within the cumulant expansion formalism, we find for the derivative:

$$\frac{1}{\hbar}\frac{\partial\Sigma^<_{k=0}(\omega=0)}{\partial\omega} = -\frac{\alpha}{2\pi}\left(\log\frac{\sqrt{\Omega_0}+\sqrt{E_\mathrm{F}}}{\sqrt{\Omega_0}-\sqrt{E_\mathrm{F}}}+\frac{2\sqrt{E_\mathrm{F}\,\Omega_0}}{\Omega_0-E_\mathrm{F}}\right). \tag{4.29}$$

We insert Eqs. (4.29) and (4.29) into Eqs. (2.65) and (2.98), and evaluate the quasi-

Table 4.1: Comparison of calculated and experimental quasi-particle weights

	Experiment [6]	Dyson	Cumulant
QP weight $Z_{k=0}$	0.2	0.38	0.31

particle weight using the parameters

$$\alpha = 3, \quad \hbar\omega_0 = 102.9\text{meV} \quad m_0 = 1.3\text{m}_e \quad E_\text{F} = 23\text{meV}.$$

The resulting quasi-particle weight is reported in table 4.1. We find that the calculated Dyson and cumulant QP weights over-estimate the measured weight by a factor of 2 and 1.5, respectively. For case of the cumulant expansion, this inconsistency between theoretical and experimental spectra has been discussed the literature, see e.g. Ref. [73]. In this study, the authors are able to show how additional satellite intensity arises from inelastic scattering of the outgoing photoelectron in experiment.

5

Phonon-mediated superconductivity in doped oxides

In this chapter, we investigate the superconducting pairing potential in doped polar semiconductors with Fröhlich-type electron-phonon coupling. Our analytical perspective allows us to gain insight into the subtle interplay between attractive electron-phonon coupling and the repulsive Coulomb interaction.

In almost all *ab initio* implementations of the theory of superconductivity, ranging from the semiempirical McMillan equation [Sec. 2.2.5] to anisotropic ME theory restricted to the Fermi surface [Sec. 2.2.4], the solution of the ME equations is restricted to states *on the Fermi surface*. By only considering interactions between electrons with energy $\epsilon_{n\mathbf{k}} = E_\mathrm{F}$, one achieves a substantial reduction of the computational cost, making numerical calculations feasible.

The restriction of the ME equations to the Fermi surface is a very good approximation for systems in which electron-phonon interactions are mostly short-ranged, e.g. in metallic systems with high Fermi levels. In polar semiconductors, on the other hand, electron-phonon interactions are dominated by the long-range Fröhlich interaction. This is incompatible with most widely used approximations to ME theory, and forces us to extend the momentum integration in our equations to the entire Brillouin zone. The

adaptation of the full ME equations to accurately treat Fröhlich-type electron-phonon coupling is presented in this chapter.

In section 2.2, we started from the most general formulation of ME theory, and then progressively added assumptions about the described system, which led to further and further simplified expressions. In this chapter, we will work our way in the opposite direction: In Sec. 5.1, we prove that Fröhlich-type electron-phonon coupling causes the appearance of an essential singularity in the McMillan equation. Moreover, the same singularity also appears in the Fermi-surface restricted ME equations, as we show in Sec. 5.2.

In Sec. 5.3 we then propose a theoretically rigorous solution to this problem: The full set of linearised ME equations allow us to solve the superconducting gap equation for the isotropic Fröhlich model in a numerically efficient and accurate way. An important detail of this approach is the treatment of free-carrier screening of the long-range electron-phonon and electron-electron interactions, which we discuss in Sec. 5.3.1.

The subsequent chapters are dedicated to the application of the linearised ME equations to calculating the superconducting critical temperature of doped STO. Chapter 6 discusses all the detail of our numerical implementation, and chapter 7 discusses the results and avenues for further improvements of the model.

5.1 McMillan equation

We derive an analytical expression for the superconducting critical temperature using the McMillan formula from Sec. 2.2.5 for the case of a system with Fröhlich interactions:

$$k_{\mathrm{B}}T_{\mathrm{C}} = \frac{\hbar\omega_{\log}}{1.2}\exp\left(-\frac{1.04\ (1+\lambda)}{\lambda-\mu^*\ (1+0.62\lambda)}\right). \tag{2.164}$$

The scalar λ in the case of Fröhlich coupling is given as:

$$\begin{aligned}\lambda &= \frac{2}{N_{\mathrm{F}}}\int\frac{d\mathbf{k}\,d\mathbf{k}'}{\Omega_{\mathrm{BZ}}^2}\frac{|g(\mathbf{k},\mathbf{k}')|^2}{\hbar\omega_0}\delta\left(\epsilon_{\mathbf{k}}-E_{\mathrm{F}}\right)\delta\left(\epsilon_{\mathbf{k}'}-E_{\mathrm{F}}\right)\\ &= \frac{\alpha\,\hbar}{\pi^2 N_{\mathrm{F}}\,\Omega_{\mathrm{BZ}}}\sqrt{\frac{\hbar\omega_0}{2m_0}}\int\frac{d\mathbf{k}\,d\mathbf{k}'}{|\mathbf{k}-\mathbf{k}'|^2}\,\delta\left(\epsilon_{\mathbf{k}}-E_{\mathrm{F}}\right)\delta\left(\epsilon_{\mathbf{k}'}-E_{\mathrm{F}}\right)\end{aligned} \tag{5.1}$$

After conversion to spherical coordinates, the integrals over $\mathbf{k}$ and $\mathbf{k}'$ become:

$$\begin{aligned}
&\int \frac{d\mathbf{k}\, d\mathbf{k}'}{|\mathbf{k}-\mathbf{k}'|^2}\, \delta\left(\epsilon_{\mathbf{k}} - E_{\mathrm{F}}\right) \delta\left(\epsilon_{\mathbf{k}'} - E_{\mathrm{F}}\right) \qquad (5.2)\\
&= 8\pi^2 \int_0^\infty dk\, k^2 \int_0^\infty dk'\, k'^2 \left(\frac{2m_0}{\hbar^2} \delta(k - k_{\mathrm{F}}) \delta(k' - k_{\mathrm{F}}) \right)\\
&\times \int_0^\pi d\theta \frac{\sin\theta}{k^2 + k'^2 - 2kk'\cos\theta}
\end{aligned}$$

where θ is the angle between $\mathbf{k}$ and $\mathbf{k}'$. We evaluate the Dirac deltas, and find:

$$\int \frac{d\mathbf{k}\, d\mathbf{k}'}{|\mathbf{k}-\mathbf{k}'|^2}\, \delta\left(\epsilon_{\mathbf{k}} - E_{\mathrm{F}}\right) \delta\left(\epsilon_{\mathbf{k}'} - E_{\mathrm{F}}\right) = \frac{4\pi^2 k_{\mathrm{F}}\, 2m_0}{\hbar^2} \int_0^\pi d\theta \frac{\sin\theta}{1-\cos\theta}. \qquad (5.3)$$

The integral in equation (5.3) does not converge on $(0, \pi)$, as the primitive,

$$\int d\theta \frac{\sin\theta}{1-\cos\theta} = 2\log\cos\frac{\theta}{2} + 2\log\sin\frac{\theta}{2}, \qquad (5.4)$$

has a logarithmic singularity at $\theta = \pi$.

We can understand this problem by looking at its geometry in reciprocal space. The McMillan equation (2.164) was derived for nonpolar metallic systems in which the strength of electron-phonon coupling is approximately a constant at the Fermi surface, and negligible everywhere else. In this case, an average over the surface defined by $\delta\left(\epsilon_{\mathbf{k}} - E_{\mathrm{F}}\right) \delta\left(\epsilon_{\mathbf{k}'} - E_{\mathrm{F}}\right)$ is well defined.

Long-range Fröhlich coupling, on the other hand, is peaked in the small-q limit. While it is possible to integrate over the q^{-2} potential in a three-dimensional Brillouin zone, as we have seen in chapter 4, the restriction of the potential to a two-dimensional surface, as in Eq. (5.3), leads to the appearance of this singularity.

This is an important result in the context of *ab initio* calculations: Numerical implementations of Eq. (2.164) generally represent Dirac deltas by a sharply peaked Gaussian or Lorentz function with small - but finite - broadening:

$$\delta(x - x_0) \approx \frac{1}{\sqrt{\pi}\,\sigma} \exp\left(-\frac{(x-x_0)^2}{\sigma} \right). \qquad (5.5)$$

In the case of polar semiconductors, a naive numerical evaluation of T_{C} will wrongly yield a finite result. This spurious solution crucially depends on the chosen value for the electronic broadening, σ, and has no physical significance, since in the limit of vanishing σ the temperature diverges.

McMillan equation and free-carrier screening

Before we move on, we briefly consider the intermediate scenario between semiconductors and metals, namely that of a (heavily) doped semiconductor. We modify the electron-phonon coupling matrix element according to Eq. (3.21), and consider the truncated second-order expansion of the screened coupling matrix near the divergence at $|\mathbf{k}-\mathbf{k}'| \to 0$ using the result from Eq. (3.15):

$$\begin{aligned}\lambda &= \frac{2}{N_\mathrm{F}} \int \frac{d\mathbf{k}\, d\mathbf{k}'}{\Omega_\mathrm{BZ}^2} \frac{|g(\mathbf{k},\mathbf{k}')|^2}{|\varepsilon^\mathrm{RPA}(|\mathbf{k}-\mathbf{k}'|,\omega_0)|^2} \frac{1}{\hbar\omega_0} \delta\left(\epsilon_\mathbf{k} - E_\mathrm{F}\right) \delta\left(\epsilon_{\mathbf{k}'} - E_\mathrm{F}\right) \\ &\approx \frac{\alpha\,\hbar}{\pi^2\, N_\mathrm{F}\, \Omega_\mathrm{BZ}} \sqrt{\frac{\hbar\omega_0}{2m_0}} \int \frac{d\mathbf{k}\, d\mathbf{k}'}{|\mathbf{k}-\mathbf{k}'|^2} \delta\left(\epsilon_\mathbf{k} - E_\mathrm{F}\right) \delta\left(\epsilon_{\mathbf{k}'} - E_\mathrm{F}\right) \\ &\times \left(\frac{(\omega_0 + i/\tau)^4}{\left((\omega_0 + i/\tau)^2 - \omega_\mathrm{pl}^2\right)^2} - \frac{6}{5} \frac{(\omega_0 + i/\tau)^2\, \omega_\mathrm{pl}^2}{((\omega_0 + i/\tau)^2 - \omega_\mathrm{pl}^2)^3} \left(v_\mathrm{F}\, q\right)^2 \right) \end{aligned} \tag{5.6}$$

As before, we evaluate the Lindhard function at $\omega = \omega_0 + i/\tau$, where $\tau > 0$ is the finite lifetime of the interacting electron-phonon state, ω_pl is the plasma frequency of the uniform electron gas, and v_F is the Fermi velocity.

We find that in the evaluation of Eq. (5.6), the constant term in the expansion of ε^RPA still gives rise to a logarithmic singularity at $|\mathbf{k}-\mathbf{k}'| = 0$, albeit with an additional prefactor of

$$\varepsilon^\mathrm{RPA}(|\mathbf{k}-\mathbf{k}'| = 0, \omega_0 + i/\tau) = \frac{(\omega_0 + i/\tau)^4}{\left((\omega_0 + i/\tau)^2 - \omega_\mathrm{pl}^2\right)^2}. \tag{5.7}$$

The screening prefactor is non-zero even for heavily doped semiconductors, and would only vanish in the adiabatic limit, i.e. when $\omega_0/\omega_\mathrm{pl} \to 0$. This limit describes the situation in a standard metal, in which electron-phonon interactions can no longer be described within the Fröhlich model. We therefore conclude that screening by free charges alone fails to remedy the McMillan equation for Fröhlich-type semiconductors.

5.2 Fermi-surface restricted Migdal-Eliashberg

Next, we apply the Fermi-surface restricted ME equations introduced in Sec. 2.2.4 to the doped Fröhlich solid. The most advanced first-principles calculations of superconducting T_C are generally performed at this level of theory.

Adapting Eqs. (2.156) and (2.157) for the Fröhlich solid, we find:

$$Z_{\mathbf{k}}(i\omega_j) = 1 + \frac{\pi\, k_{\mathrm{B}}T}{\hbar\omega_j\, N_{\mathrm{F}}} \sum_{\mathbf{k}'\omega'_j} \delta\left(\epsilon_{\mathbf{k}'} - E_{\mathrm{F}}\right) \frac{\hbar\omega'_j\, \lambda_{\mathbf{k}\mathbf{k}'}(i\omega_j - i\omega'_j)}{\sqrt{\hbar^2\omega_j'^2 + \Delta^2_{\mathbf{k}'}(i\omega'_j)}} \tag{5.8}$$

$$Z_{\mathbf{k}}(i\omega_j)\Delta_{\mathbf{k}}(i\omega_j) = \frac{\pi\, k_{\mathrm{B}}T}{N_{\mathrm{F}}} \sum_{\mathbf{k}'\omega'_j} \delta\left(\epsilon_{\mathbf{k}'} - E_{\mathrm{F}}\right) \frac{\lambda_{\mathbf{k}\mathbf{k}'}(i\omega_j - i\omega'_j) - N_{\mathrm{F}}\, V_{\mathbf{k}\mathbf{k}'}}{\sqrt{\hbar^2\omega_j'^2 + \Delta^2_{\mathbf{k}'}(i\omega'_j)}} \Delta_{\mathbf{k}'}(i\omega'_j), \tag{5.9}$$

where the mass renormalisation function $Z_{\mathbf{k}}(i\omega_j)$ and the gap function $\Delta_{\mathbf{k}}(i\omega_j)$ are only defined for a single parabolic band. As before, Eqs. (5.8) and (5.9) are only valid at the Fermi surface, i.e. for $\epsilon_{\mathbf{k}} = \epsilon_{\mathbf{k}'} = E_{\mathrm{F}}$.

The momentum-resolved coupling function for the Fröhlich model is given by

$$\begin{aligned} \lambda_{\mathbf{k}\mathbf{k}'}(i\omega_j - i\omega'_j) &= \frac{2N_{\mathrm{F}}}{\hbar} |g(\mathbf{k},\mathbf{k}')|^2 \frac{\omega_0}{(\omega_j - \omega'_j)^2 + \omega_0^2} \\ &= \frac{2N_{\mathrm{F}}}{\hbar} \frac{4\pi\,\alpha\,\hbar(\hbar\omega_0)^{3/2}}{\sqrt{2m_0}\,\Omega} \frac{\omega_0}{(\omega_j - \omega'_j)^2 + \omega_0^2} \frac{1}{|\mathbf{k} - \mathbf{k}'|^2}. \end{aligned} \tag{5.10}$$

The statically screened Coulomb matrix was already introduced in Eq. (3.11):

$$V_{\mathbf{k}\mathbf{k}'} = \frac{e^2}{\epsilon_0\, \varepsilon_\infty\, \Omega} \frac{1}{|\mathbf{k} - \mathbf{k}'|^2}, \tag{3.11}$$

As the system is fully isotropic, we can transform the momentum integration to spherical coordinates, and integrate out the angle dependence. We have $Z_{\mathbf{k}} = Z_{k_{\mathrm{F}}}$ and $\Delta_{\mathbf{k}} = \Delta_{k_{\mathrm{F}}}$, and:

$$\begin{aligned} Z_{k_{\mathrm{F}}}(i\omega_j) &= 1 + \frac{\pi^2\, k_{\mathrm{B}}T}{\hbar\omega_j\, N_{\mathrm{F}}\, \Omega_{\mathrm{BZ}}} \frac{m_0}{\hbar^2 k_{\mathrm{F}}} \\ &\times \sum_{\omega'_j} \lambda^{\mathrm{F}}(\omega_j - \omega'_j) \frac{\hbar\omega'_j}{\sqrt{\hbar^2\omega_j'^2 + \Delta^2_{k_{\mathrm{F}}}(i\omega'_j)}} \int_0^\pi d\theta \frac{\sin\theta}{1 - \cos\theta} \end{aligned} \tag{5.11}$$

$$\begin{aligned} Z_{k_{\mathrm{F}}}(i\omega_j)\Delta_{k_{\mathrm{F}}}(i\omega_j) &= \frac{\pi^2\, k_{\mathrm{B}}T}{N_{\mathrm{F}}\, \Omega_{\mathrm{BZ}}} \frac{m_0}{\hbar^2 k_{\mathrm{F}}} \\ &\times \sum_{\omega'_j} \frac{\Delta_{k_{\mathrm{F}}}(i\omega'_j)}{\sqrt{\hbar^2\omega_j'^2 + \Delta^2_{k_{\mathrm{F}}}(i\omega'_j)}} \left[\lambda^{\mathrm{F}}(\omega_j - \omega'_j) - N_{\mathrm{F}} V^0\right] \int_0^\pi d\theta \frac{\sin\theta}{1 - \cos\theta}, \end{aligned} \tag{5.12}$$

Again, we encounter the divergent integral

$$\int_0^\pi d\theta \frac{\sin\theta}{1 - \cos\theta}. \tag{5.13}$$

As in Sec. 5.1, we observe that the q^{-2} divergence of the coupling matrix element does not allow an integration over the Fermi surface alone. This approximation of the ME

equations - despite yielding dependable results for metallic systems - does not admit a finite solution for the case of polar semiconductors.

We stress that this is an important result for first-principles calculations within anisotropic Migdal-Eliashberg theory: numerical results for strongly polar systems with a divergent coupling matrix element g at the Γ point cannot be trusted, as the numerical result of an integral similar to Eq. (5.13) will only depend on the finite electronic broadening used in the calculation.

5.3 Linearised Migdal-Eliashberg

As our attempts to solve the ME equations with Fröhlich coupling on the Fermi surface have not been successful, we now move to include coupling between states away from k_F. In our model system, we hence extend the momentum integration over all $k \in [0, \infty)$. In numerical calculations, we find that most contribution to electron-phonon coupling are from states $k \in [0, 2k_\mathrm{F}]$, as we will discuss in Ch. 6.

We adapt the linearised ME equations which we introduced in Sec. 2.2.2 for the doped Fröhlich model. After a transformation to spherical coordinates via [see also Appendix H]:

$$\sum_{\mathbf{k}'} \to \int_{\mathbb{R}^3} \frac{d\mathbf{k}'}{\Omega_\mathrm{BZ}} \to \int_0^{2\pi} d\phi \int_0^{\pi} d\theta \sin\theta \int_0^{\infty} \frac{dk'\, k'^2}{\Omega_\mathrm{BZ}} \to \sum_{k'} \frac{4\pi\, \Delta k' k'^2}{\Omega_\mathrm{BZ}}, \tag{5.14}$$

we can write down the electron-phonon coupling function and Coulomb interaction for the isotropic Fröhlich model [cf. Eqs. (5.10) and (3.11)]:

$$\lambda_{kk'}(i\omega_j - i\omega'_j) = \frac{2N_\mathrm{F}}{\hbar} \frac{4\pi\, \alpha\, \hbar(\hbar\omega_0)^{3/2}}{\sqrt{2m_0}\, \Omega_\mathrm{UC}} \frac{\omega_0}{(\omega_j - \omega'_j)^2 + \omega_0^2} \frac{1}{4kk'} \log \frac{(k+k')^2}{(k-k')^2}, \tag{5.15}$$

$$V_{kk'} = \frac{e^2}{\epsilon_0\, \varepsilon_\infty\, \Omega_\mathrm{UC}} \frac{1}{4kk'} \log \frac{(k+k')^2}{(k-k')^2}. \tag{5.16}$$

Note that for each pair of k and k', Eqs. (5.15) and (5.16) are proportional. Unlike Eq. (5.13), the momentum integrals over $\lambda_{kk'}$ and $V_{kk'}$ converge, and our linearised

isotropic Migdal-Eliashberg equations are well defined:

$$Z_k(i\omega_j) = 1 + \frac{k_\mathrm{B}T}{\hbar\omega_j\, N_\mathrm{F}} \sum_{k'\omega'_j} w_{k'} \frac{\lambda_{kk'}(i\omega_j - i\omega'_j)\, \hbar\omega'_j\, Z_{k'}(i\omega'_j)}{\left[\hbar\omega'_j\, Z_{k'}(i\omega'_j)\right]^2 + \left[\epsilon_{k'} - \mu_\mathrm{C} + \chi_{k'}(i\omega'_j)\right]^2} \tag{5.17}$$

$$\chi_k(i\omega_j) = -\frac{k_\mathrm{B}T}{N_\mathrm{F}} \sum_{k'\omega'_j} w_{k'} \frac{\lambda_{kk'}(i\omega_j - i\omega'_j)\, \left[\epsilon_{k'} - \mu_\mathrm{C} + \chi_{k'}(i\omega'_j)\right]}{\left[\hbar\omega'_j\, Z_{k'}(i\omega'_j)\right]^2 + \left[\epsilon_{k'} - \mu_\mathrm{C} + \chi_{k'}(i\omega'_j)\right]^2} \tag{5.18}$$

$$n_e = 1 - 2k_\mathrm{B}T \sum_{k'\omega'_j} w_{k'} \frac{\epsilon_{k'} - \mu_\mathrm{C} + \chi_{k'}(i\omega'_j)}{\left[\hbar\omega'_j\, Z_{k'}(i\omega'_j)\right]^2 + \left[\epsilon_{k'} - \mu_\mathrm{C} + \chi_{k'}(i\omega'_j)\right]^2}. \tag{5.19}$$

We express the order parameter in terms of the kernel matrix:

$$K_{kk'}(i\omega_j - i\omega'_j; T) = \frac{k_\mathrm{B}T}{N_\mathrm{F}}\, w_{k'} \frac{\lambda_{kk'}(i\omega_j - i\omega'_j) - N_\mathrm{F}V_{kk'}}{\left[\hbar\omega'_j\, Z_{k'}(i\omega'_j)\right]^2 + \left[\epsilon_{k'} - \mu_\mathrm{C} + \chi_{k'}(i\omega'_j)\right]^2} \tag{5.20}$$

$$\phi_k(i\omega_j) = \sum_{k'\omega'_j} K_{kk'}(i\omega_j - i\omega'_j; T)\, \phi_{k'}(i\omega'_j). \tag{5.21}$$

In Eqs. (5.17)-(5.21), the weight of a single k point along the one-dimensional momentum axis is given by:

$$w_{k'} = \frac{4\pi\, \Delta k'\, k'^2}{\Omega_\mathrm{BZ}}, \tag{5.22}$$

with $\Delta k'$ equal to the step size along the momentum axis.

At last, we have found a set of equations which admit a finite solution for long-range Fröhlich-type electron-phonon interactions. A first numerical result obtained with Eqs. (5.17)-(5.21) is shown in Fig. 5.1: we show the calculated superconducting T_C for doped STO [parameters given in Tab. 3.2] *without electron-electron interactions*, i.e. for

$$V_{kk'} \equiv 0 \qquad \text{and} \qquad \varepsilon^\mathrm{RPA} \equiv 1. \tag{5.23}$$

The many-body potential used to calculate Fig. 5.1 is purely attractive and hence neither the absolute value of the critical temperature nor the fact that T_C is finite up to extremely high doping levels are realistic. Nevertheless, this result is extremely interesting: It appears that the combination of the Fröhlich interaction and the geometry of the band bottom together give rise to a superconducting dome. This is an unexpected result and it could only be obtained by taking into account the full momentum dependence of the ME equations.

The exact origin of this dome remains unclear, but the working hypothesis is the following: The long-range Fröhlich interaction peaks for $\mathbf{q} = 0$, which means that electronic

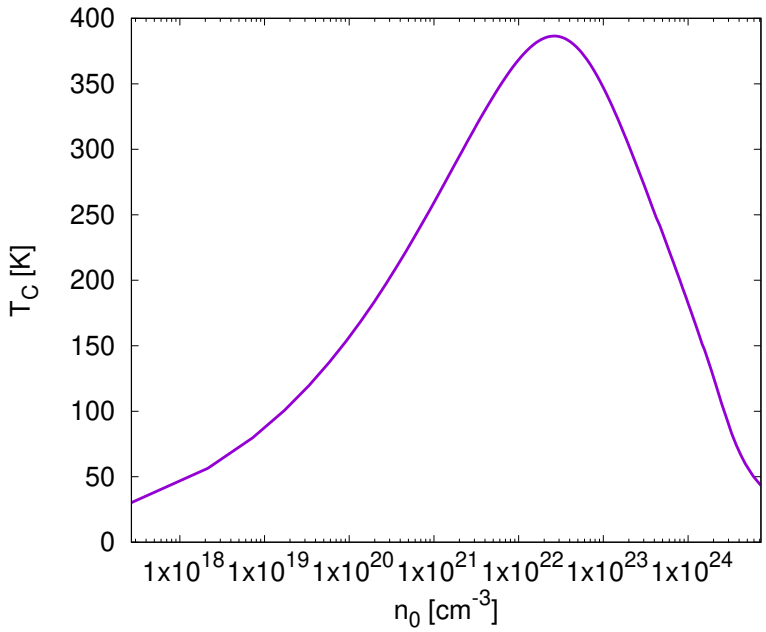


Figure 5.1: Calculated superconducting temperature of STO as a function of charge-carrier density without repulsive electron-electron interactions.

states that are close to each other in momentum space couple particularly strongly. Due to the geometry of the band, this interaction is on average strongest near the bottom of the band, before it declines at higher energies. At the same time, the total coupling strength grows linearly with the number of states at or near the Fermi surface, as in conventional BCS superconductors. Taken together, these two interactions give rise to the dome shape seen in Fig. 5.1.

5.3.1 The role of electron-electron interactions in real systems

To model real systems, an accurate treatment of electron-electron interactions is vital. In the present case, the repulsive Coulomb interaction should reduce the hypothetical T_C shown in Fig 5.1 by a factor of 10^3 to the real measured T_C of ≈ 0.4 K, cf. Fig. 1.3. In fact, this is easily achieved because the repulsive Coulomb interaction is generally stronger than the attractive Fröhlich potential.

To see this more clearly, we take a closer look at the kernel function (5.20): We know that the coupling strength α, effective mass m_0 and dielectric constant ε_∞ are connected via Eq. (1.2). In particular, this implies an intimate relationship between $\lambda_{kk'}$ and $V_{kk'}$ given in Eqs. (5.15) and (5.16).

$$K \propto \left[\frac{2N_\mathrm{F}}{\hbar} \frac{4\pi\,\alpha\,\hbar(\hbar\omega_0)^{3/2}}{\sqrt{2m_0}\,\Omega_\mathrm{UC}} \frac{\omega_0}{(\omega_j-\omega_j')^2+\omega_0^2} - \frac{N_\mathrm{F}\,e^2}{\epsilon_0\,\varepsilon_\infty\,\Omega_\mathrm{UC}} \right] \frac{1}{4kk'} \log\frac{(k+k')^2}{(k-k')^2}. \tag{5.24}$$

The attractive force is strongest at $\omega_j = \omega_j'$, cf. Eq. (5.15). In this case, we can simplify further by focusing on the two terms in brackets:

$$K \propto \frac{N_\mathrm{F}\,e^2}{\Omega_\mathrm{UC}} \frac{1}{\epsilon_0} \left(\frac{1}{\varepsilon_\infty} - \frac{1}{\varepsilon_0} \right) - \frac{N_\mathrm{F}\,e^2}{\Omega_\mathrm{UC}\,\epsilon_0\,\varepsilon_\infty} < 0. \tag{5.25}$$

It follows that the kernel function is negative definite for $\omega_j = \omega_j'$, and hence for all frequencies and momenta. With negative eigenvalues at all temperatures, $T_\mathrm{C} \equiv 0$.

The Coulomb interaction suppresses the critical temperature by more than we hoped for. How, then, can a polar semiconductor become superconducting at all? The answer lies in the screening of the long-range interactions by the free carriers. As we have seen in Sec. 3.3.1, screening of the electron-phonon and electron-electron interactions becomes effective at different carrier concentrations [cf. Figs. 3.10 and 3.11]: Coulomb interactions experience screening immediately upon doping, whereas screening of the Fröhlich interaction remains very weak until the plasma frequency of the dopant electrons becomes comparable to the phonon energy. This delayed onset of the screening of the attractive electron-phonon interactions relative to the Coulomb repulsion drives the formation of a superconducting dome in our model.

We find that our numerical results are extremely sensitive with respect to the screening function used. This delicate interaction will be discussed in more detail in Chapter 7.

6 Computational setup

To study the superconducting pairing interaction in doped polar semiconductors, we have built a numerical implementation of the linearised ME equations [Eqs. (5.17) -(5.20)]. In Sec. 6.1, we relate details of our implementation. In particular, we discuss how we evaluate the renormalisation functions and the chemical potential, and we show how we approximate the dielectric screening function in our model system. Section 6.2 shows how our calculation results converge with respect to the main convergence parameters. Eventually, in Sec. 6.3, we test our implementation on the example of nonpolar hole-doped diamond. We show that our method allows us to reproduce previously obtained numerical and experimental results, confirming the validity of our approach.

6.1 Implementation

In this section, we provide details about our computational implementation of the linearised ME equations derived in Sec. 5.3.

The following steps are carried out for a set of temperatures T specified by the user. The Eqs. (5.17)-(5.20) are solved on a combined frequency and momentum mesh (ω_j, k) involving n_ω Matsubara frequencies up to an energy cutoff ω_{cut}, and n_k grid points along the momentum axis k with a cutoff k_{cut} and a step size of Δk.

Given the extreme size of the calculations, we find that the following cutoff values for the frequency and momentum integrations are reasonable: Consider the frequency term in $\lambda_{kk'}(i\omega_j - i\omega'_j)$ [Eq. (5.15)]: at $\omega_{\mathrm{cut}} \approx 2\hbar\omega_{\mathrm{ph}}$, this factor becomes as small as $(5\hbar\omega_0)^{-1}$. For the momentum integration, the term $[\epsilon_k - \mu_{\mathrm{C}}]^{-2}$ in the kernel function [Eq. (5.20)] becomes as small as E_{F}^{-2} when $k_{\mathrm{cut}} \approx 2k_{\mathrm{F}}$.

At each temperature, the biggest computational effort is spent on the diagonalisation of the kernel matrix $K_{kk'}(i\omega_j - i\omega'_j)$ [Eq. (5.20)], which has the dimension $(n_\omega \times n_k) \times (n_\omega \times n_k)$. To reduce the size of this matrix, we note that the summation over ω_j extends over the positive and negative imaginary axis. Recalling the definition of the Matsubara frequencies,

$$\hbar\omega_j = (2j+1)\pi\, k_{\mathrm{B}}T, \quad \text{we have} \quad \hbar\omega_{j=l} = -\hbar\omega_{j=-l-1} \quad \text{for } j, l \in \mathbb{Z}. \tag{6.1}$$

We find that the energy shift $\chi_k(\omega_j)$, the particle number equation n_e and the kernel $K_{kk'}(\omega_j - \omega'_j)$ are symmetric under the mirror operation $\omega_j \to -\omega_j$, and the mass renormalisation function $Z_k(i\omega_j)$ is antisymmetric under the same operation.

This symmetry allows us to reduce the number of Matsubara frequencies n_ω used in the calculation by one half, which in turn reduces the size of the kernel matrix by three quarters.

In addition, following our discussion in Sec. 5.3.1, we include full dynamical screening of the electron-phonon and Coulomb matrix elements in our calculation.

6.1.1 Initialisation

After the Matsubara frequency and momentum grids have been set up, the dynamically screened electron-phonon coupling function λ and Coulomb matrix elements are evaluated from the user-generated input of the parameters.

Dynamically screened electron-phonon coupling function

Starting with the dynamically screened λ function, we construct the angle-averaged electron-phonon coupling matrix element [cf. (3.21)]:

$$|g|^2_{kk'} = \frac{4\pi\,\alpha\,\hbar(\hbar\omega_0)^{3/2}}{\sqrt{2m_0}\,\Omega_{\mathrm{UC}}\,|\varepsilon^{\mathrm{RPA}}(q=0,\omega_0+i/\tau)|^2}\,\frac{1}{4\,kk'}\log\frac{(k+k')^2}{(k-k')^2}, \tag{6.2}$$

with the limits

$$|g|^2_{k,k'=0} = \frac{4\pi\,\alpha\,\hbar(\hbar\omega_0)^{3/2}}{\sqrt{2m_0}\,\Omega_{\rm UC}\,|\varepsilon^{\rm RPA}(q=0,\omega_0+i/\tau)|^2\,k^2}. \tag{6.3}$$

and

$$|g|^2_{k=0,k'} = \frac{4\pi\,\alpha\,\hbar(\hbar\omega_0)^{3/2}}{\sqrt{2m_0}\,\Omega_{\rm UC}\,|\varepsilon^{\rm RPA}(q=0,\omega_0+i/\tau)|^2\,k'^2}. \tag{6.4}$$

For the symmetrised and anti-symmetrised Matsubara frequency contributions to λ [cf.Eq. (5.15)], we construct the matrices:

$$m^{\rm S}_{\omega_j,\omega'_j} = \frac{2N_{\rm F}}{\hbar}\left[\frac{\omega_0}{(\omega_j-\omega'_j)^2+\omega_0^2}+\frac{\omega_0}{(\omega_j+\omega'_j)^2+\omega_0^2}\right], \tag{6.5}$$

and

$$m^{\rm A}_{\omega_j,\omega'_j} = \frac{2N_{\rm F}}{\hbar}\left[\frac{\omega_0}{(\omega_j-\omega'_j)^2+\omega_0^2}-\frac{\omega_0}{(\omega_j+\omega'_j)^2+\omega_0^2}\right]. \tag{6.6}$$

This allows us to write down the electron-phonon coupling function in both a symmetrised and anti-symmetrised (in ω_j) form:

$$\lambda^{\rm S}_{kk'}(i\omega_j - i\omega'_j) = |g|^2_{k,k'}\,m^{\rm S}_{\omega_j,\omega'_j}, \tag{6.7}$$

$$\lambda^{\rm A}_{kk'}(i\omega_j - i\omega'_j) = |g|^2_{k,k'}\,m^{\rm A}_{\omega_j,\omega'_j}. \tag{6.8}$$

Dynamically screened Coulomb interaction

We approximate the dynamically screened Coulomb matrix element $W_{kk'}(i\omega_j - i\omega'_j)$, given in Eq. (3.24), using the second-order expansion of the inverse of the Lindhard function at $q = 0$, given in Eq. (3.15). Starting from the anisotropic expression:

$$\begin{aligned} W_{\mathbf{kk'}}(i\omega_j - i\omega'_j) &= \frac{V_{\mathbf{kk'}}}{\varepsilon^{\rm RPA}(i\omega_j - i\omega'_j)} \\ &\approx \frac{e^2}{\epsilon_0\,\varepsilon_\infty\,\Omega_{\rm UC}\,|\mathbf{k}-\mathbf{k'}|}\left[\frac{(\omega_j-\omega'_j)^4}{\left((\omega_j-\omega'_j)^2+\omega_{\rm pl}^2\right)^2}\right. \\ &- \left.\frac{6}{5}\frac{(\omega_j-\omega'_j)^2\,\omega_{\rm pl}^2\,v_{\rm F}^2\,|\mathbf{k}-\mathbf{k'}|^2}{\left((\omega_j-\omega'_j)^2+\omega_{\rm pl}^2\right)^3}\right], \end{aligned} \tag{6.9}$$

we obtain the isotropic expression after averaging over the angle between $\mathbf{k}$ and $\mathbf{k}'$:

$$\begin{aligned} W_{kk'}(i\omega_j - i\omega'_j) &= \frac{e^2}{\epsilon_0\,\varepsilon_\infty\,\Omega_{\rm UC}}\frac{(\omega_j-\omega'_j)^4}{\left((\omega_j-\omega'_j)^2+\omega_{\rm pl}^2\right)^2}\frac{1}{4\,kk'}\log\frac{(k+k')^2}{(k-k')^2} \\ &- \frac{e^2}{\epsilon_0\,\varepsilon_\infty\,\Omega_{\rm UC}}\frac{6}{5}\frac{(\omega_j-\omega'_j)^2\,\omega_{\rm pl}^2\,v_{\rm F}^2}{\left((\omega_j-\omega'_j)^2+\omega_{\rm pl}^2\right)^3}, \end{aligned} \tag{6.10}$$

where the first term has the same dispersion in k as the electron-phonon coupling function λ, and the second term is a constant.

To implement Eq. (6.10) in the Matsubara-symmetrised form, we construct the matrices

$$\varepsilon^{\mathrm{S}\,(1)}_{\omega_j,\omega'_j} = \frac{(\omega_j-\omega'_j)^4}{\Big((\omega_j-\omega'_j)^2+\omega_{\mathrm{pl}}^2\Big)^2} + \frac{(\omega_j+\omega'_j)^4}{\Big((\omega_j+\omega'_j)^2+\omega_{\mathrm{pl}}^2\Big)^2}, \tag{6.11}$$

$$\varepsilon^{\mathrm{S}\,(2)}_{\omega_j,\omega'_j} = -\frac{e^2\,\omega_{\mathrm{pl}}^2\,v_{\mathrm{F}}^2}{\epsilon_0\,\varepsilon_\infty\,\Omega_{\mathrm{UC}}}\frac{6}{5}\left[\frac{(\omega_j-\omega'_j)^2}{\Big((\omega_j-\omega'_j)^2+\omega_{\mathrm{pl}}^2\Big)^3} + \frac{(\omega_j+\omega'_j)^2}{\Big((\omega_j+\omega'_j)^2+\omega_{\mathrm{pl}}^2\Big)^3}\right], \tag{6.12}$$

and

$$V_{k,k'} = \frac{e^2}{\epsilon_0\,\varepsilon_\infty\,\Omega_{\mathrm{UC}}}\frac{1}{4\,kk'}\log\frac{(k+k')^2}{(k-k')^2}, \tag{6.13}$$

with the limits

$$V_{k,k'=0} = \frac{e^2}{\epsilon_0\,\varepsilon_\infty\,\Omega_{\mathrm{UC}}\,k^2} \qquad \text{and} \qquad V_{k=0,k'} = \frac{e^2}{\epsilon_0\,\varepsilon_\infty\,\Omega_{\mathrm{UC}}\,k'^2}. \tag{6.14}$$

The screened Coulomb interaction can then be written as:

$$W^{\mathrm{S}}_{kk'}(i\omega_j - i\omega'_j) = \varepsilon^{\mathrm{S}\,(1)}_{\omega_j,\omega'_j} V_{kk'} + \varepsilon^{\mathrm{S}\,(2)}_{\omega_j,\omega'_j}. \tag{6.15}$$

6.1.2 Calculation of the renormalisation functions

The mass renormalisation function, the energy shift and the chemical potential μ_{C} are evaluated self-consistently within two nested iteration loops. The outer loop iterates over the inner loops for Z_k, χ_k and μ_{C} consecutively. Within the inner loop, the respective function is iterated over while keeping all others fixed.

The mass renormalisation function and energy shift are evaluated according to:

$$Z_k(i\omega_j) = 1 + \frac{k_{\mathrm{B}}T}{\hbar\omega_j}\sum_{k'\omega'_j\geq 0} w_{k'}\frac{\lambda^{\mathrm{A}}_{kk'}(i\omega_j - i\omega'_j)\,\hbar\omega'_j\,Z_{k'}(i\omega'_j)}{\Big[\hbar\omega'_j\,Z_{k'}(i\omega'_j)\Big]^2 + \Big[\epsilon_{k'} - \mu_{\mathrm{C}} + \chi_{k'}(i\omega'_j)\Big]^2}, \tag{6.16}$$

$$\chi_k(i\omega_j) = -k_{\mathrm{B}}T\sum_{k'\omega'_j\geq 0} w_{k'}\frac{\lambda^{\mathrm{S}}_{kk'}(i\omega_j - i\omega'_j)\,\Big[\epsilon_{k'} - \mu_{\mathrm{C}} + \chi_{k'}(i\omega'_j)\Big]}{\Big[\hbar\omega'_j\,Z_{k'}(i\omega'_j)\Big]^2 + \Big[\epsilon_{k'} - \mu_{\mathrm{C}} + \chi_{k'}(i\omega'_j)\Big]^2}, \tag{6.17}$$

using definitions (6.7) and (6.8). We start with a seed of $Z_k(i\omega_j) \equiv 1$ and $\chi_k(i\omega_j) \equiv 0$, respectively. Using convergence thresholds of

$$\sum_{\omega_j,\,k}\sqrt{|Z_k(i\omega_j)|^2} < 10^{-6} \qquad \text{and} \qquad \sum_{\omega_j,\,k}\sqrt{|\chi_k(i\omega_j)|^2} < 10^{-4}\ \text{meV}, \tag{6.18}$$

we have achieved convergence of the critical temperature to within 0.1 K.

To evaluate the chemical potential μ_{C}, we first calculate the particle number of the noninteracting system:

$$n_e^{\mathrm{NI}} = 1 - 4k_{\mathrm{B}}T \sum_{k'\omega'_j \geq 0} w_{k'} \frac{\epsilon_{k'} - E_{\mathrm{F}}}{\hbar^2\omega'^2_j + \left[\epsilon_{k'} - E_{\mathrm{F}}\right]^2}. \tag{6.19}$$

Then, we evaluate the particle number of the fully interacting system for a mesh of chemical potentials $\mu_{\mathrm{C}}^{\mathrm{test}}$ with a step size of 0.1 meV and a range of 100 meV around the noninteracting Fermi energy:

$$n_e(\mu_{\mathrm{C}}^{\mathrm{test}}) = 1 - 4k_{\mathrm{B}}T \sum_{k'\omega'_j \geq 0} w_{k'} \frac{\epsilon_{k'} - \mu_{\mathrm{C}}^{\mathrm{test}} + \chi_{k'}(i\omega'_j)}{\left[\hbar\omega'_j\, Z_{k'}(i\omega'_j)\right]^2 + \left[\epsilon_{k'} - \mu_{\mathrm{C}}^{\mathrm{test}} + \chi_{k'}(i\omega'_j)\right]^2} \tag{6.20}$$

The energy $\mu_{\mathrm{C}}^{\mathrm{test}}$ at which $n_e(\mu_{\mathrm{C}}^{\mathrm{test}}) = n_e^{\mathrm{NI}}$ gives us our new chemical potential, μ_{C}.

6.1.3 Diagonalisation of the kernel matrix

In the next step, we construct the kernel matrix according to:

$$K_{kk'}(i\omega_j - i\omega'_j; T) = k_{\mathrm{B}}T \sum_{k'\omega'_j \geq 0} w_{k'} \frac{\lambda^{\mathrm{S}}_{kk'}(i\omega_j - i\omega'_j) - W^{\mathrm{S}}_{kk'}(i\omega_j - i\omega'_j)}{\left[\hbar\omega'_j\, Z_{k'}(i\omega'_j)\right]^2 + \left[(\epsilon_{k'} - \mu_{\mathrm{C}}) + \chi_{k'}(i\omega'_j)\right]^2}. \tag{6.21}$$

Then, we use the iterative power method to extract the largest eigenvalue

$$K_{kk'}(i\omega_j - i\omega'_j; T)\, v_{\max}(T) = \kappa_{\max}(T) v_{\max}(T). \tag{6.22}$$

We find that the condition number of the matrix is not constant across the temperature range. Therefore, we monitor the numerical error of the calculated $\kappa_{\max}(T)$ via

$$\mathrm{Err} = \sqrt{|K_{kk'}(i\omega_j - i\omega'_j; T) v_{\max} - \kappa_{\max}(T) v_{\max}|^2}, \tag{6.23}$$

To ensure an uncertainty in the temperature of less than 0.1 K, we converge the eigenvalue to within $\mathrm{Err} < 10^{-6}$.

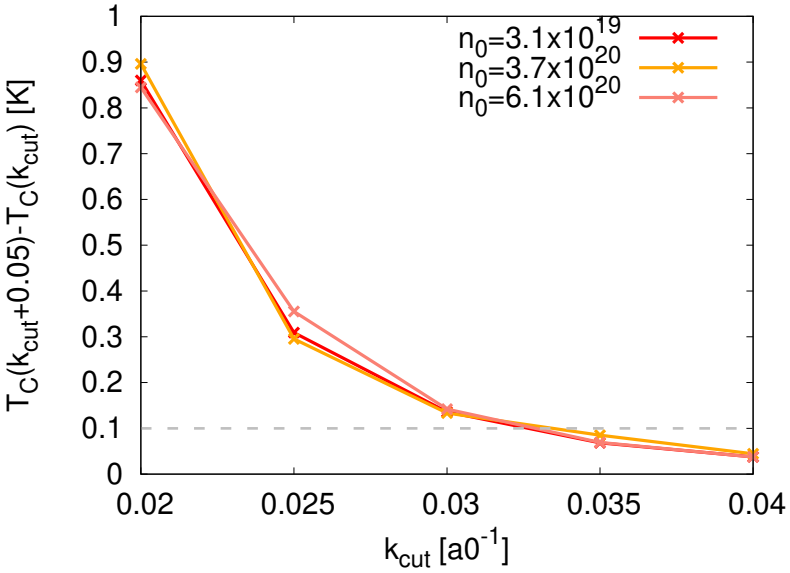


Figure 6.1: Convergence of the critical temperature with respect to the cutoff value k_{cut} for constant spacing between k points of $\Delta k = 0.0002 a_0^{-1}$

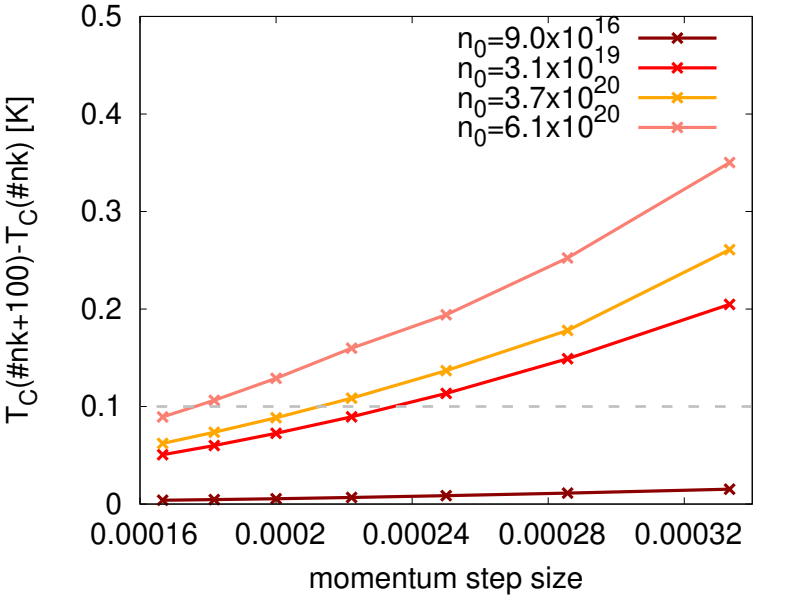


Figure 6.2: Convergence of the critical temperature with the density of the k mesh for four different doping levels. Shown is the difference between the T_{C} calculated with nk+100 k-points and T_{C} at nk k-points for nk between 1200 and 2400. In all cases, the cutoff for the momentum grid is $k_{\mathrm{cut}} = 0.4$.

6.2 Convergence of computational parameters for T_{C} calculation

In the computational setup presented in Sec. 6.1, there are three numerical parameters with respect to which calculations of the superconducting T_{C} must be converged. These are, for the point mesh in momentum space, the number of k points and their cutoff value k_{cut}, and the cutoff frequency for the summation over Matsubara frequencies, $\hbar\omega_{\mathrm{cut}}$. Converging calculations of the superconducting T_{C} with respect to the Matsubara frequency cutoff is

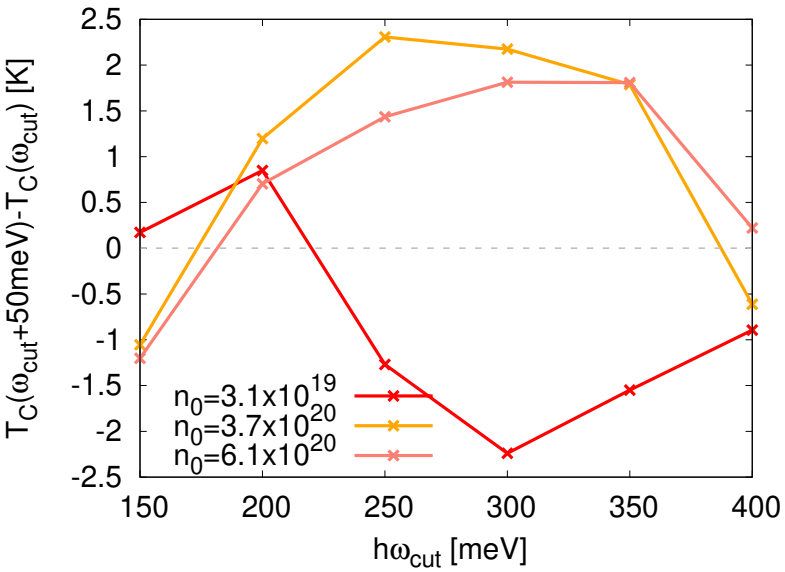


Figure 6.3: Convergence of the critical temperature with respect to the Matsubara frequency cutoff energy $\hbar\omega_{\mathrm{cut}}$.

a known challenge, especially for *ab initio* calculations. Ultimately, finite computational resources set an upper bound to realistically usable frequency cutoff values. Considering the convergence of T_{C} for the Fröhlich model as a function of $\hbar\omega_{\mathrm{cut}}$ solid as shown in Fig. 6.3, one would in principle like to use a cutoff value of 400 meV or higher, this would correspond to four times the energy of the relevant phonon mode. However, to keep the calculations tractable we decide to use a value of $\hbar\omega_{\mathrm{cut}} = 200$ meV. This cutoff value is used for all calculations, so that the results are in any case comparable among each other.

6.3 Test case: Non-polar hole-doped diamond

The isotropic full-bandwidth Migdal-Eliashberg equations are a generalisation of conventional approximations to the Migdal-Eliashberg equations which allow a microscopic description of Cooper pair formation in polar semiconductors. As such, we wish to ensure that our approach and the computational setup introduced in Sec. 6.1 correctly reproduces previously obtained results.

We consider hole-doped diamond as a simple example of a semiconducting superconductor with parabolic bands and short-range electron-phonon coupling. In this system, the approximation that most electron pairing occurs across the Fermi surface is very well justified. As a result, simple approaches like the McMillan formula, which only takes

into account electron-phonon coupling between electronic states with energies $\epsilon_{n\mathbf{k}} = E_\mathrm{F}$, give reliable predictions for the superconducting T_C.

Our implementation of the linearised ME equation, on the other hand, considers electron pairing between all states in the Brillouin zone. When applying our approach to a system with high Fermi energy, such as diamond, the functional form of the kernel matrix naturally selects for states near the Fermi level. Consider again the kernel matrix introduced in Sec. 6.1.3:

$$K_{kk'}(i\omega_j - i\omega'_j; T) = k_\mathrm{B}T \sum_{k'\omega'_j \geq 0} w_{k'} \frac{\lambda^\mathrm{S}_{kk'}(i\omega_j - i\omega'_j) - W^\mathrm{S}_{kk'}(i\omega_j - i\omega'_j)}{\left[\hbar\omega'_j\, Z_{k'}(i\omega'_j)\right]^2 + \left[(\epsilon_{k'} - \mu_\mathrm{C}) + \chi_{k'}(i\omega'_j)\right]^2}. \quad (6.21)$$

The energy range of the first term in the denominator consisting of a Matsubara frequency and the renormalisation constant is of the order of the phonon energy. The second term in the denominator, on the other hand, contains electronic energies. In the adiabatic limit, one therefore finds:

$$\begin{aligned} &\lim_{\hbar\omega_\mathrm{ph}/E_\mathrm{F} \to 0} K_{kk'}(i\omega_j - i\omega'_j; T) \\ &\quad \approx \pi k_\mathrm{B}T \sum_{k'\omega'_j \geq 0} w_{k'} \left[\lambda^\mathrm{S}_{kk'}(i\omega_j - i\omega'_j) - W^\mathrm{S}_{kk'}(i\omega_j - i\omega'_j)\right] \delta\left(\epsilon_{k'} - \mu_\mathrm{C} + \chi_{k'}(i\omega'_j)\right), \end{aligned} \quad (6.24)$$

which is simply the zero-broadening limit of a Lorentzian. We expect therefore that our approach give very similar results to Fermi-surface restricted approaches.

There is ample experimental and computational data on the superconducting properties of hole-doped diamond,[177–179] making it an ideal test case for our formalism and implementation. Its electron-phonon coupling function λ can be regarded as constant across the Fermi surface, and the Coulomb repulsion is well captured by the Morel-Anderson parameter $\mu^* \approx 0.1$-0.2.

We aim to reproduce the relationship between λ and T_C in this system as discussed by Boeri, Kortus and Andersen, see Ref. [178]. In this (theoretical) report, the authors estimate the electron-phonon coupling strength from first principles, and employ the McMillan equation [see Eq. (2.164)] to calculate T_C. They consider three different doping levels, $x = 0.03, 0.05, 0.1$, where x is the number of holes per carbon atom. For $x = 0.03$, they achieve very good agreement with available experimental data; higher doping levels are not accessible in experiment.

We use the computational framework presented in Sec. 6.1 to calculate the critical temperature for the three considered doping levels within our model. Firstly, we map the Γ-centred diamond valence band onto a single hole band with the same density of states by setting the bare band mass to $m_0 = 3.56$. The density of states N_F provided in the reference work can then be mapped to a given Fermi energy E_F, which we use as input for our calculation.

Next, we replace the coupling matrix element in Eq. (6.2) by an expression that is a constant in $\mathbf{q}$:

$$|g_{mn\nu}(\mathbf{k}, \mathbf{q})|^2 \to |g_0|^2. \tag{6.25}$$

This approximation is well justified in metals and highly doped semiconductors. For each doping level, we evaluate T_C for a range of values g_0, and relate it to an effective electron-phonon coupling strength λ by fitting the curves $T_\mathrm{C}(g_0)$ to the McMillan formula. We use the same Morel-Anderson parameter as in the reference with $\mu^* = 0.1$.

Across the considered range, we found a linear relationship between λ and $|g_0|^2$:

$$\lambda = c_1 \times |g_0|^2 \qquad \text{where} \qquad c_1 \approx 12.2 \times 10^{-6}\mathrm{meV}^{-2}. \tag{6.26}$$

The resulting relationship between λ and the T_C is shown in Table 6.1.

For a complete $T_\mathrm{C}(\lambda)$ curve, we calculate the superconducting T_C for 76 data points between $g_0 = 144$ meV and $g_0 = 220$ meV, and plot the critical temperature against the corresponding λ. This is shown in Fig. 6.4.

The agreement between the two data sets shown in Table 6.1 and Fig. 6.4 is very good. This finding supports not only the validity of our approach, but also its applicability to a wider class of superconductors.

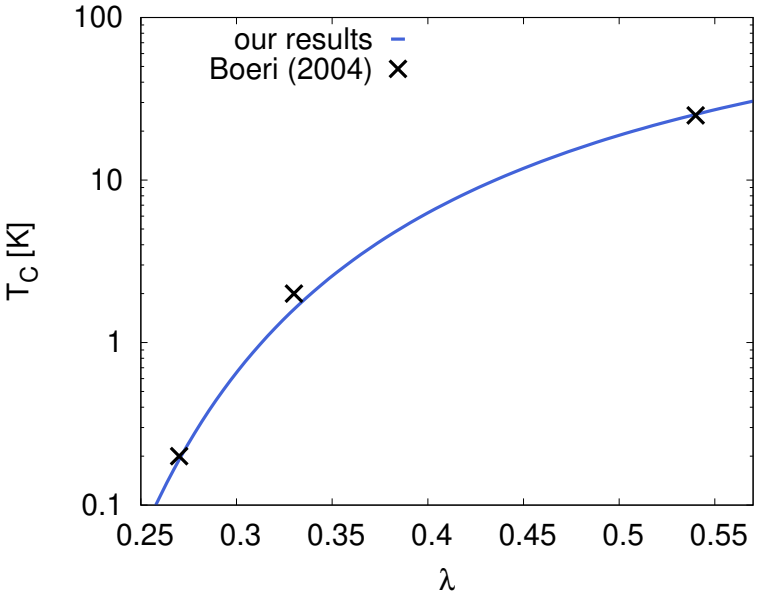


Figure 6.4: Calculated critical temperature as a function of coupling strength λ (blue line). The benchmark results from Ref. [178] are shown as black crosses.

			Ref. [178]		our results		
x	$\hbar\omega_{\mathrm{ph}}$ [meV]	λ	N_{F} [eV^{-1}]	T_{C} [K]	g_0 [meV]	E_{F} [meV]	T_{C} [K]
0.03	133	0.27	0.07	0.2	181	321	0.26
0.05	127	0.33	0.08	2	162	468	1.70
0.10	118	0.54	0.11	25	185	681	24.28

Table 6.1: Model parameters and superconducting T_{C} for hole-doped diamond, comparing data from Ref. [178] and our calculations using the linearised ME equations: doping concentration x,given as the number of holes per carbon atom in the crystal, renormalised phonon energy $\hbar\omega_{\mathrm{ph}}$, effective electron-phonon coupling constant λ, density of electronic states N_{F} and superconducting T_{C} obtained in Ref. [178]. Constant electron-phonon coupling matrix element g_0, Fermi energy and superconducting T_{C} obtained using the linearised ME equations. A Morel-Anderson parameter of $\mu^* = 0.1$ was used in all calculations. The band mass used in the model calculation is $m_0 = 3.65$.

7

Superconducting dome in doped $SrTiO_3$

In this chapter, we present the results of our calculation of the superconducting critical temperature of a doped Fröhlich solid modelling the ground state of tetragonal $SrTiO_3$. Starting from the bare kernel equation (6.21), we analyse the different contributions to the full ME equations by adding step-by-step Eqs. (6.16), (6.17) and (6.20) for, $Z_{n\mathbf{k}}$, $\chi_{n\mathbf{k}}$ and μ_{C}, respectively.In all calculations shown below, we explicitly take into account electron-phonon interaction [$\lambda_{kk'}(i\omega_j - i\omega'_j)$, Eq. (5.15)], electron-electron interaction [$N_{\mathrm{F}}V_{kk'}$, Eq. (5.16)], and full RPA screening of both the electron-phonon and electron-electron interactions.

The parameters for this calculation were extracted in Sec. 3.1. For convenience, they are reprinted in Table 7.1 below.

We benchmark our results against experimental measurements of the superconducting dome in STO. In Sec. 7.1 we start from a crude approximation of the full ME system by neglecting all contributions from the mass renormalisation function Z_k, the energy shift χ_k and by setting $\mu_{\mathrm{C}} = E_{\mathrm{F}}$. Next, in sections 7.2-7.4, we progressively refine our calculations by adding solutions to the remaining ME equations. First Z_k and then

α	$\hbar\omega_0$ [meV]	m_0 [m_e]	ε_∞
1.4	102.9	1.3	6.25

Table 7.1: Parametrisation of the doped Fröhlich solid based on first-principles calculations of $SrTiO_3$.

χ_k are evaluated self-consistently, and added into the kernel function. In the last step, we explicitly enforce the particle number conservation by re-evaluating the chemical potential for the fully interacting systems.

The characteristic dome shape of the superconducting T_C as a function of the Fermi energy is captured in all our calculations. However, we find that our approach generally over-estimates the critical temperature. In Sec. 7.6 we argue that a more sophisticated model of the free-carrier screening is required to overcome this discrepancy.

7.1 Bare kernel

We calculate the superconducting T_C in our STO model for doping concentrations given in Table 7.2, i.e. in the range across which the superconducting dome is observed in experiment. Note that with an LO phonon energy of $\hbar\omega_0 = 102.9$ meV, all our calculations are performed in the anti-adiabatic regime $E_F \ll \hbar\omega_{ph}$.

In this first set of calculations, we only solve the kernel equation, Eq. (6.21), and set $Z_k \equiv 1$, $\chi_k \equiv 0$, $\mu_C = E_F$. For each doping level, we calculate the largest eigenvalue $\kappa_{max}(T)$ of the matrix $K_{kk'}(i\omega_j - i\omega'_j; T)$ for a range of temperatures T. The critical temperature is then extracted from a linear interpolation between the two closest data points above and below $\kappa_{max} = 1$. In Fig. 7.1, this procedure is illustrated for the peak of the superconducting dome at $n_0 = 8.5 \times 10^{19}\text{cm}^{-3}$ [cf. the blue line in Fig. 7.6].

The resulting T_C dome is shown by the blue line in Fig. 7.6. At the lowest considered doping level $n_0^{min} = 9 \times 10^{16}$ cm^{-3}, we obtain a critical temperature $T_C(n_0^{min}) = 7.7$ K. With increasing charge-carrier concentration, free-carrier screening of the Coulomb interaction increases, reducing the repulsive interaction between the electrons. At the same time,

charge-carrier density n_0 [cm^{-3}]	10^{17}	10^{18}	10^{19}	10^{20}	4×10^{20}
Fermi momentum k_F [a_0^{-1}]	0.005	0.012	0.025	0.052	0.82
Fermi energy E_F [meV]	0.262	1.507	6.541	28.300	70.373

Table 7.2: Charge-carrier concentration, Fermi momentum and Fermi energy for the doping range of the superconducting dome in STO

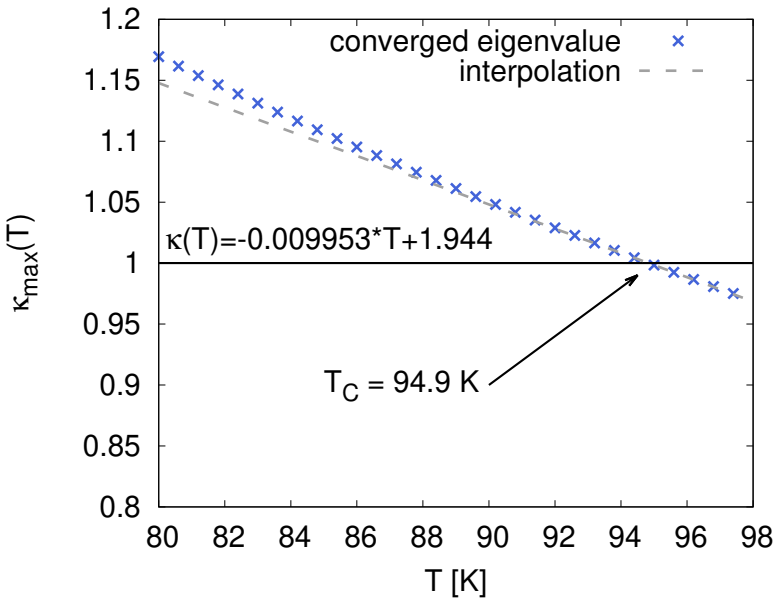


Figure 7.1: Largest eigenvalue $\kappa_{\max}(T)$ of the kernel function $K_{kk'}(i\omega_j - i\omega'_j; T)$ for a range of temperatures around T_C near the peak of the superconducting dome at $n_0 = 8.5 \times 10^{19}$ cm^{-3}. The equation for the linear interpolation of $\kappa_{\max}(T) = 1$ near T_C is shown. We find $T_C = 94.9$ K near the peak of the superconducting dome for the bare kernel; cf. the blue line in Fig. 7.6

the electron-phonon matrix element remains largely unscreened up to the peak of the dome at $n_0^{\max} = 8.5 \times 10^{19}$ cm^{-3}, cf. Fig. 3.10.

The bare kernel equation yields a maximum critical temperature $T_C^{\max} = 94.9$ K, which overestimates the experimental value by more than a factor of 200. After the peak, the dome drops off rapidly, owing to the strongly enhanced screening of the electron-phonon interaction once the corresponding plasma frequency exceeds the phonon frequency.

A small discrepancy in the experimental data shown in Fig. 7.6 is the fact that Lin *et al.* [Ref. [23]] report the measurement of two superconducting domes at different doping concentrations. As the three lowest conduction bands in the tetragonal ground state of STO are separated by a band splitting of several tens of meV, they attribute the double dome to the consecutive filling of these bands. At this stage, we only consider coupling within a single electron band, and we can therefore only recover one superconducting dome.

7.2 Mass renormalisation function

In the next step, we improve the sophistication of our T_C estimate by taking into account the mass renormalisation function Z_k. Again, we evaluate the critical temperature for the doping range given in Table 7.2. However, this time the renormalisation of the electron

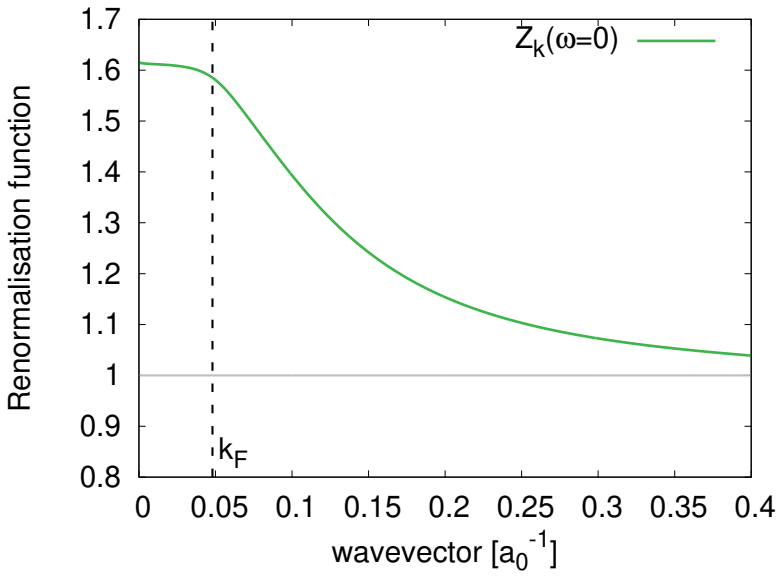


Figure 7.2: Renormalisation function $Z_k(\omega = 0)$ at zero frequency for the STO Fröhlich model at the peak of the superconducting dome at $n_0 = 7.9 \times 10^{19}\text{cm}^{-3}$ near the critical temperature $T_\text{C} = 50.6K$. We show the evolution of Z_k as a function of momentum up to $k = k_\text{cut}$. The dashed vertical line indicates the Fermi momentum at $k_\text{F} = 0.048a_0^{-1}$.

dispersion is evaluated self-consistently according to Eq. (6.16), and added to the kernel function in Eq. (6.21). Meanwhile, the energy shift is still neglected: $\chi_{n\mathbf{k}} \equiv 0$ and $\mu_\text{C} = E_\text{F}$.

As we discussed in Sec. 2.2.4, this approximation has been very successful in *ab initio* calculations of the superconducting T_C in metals and semimetals. In those systems, the bare electron band is anti-symmetric about the Fermi surface, and hence the energy shift related to $\chi_{n\mathbf{k}}$ averages to zero.

Figure 7.2 shows the calculated renormalisation function at the new peak of the superconducting dome at $n_0^\text{max} = 7.9 \times 10^{19}$ cm^{-3}. We plot $Z_k(\omega = 0)$ across the Brillouin zone up to the cutoff value k_cut.

From Eq. (2.137), the function Z_k can be understood as a renormalisation of the effective mass of the paired electrons. While our numerical implementation currently does not support continuation of complex quantities to the real axis, we do have access to the value of the renormalisation function at $\omega = 0$. We find that the renormalisation of the electron band is strongest across the occupied states in the Fermi sea, and declines unity far away from k_F. In fact, we observe that in our system, Z_k is approximately constant up to the Fermi edge, before it drops off towards the edge of the Brillouin zone.

Note that the inclusion of Z_k has moved the peak of the superconducting dome in Fig. 7.6 to a slightly lower doping level. Moreover, it strongly modifies our initial estimate

of the maximum critical temperature in the system. Including Z_k, we find $T_{\mathrm{C}}^{\max} = 50.6$ K, which corresponds to a reduction of 47% with respect to the bare kernel.

7.3 Energy shift

Across the considered doping range, the Fermi edge in our system is always very close to the band bottom. Hence the assumption that the electron energies are antisymmetric around μ_{C} is not valid, and one must expect a finite contribution to the shift of the band energy via χ_k.

The equations for Z_k and χ_k are solved self-consistently according to Eqs. (6.16) and (6.17). When applying a rigid shift to the band energy, one must generally re-evaluate the chemical potential to ensure that the particle number is conserved. We will take into account this contribution in the next section. Here, we still assume $\mu_{\mathrm{C}} = E_{\mathrm{F}}$.

Fig. 7.3 shows the calculated energy shift at the peak of the superconducting dome at $n_0^{\max} = 1.1 \times 10^{20}\mathrm{cm}^{-3}$. The function is plotted across the Brillouin zone for $\omega = 0$. In Fig. 7.4, we relate this energy shift to the electronic energy range by plotting the shifted function $\epsilon_k - E_{\mathrm{F}} + \chi_k(\omega = 0)$ alongside the non-interacting electron band $\epsilon_k - E_{\mathrm{F}}$. This energy shift affects strongest empty electronic states that are between one and two phonon energies above the bottom of the conduction band.

As before, we observe that the Fröhlich coupling is strongly peaked for interactions between states separated by small $q = |\mathbf{k} - \mathbf{k}'|$, and falls off quickly for more separated states. At the same time, we have found in Sec. 2.2.4 that pair formation near the edge of the Fermi sea is favoured. In Fig. 7.4, we can see clearly that the energy shift in fact pushes the strongly coupled electronic states at the apex of the band further away from the Fermi edge, reducing the overall strength of the electron-phonon coupling.

The result is a further suppressed critical temperature with a maximum of $T_{\mathrm{C}}^{\max} = 14.1$ K at $n_0^{\max} = 1.1 \times 10^{20}$ cm^{-3} [cf. Fig. 7.6].

7.4 Chemical potential

As we have seen, the energy of the interacting electron-phonon system is renormalised by several tens of meV due to the inclusion of the energy shift function χ_k. In the previous

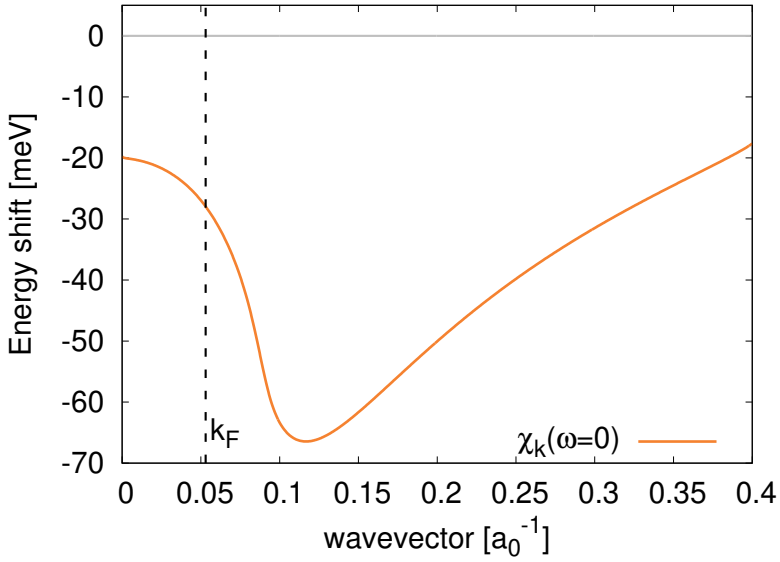


Figure 7.3: Energy shift function $\chi_k(\omega = 0)$ for the Fröhlich system doped at $n_0 = 1.1 \times 10^{20}$ cm^{-3} near the critical temperature $T_C = 19.6$ K. The function χ_k is shown for all k up to $k = k_{\text{cut}}$. The dashed vertical line indicates the Fermi momentum at $k_F = 0.053 a_0^{-1}$.

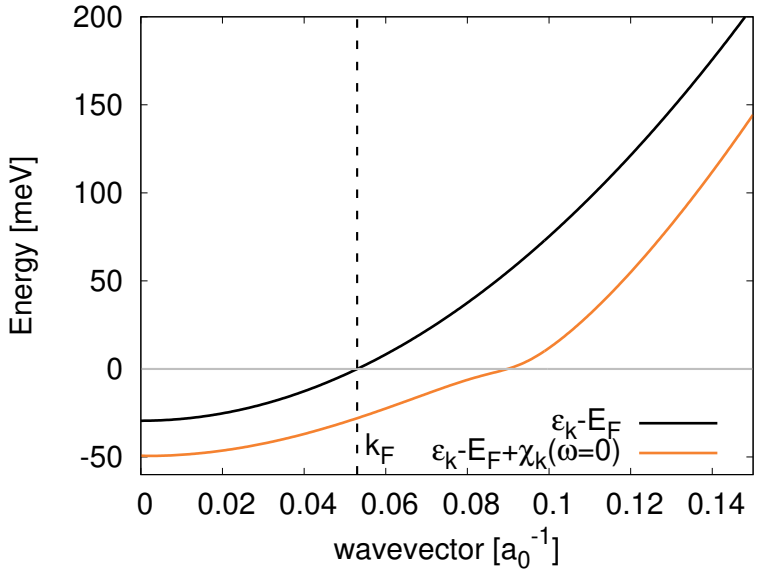


Figure 7.4: Renormalised energy $\epsilon_k - E_F + \chi_k(\omega = 0)$ at $n_0 = 1.1 \times 10^{20}$ cm^{-3} (shown in orange) alongside the noninteracting electron band $\epsilon_k - E_F$ (solid black line). The Fermi momentum is indicated by the dashed vertical line.

section, we kept the Fermi energy the same as in the independent particle picture, which implicitly increases the size of the Fermi sea in the conduction band, cf. Fig. 7.4.

Now, we add the last of the Migdal-Eliashberg equations, Eq. (6.20), to enforce the conservation of the number of particles. First, we evaluate n_e for the noninteracting system, i.e. for $Z_k \equiv 1$ and $\chi_k \equiv 0$ and obtain n_e^{NI}. Then we evaluate $n_e(\mu_{\text{test}})$ with the calculated mass renormalisation and energy shift functions on a fine energy grid μ_{test} around E_F. The energy at which we recover the noninteracting particle energy n_e^{NI} is our new chemical potential μ_C.

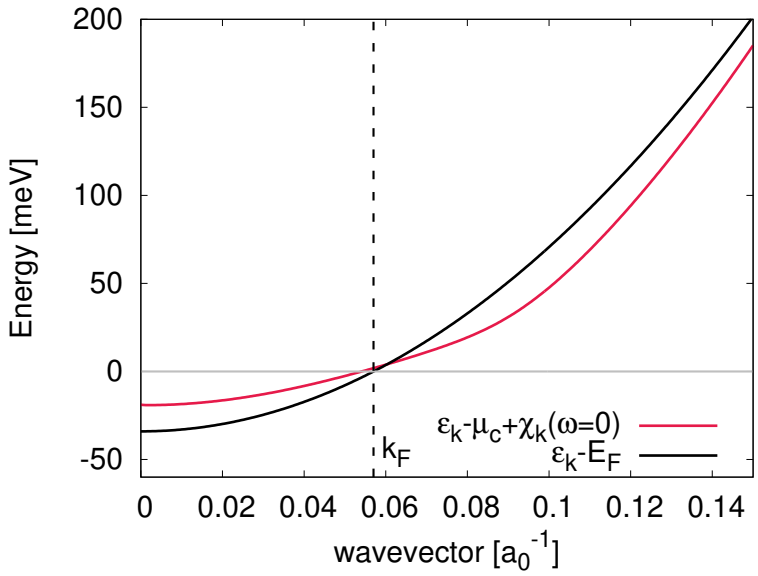


Figure 7.5: Renormalised energy $\epsilon_k - \mu_C + \chi_k(\omega = 0)$ at $n_0 = 1.3 \times 10^{20}$ cm^{-3} (shown in red) alongside the noninteracting electron band ϵ_k relative to the Fermi energy of the noninteracting system, E_F (solid black line). The Fermi momentum is indicated by the dashed vertical line.

Figure 7.5 shows the renormalised quasiparticle energy $\epsilon_k - \mu_C + \chi_k(\omega = 0)$ at the peak of the superconducting dome at $n_0^{max} = 1.3 \times 10^{20}$ cm^{-3}. This function is similar to the one shown in Fig. 7.4, however this time the reference energy is the new chemical potential $\mu_C = -10.7$ meV, and not the Fermi energy of the noninteracting system, $E_F = 34.1$ meV.

The re-evaluation of the chemical potential moves the Fermi edge again closer to the strongly-coupled low-q states near the band bottom. The resulting critical temperature is therefore strongly enhanced, as shown in Fig. 7.6. We find the peak of the superconducting dome at $T_C^{max} = 53.6$ K

7.5 Superconducting dome in doped $SrTiO_3$

Our results for the superconducting dome of STO are shown in Fig. 7.6. We compare the calculated critical temperature obtained within the four discussed approximations to experimental data from Refs. [23] and [22].

At all levels of theory, we observe remarkable qualitative agreement of our results with the experimentally observed superconducting dome. Notably, we find that it is not symmetric about its peak. Across the first half up to doping levels of around $n_0^{peak} \approx 1 \times 10^{20}$ cm-3, electronic screening of the repulsive Coulomb interaction increases with the density of states, progressively enhancing the effective pairing potential. Screening

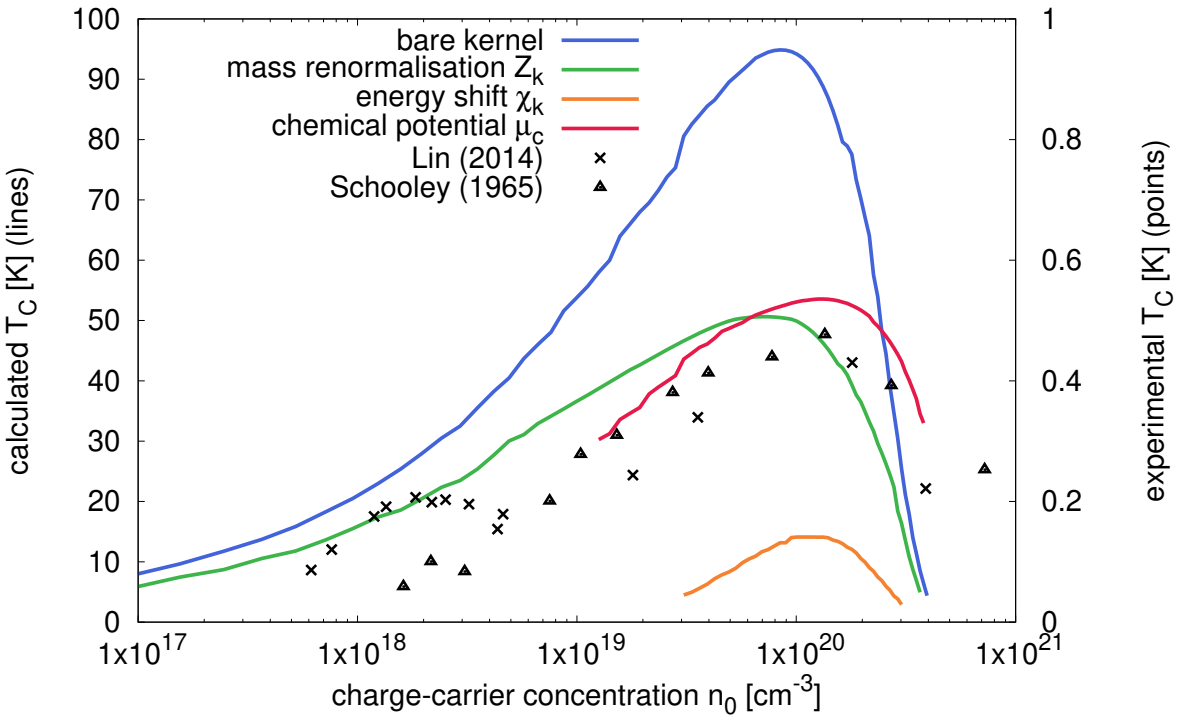


Figure 7.6: Superconducting dome for the STO Fröhlich model system using the parameters given in Table 7.1 for the four approximations considered.Experimental measurements are shown as black crosses [Ref. [23]] and triangles [Ref. [22]]; the corresponding temperatures are indicated on the right axis. Our calculated superconducting domes are shown as lines, the corresponding temperatures are given on the left axis. The result for the bare kernel equation is shown in blue. After including the mass renormalisation function we obtain the green line. Adding the energy shift function yields the T_C curve shown in orange, and the red line shows the full calculation including the renormalised chemical potential.

of the electron-phonon coupling only becomes noticeable above n_0^{peak}, but then causes a rapid decline of the attractive interaction.

The bare kernel equation $K_{kk'}$ yields the highest critical temperature (blue line in Fig. 7.6), as this approximation does not include any renormalisation of the electron state due to electron-phonon interaction. In the present case, these renormalisation effects are very important for the critical temperature, as e.g. the renormalisation function achieves values as high as $Z_k \lesssim 1.6$.

To relate the T_C in our doped semiconductor to that in a simple metal, we can estimate the total effective electron-phonon coupling strength λ via the relation:[30]

$$Z \approx 1 + \lambda, \qquad \text{which yields} \qquad \lambda \approx 0.6. \tag{7.1}$$

element	λ	$\hbar\omega_{\mathrm{Debye}}$ [meV]	T_{C}
Al	0.38	36.9	1.16
Ti	0.38	36.6	2.38
Ga	0.40	28.0	1.08
Hg	1.00	6.2	4.16
Pb	1.12	9.1	7.19

Table 7.3: Empirical electron-phonon coupling constant λ, phonon energy and superconducting critical temperature for a selection of elemental metals, reprinted from Ref. [30]

Alternatively, we can employ the McMillan equation [Eq. (2.164)] using a conventional value of $\mu^* = 0.1$ for the Morel-Anderson parameter, and setting $\hbar\omega_{\log} = 100$ meV, to estimate the electron-phonon coupling strength. We find

$$k_{\mathrm{B}}T_{\mathrm{C}}[\mathrm{McMillan}] = 54.4\mathrm{K} \qquad \text{for} \qquad \lambda \approx 0.8. \tag{7.2}$$

In metallic systems, a coupling strength as large as $\lambda \approx 0.6 - 0.8$ would be considered high although e.g. elemental lead achieves an even higher value, cf. Table 7.3. The even higher critical temperature in our model is explained explained by the much larger energy of the LO phonon.

Our results also show that it is crucial to reevaluate the chemical potential when adding the energy shift χ_k. No real physical significance can be attributed to the orange T_{C} line in Fig. 7.6, in which χ_k is included but the kernel is evaluated at the noninteracting E_{F}. The full calculation, shown in red, on the other hand, is again closer to our result obtained with only the mass renormalisation function. This suggests that setting $\chi_k \equiv 1$ would be a reasonable approximation for the present case.

Lastly, we need to address the fact that our predicted critical temperature overestimates the measured T_{C} by two orders of magnitude. In the following section we argue that this is due to an incomplete description of the free-carrier screening of the long-range many-body interactions, and we propose an empirical solution to the problem.

7.6 Electronic screening

At the end of this chapter, we want to discuss the question why our calculations systematically overestimate the critical temperature by two orders of magnitude, and we outline next steps for future investigations into what is missing from our approach.

Our results for the critical temperature are extremely sensitive to small variations in the dielectric screening function $\varepsilon^{\mathrm{RPA}}$. This quantity is not evaluated from first principles, but rather calculated using a model of the electron gas which assumes that the free electrons can be described as independent particles. In Sec. 3.3.2, we saw that this model screening function can very effectively suppress the Coulomb interaction between two electrons of a Cooper pair at all doping levels. More effective screening of $V_{kk'}$ means a reduced repulsive contribution to the total potential and hence a higher T_{C}.

One interaction that can affect the dielectric function of the free electron gas are correlations between dopant electrons. The importance of electron correlation effects in STO have been discussed in the literature,[180,181] and their effect on the bandstructure and screening properties may explain some of the discrepancy between our calculated T_{C} values and experimental data.

It is an interesting question to ask what value of the dielectric screening function would reproduce the measured critical temperature exactly. To investigate this, we replace the RPA screening of the Coulomb term $\varepsilon^{\mathrm{RPA}}$ by a tuneable parameter $\tilde{\varepsilon}$ [cf. Eq. (6.21)]:

$$\frac{N_{\mathrm{F}}\, V}{\varepsilon^{\mathrm{RPA}}(q, i\omega_j - i\omega'_j)} \qquad \rightarrow \qquad \frac{N_{\mathrm{F}} V}{\tilde{\varepsilon}}. \tag{7.3}$$

Equation (7.3) is the simplest possible screening model. By varying $\tilde{\varepsilon}$, we can tune the superconducting T_{C} in our calculations. Once we have found the correct average screening value, we can then compare it to calculated averages of the Lindhard screening function.

In Fig. 7.7, we show the calculated T_{C} using the parameter $\tilde{\varepsilon} = 1.78$. Quantitative agreement with experimental data is within less than 0.5 K. Note that the dielectric screening of the Lindhard model, which gave a critical temperature of $T_{\mathrm{C}} \approx 50$ K corresponds to a value $\tilde{\varepsilon} = 2.15$. This highlights the fact that small variations in the screening function can lead to order-of-magnitude differences in the critical temperature.

The two peaks are obtained by evaluating the kernel expression for two different effective masses. This is supported by the analysis of the experimental data in Ref. [23]:

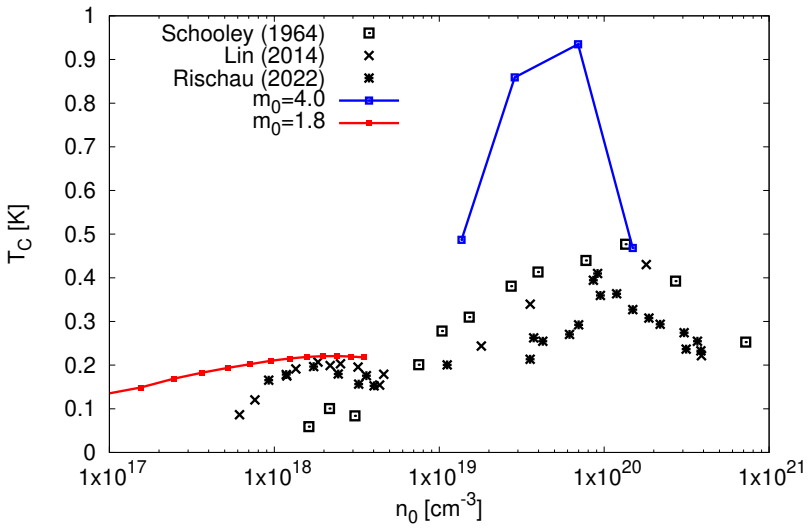


Figure 7.7: Superconducting critical temperature of doped $SrTiO_3$ calculated with an empirical screening parameter of $\tilde{\varepsilon} = 1.78$. Calculations of the superconducting dome for two values of the bare band mass $m_0 = 1.8\,m_e$ and $m_0 = 4.0\,m_e$ give rise to a two-peak structure.

The authors find that the double-dome structure is due to consecutive filling of the lowest and second-lowest conduction bands in STO [cf. our discussion of the conduction band bottom in the tetragonal phase given in Sec. 3.1.2].

This concludes our analysis of the superconducting pairing interaction in doped polar STO. The linearised ME equations introduced in Sec. 2.2.2 provide a solid foundation to investigate the intricate many-body interaction in Fröhlich-type semiconductors: Expanding on the formalism introduced in this thesis, modifications to include further many-body interactions can be achieved in a clear and unambiguous way.

8
Conclusions

In the preceding chapters, we have presented a quantitative discussion of long-range electron-phonon interactions in doped polar semiconductors and superconductors. To facilitate this analysis, we have introduced the doped Fröhlich solid to derive robust analytical solutions both above and below the superconducting critical temperature.

For the normal state, we derived exact analytical expressions for the many-body QP spectra in the presence of free carriers. These expressions allowed us to analyse in detail the role of Pauli blocking and free carrier screening in the electron spectral functions.

Our analytical approach has provided new insight into the Fröhlich polaron problem, and allows us to draw the following conclusions: To capture the low-energy many-body physics of doped polar semiconductors, especially in the presence of doping (as needed in ARPES measurements), it is crucial to explicitly account for the small but non-zero electron occupations in the conduction band. We have demonstrated that neglecting finite occupations leads to incorrect satellite energetics and excessive electron-phonon renormalisation. In the case of high doping levels, further many-body effects in the form of free-carrier screening of the electron-phonon matrix element must also be included to achieve a meaningful description of QP shifts and effective mass renormalisation.

Moreover, we have found that a significant portion of the coupling-doping phase diagram exhibits regions with anomalously strong mass enhancement, as well as regions where the band curvature is inverted, leading to a breakdown of the QP picture. These

findings indicate that caution must be used when studying electron-phonon coupling in doped polar materials, as the standard second-order Fan-Migdal self-energy might not provide a physically accurate picture in the anomalous regions of the phase diagram identified in this thesis.

We also found that, in the presence of doping, the mass renormalisation depends both on the electron-phonon coupling strength *and* the Fermi level. This finding implies that the use of the standard relation $m^*/m_0 = 1 + \alpha/6$ for extracting the Fröhlich coupling from experiments is not justified, and should be replaced by the generalised expression obtained in this thesis, Eq. (4.22).

In line with previous literature, we can confirm that the second-order cumulant spectral function improves the description of polaron satellites compared to the conventional first-order Dyson approach. The intensity and binding energy of the sidebands provided by the cumulant method agree well with the equidistant satellites observed in experiments. On the other hand, the cumulant method appears to provide a worse description of the QP band. Indeed, we have shown that the cumulant approach leads to an inversion of the band curvature over a much wider region of the phase diagram as compared to the Dyson method, and that the cumulant spectral function exhibits unphysical vertical streaks that are intrinsic to the theoretical framework (rather than being numerical artefacts).

Our comparative analysis of the cumulant and Dyson approaches highlights the fact that a complete description of the Fröhlich problem in the presence of doping is not yet feasible given the theoretical methods available today. Rather, we find that investigations into including self-energy diagrams beyond the second order are advised. The benefits of such investigations go beyond the accurate modelling of experimental spectra: Interesting properties of doped semiconductors, such as the electron mobility and superconducting T_C depend strongly on the dispersion and spectral weight of the interacting electron. A predictive model of these effects may prove very useful for the design and engineering of novel semiconductors.

Also within the Fröhlich model, we investigated the application of ME theory to modelling the superconducting state in doped polar semiconductors.

First, we investigated the failure of some of the most common approximations to ME theory when applied to Fröhlich solids, and found that the description of the long range of the electron-phonon interaction must necessarily extend beyond the two-dimensional Fermi surface. Moreover, given the relatively strong pairing interaction and resulting small size of the Cooper pairs, we found that the Coulomb repulsion between the paired electrons is substantially increased compared to metallic systems in the adiabatic limit, and cannot be included via a simple semiempirical parameter.

Next, we developed an alternative computational framework for modelling isotropic polar crystals. In this approach, we treat electron-phonon and electron-electron interactions explicitly as a function of momentum and frequency. In addition, we account for dynamical screening of the long-range interactions by free charge carriers. In fact, we find that physically meaningful results depend crucially on the accurate description of these screening effects.

We employed our framework to model the superconducting critical temperature of n-doped bulk $SrTiO_3$ as a function of charge-carrier density. We explicitly calculated the renormalisation function, energy shift, and order parameter, and discussed their individual contributions to the final T_C.

Our results show a strong qualitative agreement with the overall trend of the critical temperature measured in experiment, and indicate that the appearance of the superconducting dome is closely connected to the delayed onset of dielectric screening of the electron-phonon coupling matrix element. The fact that our calculations overestimate the experimental T_C indicates the need for a more realistic model of the dopant Fermi sea.

Understanding the superconducting pairing mechanism in doped $SrTiO_3$ is the first step towards a more predictive theory of superconductivity in oxide superconductors.

On the one hand, more efficient and comprehensive implementations of the Migdal-Eliashberg equations will undoubtedly lead to improvements in the accuracy of *ab initio* calculations. This is particularly interesting from a materials discovery perspective, where one would like to scan a larger phase space of the periodic table for compounds with potentially high superconducting T_C. A good starting point for such an investigation would be a systems like the T_C-record setting $FeSe/SrTiO_3$ interface.

On the other hand, analytical approaches such as the one we presented here can be very useful in the development of new semiempirical T_{C} equations, similar to McMillan's equation for nonpolar metals. In practice, a simple formula for the critical temperature that is robust for a large class of materials would be extremely useful and certainly further improve our understanding of the emergence of the superconducting state.

Appendix

A

Born-von Kármán boundary conditions

To introduce boundary conditions in crystals in a rigorous way we start with the notion of the Born-von Kármán supercell, which consists of $N_p = N_1 \cdot N_2 \cdot N_3$ unit cells of the crystal. If the unit cell has the primitive lattice vectors $\boldsymbol{a}_{1,2,3}$ then the lattice vector of the p-th unit cell is given by $\boldsymbol{R}_p = \sum_i n_i \boldsymbol{a}_i$, with n_i integers between 0 and $N_i - 1$.

A given function which has the periodicity of the crystal, $f(\mathbf{r}, \mathbf{R}_p)$, is defined on a discrete grid $\mathbf{r} + \mathbf{R}_p$ within the crystal, where $\mathbf{R}_p$ indicates unit cell within the BvK supercell, and $\mathbf{r}$ denotes the position within that unit cell. The Fourier transformation of such a function from reciprocal space is defined as

$$f(\mathbf{r} + \mathbf{R}_p) = \frac{1}{N_p} \sum_{\mathbf{k}} \sum_{\mathbf{G}} e^{i(\mathbf{k}+\mathbf{G})(\mathbf{r}+\mathbf{R}_p)} f(\mathbf{k} + \mathbf{G}), \tag{A.1}$$

where $\mathbf{G}$ is a reciprocal lattice vector, and $\mathbf{k}$ is a wavevector within the first Brillouin zone. In one dimension, $|\mathbf{k}| \leq |\mathbf{G}|/2 = \pi/a_{\text{lat}}$. At this point, both the $\mathbf{r} + \mathbf{R}_p$ grid and the $\mathbf{k} + \mathbf{G}$ grids are finite and discretised. They consist of $N_p + N_{\mathbf{G}}$ grid points, where $N_{\mathbf{G}}$ is the number of reciprocal lattice vectors included in the description. We have

$$\sum_{\mathbf{G}} e^{i\mathbf{G}\cdot\mathbf{r}} = \delta_{\mathbf{r}0} \qquad \Longleftrightarrow \qquad \sum_{\mathbf{r}} e^{i\mathbf{G}\cdot\mathbf{r}} = \delta_{\mathbf{G}0}, \tag{A.2}$$

which implies that the spatial resolution of $\mathbf{r}$ within the unit cell cannot be smaller than $2\pi/|\mathbf{G}_{\text{max}}|$. Equivalently, with

$$\sum_{\mathbf{k}} \exp\left(i\mathbf{k} \cdot \mathbf{R}_p\right) = N_p \delta_{p0} \qquad \Longleftrightarrow \qquad \sum_{p} \exp\left(i\mathbf{k} \cdot \mathbf{R}_p\right) = N_p \delta_{\mathbf{k}0}, \tag{A.3}$$

we find that the number N_p of unit cells in the BvK supercell determines the resolution of the crystal momentum $\mathbf{k}$.

As the number of unit cells in the BvK supercell goes to infinity, $N_p \to \infty$, the resolution of $\mathbf{k}$ within the first Brillouin zone becomes infinitesimal and the Fourier transform becomes:

$$\begin{aligned} \lim_{N_p\to\infty} f(\mathbf{r}+\mathbf{R}_p) &= \lim_{N_p\to\infty} \frac{1}{N_p\,(\Delta\mathbf{k})} \sum_{\mathbf{k}} (\Delta\mathbf{k})\, e^{i(\mathbf{k}+\mathbf{G})(\mathbf{r}+\mathbf{R}_p)} f(\mathbf{k}+\mathbf{G}) \\ &= \sum_{\mathbf{G}} \int_{\mathrm{BZ}} \frac{d\mathbf{k}}{\Omega_{\mathrm{BZ}}} e^{i(\mathbf{k}+\mathbf{G})(\mathbf{r}+\mathbf{R}_p)} f(\mathbf{k}+\mathbf{G}), \end{aligned} \tag{A.4}$$

where we used $\Omega_{\mathrm{BZ}} = N_p\,(\Delta\mathbf{k})$, with the volume of the first Brillouin zone, Ω_{BZ}.

At the level of Eq. (A.4), the mesh of position vectors $\mathbf{r}$ is still discrete, as $N_{\mathbf{G}}$ is still a finite number and the integration on the right-hand side only extends over the continuous range $\mathbf{k}+\mathbf{G} < G_{\max}$. Define the new variables $\tilde{\mathbf{r}} = \mathbf{r}+\mathbf{R}_p$ and $\tilde{\mathbf{k}} = \mathbf{k}+\mathbf{G}$, and write

$$f(\tilde{\mathbf{r}}) = \int_{|\tilde{\mathbf{k}}|\le|\mathbf{G}_{\max}|} \frac{d\tilde{\mathbf{k}}}{\Omega_{\mathrm{BZ}}} e^{i\tilde{\mathbf{k}}\cdot\tilde{\mathbf{r}}} f(\tilde{\mathbf{k}}). \tag{A.5}$$

Now, we can let $N_{\mathbf{G}} \to \infty$, and the integration boundaries are extended to infinity:

$$f(\mathbf{r}) = \int \frac{d\mathbf{k}}{\Omega_{\mathrm{BZ}}} e^{i\mathbf{k}\cdot\mathbf{r}} f(\mathbf{k}). \tag{A.6}$$

B

Debye-Waller self-energy

In this appendix, we show that the QP shift arising from the Debye-Waller self-energy[50] vanishes in the Fröhlich model. We start from the compact expression for the Debye-Waller matrix element in the rigid-ion approximation derived in Ref.[182]:

$$D^{\kappa\alpha\alpha'}(\mathbf{k}) = i\langle u_{\mathbf{k}}|\Big[\partial_{\Gamma\kappa\alpha}\hat{V}^{\mathrm{L}}, \hat{p}_{\alpha'}\Big]|u_{\mathbf{k}}\rangle, \tag{B.1}$$

where α, α' are Cartesian coordinates, κ is the atomic index, $u_{\mathbf{k}}$ are the Bloch-periodic components of the electron wavefunctions, $\hat{V}^{\mathrm{L}}$ is the long-range part of the interaction potential, and

$$\hat{p}_{\alpha} = \sum_{\kappa\alpha'} Z_{\kappa\alpha\alpha'}\Delta\tau_{\kappa\alpha'} \tag{B.2}$$

is the momentum operator in direction α arising from the displacement of atom κ with Born effective charge $Z_{\kappa\alpha\alpha'}$ along the direction $\Delta\tau_{\kappa\alpha'}$. The potential derivative in Eq.(B.1) is defined as[50]

$$\partial_{\mathbf{q}\kappa\alpha}\hat{V} = \sum_{p} e^{-i\mathbf{q}\cdot(\mathbf{r}-\mathbf{R}_p)}\frac{\partial V}{\partial\tau_{\kappa\alpha}}\bigg|_{\mathbf{r}-\mathbf{R}_p}, \tag{B.3}$$

where $\mathbf{R}_p$ is the lattice vector of the p-th unit cell in the supercell, and $\tau_{\kappa\alpha}$ is the coordinate of atom κ in cartesian direction α.

In the doped Fröhlich solid, the electronic states are plane wave and the long-range part of the Fröhlich potential is [51]

$$\begin{aligned} \hat{V}^{\mathrm{L}}(\mathbf{r}) &= -i\frac{4\pi}{4\pi\epsilon_0\, N\Omega_{\mathrm{UC}}} \\ &\times \sum_{\substack{\mathbf{q}\\ \mathbf{G}\neq-\mathbf{q}}}\sum_{\kappa\alpha\alpha'} Z_{\kappa\alpha\alpha'}\Delta\tau_{\kappa\alpha'}\frac{(\mathbf{q}+\mathbf{G})_\alpha\, e^{i(\mathbf{q}+\mathbf{G})\cdot\mathbf{r}}}{(\mathbf{q}+\mathbf{G})\cdot\boldsymbol{\varepsilon}\cdot(\mathbf{q}+\mathbf{G})}. \end{aligned} \tag{B.4}$$

Here, $\mathbf{G}$ is a reciprocal lattice vector, and $\boldsymbol{\varepsilon}$ is the static dielectric tensor of the crystal. Using the isotropy of our system to simplify the Born effective charge and dielectric tensors, $Z_{\kappa\alpha\alpha'} = Z_\kappa\delta_{\alpha\alpha'}$ and $\varepsilon_{\alpha\alpha'} = \epsilon_\infty\delta_{\alpha\alpha'}$, we can calculate the derivative

$$\partial_{\Gamma\kappa\alpha}\hat{V} = -\frac{i}{\epsilon_0\,\epsilon_\infty\,\Omega_{\mathrm{UC}}}\sum_{\mathbf{G}\neq0} Z_\kappa\frac{G_\alpha\, e^{i\mathbf{G}\cdot\mathbf{r}}}{|\mathbf{G}|^2}. \tag{B.5}$$

After calculating the commutator of this function with the dipole $\hat{p}_\alpha$, we obtain a lattice periodic expression, and as the eigenstates of our system are plane waves, we find

$$\langle u_{\mathbf{k}}|e^{i\mathbf{G}\cdot\mathbf{r}}|u_{\mathbf{k}}\rangle = 0. \tag{B.6}$$

This result shows that the Debye-Waller correction vanishes for the Fröhlich model.

C

Phonon-plasmon polaritons

The concept of a polariton was first discussed in the context of light-matter interactions. If photons impinge on a crystal, eigenmodes of the electron plasma and the photons can hybridise and form a new coupled boson. The dispersion of the new coupled boson consists of two branches separated by a finite energy band.[183]

In a crystal with a dielectric function $\varepsilon(\mathbf{q},\omega)$, the dispersion of a photon is given by:[29]

$$\omega^2\varepsilon_{\mathrm{T}}(\mathbf{q},\omega) = \omega_{\mathbf{q}}^2 = (q\,c)^2, \tag{C.1}$$

where ε_{T} is the transverse component of the dielectric function.

The normal modes are all values Ω_q that satisfy Eq. (C.1) for a given dielectric function. Assume that the dielectric function of a polar crystal is well approximated by:

$$\varepsilon_{\mathrm{T}}(\omega) = \varepsilon_\infty + \frac{\varepsilon_0 - \varepsilon_\infty}{1 - \omega^2/\omega_{\mathrm{TO}}^2}. \tag{C.2}$$

Inserting Eq. (C.2) into Eq. (C.1), one obtains a quadratic equation for ω^2. The resulting dispersion is given by:[29]

$$\Omega_q^2 = \frac{1}{2}\left(\tilde{\omega}_q^2 + \omega_{\mathrm{LO}}^2\right) \pm \frac{1}{2}\sqrt{\left(\tilde{\omega}_q^2 + \omega_{\mathrm{LO}}^2\right)^2 - 4\tilde{\omega}_q^2\,\omega_{\mathrm{TO}}^2}, \tag{C.3}$$

where $\tilde{\omega}_q = (c\,q)^2/\varepsilon_\infty$.

The same type of coupling can also occur between plasmons and phonons,[165] in which case it is referred to as the formation of a phonon-plasmon polariton.[164]. In this case, one simply replaces the phonon frequency $\tilde{\omega}_q$ by the plasma frequency ω_{pl} of the electron gas.

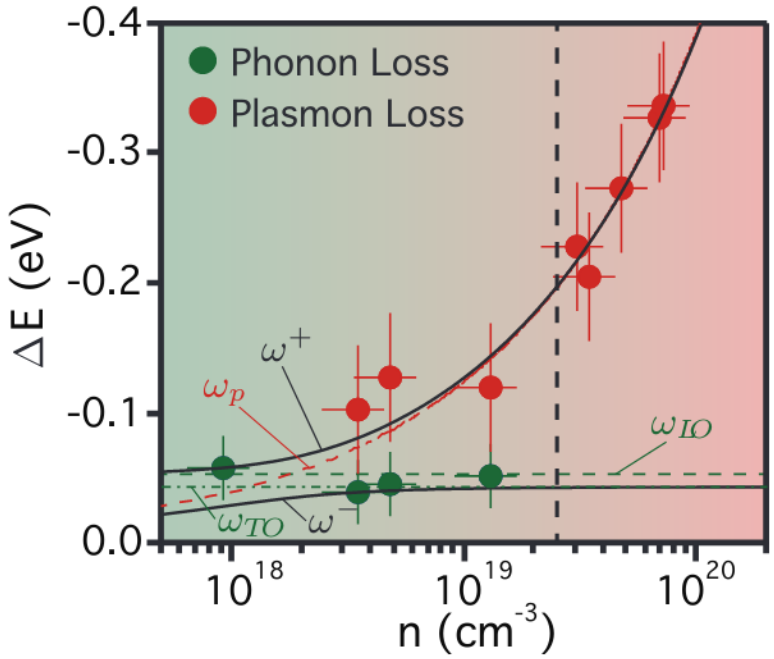


Figure C.1: Quasiparticle-satellite peak separation as a function of electron doping in the photoemission spectrum of doped EuO, reprinted from Ref. [9]. The red and green dots indicate experimental data, and the black line shows the expected dispersion following Eq. (C.3). The dashed green lines indicate the noninteracting energies of the LO and TO phonons, respectively. The dashed red line is the dispersion of the noninteracting plasmon.

In experiment, it has been observed e.g. in GaAs[184], or, more recently, in EuO.[9]. In Fig. C.1, we reprint the calculated and measured polariton dispersion in doped EuO from Ref. [9]. In this experiment, the authors observed quasiparticle satellites in photoemission spectroscopy as a function of electron doping. Shown as red and green dots is the measured peak separation between the QP and first satellite, from which one extracts the energy of the coupled boson. The black lines indicate the dispersion calculated from Eq. (C.3). Note the forbidden energy band between the LO and TO phonon frequencies, indicated by the dashed horizontal lines.

D

Derivation of the Fan-Migdal self-energy

In this section, we outline the derivation of the various self-energy expressions used in this manuscript, starting from the definition of the Fan-Migdal self-energy given in Eqs. (4.14) and (4.1).

D.1 Single electron in the conduction band

In the case of a single electron added to the conduction band, the occupation factor $f_{\mathbf{k}+\mathbf{q}}$ vanishes everywhere, cancelling all contributions from the lesser self-energy.

At the Γ point ($\mathbf{k} = 0$), we integrate Eq. (4.1) by introducing spherical coordinates. We write:

$$\Sigma^{>}_{k=0}(\omega) = 4\pi \int_0^\infty \frac{dq\, q^2}{(2\pi)^3} \frac{|g(q)|^2}{\hbar\omega - \frac{\hbar^2 q^2}{2m_0} - \Omega_0}, \tag{D.1}$$

and find:

$$\Sigma^{>}_{k=0}(\omega) = -i\, \frac{\alpha\, (\hbar\omega_0)^{3/2}}{\sqrt{\hbar\omega - \Omega_0}}, \tag{D.2}$$

where we used the definition of the Fröhlich matrix element, Eq. (1.1). Equation (D.1) leads directly to Eq. (4.4).

For general k, we write Eq. (4.1) as

$$\Sigma^{>}_{\mathbf{k}}(\omega) = \int \frac{d\mathbf{q}}{(2\pi)^3} \frac{|g(\mathbf{q}-\mathbf{k})|^2}{\hbar\omega - \frac{\hbar^2 \mathbf{q}^2}{2m_0} - \Omega_0}. \tag{D.3}$$

After transforming to spherical coordinates, we use the identity

$$\int_0^\pi \frac{d\theta\, \sin\theta}{k^2+q^2-2kq\cos\theta} = \frac{1}{2kq}\log\frac{(k+q)^2}{(k-q)^2}, \tag{D.4}$$

and the definition of the Fröhlich matrix element, Eq. (1.1), to obtain:

$$\Sigma_k^>(\omega) = \frac{\alpha\,\hbar(\hbar\omega_0)^{3/2}}{2\pi\, k\,\sqrt{2m_0}}\int_0^\infty \frac{dq\, q}{\hbar\omega - \frac{\hbar^2q^2}{2m_0} - \Omega_0}\log\frac{(k+q)^2}{(k-q)^2}. \tag{D.5}$$

The integrand in Eq. (D.5) has the primitive:

$$\begin{aligned} I(q) \;=\; & -\Bigg[\log\frac{\hbar\omega - \frac{\hbar^2q^2}{2m_0} - \Omega_0}{\hbar\omega - \frac{\hbar^2k^2}{2m_0} - \Omega_0}\log\left|\frac{q+k}{q-k}\right| \\ & + \mathrm{Li}_2\frac{\frac{\hbar(k+q)}{\sqrt{2m_0}}}{\frac{\hbar k}{\sqrt{2m_0}} - \sqrt{\hbar\omega-\Omega_0}} + \mathrm{Li}_2\frac{\frac{\hbar(k+q)}{\sqrt{2m_0}}}{\frac{\hbar k}{\sqrt{2m_0}} + \sqrt{\hbar\omega-\Omega_0}} \\ & - \mathrm{Li}_2\frac{\frac{\hbar(k-q)}{\sqrt{2m_0}}}{\frac{\hbar k}{\sqrt{2m_0}} + \sqrt{\hbar\omega-\Omega_0}} - \mathrm{Li}_2\frac{\frac{\hbar(k-q)}{\sqrt{2m_0}}}{\frac{\hbar k}{\sqrt{2m_0}} - \sqrt{\hbar\omega-\Omega_0}}\Bigg]. \end{aligned} \tag{D.6}$$

We find $I(q=0)=0$; in the limit $q\to\infty$, only the dilogarithms Li_2 survive and converge to:

$$\lim_{q\to\infty} I(q) = -i\pi\log\frac{\sqrt{\hbar\omega-\Omega_0}+\sqrt{\epsilon_k}}{\sqrt{\hbar\omega-\Omega_0}-\sqrt{\epsilon_k}}. \tag{D.7}$$

Inserting Eq. (D.7) into Eq. (D.5), we find Eq. (4.2) from the main text.

D.2 Finite Fermi level in the conduction band

We now consider the scenario where we have a finite electron density in the conduction band. At $k=0$, the lesser self-energy is defined as

$$\Sigma_{k=0}^<(\omega) = 4\pi\int_0^{k_\mathrm{F}} \frac{dq\, q^2}{(2\pi)^3}\frac{|g(q)|^2}{\hbar\omega - \frac{\hbar^2q^2}{2m_0} + \Omega_0}, \tag{D.8}$$

which can be integrated to give

$$\Sigma_{k=0}^<(\omega) = \frac{\alpha\,(\hbar\omega_0)^{3/2}}{\pi\sqrt{\hbar\omega+\Omega_0}}\log\frac{\sqrt{\hbar\omega+\Omega_0}+\sqrt{E_\mathrm{F}}}{\sqrt{\hbar\omega+\Omega_0}-\sqrt{E_\mathrm{F}}}. \tag{D.9}$$

For the greater self-energy, we have

$$\Sigma_{k=0}^>(\omega) = 4\pi\int_{k_\mathrm{F}}^\infty \frac{dq\, q^2}{(2\pi)^3}\frac{|g(q)|^2}{\hbar\omega - \frac{\hbar^2q^2}{2m_0} - \Omega_0}, \tag{D.10}$$

and hence

$$\Sigma^{>}_{k=0}(\omega) = -\frac{\alpha\,(\hbar\omega_0)^{3/2}}{\pi\sqrt{\hbar\omega-\Omega_0}}\left[\log\frac{\sqrt{\hbar\omega-\Omega_0}+\sqrt{E_\mathrm{F}}}{\sqrt{\hbar\omega-\Omega_0}-\sqrt{E_\mathrm{F}}}+i\pi\right]. \tag{D.11}$$

For general k, the lesser self-energy is obtained from an expression similar to that of Eq. (D.6), but with the sign of Ω_0 inverted, which then needs to be evaluated at $q=0$ and at $q=k_\mathrm{F}$, respectively, to give Eq. (4.16). The greater self-energy at $k\neq 0$ is obtained from Eq. (D.6) evaluated at $q=k_\mathrm{F}$ and $q\to\infty$, which leads to Eq. (4.18).

D.3 Finite Fermi level including free-carrier screening

In this section we provide details on the calculation of the self-energy in the presence of free-carrier screening. Inserting the screened coupling matrix element given in Eq. (4.1) into Eqs. (4.14) and (4.1), we obtain for the self-energy at $k=0$:

$$\Sigma^{<}_{k=0}(\omega) = \int_0^\infty \frac{dq\,q^2}{2\pi^2}\frac{|g(q)|^2}{|\varepsilon^{\mathrm{RPA}}(q)|^2}\frac{\theta\,(k_\mathrm{F}^2-q^2)}{\hbar\omega-\frac{\hbar^2q^2}{2m_0}+\Omega_0}, \tag{D.12}$$

$$\Sigma^{>}_{k=0}(\omega) = \int_0^\infty \frac{dq\,q^2}{2\pi^2}\frac{|g(q)|^2}{|\varepsilon^{\mathrm{RPA}}(q)|^2}\frac{\theta\,(q^2-k_\mathrm{F}^2)}{\hbar\omega-\frac{\hbar^2q^2}{2m_0}-\Omega_0}. \tag{D.13}$$

Using the Fröhlich matrix element in Eq. (1.1), we recover Eqs. (4.25) and (4.27) from the main text.

For general k, we write

$$\Sigma^{<}_{k}(\omega) = \int_0^{2\pi}d\phi\int_0^{\pi}d\theta\sin\theta\int_0^\infty \frac{dq\,q^2}{(2\pi)^3}\frac{|g(q)|^2}{|\varepsilon^{\mathrm{RPA}}(q)|^2}\frac{\theta\,(k_\mathrm{F}^2-(k^2+q^2+2kq\cos\theta))}{\hbar\omega-\frac{\hbar^2(k^2+q^2+2kq\cos\theta)}{2m_0}+\Omega_0}, \tag{D.14}$$

$$\Sigma^{>}_{k}(\omega) = \int_0^{2\pi}d\phi\int_0^{\pi}d\theta\sin\theta\int_0^\infty \frac{dq\,q^2}{(2\pi)^3}\frac{|g(q)|^2}{|\varepsilon^{\mathrm{RPA}}(q)|^2}\frac{\theta\,((k^2+q^2+2kq\cos\theta)-k_\mathrm{F})}{\hbar\omega-\frac{\hbar^2(k^2+q^2+2kq\cos\theta)}{2m_0}-\Omega_0}, \tag{D.15}$$

where ϕ and θ are relative angles between vectors $\mathbf{k}$ and $\mathbf{q}$. For the integration over angle θ, we use the substitution $x = k_\mathrm{F} - k^2 - q^2 - 2kq\cos\theta$ to obtain:

$$\Sigma_k^<(\omega) = \frac{2\pi}{\hbar}\frac{1}{2k}\int_0^\infty \frac{dq\,q}{(2\pi)^3}\frac{|g(q)|^2}{|\varepsilon^\mathrm{RPA}(q)|^2}\int_{k_\mathrm{F}^2-(k+q)^2}^{k_\mathrm{F}^2-(k-q)^2} dx \frac{\theta\left(x\right)}{\hbar\omega - \frac{\hbar^2(k_\mathrm{F}^2-x)}{2m_0} + \Omega_0}, \tag{D.16}$$

$$\Sigma_k^>(\omega) = \frac{2\pi}{\hbar}\frac{1}{2k}\int_0^\infty \frac{dq\,q}{(2\pi)^3}\frac{|g(q)|^2}{|\varepsilon^\mathrm{RPA}(q)|^2}\int_{k_\mathrm{F}^2-(k+q)^2}^{k_\mathrm{F}^2-(k-q)^2} dx \frac{\theta\left(-x\right)}{\hbar\omega - \frac{\hbar^2(k_\mathrm{F}^2-x)}{2m_0} - \Omega_0}. \tag{D.17}$$

As we are using spherical coordinates, we have
$k \geq 0$, $q \geq 0$ and $k_\mathrm{F} > 0$, and hence

$$k_\mathrm{F}^2 - (k-q)^2 \geq k_\mathrm{F}^2 - (k+q)^2, \tag{D.18}$$

allowing us to identify three ranges for the integration over q: For the lesser self-energy [Eq. (D.16)] we have: (i) If $k_\mathrm{F}^2 \geq (k+q)^2$, then $\theta\left(x\right) = 1$ and

$$\int_{k_\mathrm{F}^2-(k+q)^2}^{k_\mathrm{F}^2-(k-q)^2} \frac{dx}{\hbar\omega - \frac{\hbar^2(k_\mathrm{F}^2-x)}{2m_0} + \Omega_0} = \log\frac{\hbar\omega - \frac{\hbar^2(k+q)^2}{2m_0} + \Omega_0}{\hbar\omega - \frac{\hbar^2(k-q)^2}{2m_0} + \Omega_0}. \tag{D.19}$$

(ii) If $(k+q)^2 \geq k_\mathrm{F}^2 \geq (k-q)^2$, we have

$$\int_{0}^{k_\mathrm{F}^2-(k-q)^2} \frac{dx}{\hbar\omega - \frac{\hbar^2(k_\mathrm{F}^2-x)}{2m_0} + \Omega_0} = \log\frac{\hbar\omega - E_\mathrm{F} + \Omega_0}{\hbar\omega - \frac{\hbar^2(k-q)^2}{2m_0} + \Omega_0}. \tag{D.20}$$

(iii) For $(k-q)^2 \geq k_\mathrm{F}$, the Heaviside function in (D.16) vanishes everywhere. In particular, there is no contribution for $q \geq k_\mathrm{F}$. Combining Eqs. (D.16), (D.19) and (D.20), we recover Eq. (4.25) from the main text.

For the greater self-energy [Eq. (D.17)], we have (i) $\theta\left(-x\right) = 0$ whenever $k_\mathrm{F}^2 \geq (k+q)^2$, cancelling all contributions for $q < k_\mathrm{F}$. (ii) If $(k+q)^2 \geq k_\mathrm{F}^2 \geq (k-q)^2$, we have

$$\int_{k_\mathrm{F}^2-(k+q)^2}^{0} \frac{dx}{\hbar\omega - \frac{\hbar^2(k_\mathrm{F}^2-x)}{2m_0} - \Omega_0} = \log\frac{\hbar\omega - \frac{\hbar^2(k+q)^2}{2m_0} - \Omega_0}{\hbar\omega - \frac{\hbar^2(k-q)^2}{2m_0} - \Omega_0}. \tag{D.21}$$

(iii) For $(k-q)^2 \geq k_\mathrm{F}^2$, we obtain

$$\int_{k_\mathrm{F}^2-(k+q)^2}^{k_\mathrm{F}^2-(k-q)^2} \frac{dx}{\hbar\omega - \frac{\hbar^2(k_\mathrm{F}^2-x)}{2m_0} - \Omega_0} = \log\frac{\hbar\omega - \frac{\hbar^2(k+q)^2}{2m_0} - \Omega_0}{\hbar\omega - \frac{\hbar^2(k-q)^2}{2m_0} - \Omega_0}. \tag{D.22}$$

Combining Eqs. (D.17), (D.21) and (D.22), we recover Eq. (4.27) from the main text.

E

Effective mass of the retarded cumulant

In the framework of the retarded cumulant, the effective mass at $k = 0$ is defined as:

$$\frac{m^*}{m_0} = \left[1 + \frac{1}{\hbar}\frac{\partial \operatorname{Re}\Sigma_k(\omega)}{\partial \omega} + \frac{\partial \operatorname{Re}\Sigma_k(\omega)}{\partial \epsilon_k}\right]^{-1}_{\epsilon_k=0,\omega=0}, \tag{E.1}$$

where $\Sigma_k(\omega)$ is now the full retarded self-energy. Following the same steps as in the main text, one finds for the expansion to first order in α:

$$\begin{aligned}\frac{m^*}{m_0} &= 1 - \frac{\alpha}{6\pi}\left(\frac{8\hbar^2\omega_0^2 + 4E_\mathrm{F}^2}{E_\mathrm{F}^2 - \Omega_0^2}\sqrt{\frac{\hbar\omega_0}{E_\mathrm{F}}} - \pi\right. \\ &+ \left. 2\left(\tan^{-1}\sqrt{\frac{E_\mathrm{F}}{\hbar\omega_0}} - \tanh^{-1}\sqrt{\frac{E_\mathrm{F}}{\hbar\omega_0}}\right)\right) + \mathcal{O}\left(\alpha\right)^2\end{aligned} \tag{E.2}$$

Taking the limit $E_\mathrm{F} \to 0$, we reach

$$\lim_{E_\mathrm{F}\to 0}\frac{m^*}{m_0} = 1 + \frac{4\alpha}{3\pi}\sqrt{\frac{\hbar\omega_0}{E_\mathrm{F}}} + \frac{\alpha}{6} + \mathcal{O}\left(E_\mathrm{F}\right)^{3/2}, \tag{E.3}$$

which has the same behaviour for small E_F as Eq. (4.24) in the main text.

F

Quasiparticle energy and effective mass at finite Fermi energy

In both Dyson's and cumulant approaches we find that QP energy and effective mass are strongly doping-dependent. Starting with the Dyson approach, the dressed electron energy is found to be:

$$\begin{aligned} E_k &= \epsilon_k - \frac{\alpha\,(\hbar\omega_0)^{3/2}}{2\pi\sqrt{\epsilon_k}}\mathrm{Re}\Bigg[\log\frac{E_k+\Omega_0^*-E_\mathrm{F}}{E_k+\Omega_0^*-\epsilon_k}\log\left|\frac{\sqrt{E_\mathrm{F}}+\sqrt{\epsilon_k}}{\sqrt{E_\mathrm{F}}-\sqrt{\epsilon_k}}\right| \\ &- \log\frac{E_k-\Omega_0-E_\mathrm{F}}{E_k-\Omega_0+\epsilon_k}\log\left|\frac{\sqrt{E_\mathrm{F}}+\sqrt{\epsilon_k}}{\sqrt{E_\mathrm{F}}-\sqrt{\epsilon_k}}\right| + L\left(\sqrt{E_\mathrm{F}/\epsilon_k},\sqrt{(E_k+\Omega_0^*)/\epsilon_k}\right) \\ &- L\left(\sqrt{E_\mathrm{F}/\epsilon_k},\sqrt{(E_k-\Omega_0)/\epsilon_k}\right) + i\pi\log\frac{\sqrt{E_k-\Omega_0}+\sqrt{\epsilon_k}}{\sqrt{E_k-\Omega_0}-\sqrt{\epsilon_k}}\Bigg] - \mathrm{Re}\,\Sigma_{k_\mathrm{F}}(E_\mathrm{F}). \end{aligned} \tag{F.1}$$

At the bottom of the conduction band ($k=0$), this result yields the following expressions for the QP energy and the effective mass:

$$\begin{aligned} \frac{E_0}{\hbar\omega_0} &= \frac{\alpha}{\pi}\mathrm{Re}\Bigg[\frac{\sqrt{\hbar\omega_0}}{\sqrt{E_0+\Omega_0^*}}\log\frac{\sqrt{E_0+\Omega_0^*}+\sqrt{E_\mathrm{F}}}{\sqrt{E_0+\Omega_0^*}-\sqrt{E_\mathrm{F}}} \\ &- \frac{\sqrt{\hbar\omega_0}}{\sqrt{E_0-\Omega_0}}\left(\log\frac{\sqrt{E_0-\Omega_0}+\sqrt{E_\mathrm{F}}}{\sqrt{E_0-\Omega_0}-\sqrt{E_\mathrm{F}}}+i\pi\right) \\ &+ \frac{1}{2}\sqrt{\frac{\hbar\omega_0}{E_\mathrm{F}}}\Bigg(i\pi\log\frac{\sqrt{E_\mathrm{F}-\Omega_0}+\sqrt{E_\mathrm{F}}}{\sqrt{E_\mathrm{F}-\Omega_0}-\sqrt{E_\mathrm{F}}}+\mathrm{Li}_2\frac{2\sqrt{E_\mathrm{F}}}{\sqrt{E_\mathrm{F}}+\sqrt{E_\mathrm{F}+\Omega_0^*}} \\ &+ \mathrm{Li}_2\frac{2\sqrt{E_\mathrm{F}}}{\sqrt{E_\mathrm{F}}-\sqrt{E_\mathrm{F}+\Omega_0^*}}-\mathrm{Li}_2\frac{2\sqrt{E_\mathrm{F}}}{\sqrt{E_\mathrm{F}}+\sqrt{E_\mathrm{F}-\Omega_0}}-\mathrm{Li}_2\frac{2\sqrt{E_\mathrm{F}}}{\sqrt{E_\mathrm{F}}-\sqrt{E_\mathrm{F}-\Omega_0}}\Bigg)\Bigg], \end{aligned} \tag{F.2}$$

and

$$\begin{aligned}
\frac{m^*}{m_0} &= \left[1+\frac{\alpha(\hbar\omega_0)^{3/2}}{2\pi\,(E_0+\Omega_0^*)^{3/2}}\left(\log\frac{\sqrt{E_0+\Omega_0^*}+\sqrt{E_\mathrm{F}}}{\sqrt{E_0+\Omega_0^*}-\sqrt{E_\mathrm{F}}}+\frac{2\sqrt{E_\mathrm{F}\,(E_0+\Omega_0^*)}}{E_0-E_\mathrm{F}+\Omega_0^*}\right)\right.\\
&- \left.\frac{\alpha(\hbar\omega_0)^{3/2}}{2\pi\,(E_0-\Omega_0)^{3/2}}\left(\log\frac{\sqrt{E_0-\Omega_0}+\sqrt{E_\mathrm{F}}}{\sqrt{E_0-\Omega_0}-\sqrt{E_\mathrm{F}}}+\frac{2\sqrt{E_\mathrm{F}\,(E_0-\Omega_0)}}{E_0-E_\mathrm{F}-\Omega_0}-i\pi\right)\right]\\
&\times \left[1+\frac{2\alpha\,(\hbar\omega_0)^{3/2}}{3\pi}\left(\frac{E_0+\Omega_0^*}{E_\mathrm{F}\,(E_0-E_\mathrm{F}+\Omega_0^*)^2}-\frac{E_0-\Omega_0}{E_\mathrm{F}\,(E_0-E_\mathrm{F}-\Omega_0)^2}\right.\right.\\
&+ \frac{\tanh^{-1}\frac{\sqrt{E_\mathrm{F}}}{\sqrt{E_0+\Omega_0^*}}}{(E_0+\Omega_0^*)^{3/2}}-\frac{\tanh^{-1}\frac{\sqrt{E_\mathrm{F}}}{\sqrt{E_0-\Omega_0}}-\pi/2}{(E_0-\Omega_0)^{3/2}}\\
&- \left.\left.\frac{\sqrt{E_\mathrm{F}}\,(E_\mathrm{F}-2E_0-2\Omega_0^*)}{(E_0+\Omega_0^*)\,(E_\mathrm{F}-E_0-\Omega_0^*)^2}+\frac{\sqrt{E_\mathrm{F}}\,(E_\mathrm{F}-2E_0+2\Omega_0)}{(E_0-\Omega_0)\,(E_\mathrm{F}-E_0+\Omega_0)^2}\right)\right]^{-1}.
\end{aligned}$$

The weak-coupling expansions of Eqs. (F.3) and (F.2) are given by:

$$\begin{aligned}
\frac{E_0}{\hbar\omega_0} &= \frac{\alpha}{\pi}\mathrm{Re}\left[\log\frac{\sqrt{\Omega_0}+\sqrt{E_\mathrm{F}}}{\sqrt{\Omega_0}-\sqrt{E_\mathrm{F}}}+\left(i\log\frac{i\sqrt{\Omega_0^*}+\sqrt{E_\mathrm{F}}}{i\sqrt{\Omega_0^*}-\sqrt{E_\mathrm{F}}}-\pi\right)\right.\\
&+ \frac{1}{2}\sqrt{\frac{\hbar\omega_0}{E_\mathrm{F}}}\left(\mathrm{Li}_2\frac{2\sqrt{E_\mathrm{F}}}{\sqrt{E_\mathrm{F}}+\sqrt{E_\mathrm{F}+\Omega_0}}-\mathrm{Li}_2\frac{2\sqrt{E_\mathrm{F}}}{\sqrt{E_\mathrm{F}}-\sqrt{E_\mathrm{F}+\Omega_0}}-\mathrm{Li}_2\frac{2\sqrt{E_\mathrm{F}}}{\sqrt{E_\mathrm{F}}+\sqrt{E_\mathrm{F}-\Omega_0^*}}\right.\\
&+ \left.\left.\mathrm{Li}_2\frac{2\sqrt{E_\mathrm{F}}}{\sqrt{E_\mathrm{F}}-\sqrt{E_\mathrm{F}-\Omega_0^*}}+i\pi\log\frac{\sqrt{E_\mathrm{F}-\Omega_0^*}+\sqrt{E_\mathrm{F}}}{\sqrt{E_\mathrm{F}-\Omega_0^*}-\sqrt{E_\mathrm{F}}}\right)\right]+\mathcal{O}(\alpha)^2, \qquad \text{(F.3)}
\end{aligned}$$

and

$$\begin{aligned}
\frac{m^*}{m_0} &= 1+\frac{\alpha(\hbar\omega_0)^{3/2}}{2\pi\,\Omega_0^{3/2}}\left(\log\frac{\sqrt{\Omega_0}+\sqrt{E_\mathrm{F}}}{\sqrt{\Omega_0}-\sqrt{E_\mathrm{F}}}+\frac{2\sqrt{E_\mathrm{F}\,\Omega_0}}{-E_\mathrm{F}+\Omega_0}\right)\\
&- \frac{\alpha(\hbar\omega_0)^{3/2}}{2\pi\,(-\Omega_0^*)^{3/2}}\left(\log\frac{\sqrt{-\Omega_0^*}+\sqrt{E_\mathrm{F}}}{\sqrt{-\Omega_0^*}-\sqrt{E_\mathrm{F}}}+\frac{2\sqrt{E_\mathrm{F}\,(-\Omega_0^*)}}{-E_\mathrm{F}-\Omega_0^*}-i\pi\right)\\
&- \frac{2\alpha}{3\pi}\left(\tanh^{-1}\frac{\sqrt{E_\mathrm{F}}}{\sqrt{\Omega_0}}-\tanh^{-1}\frac{\sqrt{E_\mathrm{F}}}{\sqrt{-\Omega_0^*}}-\frac{\pi}{2\Omega_0^{*\,3/2}}\right.\\
&- \left.\frac{\sqrt{E_\mathrm{F}\,\hbar\omega_0}\,(E_\mathrm{F}-2\Omega_0)}{(E_\mathrm{F}-\Omega_0)^2}-\frac{\sqrt{E_\mathrm{F}\,\hbar\omega_0}(E_\mathrm{F}-2\Omega_0^*)}{(E_\mathrm{F}+\Omega_0^*)^2}\right)\\
&+ \left.\frac{4\alpha\,(\hbar\omega_0)^{3/2}\,(E_\mathrm{F}^2+\Omega_0^2)}{3\pi\,\sqrt{E_\mathrm{F}}(E_\mathrm{F}^2-\Omega_0^2)^2}\right]^{-1} \qquad \text{(F.4)}
\end{aligned}$$

As in the undoped case, all quantities in the Dyson approach are defined self-consistently. In the cumulant approach, the QP energy and effective mass are again evaluated at the

independent particle energy, and the self-energy is always linear in α. The k-dependent QP energy in the cumulant approach is given by:

$$E_k^< = \epsilon_k + \mathrm{Re}\left[\frac{\alpha\,(\hbar\omega_0)^{3/2}}{\pi\sqrt{\epsilon_k+\Omega_0}}\log\frac{\sqrt{\epsilon_k+\Omega_0}+\sqrt{E_\mathrm{F}}}{\sqrt{\epsilon_k+\Omega_0}-\sqrt{E_\mathrm{F}}} - \Sigma^<_{k_\mathrm{F}}(E_\mathrm{F})\right]. \tag{F.5}$$

At the Γ point, this becomes:

$$\begin{aligned}\frac{E_0^<}{\hbar\omega_0} &= \frac{\alpha}{\pi}\mathrm{Re}\left[\log\frac{\sqrt{\Omega_0}+\sqrt{E_\mathrm{F}}}{\sqrt{\Omega_0}-\sqrt{E_\mathrm{F}}} + \frac{1}{2}\sqrt{\frac{\hbar\omega_0}{E_\mathrm{F}}}\right. \\ &\times \left.\left(\mathrm{Li}_2\frac{2\sqrt{E_\mathrm{F}}}{\sqrt{E_\mathrm{F}}+\sqrt{E_\mathrm{F}+\Omega_0}} + \mathrm{Li}_2\frac{2\sqrt{E_\mathrm{F}}}{\sqrt{E_\mathrm{F}}-\sqrt{E_\mathrm{F}+\Omega_0}}\right)\right].\end{aligned} \tag{F.6}$$

The cumulant effective mass is given by

$$\begin{aligned}\frac{m^*}{m_0} &= \left[1 - \frac{\alpha}{2\pi}\left(\log\frac{\sqrt{\Omega_0}+\sqrt{E_\mathrm{F}}}{\sqrt{\Omega_0}-\sqrt{E_\mathrm{F}}} + \frac{2\sqrt{E_\mathrm{F}\,\Omega_0}}{\Omega_0 - E_\mathrm{F}}\right)\right. \\ &- \left.\frac{2\alpha}{3\pi\sqrt{E_\mathrm{F}}}\left(\sqrt{\hbar\omega_0} - \sqrt{E_\mathrm{F}}\tanh^{-1}\frac{\sqrt{E_F}}{\sqrt{\Omega_0}}\right)\right]^{-1}.\end{aligned} \tag{F.7}$$

G

Quasiparticle energy and effective mass at finite Fermi energy including free-carrier screening

Upon including free-carrier screening, the Dyson QP energy can be expressed in terms of the one-dimensional integral

$$
\begin{aligned}
E_k &= \epsilon_k - \frac{\alpha\,(\hbar\omega_0)^{3/2}}{2\pi\sqrt{\epsilon_k}}\mathrm{Re}\Bigg[\int_0^{k_\mathrm{F}-k}\frac{dq}{|\varepsilon^{\mathrm{RPA}}(q)|^2\,q}\log\frac{E_k-\frac{\hbar^2(k+q)^2}{2m_0}+\Omega_0^*}{E_k-\frac{\hbar^2(k-q)^2}{2m_0}+\Omega_0^*} \\
&+ \int_{k_\mathrm{F}-k}^{k_\mathrm{F}+k}\frac{dq}{|\varepsilon^{\mathrm{RPA}}(q)|^2\,q}\log\frac{E_k-E_\mathrm{F}+\Omega_0^*}{E_k-\frac{\hbar^2(k-q)^2}{2m_0}+\Omega_0^*} \\
&+ \int_{k_\mathrm{F}-k}^{k_\mathrm{F}+k}\frac{dq}{|\varepsilon^{\mathrm{RPA}}(q)|^2\,q}\log\frac{E_k-\frac{\hbar^2(k+q)^2}{2m_0}-\Omega_0}{E_k-E_\mathrm{F}-\Omega_0} \\
&+ \int_{k_\mathrm{F}+k}^{\infty}\frac{dq}{|\varepsilon^{\mathrm{RPA}}(q)|^2\,q}\log\frac{E_k-\frac{\hbar^2(k+q)^2}{2m_0}-\Omega_0}{E_k-\frac{\hbar^2(k-q)^2}{2m_0}-\Omega_0}\Bigg] - \mathrm{Re}\Sigma^<_{k_\mathrm{F}}(E_\mathrm{F}) - \mathrm{Re}\Sigma^>_{k_\mathrm{F}}(E_\mathrm{F}).
\end{aligned}
\tag{G.1}
$$

In particular, the occupied state at the band bottom becomes

$$\begin{aligned}
\frac{E_0}{\hbar\omega_0} &= \frac{\alpha}{\pi}\,\mathrm{Re}\Bigg[\int_0^{k_\mathrm{F}} \frac{dq/k_\mathrm{F}}{|\varepsilon^\mathrm{RPA}(q)|^2}\,\frac{2\sqrt{E_\mathrm{F}\,\hbar\omega_0}}{E_0-\frac{\hbar^2q^2}{2m_0}+\Omega_0^*} \\
&+ \int_{k_\mathrm{F}}^{\infty} \frac{dq/k_\mathrm{F}}{|\varepsilon^\mathrm{RPA}(q)|^2}\,\frac{2\sqrt{E_\mathrm{F}\,\hbar\omega_0}}{E_0-\frac{\hbar^2q^2}{2m_0}-\Omega_0} \\
&+ \frac{1}{2\pi}\sqrt{\frac{\hbar\omega_0}{E_\mathrm{F}}}\int_0^{2k_\mathrm{F}} \frac{dq}{|\varepsilon^\mathrm{RPA}(q)|^2\,q}\left(\log\frac{\Omega_0^*}{E_\mathrm{F}-\frac{\hbar^2(k_\mathrm{F}-q)^2}{2m_0}+\Omega_0^*}\right. \\
&+ \left.\log\frac{E_\mathrm{F}-\frac{\hbar^2(k_\mathrm{F}+q)^2}{2m_0}-\Omega_0}{-\Omega_0}\right) \\
&+ \frac{1}{2\pi}\sqrt{\frac{\hbar\omega_0}{E_\mathrm{F}}}\int_{2k_\mathrm{F}}^{\infty} \frac{dq}{|\varepsilon^\mathrm{RPA}(q)|^2\,q}\log\frac{E_\mathrm{F}-\frac{\hbar^2(k_\mathrm{F}+q)^2}{2m_0}-\Omega_0}{E_\mathrm{F}-\frac{\hbar^2(k_\mathrm{F}-q)^2}{2m_0}-\Omega_0}\Bigg].
\end{aligned} \tag{G.2}$$

The effective mass at the zone centre is given by:

$$\begin{aligned}
\frac{m^*}{m_0} &= \mathrm{Re}\Bigg[1+\frac{2\,\alpha\,(\hbar\omega_0)^{3/2}}{\pi\sqrt{E_\mathrm{F}}}\left(\int_0^{k_\mathrm{F}}\frac{dq/k_\mathrm{F}}{|\varepsilon^\mathrm{RPA}(q)|^2}\,\frac{E_\mathrm{F}}{\left(E_0-\frac{\hbar^2q^2}{2m_0}+\Omega_0^*\right)^2}\right. \\
&+ \left.\int_{k_\mathrm{F}}^{\infty}\frac{dq/k_\mathrm{F}}{|\varepsilon^\mathrm{RPA}(q)|^2}\,\frac{E_\mathrm{F}}{\left(E_0-\frac{\hbar^2q^2}{2m_0}-\Omega_0\right)^2}\right] \\
&\times \Bigg[1+\frac{2\alpha\,(\hbar\omega_0)^{3/2}}{3\pi\sqrt{E_\mathrm{F}}}\left(\int_0^{k_\mathrm{F}}\frac{dq/k_\mathrm{F}}{|\varepsilon^\mathrm{RPA}(q)|^2}\,\frac{E_\mathrm{F}\left(3E_0+\frac{\hbar^2q^2}{2m_0}+3\Omega_0^*\right)}{\left(E_0-\frac{\hbar^2q^2}{2m_0}+\Omega_0^*\right)^3}\right. \\
&+ \left.\int_{k_\mathrm{F}}^{\infty}\frac{dq/k_\mathrm{F}}{|\varepsilon^\mathrm{RPA}(q)|^2}\,\frac{E_\mathrm{F}\left(3E_0+\frac{\hbar^2q^2}{2m_0}-3\Omega_0\right)}{\left(E_0-\frac{\hbar^2q^2}{2m_0}-\Omega_0\right)^3}\right. \\
&- \left.\frac{1}{|\varepsilon^\mathrm{RPA}(k_\mathrm{F})|^2}\left(\frac{\Omega_0^*+E_0}{(E_0-E_\mathrm{F}+\Omega_0^*)^2}+\frac{\Omega_0-E_0}{(E_0-E_\mathrm{F}-\Omega_0)^2}\right)\right)\Bigg]^{-1}.
\end{aligned} \tag{G.3}$$

To linear order in α, the weak-coupling limit of Eq. (G.2) is simply given by:

$$\begin{aligned}
\frac{E_0}{\hbar\omega_0} &= \frac{\alpha}{\pi}\mathrm{Re}\Bigg[\int_0^{k_\mathrm{F}}\frac{dq/k_\mathrm{F}}{|\varepsilon^\mathrm{RPA}(q)|^2}\,\frac{2\sqrt{E_\mathrm{F}\,\hbar\omega_0}}{-\frac{\hbar^2q^2}{2m_0}+\Omega_0^*}+\int_{k_\mathrm{F}}^{\infty}\frac{dq/k_\mathrm{F}}{|\varepsilon^\mathrm{RPA}(q)|^2}\,\frac{2\sqrt{E_\mathrm{F}\,\hbar\omega_0}}{-\frac{\hbar^2q^2}{2m_0}-\Omega_0} \\
&+ \frac{1}{2}\sqrt{\frac{\hbar\omega_0}{E_\mathrm{F}}}\int_0^{2k_\mathrm{F}}\frac{dq}{|\varepsilon^\mathrm{RPA}(q)|^2\,q}\left(\log\frac{\Omega_0^*}{E_\mathrm{F}-\frac{\hbar^2(k_\mathrm{F}-q)^2}{2m_0}+\Omega_0^*}+\log\frac{E_\mathrm{F}-\frac{\hbar^2(k_\mathrm{F}+q)^2}{2m_0}-\Omega_0}{-\Omega_0}\right) \\
&+ \frac{1}{2}\sqrt{\frac{\hbar\omega_0}{E_\mathrm{F}}}\int_{2k_\mathrm{F}}^{\infty}\frac{dq}{|\varepsilon^\mathrm{RPA}(q)|^2\,q}\log\frac{E_\mathrm{F}-\frac{\hbar^2(k_\mathrm{F}+q)^2}{2m_0}-\Omega_0}{E_\mathrm{F}+\frac{\hbar^2(k_\mathrm{F}-q)^2}{2m_0}-\Omega_0}\Bigg]+\mathcal{O}(\alpha^2).
\end{aligned} \tag{G.4}$$

For Eq. (G.3), we find at small α:

$$\begin{aligned}\frac{m^*}{m_0} &= 1+\frac{2\,\alpha\,(\hbar\omega_0)^{3/2}}{3\pi\,\sqrt{E_{\rm F}}}{\rm Re}\Bigg[\int_0^{k_{\rm F}}\frac{dq/k_{\rm F}}{|\varepsilon^{\rm RPA}(q)|^2}\frac{3E_{\rm F}}{\left(\frac{\hbar^2q^2}{2m_0}-\Omega_0^*\right)^2}+\int_{k_{\rm F}}^{\infty}\frac{dq/k_{\rm F}}{|\varepsilon^{\rm RPA}(q)|^2}\frac{3E_{\rm F}}{\left(\frac{\hbar^2q^2}{2m_0}+\Omega_0\right)^2}\\ &- \int_0^{k_{\rm F}}\frac{dq/k_{\rm F}}{|\varepsilon^{\rm RPA}(q)|^2}\frac{E_{\rm F}\left(\frac{\hbar^2q^2}{2m_0}+3\Omega_0^*\right)}{\left(\frac{\hbar^2q^2}{2m_0}-\Omega_0^*\right)^3}-\int_{k_{\rm F}}^{\infty}\frac{dq/k_{\rm F}}{|\varepsilon^{\rm RPA}(q)|^2}\frac{E_{\rm F}\left(\frac{\hbar^2q^2}{2m_0}-3\Omega_0\right)}{\left(\frac{\hbar^2q^2}{2m_0}+\Omega_0\right)^3}\\ &- \frac{1}{|\varepsilon^{\rm RPA}(k_{\rm F})|^2}\left(\frac{\Omega_0^*}{\left(E_{\rm F}-\Omega_0^*\right)^2}+\frac{\Omega_0}{\left(E_{\rm F}+\Omega_0\right)^2}\right)\Bigg]+\mathcal{O}(\alpha^2).\end{aligned} \tag{G.5}$$

In the case of the cumulant approach, the QP energy for $k<k_{\rm F}$ is given by

$$\begin{aligned}E_k &= \epsilon_k-\frac{\alpha\,(\hbar\omega_0)^{3/2}}{2\pi\,\sqrt{\epsilon_k}}{\rm Re}\Bigg[\int_0^{k_{\rm F}-k}\frac{dq}{|\varepsilon^{\rm RPA}(q)|^2\,q}\log\frac{\Omega_0-\frac{\hbar^2(q^2+2kq)}{2m_0}}{\Omega_0-\frac{\hbar^2(q^2-2kq)}{2m_0}}\\ &+ \int_{k_{\rm F}-k}^{k_{\rm F}+k}\frac{dq}{|\varepsilon^{\rm RPA}(q)|^2\,q}\log\frac{\Omega_0+\epsilon_k-E_{\rm F}}{\Omega_0-\frac{\hbar^2(q^2-2kq)}{2m_0}}\Bigg]-{\rm Re}\Sigma^<_{k_{\rm F}}(E_{\rm F}).\end{aligned} \tag{G.6}$$

In the limit $k\to 0$, we recover

$$\begin{aligned}\frac{E_0}{\hbar\omega_0} &= \frac{\alpha}{\pi}{\rm Re}\Bigg[\int_0^{k_{\rm F}}\frac{dq/k_{\rm F}}{|\varepsilon^{\rm RPA}(q)|^2}\frac{2\sqrt{E_{\rm F}\,\hbar\omega_0}}{\Omega_0-\frac{\hbar^2q^2}{2m_0}}\\ &+ \frac{1}{2}\sqrt{\frac{\hbar\omega_0}{E_{\rm F}}}\int_0^{2k_{\rm F}}\frac{dq}{|\varepsilon^{\rm RPA}(q)|^2\,q}\log\frac{\Omega_0}{E_F-\frac{\hbar^2(k_{\rm F}-q)^2}{2m_0}+\Omega_0}\Bigg],\end{aligned} \tag{G.7}$$

which is already linear in α. Lastly, the cumulant effective mass at Γ is given by:

$$\begin{aligned}\frac{m^*}{m_0} &= {\rm Re}\Bigg[1-\frac{2\alpha\,(\hbar\omega_0)^{3/2}}{\pi\,k_{\rm F}/\sqrt{E_{\rm F}}}\int_0^{k_{\rm F}}\frac{dq}{|\varepsilon^{\rm RPA}(q)|^2}\left[\frac{1}{\left(-\frac{\hbar^2q^2}{2m_0}+\Omega_0\right)^2}+\frac{\frac{\hbar^2q^2}{2m_0}+3\Omega_0}{3\left(\frac{\hbar^2q^2}{2m_0}-\Omega_0\right)^3}\right]\\ &- \frac{2\alpha\,\hbar\omega_0}{3\pi}\sqrt{\frac{\hbar\omega_0}{E_{\rm F}}}\frac{1}{|\varepsilon^{\rm RPA}(k_{\rm F})|^2}\frac{\Omega_0}{(-E_{\rm F}+\Omega_0)^2}\Bigg]^{-1},\end{aligned} \tag{G.8}$$

and its small-α expansion is equal to

$$\begin{aligned}\frac{m^*}{m_0} &= {\rm Re}\Bigg[1+\frac{2\alpha\,(\hbar\omega_0)^{3/2}}{\pi\,k_{\rm F}/\sqrt{E_{\rm F}}}\int_0^{k_{\rm F}}\frac{dq}{|\varepsilon^{\rm RPA}(q)|^2}\left[\frac{1}{\left(-\frac{\hbar^2q^2}{2m_0}+\Omega_0\right)^2}+\frac{\frac{\hbar^2q^2}{2m_0}+3\Omega_0}{3\left(\frac{\hbar^2q^2}{2m_0}-\Omega_0\right)^3}\right]\\ &+ \frac{2\alpha\,\hbar\omega_0}{3\pi}\sqrt{\frac{\hbar\omega_0}{E_{\rm F}}}\frac{1}{|\varepsilon^{\rm RPA}(k_{\rm F})|^2}\frac{\Omega_0}{(-E_{\rm F}+\Omega_0)^2}\Bigg]+\mathcal{O}\left(\alpha^2\right).\end{aligned}$$

H

Anisotropic linearised Migdal-Eliashberg equations for the doped Fröhlich solid

$$Z_{\mathbf{k}}(i\omega_j) = 1 + \frac{k_{\mathrm{B}}T}{\hbar\omega_j\, N_{\mathrm{F}}} \sum_{\mathbf{k}'\omega'_j} \frac{\lambda_{\mathbf{k}\mathbf{k}'}(i\omega_j - i\omega'_j)\, \hbar\omega'_j\, Z_{\mathbf{k}'}(i\omega'_j)}{\left[\hbar\omega'_j\, Z_{\mathbf{k}'}(i\omega'_j)\right]^2 + \left[\epsilon_{\mathbf{k}'} - \mu_{\mathrm{C}} + \chi_{\mathbf{k}'}(i\omega'_j)\right]^2} \tag{H.1}$$

$$\chi_{\mathbf{k}}(i\omega_j) = -\frac{k_{\mathrm{B}}T}{N_{\mathrm{F}}} \sum_{\mathbf{k}'\omega'_j} \frac{\lambda_{\mathbf{k}\mathbf{k}'}(i\omega_j - i\omega'_j)\, \left[\epsilon_{\mathbf{k}'} - \mu_{\mathrm{C}} + \chi_{\mathbf{k}'}(i\omega'_j)\right]}{\left[\hbar\omega'_j\, Z_{\mathbf{k}'}(i\omega'_j)\right]^2 + \left[\epsilon_{\mathbf{k}'} - \mu_{\mathrm{C}} + \chi_{\mathbf{k}'}(i\omega'_j)\right]^2} \tag{H.2}$$

$$n_e = 1 - 2k_{\mathrm{B}}T \sum_{\mathbf{k}'\omega'_j} \frac{\epsilon_{\mathbf{k}'} - \mu_{\mathrm{C}} + \chi_{\mathbf{k}'}(i\omega'_j)}{\left[\hbar\omega'_j\, Z_{\mathbf{k}'}(i\omega'_j)\right]^2 + \left[\epsilon_{\mathbf{k}'} - \mu_{\mathrm{C}} + \chi_{\mathbf{k}'}(i\omega'_j)\right]^2} \tag{H.3}$$

are the renormalisation function, energy shift and particle number conservation condition for a single parabolic band $\mathbf{k}$. In the context of the doped Fröhlich solid, Eq. (H.3) describes the number of electrons *per unit cell*, n_e, and not the total number of electrons in a (finite) Born-von Kármán supercell, N_e [cf. Eq. (2.140)]. This discrepancy appears because we discuss the doped Fröhlich solid as an infinite crystal, i.e. the summation over momenta extends to $\pm\infty$. For details see Appendix A.

The kernel is defined as:

$$K_{\mathbf{k}\mathbf{k}'}(i\omega_j - i\omega'_j; T) = \frac{k_{\mathrm{B}}T}{N_{\mathrm{F}}} \frac{\left[\lambda_{\mathbf{k}\mathbf{k}'}(i\omega_j - i\omega'_j) - N_{\mathrm{F}}\, V_{\mathbf{k}\mathbf{k}'}\right]}{\left[\hbar\omega'_j\, Z_{\mathbf{k}'}(i\omega'_j)\right]^2 + \left[\epsilon_{\mathbf{k}'} - \mu_{\mathrm{C}} + \chi_{\mathbf{k}'}(i\omega'_j)\right]^2}, \tag{H.4}$$

and the order parameter is again given by:

$$\phi_{\mathbf{k}}(i\omega_j) = \sum_{\mathbf{k}'\omega'_j} K_{\mathbf{k}\mathbf{k}'}(i\omega_j - i\omega'_j; T)\phi_{\mathbf{k}'}(i\omega'_j). \tag{H.5}$$

When the largest eigenvalue of $K_{\mathbf{k}\mathbf{k}'}(i\omega_j - i\omega'_j; T)$ becomes equal to unity, Eq. (H.5) is fulfilled and $T = T_{\mathrm{C}}$.

References

[1] H. Fröhlich, H. Pelzer, and S. Zienau. "Properties of slow electrons in polar materials". In: *The London, Edinburgh, and Dublin Philosophical Magazine and Journal of Science* 41.314 (1950), pp. 221–242. URL: https://doi.org/10.1080/14786445008521794.

[2] A. F. Santander-Syro et al. "Two-dimensional electron gas with universal subbands at the surface of $SrTiO_3$". In: *Nature* 469 (2011), pp. 189–193. URL: https://doi.org/10.1038/nature09720.

[3] W. Meevasana et al. "Creation and control of a two-dimensional electron liquid at the bare $SrTiO_3$ surface". In: *Nat. Mater.* 10 (2011), pp. 114–118. URL: https://doi.org/10.1038/nmat2943.

[4] S. Moser et al. "Tunable Polaronic Conduction in Anatase TiO_2". In: *Phys. Rev. Lett.* 110 (2013), p. 196403. URL: https://link.aps.org/doi/10.1103/PhysRevLett.110.196403.

[5] J. J. Lee et al. "Interfacial mode coupling as the origin of the enhancement of T_C in FeSe films on $SrTiO_3$". In: *Nature* 515 (2014), pp. 245–248. URL: https://doi.org/10.1038/nature13894.

[6] Z. Wang et al. "Tailoring the nature and strength of electron-phonon interactions in the $SrTiO_3$ (001) 2D electron liquid". In: *Nat. Mater.* 15 (2016), pp. 835–839. URL: https://doi.org/10.1038/nmat4623.

[7] C. Chen et al. "Observation of a two-dimensional liquid of Fröhlich polarons at the bare $SrTiO_3$ surface". In: *Nat. Commun.* 6.8585 (2015). URL: https://doi.org/10.1038/ncomms9585.

[8] C. Cancellieri et al. "Polaronic metal state at the $LaAlO_3/SrTiO_3$ interface". In: *Nat. Commun.* 7.10386 (2016). URL: https://doi.org/10.1038/ncomms10386.

[9] J. M. Riley et al. "Crossover from lattice to plasmonic polarons of a spin-polarised electron gas in ferromagnetic EuO". In: *Nat. Comm.* 9.2305 (2018). URL: https://doi.org/10.1038/s41467-018-04749-w.

[10] M.-A. Husanu et al. "Electron-polaron dichotomy of charge carriers in perovskite oxides". In: *Commun. Phys* 3.62 (2020). URL: https://doi.org/10.1038/s42005-020-0330-6.

[11] R. Yukawa et al. "Phonon-dressed two-dimensional carriers on the ZnO surface". In: *Phys. Rev. B* 94 (2016), p. 165313. URL: https://link.aps.org/doi/10.1103/PhysRevB.94.165313.

[12] L. Brillouin. In: *J. Phys. Paris* 3 (1932), p. 379.

[13] L. Brillouin. In: *J. Phys. Paris* 4 (1933), p. 1.

[14] E. P. Wigner. In: *Math. U. Naturw. Anz. Ungar. Akad. Wiss.* 53 (1935), p. 477.

[15] R. P. Feynman. "Slow Electrons in a Polar Crystal". In: *Phys. Rev.* 97 (1955), pp. 660–665. URL: https://link.aps.org/doi/10.1103/PhysRev.97.660.

[16] S. Pekar. "Autolocalization of the electron in a dielectric inertially polarizing medium". In: *J. Exp. Theor. Phys.* 16 (1946), pp. 335–40.

[17] F. Caruso and F. Giustino. "Spectral fingerprints of electron-plasmon coupling". In: *Phys. Rev. B* 92 (2015), p. 045123. URL: https://link.aps.org/doi/10.1103/PhysRevB.92.045123.

[18] E. Młyńczak et al. "Kink far below the Fermi level reveals new electron-magnon scattering channel in Fe". In: *Nat. Commun.* 10 (2019), p. 505. URL: https://doi.org/10.1038/s41467-019-08445-1.

[19] S. Engelsberg and J. R. Schrieffer. "Coupled Electron-Phonon System". In: *Phys. Rev.* 131 (1963), pp. 993–1008. URL: https://link.aps.org/doi/10.1103/PhysRev.131.993.

[20] T. Valla et al. "Many-Body Effects in Angle-Resolved Photoemission: Quasiparticle Energy and Lifetime of a Mo(110) Surface State". In: *Phys. Rev. Lett.* 83 (1999), pp. 2085–2088. URL: https://link.aps.org/doi/10.1103/PhysRevLett.83.2085.

[21] A. B. Migdal. "Interaction between electrons and lattice vibrations in a normal metal". In: *Sov. Phys. JETP* 7 (1958), pp. 996–1001. URL: http://www.jetp.ac.ru/cgi-bin/e/index/e/7/6/p996?a=list.

[22] J. F. Schooley et al. "Dependence of the Superconducting Transition Temperature on Carrier Concentration in Semiconducting $SrTiO_3$". In: *Phys. Rev. Lett.* 14 (1965), pp. 305–307. URL: https://link.aps.org/doi/10.1103/PhysRevLett.14.305.

[23] X. Lin et al. "Critical Doping for the Onset of a Two-Band Superconducting Ground State in $SrTiO_{3-\delta}$". In: *Phys. Rev. Lett.* 112 (2014), p. 207002. URL: https://link.aps.org/doi/10.1103/PhysRevLett.112.207002.

[24] L. N. Cooper. "Bound Electron Pairs in a Degenerate Fermi Gas". In: *Phys. Rev.* 104 (1956), pp. 1189–1190. URL: https://link.aps.org/doi/10.1103/PhysRev.104.1189.

[25] J. Bardeen, L. N. Cooper, and J. R. Schrieffer. "Theory of Superconductivity". In: *Phys. Rev.* 108 (1957), pp. 1175–1204. URL: https://link.aps.org/doi/10.1103/PhysRev.108.1175.

[26] I. Giaever. "Electron Tunneling Between Two Superconductors". In: *Phys. Rev. Lett.* 5 (1960), pp. 464–466. URL: https://link.aps.org/doi/10.1103/PhysRevLett.5.464.

[27] E. Maxwell. "Isotope Effect in the Superconductivity of Mercury". In: *Phys. Rev.* 78 (1950), pp. 477–477. URL: https://link.aps.org/doi/10.1103/PhysRev.78.477.

[28] H. Fröhlich. "Theory of the Superconducting State. I. The Ground State at the Absolute Zero of Temperature". In: *Phys. Rev.* 79 (1950), pp. 845–856. URL: https://link.aps.org/doi/10.1103/PhysRev.79.845.

[29] G. D. Mahan. *Many-Particle Physics*. Second. New York: Plenum Publishers, 1993.

[30] W. L. McMillan. "Transition Temperature of Strong-Coupled Superconductors". In: *Phys. Rev.* 167 (1968), pp. 331–344. URL: https://link.aps.org/doi/10.1103/PhysRev.167.331.

[31] M. L. Cohen. "The Existence of a Superconducting State in Semiconductors". In: *Rev. Mod. Phys.* 36 (1964), pp. 240–243. URL: https://link.aps.org/doi/10.1103/RevModPhys.36.240.

[32] M. L. Cohen. "Superconductivity in Many-Valley Semiconductors and in Semimetals". In: *Phys. Rev.* 134 (1964), A511–A521. URL: https://link.aps.org/doi/10.1103/PhysRev.134.A511.

[33] L.V. Gurevich, A.I. Larkin, and Y.A. Firsov. "Possibility of superconductivity in semiconductors". In: *Sov. Phys. Sol. State* 131 (1962).

[34] J.K. Hulm et al. "Chapter 5 Superconductivity in Semiconductors and Semi-Metals". In: ed. by C.J. Gorter. Vol. 6. Progress in Low Temperature Physics. Elsevier, 1970, pp. 205–242. URL: https://www.sciencedirect.com/science/article/pii/S0079641708600645.

[35] E. Bustarret. "Superconductivity in doped semiconductors". In: *Physica C: Superconductivity and its Applications* 514 (2015). Superconducting Materials: Conventional, Unconventional and Undetermined, pp. 36–45. URL: https://www.sciencedirect.com/science/article/pii/S0921453415000489.

[36] Q.-Y. Wang et al. "Interface-Induced High-Temperature Superconductivity in Single Unit-Cell FeSe Films on $SrTiO_3$". In: *Chinese Physics Letters* 29.3 (2012), p. 037402. URL: https://doi.org/10.1088/0256-307x/29/3/037402.

[37] D. Liu et al. "Electronic origin of high-temperature superconductivity in single-layer FeSe superconductor". In: *Nat. Commun.* 3.931 (2012). URL: https://doi.org/10.1038/ncomms1946.

[38] S. Tan et al. "Interface-induced superconductivity and strain-dependent spin density waves in FeSe/$SrTiO_3$ thin films". In: *Nat. Mater.* 12 (2013), pp. 634–640. URL: https://doi.org/10.1038/nmat3654.

[39] R. Peng et al. "Measurement of an Enhanced Superconducting Phase and a Pronounced Anisotropy of the Energy Gap of a Strained FeSe Single Layer in FeSe/Nb : $SrTiO_3$/$KTaO_3$ Heterostructures Using Photoemission Spectroscopy". In: *Phys. Rev. Lett.* 112 (2014), p. 107001. URL: https://link.aps.org/doi/10.1103/PhysRevLett.112.107001.

[40] R. Peng et al. "Tuning the band structure and superconductivity in single-layer FeSe by interface engineering". In: *Nat. Comm.* 5.5044 (2014). URL: https://doi.org/10.1038/ncomms6044.

[41] Z. Zhang et al. "Onset of the Meissner effect at 65 K in FeSe thin film grown on Nb-doped SrTiO3 substrate". In: *Sci. Bull.* 60 (2015), pp. 1301–1304. URL: https://doi.org/10.1007/s11434-015-0842-8.

[42] J.-F. Ge et al. "Superconductivity above 100 K in single-layer FeSe films on doped $SrTiO_3$". In: *Nat. Mater.* 14.285 (2014). URL: https://doi.org/10.1038/nmat4153.

[43] Y. Xu et al. "Spectroscopic evidence of superconductivity pairing at 83K in single-layer FeSe/$SrTiO_3$ films". In: *Nat. Commun.* 12.2840 (2021). URL: https://doi.org/10.1038/s41467-021-23106-y.

[44] E. R. Margine and F. Giustino. "Anisotropic Migdal-Eliashberg theory using Wannier functions". In: *Phys. Rev. B* 87 (2013), p. 024505. URL: https://link.aps.org/doi/10.1103/PhysRevB.87.024505.

[45] M. Lüders et al. "Ab initio theory of superconductivity. I. Density functional formalism and approximate functionals". In: *Phys. Rev. B* 72 (2005), p. 024545. URL: https://link.aps.org/doi/10.1103/PhysRevB.72.024545.

[46] M. A. L. Marques et al. "Ab initio theory of superconductivity. II. Application to elemental metals". In: *Physical Review B* 72.2 (2005). URL: http://dx.doi.org/10.1103/PhysRevB.72.024546.

[47] H. Fröhlich. "Electrons in lattice fields". In: *Advances in Physics* 3.11 (1954), pp. 325–361. eprint: https://doi.org/10.1080/00018735400101213. URL: https://doi.org/10.1080/00018735400101213.

[48] J. T. Devreese. arXiv: cond-mat/0004497.

[49] J. T Devreese and A. S Alexandrov. "Fröhlich polaron and bipolaron: recent developments". In: *Rep. Prog. Phys.* 72.6 (2009), p. 066501. URL: https://doi.org/10.1088/0034-4885/72/6/066501.

[50] F. Giustino. "Electron-phonon interactions from first principles". In: *Rev. Mod. Phys.* 89 (2017), p. 015003. URL: https://link.aps.org/doi/10.1103/RevModPhys.89.015003.

[51] C. Verdi and F. Giustino. "Fröhlich Electron-Phonon Vertex from First Principles". In: *Phys. Rev. Lett.* 115 (2015), p. 176401. URL: https://link.aps.org/doi/10.1103/PhysRevLett.115.176401.

[52] J. Sjakste et al. "Wannier interpolation of the electron-phonon matrix elements in polar semiconductors: Polar-optical coupling in GaAs". In: *Phys. Rev. B* 92 (2015), p. 054307. URL: https://link.aps.org/doi/10.1103/PhysRevB.92.054307.

[53] J. Park et al. "Long-range quadrupole electron-phonon interaction from first principles". In: *Phys. Rev. B* 102 (2020), p. 125203. URL: https://link.aps.org/doi/10.1103/PhysRevB.102.125203.

[54] G. Brunin et al. "Electron-Phonon beyond Fröhlich: Dynamical Quadrupoles in Polar and Covalent Solids". In: *Phys. Rev. Lett.* 125 (2020), p. 136601. URL: https://link.aps.org/doi/10.1103/PhysRevLett.125.136601.

[55] S. M. Story et al. "Cumulant expansion for phonon contributions to the electron spectral function". In: *Phys. Rev. B* 90 (2014), p. 195135. URL: https://link.aps.org/doi/10.1103/PhysRevB.90.195135.

[56] C. Verdi, F. Caruso, and F. Giustino. "Origin of the crossover from polarons to Fermi liquids in transition metal oxides". In: *Nat. Commun.* 8.15769 (2017). URL: https://doi.org/10.1038/ncomms15769.

[57] J. P. Nery et al. "Quasiparticles and phonon satellites in spectral functions of semiconductors and insulators: Cumulants applied to the full first-principles theory and the Fröhlich polaron". In: *Phys. Rev. B* 97 (2018), p. 115145. URL: https://link.aps.org/doi/10.1103/PhysRevB.97.115145.

[58] J.-J. Zhou and M. Bernardi. "Predicting charge transport in the presence of polarons: The beyond-quasiparticle regime in $SrTiO_3$". In: *Phys. Rev. Res.* 1 (2019), p. 033138. URL: https://link.aps.org/doi/10.1103/PhysRevResearch.1.033138.

[59] N. Kandolf, C. Verdi, and F. Giustino. "Many-body Green's function approaches to the doped Fröhlich solid: Exact solutions and anomalous mass enhancement". In: *Phys. Rev. B* 105 (2022), p. 085148. URL: https://link.aps.org/doi/10.1103/PhysRevB.105.085148.

[60] D. C. Langreth. "Singularities in the X-Ray Spectra of Metals". In: *Phys. Rev. B* 1 (1970), pp. 471–477. URL: https://link.aps.org/doi/10.1103/PhysRevB.1.471.

[61] L. Hedin. "Effects of Recoil on Shake-Up Spectra in Metals". In: *Physica Scripta* 21.3-4 (1980), pp. 477–480. URL: https://doi.org/10.1088/0031-8949/21/3-4/039.

[62] F. Aryasetiawan, L. Hedin, and K. Karlsson. "Multiple Plasmon Satellites in Na and Al Spectral Functions from Ab Initio Cumulant Expansion". In: *Phys. Rev. Lett.* 77 (1996), pp. 2268–2271. URL: https://link.aps.org/doi/10.1103/PhysRevLett.77.2268.

[63] J. Lischner, D. Vigil-Fowler, and S. G. Louie. "Physical Origin of Satellites in Photoemission of Doped Graphene: An Ab Initio GW Plus Cumulant Study". In: *Phys. Rev. Lett.* 110 (2013), p. 146801. URL: https://link.aps.org/doi/10.1103/PhysRevLett.110.146801.

[64] J. J. Kas, J. J. Rehr, and L. Reining. "Cumulant expansion of the retarded one-electron Green function". In: *Phys. Rev. B* 90 (2014), p. 085112. URL: https://link.aps.org/doi/10.1103/PhysRevB.90.085112.

[65] F. Caruso, H. Lambert, and F. Giustino. "Band Structures of Plasmonic Polarons". In: *Phys. Rev. Lett.* 114 (2015), p. 146404. URL: https://link.aps.org/doi/10.1103/PhysRevLett.114.146404.

[66] F. Caruso and F. Giustino. "Theory of electron-plasmon coupling in semiconductors". In: *Phys. Rev. B* 94 (2016), p. 115208. URL: https://link.aps.org/doi/10.1103/PhysRevB.94.115208.

[67] F. Caruso and F. Giustino. "The GW plus cumulant method and plasmonic polarons: application to the homogeneous electron gas". In: *Eur. Phys. J B* 89.11 (2016), p. 238. URL: https://doi.org/10.1140/epjb/e2016-70028-4.

[68] B. Gumhalter et al. "On the combined use of GW approximation and cumulant expansion in the calculations of quasiparticle spectra: The paradigm of Si valence bands". In: *Phys. Rev. B* 94 (2016), p. 035103. URL: https://link.aps.org/doi/10.1103/PhysRevB.94.035103.

[69] J. S. Zhou et al. "Cumulant Green's function calculations of plasmon satellites in bulk sodium: Influence of screening and the crystal environment". In: *Phys. Rev. B* 97 (2018), p. 035137. URL: https://link.aps.org/doi/10.1103/PhysRevB.97.035137.

[70] M. Tzavala et al. "Nonlinear response in the cumulant expansion for core-level photoemission". In: *Phys. Rev. Research* 2 (2020), p. 033147. URL: https://link.aps.org/doi/10.1103/PhysRevResearch.2.033147.

[71] F. Caruso et al. "Electron-plasmon and electron-phonon satellites in the angle-resolved photoelectron spectra of n-doped anatase TiO_2". In: *Phys. Rev. B* 97 (2018), p. 165113. URL: https://link.aps.org/doi/10.1103/PhysRevB.97.165113.

[72] G. Antonius, Y.-H. Chan, and S. G. Louie. "Polaron spectral properties in doped ZnO and $SrTiO_3$ from first principles". In: *Phys. Rev. Res.* 2 (2020), p. 043296. URL: https://link.aps.org/doi/10.1103/PhysRevResearch.2.043296.

[73] J. S. Zhou et al. "Unraveling intrinsic correlation effects with angle-resolved photoemission spectroscopy". In: *Proc. Nat. Acad. Sci. USA* 117.46 (2020), pp. 28596–28602. URL: https://www.pnas.org/content/117/46/28596.

[74] T.-D. Lee and D. Pines. "The Motion of Slow Electrons in Polar Crystals". In: *Phys. Rev.* 88 (1952), pp. 960–961. URL: https://link.aps.org/doi/10.1103/PhysRev.88.960.

[75] J. Röseler. "A new variational ansatz in the polaron theory". In: *Phys. Status Solidi B* 25.1 (1968), pp. 311–316. URL: https://onlinelibrary.wiley.com/doi/abs/10.1002/pssb.19680250129.

[76] M.A. Smondyrev. "Diagrams in the polaron model". In: *Theor. Math. Phys.* 68 (1986). URL: https://doi.org/10.1007/BF01017794.

[77] O. V. Selyugin and M. A. Smondyrev. "Phase Transition and Padé Approximants for Fröhlich Polarons". In: *Phys. Status Solidi B* 155.1 (1989), pp. 155–167. URL: https://onlinelibrary.wiley.com/doi/abs/10.1002/pssb.2221550114.

[78] N. V. Prokof'ev and Boris V. Svistunov. "Polaron Problem by Diagrammatic Quantum Monte Carlo". In: *Phys. Rev. Lett.* 81 (1998), pp. 2514–2517. URL: https://link.aps.org/doi/10.1103/PhysRevLett.81.2514.

[79] A. S. Mishchenko et al. "Diagrammatic quantum Monte Carlo study of the Fröhlich polaron". In: *Phys. Rev. B* 62 (2000), pp. 6317–6336. URL: https://link.aps.org/doi/10.1103/PhysRevB.62.6317.

[80] Q. Song et al. "Evidence of cooperative effect on the enhanced superconducting transition temperature at the FeSe/$SrTiO_3$ interface". In: *Nat. Commun.* 10.758 (2019). URL: https://doi.org/10.1038/s41467-019-08560-z.

[81] S Gariglio et al. "Superconductivity at the $LaAlO_3$/$SrTiO_3$ interface". In: *J. Phys. C* 21.16 (2009), p. 164213. URL: https://doi.org/10.1088%2F0953-8984%2F21%2F16%2F164213.

[82] N. Reyren et al. "Superconducting Interfaces Between Insulating Oxides". In: *Science* 317.5842 (2007), pp. 1196–1199. URL: https://science.sciencemag.org/content/317/5842/1196.

[83] J. Biscaras et al. "Two-dimensional superconductivity at a Mott insulator/band insulator interface $LaTiO_3$/$SrTiO_3$". In: *Nat. Commun.* 1.89 (2010). URL: https://doi.org/10.1038/ncomms1084.

[84] N Lebedev et al. "Inhomogeneous superconductivity and quasilinear magnetoresistance at amorphous $LaTiO_3$/$SrTiO_3$ interfaces". In: *Journal of Physics: Condensed Matter* 33.5 (2020), p. 055001. URL: https://doi.org/10.1088/1361-648x/abc102.

[85] J. F. Schooley, W. R. Hosler, and Marvin L. Cohen. "Superconductivity in Semiconducting $SrTiO_3$". In: *Phys. Rev. Lett.* 12 (1964), pp. 474–475. URL: https://link.aps.org/doi/10.1103/PhysRevLett.12.474.

[86] C. Collignon et al. "Metallicity and Superconductivity in Doped Strontium Titanate". In: *Annual Review of Condensed Matter Physics* 10.1 (2019), pp. 25–44. eprint: https://doi.org/10.1146/annurev-conmatphys-031218-013144. URL: https://doi.org/10.1146/annurev-conmatphys-031218-013144.

[87] J. G. Bednorz and K. Alex Müller. "Perovskite-Type Oxides—the New Approach to High-Tc Superconductivity. Nobel Lecture". In: *Angewandte Chemie International Edition in English* 27.5 (1988), pp. 735–748. URL: https://onlinelibrary.wiley.com/doi/abs/10.1002/anie.198807351.

[88] Terence M. Bretz-Sullivan et al. arXiv: 1904.03121.

[89] P. P. Edwards and Michell J. Sienko. "Universality aspects of the metal-nonmetal transition in condensed media". In: *Phys. Rev. B* 17 (1978), pp. 2575–2581. URL: https://link.aps.org/doi/10.1103/PhysRevB.17.2575.

[90] X. Lin et al. "Fermi Surface of the Most Dilute Superconductor". In: *Phys. Rev. X* 3 (2013), p. 021002. URL: https://link.aps.org/doi/10.1103/PhysRevX.3.021002.

[91] K. A. Müller and H. Burkard. "$SrTiO_3$: An intrinsic quantum paraelectric below 4 K". In: *Phys. Rev. B* 19 (1979), pp. 3593–3602. URL: https://link.aps.org/doi/10.1103/PhysRevB.19.3593.

[92] W. Zhong and D. Vanderbilt. "Effect of quantum fluctuations on structural phase transitions in $SrTiO_3$ and $BaTiO_3$". In: *Phys. Rev. B* 53 (1996), pp. 5047–5050. URL: https://link.aps.org/doi/10.1103/PhysRevB.53.5047.

[93] A. Spinelli et al. "Electronic transport in doped $SrTiO_3$: Conduction mechanisms and potential applications". In: *Phys. Rev. B* 81 (2010), p. 155110. URL: https://link.aps.org/doi/10.1103/PhysRevB.81.155110.

[94] J. M. Edge et al. "Quantum Critical Origin of the Superconducting Dome in $SrTiO_3$". In: *Phys. Rev. Lett.* 115 (2015), p. 247002. URL: https://link.aps.org/doi/10.1103/PhysRevLett.115.247002.

[95] C. Enderlein et al. "Superconductivity mediated by polar modes in ferroelectric metals". In: *Nat. Commun* 11 (2020), p. 4852. URL: https://doi.org/10.1038/s41467-020-18438-0.

[96] C. W. Rischau et al. "Isotope tuning of the superconducting dome of strontium titanate". In: *Phys. Rev. Research* 4 (2022), p. 013019. URL: https://link.aps.org/doi/10.1103/PhysRevResearch.4.013019.

[97] M. N. Gastiasoro, J. Ruhman, and R. M. Fernandes. "Superconductivity in dilute $SrTiO_3$: A review". In: *Annals of Physics* 417 (2020). Eliashberg theory at 60: Strong-coupling superconductivity and beyond, p. 168107. URL: http://www.sciencedirect.com/science/article/pii/S0003491620300403.

[98] C. S. Koonce et al. "Superconducting Transition Temperatures of Semiconducting $SrTiO_3$". In: *Phys. Rev.* 163 (1967), pp. 380–390. URL: https://link.aps.org/doi/10.1103/PhysRev.163.380.

[99] L. P. Gor'kov. "Phonon mechanism in the most dilute superconductor n-type $SrTiO_3$". In: *Proc. Nat. Acad. Sci. USA* 113.17 (2016), pp. 4646–4651. URL: https://www.pnas.org/content/113/17/4646.

[100] P. Wölfle and A. V. Balatsky. "Superconductivity at low density near a ferroelectric quantum critical point: Doped $SrTiO_3$". In: *Phys. Rev. B* 98 (2018), p. 104505. URL: https://link.aps.org/doi/10.1103/PhysRevB.98.104505.

[101] M. N. Gastiasoro, A. V. Chubukov, and R. M. Fernandes. "Phonon-mediated superconductivity in low carrier-density systems". In: *Phys. Rev. B* 99 (2019), p. 094524. URL: https://link.aps.org/doi/10.1103/PhysRevB.99.094524.

[102] Y. Takada. "Theory of superconductivity in polar semiconductors and its application to n-type semiconducting $SrTiO_3$". In: *Jour. Phys. Soc. Japan* 49.4 (1980). URL: https://doi.org/10.1143/JPSJ.49.1267.

[103] J. Ruhman and P. A. Lee. "Superconductivity at very low density: The case of strontium titanate". In: *Phys. Rev. B* 94 (2016), p. 224515. URL: https://link.aps.org/doi/10.1103/PhysRevB.94.224515.

[104] G.M. Eliashberg. "Interactions between electrons and lattice vibrations in a superconductor". In: *JETP* 11 (1960).

[105] D. J. Scalapino. In: *Superconductivity*. Ed. by R. D. Parks. Vol. 1. New York: Dekker, 1969, p. 499.

[106] P. B. Allen and B. Mitrović. "Theory of Superconducting T_C". In: *Solid State Physics*. Ed. by Henry Ehrenreich, Frederick Seitz, and David Turnbull. Vol. 37. Solid State Physics. Academic Press, 1983, pp. 1–92. URL: http://www.sciencedirect.com/science/article/pii/S0081194708606657.

[107] F. Marsiglio and J. P. Carbotte. "Electron-Phonon Superconductivity". In: *Superconductivity*. Ed. by K. H. Bennemann and J. B. Ketterson. Springer, 2008.

[108] P. B. Allen. "Transition temperature and gap anisotropy of pure and impure semiconductors". In: *Zeitschrift fuer Physik B* 47 (1982), pp. 45–54.

[109] C. Heil et al. "Origin of Superconductivity and Latent Charge Density Wave in NbS_2". In: *Phys. Rev. Lett.* 119 (2017), p. 087003. URL: https://link.aps.org/doi/10.1103/PhysRevLett.119.087003.

[110] H. Paudyal et al. "Superconducting properties of $MoTe_2$ from ab initio anisotropic Migdal-Eliashberg theory". In: *Phys. Rev. B* 101 (2020), p. 214515. URL: https://link.aps.org/doi/10.1103/PhysRevB.101.214515.

[111] A. N. Kolmogorov and S. Curtarolo. "Prediction of different crystal structure phases in metal borides: A lithium monoboride analog to MgB_2". In: *Phys. Rev. B* 73 (2006), p. 180501. URL: https://link.aps.org/doi/10.1103/PhysRevB.73.180501.

[112] G. Savini, A. C. Ferrari, and F. Giustino. "First-Principles Prediction of Doped Graphane as a High-Temperature Electron-Phonon Superconductor". In: *Phys. Rev. Lett.* 105 (2010), p. 037002. URL: https://link.aps.org/doi/10.1103/PhysRevLett.105.037002.

[113] L. Hedin. "New Method for Calculating the One-Particle Green's Function with Application to the Electron-Gas Problem". In: *Phys. Rev.* 139 (1965), A796–A823. URL: https://link.aps.org/doi/10.1103/PhysRev.139.A796.

[114] G. Baym. "Field-theoretic approach to the properties of the solid state". In: *Annals of Physics* 14 (1961), pp. 1–42. URL: https://www.sciencedirect.com/science/article/pii/0003491661900501.

[115] L. Hedin and S. Lundqvist. "Effects of Electron-Electron and Electron-Phonon Interactions on the One-Electron States of Solids". In: *Solid State Phys.* 23 (1969), pp. 1–180.

[116] T. Kato, T. Kobayashi, and M. Namiki. "Formal Theory of Green Functions". In: *Progress of Theoretical Physics Supplement* 15 (1960), pp. 3–60. URL: https://doi.org/10.1143/PTPS.15.3.

[117] A. L. Fetter and J. D. Walecka. *Quantum Theory of Many-Particle Systems*. Dover Publications, New York, 2003.

[118] H. Y. Fan. "Temperature Dependence of the Energy Gap in Semiconductors". In: *Phys. Rev.* 82 (1951), pp. 900–905. URL: https://link.aps.org/doi/10.1103/PhysRev.82.900.

[119] P. B. Allen and V. Heine. "Theory of the temperature dependence of electronic band structures". In: *J. Phy. C* 9.12 (1976), pp. 2305–2312. URL: https://doi.org/10.1088/0022-3719/9/12/013.

[120] P. B. Allen. "Solids with thermal or static disorder. I. One-electron properties". In: *Phys. Rev. B* 18 (1978), pp. 5217–5224. URL: https://link.aps.org/doi/10.1103/PhysRevB.18.5217.

[121] A. Marini. "Ab Initio Finite-Temperature Excitons". In: *Phys. Rev. Lett.* 101 (2008), p. 106405. URL: https://link.aps.org/doi/10.1103/PhysRevLett.101.106405.

[122] F. Giustino, S. G. Louie, and M. L. Cohen. "Electron-Phonon Renormalization of the Direct Band Gap of Diamond". In: *Phys. Rev. Lett.* 105 (2010), p. 265501. URL: https://link.aps.org/doi/10.1103/PhysRevLett.105.265501.

[123] G. Antonius et al. "Many-Body Effects on the Zero-Point Renormalization of the Band Structure". In: *Phys. Rev. Lett.* 112 (2014), p. 215501. URL: https://link.aps.org/doi/10.1103/PhysRevLett.112.215501.

[124] D. Bohm and D. Pines. "A Collective Description of Electron Interactions. I. Magnetic Interactions". In: *Phys. Rev.* 82 (1951), pp. 625–634. URL: https://link.aps.org/doi/10.1103/PhysRev.82.625.

[125] D. Bohm and D. Pines. "A Collective Description of Electron Interactions: II. Collective vs Individual Particle Aspects of the Interactions". In: *Phys. Rev.* 85 (1952), pp. 338–353. URL: https://link.aps.org/doi/10.1103/PhysRev.85.338.

[126] D. Bohm and D. Pines. "A Collective Description of Electron Interactions: III. Coulomb Interactions in a Degenerate Electron Gas". In: *Phys. Rev.* 92 (1953), pp. 609–625. URL: https://link.aps.org/doi/10.1103/PhysRev.92.609.

[127] M. S. Hybertsen and S. G. Louie. "Electron correlation in semiconductors and insulators: Band gaps and quasiparticle energies". In: *Phys. Rev. B* 34 (1986), pp. 5390–5413. URL: https://link.aps.org/doi/10.1103/PhysRevB.34.5390.

[128] A. Damascelli, Z. Hussain, and Z.-X. Shen. "Angle-resolved photoemission studies of the cuprate superconductors". In: *Rev. Mod. Phys.* 75 (2003), pp. 473–541. URL: https://link.aps.org/doi/10.1103/RevModPhys.75.473.

[129] A.A. Abrikosov, L. P. Gor'kov, and I.E. Dzyaloshinski. *Methods of Quantum Field Theory in Statistical Physics*. Dover, New York, 1975.

[130] A. Eiguren, C. Ambrosch-Draxl, and P. M. Echenique. "Self-consistently renormalized quasiparticles under the electron-phonon interaction". In: *Phys. Rev. B* 79 (2009), p. 245103. URL: https://link.aps.org/doi/10.1103/PhysRevB.79.245103.

[131] M. Schlipf, S. Poncé, and F. Giustino. "Carrier Lifetimes and Polaronic Mass Enhancement in the Hybrid Halide Perovskite $CH_3NH_3PbI_3$ from Multiphonon Fröhlich Coupling". In: *Phys. Rev. Lett.* 121 (2018), p. 086402. URL: https://link.aps.org/doi/10.1103/PhysRevLett.121.086402.

[132] E. P. Gross. "Transformation Theory". In: *Mathematical Methods in Solid State and Superfluid Theory: Scottish Universities' Summer School*. Ed. by R. C. Clark and G. H. Derrick. Boston, MA: Springer US, 1968, pp. 46–120. URL: https://doi.org/10.1007/978-1-4899-6435-9_2.

[133] O. Gunnarsson, V. Meden, and K. Schönhammer. "Corrections to Migdal's theorem for spectral functions: A cumulant treatment of the time-dependent Green's function". In: *Phys. Rev. B* 50 (1994), pp. 10462–10473. URL: https://link.aps.org/doi/10.1103/PhysRevB.50.10462.

[134] R. Kubo. "Generalized Cumulant Expansion Method". In: *Journal of the Physical Society of Japan* 17.7 (1962), pp. 1100–1120.

[135] F. Aryasetiawan. "The GW Approximation and Vertex Corrections". In: *Strong Coulomb Correlations in Electronic Structure Calculations*. Ed. by V.I. Anisimov. Vol. 1. Boca Raton: CRC Press, 2000.

[136] Yoichiro Nambu. "Quasi-Particles and Gauge Invariance in the Theory of Superconductivity". In: *Phys. Rev.* 117 (1960), pp. 648–663. URL: https://link.aps.org/doi/10.1103/PhysRev.117.648.

[137] L.P Gorkov. "On the energy spectrum of superconductors". In: *JETP* 7 (1958).

[138] F. Marsiglio. "Eliashberg theory: A short review". In: *Annals of Physics* 417 (2020). Eliashberg theory at 60: Strong-coupling superconductivity and beyond, p. 168102. URL: https://www.sciencedirect.com/science/article/pii/S000349162030035X.

[139] K.-H. Lee, K. J. Chang, and M. L. Cohen. "First-principles calculations of the Coulomb pseudopotential μ^*: Application to Al". In: *Phys. Rev. B* 52 (1995), pp. 1425–1428. URL: https://link.aps.org/doi/10.1103/PhysRevB.52.1425.

[140] S. Poncé et al. "EPW: Electron–phonon coupling, transport and superconducting properties using maximally localized Wannier functions". In: *Computer Physics Communications* 209 (2016), pp. 116–133. URL: https://www.sciencedirect.com/science/article/pii/S0010465516302260.

[141] H. J. Vidberg and J. W. Serene. "Solving the Eliashberg equations by means of N-point Padé approximants". In: *Journal of Low Temperature Physics* 29 (1977), pp. 179–192. URL: https://doi.org/10.1007/BF00655090.

[142] C.R. Leavens and D.S. Ritchie. "Extension of the N-point Padé approximants solution of the Eliashberg equations to T $\approx T_C$". In: *Solid State Communications* 53.2 (1985), pp. 137–142. URL: https://www.sciencedirect.com/science/article/pii/0038109885901127.

[143] K. S. D. Beach, R. J. Gooding, and F. Marsiglio. "Reliable Padé analytical continuation method based on a high-accuracy symbolic computation algorithm". In: *Phys. Rev. B* 61 (2000), pp. 5147–5157. URL: https://link.aps.org/doi/10.1103/PhysRevB.61.5147.

[144] F. Marsiglio, M. Schossmann, and J. P. Carbotte. "Iterative analytic continuation of the electron self-energy to the real axis". In: *Phys. Rev. B* 37 (1988), pp. 4965–4969. URL: https://link.aps.org/doi/10.1103/PhysRevB.37.4965.

[145] P. Morel and P. W. Anderson. "Calculation of the Superconducting State Parameters with Retarded Electron-Phonon Interaction". In: *Phys. Rev.* 125 (1962), pp. 1263–1271. URL: https://link.aps.org/doi/10.1103/PhysRev.125.1263.

[146] D. J. Scalapino, J. R. Schrieffer, and J. W. Wilkins. "Strong-Coupling Superconductivity. I". In: *Phys. Rev.* 148 (1966), pp. 263–279. URL: https://link.aps.org/doi/10.1103/PhysRev.148.263.

[147] P. B. Allen. "Fermi-surface harmonics: A general method for nonspherical problems. Application to Boltzmann and Eliashberg equations". In: *Phys. Rev. B* 13 (1976), pp. 1416–1427. URL: https://link.aps.org/doi/10.1103/PhysRevB.13.1416.

[148] M. A. Biondi and M. P. Garfunkel. "Millimeter Wave Absorption in Superconducting Aluminum. I. Temperature Dependence of the Energy Gap". In: *Phys. Rev.* 116 (1959), pp. 853–861. URL: https://link.aps.org/doi/10.1103/PhysRev.116.853.

[149] K. van Benthem, C. Elsässer, and R. H. French. "Bulk electronic structure of SrTiO3: Experiment and theory". In: *Journal of Applied Physics* 90.12 (2001), pp. 6156–6164. URL: https://doi.org/10.1063/1.1415766.

[150] G. Shirane and Y. Yamada. "Lattice-Dynamical Study of the 110°K Phase Transition in $SrTiO_3$". In: *Phys. Rev.* 177 (1969), pp. 858–863. URL: https://link.aps.org/doi/10.1103/PhysRev.177.858.

[151] W. Zhong, R. D. King-Smith, and D. Vanderbilt. "Giant LO-TO splittings in perovskite ferroelectrics". In: *Phys. Rev. Lett.* 72 (1994), pp. 3618–3621. URL: https://link.aps.org/doi/10.1103/PhysRevLett.72.3618.

[152] R. Wahl, D. Vogtenhuber, and G. Kresse. "$SrTiO_3$ and $BaTiO_3$ revisited using the projector augmented wave method: Performance of hybrid and semilocal functionals". In: *Phys. Rev. B* 78 (2008), p. 104116. URL: https://link.aps.org/doi/10.1103/PhysRevB.78.104116.

[153] H. Uwe and T. Sakudo. "Stress-induced ferroelectricity and soft phonon modes in $SrTiO_3$". In: *Phys. Rev. B* 13 (1976), pp. 271–286. URL: https://link.aps.org/doi/10.1103/PhysRevB.13.271.

[154] A. Dal Corso. "Pseudopotentials periodic table: From H to Pu". In: *Computational Materials Science* 95 (2014), pp. 337–350. URL: https://www.sciencedirect.com/science/article/pii/S0927025614005187.

[155] L. Cao, E. Sozontov, and J. Zegenhagen. "Cubic to Tetragonal Phase Transition of $SrTiO_3$ under Epitaxial Stress: An X-Ray Backscattering Study". In: *Phys. Status Solidi A* 181.2 (2000), pp. 387–404.

[156] S. Baroni, P. Giannozzi, and A. Testa. "Green's-function approach to linear response in solids". In: *Phys. Rev. Lett.* 58 (1987), pp. 1861–1864. URL: https://link.aps.org/doi/10.1103/PhysRevLett.58.1861.

[157] X. Gonze, D. C. Allan, and M. P. Teter. "Dielectric tensor, effective charges, and phonons in α-quartz by variational density-functional perturbation theory". In: *Phys. Rev. Lett.* 68 (1992), pp. 3603–3606. URL: https://link.aps.org/doi/10.1103/PhysRevLett.68.3603.

[158] J. L. Servoin, Y. Luspin, and F. Gervais. "Infrared dispersion in $SrTiO_3$ at high temperature". In: *Phys. Rev. B* 22 (1980), pp. 5501–5506. URL: https://link.aps.org/doi/10.1103/PhysRevB.22.5501.

[159] W. G. Spitzer et al. "Far Infrared Dielectric Dispersion in $BaTiO_3$, $SrTiO_3$, and TiO_2". In: *Phys. Rev.* 126 (1962), pp. 1710–1721. URL: https://link.aps.org/doi/10.1103/PhysRev.126.1710.

[160] C. Lasota et al. "Ab initio linear response study of SrTiO3". In: *Ferroelectrics* 194.1 (1997), pp. 109–118. URL: https://doi.org/10.1080/00150199708016086.

[161] C. Verdi. "First-principles Fröhlich electron-phonon coupling and polarons in oxides and polar semiconductors". PhD thesis. University of Oxford, 2017.

[162] J. Lindhard. "On the Properties of a Gas of Charged Particles". In: *Kgl. Danske Videnskab. Selskab Mat.-fys. Medd.* 28.8 (1954).

[163] G. Grosso and G. Pastori Parravicini. *Solid State Physics*. London: Academic Press, 2000, pp. xii–xiii. URL: http://www.sciencedirect.com/science/article/pii/B9780123044600500001.

[164] B. B. Varga. "Coupling of Plasmons to Polar Phonons in Degenerate Semiconductors". In: *Phys. Rev.* 137 (1965), A1896–A1902. URL: https://link.aps.org/doi/10.1103/PhysRev.137.A1896.

[165] P. Y. Yu and M. Cardona. *Fundamentals of Semiconductors*. 4th. Springer Berlin, Heidelberg, 2010.

[166] J.-C. Ren and J.-S. Wang. *Origin of unexpected large Seebeck effect in SrTiO3: nonperturbative polaron study from ab initio cumulant expansion*. 2018. URL: https://arxiv.org/abs/1805.10722.

[167] C. Franchini et al. "Polarons in materials". In: *Nat. Rev. Mater.* 6 (2021), pp. 560–586. URL: https://doi.org/10.1038/s41578-021-00289-w.

[168] J. Lischner, D. Vigil-Fowler, and S. G. Louie. "Satellite structures in the spectral functions of the two-dimensional electron gas in semiconductor quantum wells: A *GW* plus cumulant study". In: *Phys. Rev. B* 89 (2014), p. 125430. URL: https://link.aps.org/doi/10.1103/PhysRevB.89.125430.

[169] J. Lischner et al. "Satellite band structure in silicon caused by electron-plasmon coupling". In: *Phys. Rev. B* 91 (2015), p. 205113. URL: https://link.aps.org/doi/10.1103/PhysRevB.91.205113.

[170] J. S. Zhou et al. "Dynamical effects in electron spectroscopy". In: *J. Chem. Phys.* 143.18 (2015), p. 184109. URL: https://doi.org/10.1063/1.4934965.

[171] D. Vigil-Fowler, S. G. Louie, and J. Lischner. "Dispersion and line shape of plasmon satellites in one, two, and three dimensions". In: *Phys. Rev. B* 93 (2016), p. 235446. URL: https://link.aps.org/doi/10.1103/PhysRevB.93.235446.

[172] B. K. Chang et al. arXiv: 2106.09810.

[173] J.-J. Zhou et al. arXiv: 2102.06840.

[174] J. M. Luttinger. "Fermi Surface and Some Simple Equilibrium Properties of a System of Interacting Fermions". In: *Phys. Rev.* 119 (1960), pp. 1153–1163. URL: https://link.aps.org/doi/10.1103/PhysRev.119.1153.

[175] W. Kohn and Vachaspati. "A Difficulty in Fröhlich's Theory of Superconductivity". In: *Phys. Rev.* 83 (1951), pp. 462–462. URL: https://link.aps.org/doi/10.1103/PhysRev.83.462.

[176] J. Ravichandran et al. "Tuning the electronic effective mass in double-doped $SrTiO_3$". In: *Phys. Rev. B* 83 (2011), p. 035101. URL: https://link.aps.org/doi/10.1103/PhysRevB.83.035101.

[177] E. A. Ekimov et al. "Superconductivity in Diamond". In: *Nature* 428 (2000), pp. 542–545. URL: https://doi.org/10.1038/nature02449.

[178] L. Boeri, J. Kortus, and O. K. Andersen. "Three-Dimensional MgB_2-Type Superconductivity in Hole-Doped Diamond". In: *Phys. Rev. Lett.* 93 (2004), p. 237002. URL: https://link.aps.org/doi/10.1103/PhysRevLett.93.237002.

[179] K.-W. Lee and W. E. Pickett. "Superconductivity in Boron-Doped Diamond". In: *Phys. Rev. Lett.* 93 (2004), p. 237003. URL: https://link.aps.org/doi/10.1103/PhysRevLett.93.237003.

[180] Y. J. Chang et al. "Structure and correlation effects in semiconducting $SrTiO_3$". In: *Phys. Rev. B* 81 (2010), p. 235109. URL: https://link.aps.org/doi/10.1103/PhysRevB.81.235109.

[181] S. Mandal et al. "How Correlated is the FeSe/$SrTiO_3$ System?" In: *Phys. Rev. Lett.* 119 (2017), p. 067004. URL: https://link.aps.org/doi/10.1103/PhysRevLett.119.067004.

[182] J.-M. Lihm and Cheol-Hwan Park. "Phonon-induced renormalization of electron wave functions". In: *Phys. Rev. B* 101 (2020), p. 121102. URL: https://link.aps.org/doi/10.1103/PhysRevB.101.121102.

[183] J. J. Hopfield. "Theory of the Contribution of Excitons to the Complex Dielectric Constant of Crystals". In: *Phys. Rev.* 112 (1958), pp. 1555–1567. URL: https://link.aps.org/doi/10.1103/PhysRev.112.1555.

[184] A. Mooradian and G. B. Wright. "Observation of the Interaction of Plasmons with Longitudinal Optical Phonons in GaAs". In: *Phys. Rev. Lett.* 16 (1966), pp. 999–1001. URL: https://link.aps.org/doi/10.1103/PhysRevLett.16.999.